

Ivan B. Djordjevic

# Quantum Biological Information Theory



Springer

# Quantum Biological Information Theory



Ivan B. Djordjevic

# Quantum Biological Information Theory



Springer

Ivan B. Djordjevic  
Department of Electrical and Computer Engineering  
University of Arizona  
Tucson, AZ, USA

ISBN 978-3-319-22815-0      ISBN 978-3-319-22816-7 (eBook)  
DOI 10.1007/978-3-319-22816-7

Library of Congress Control Number: 2015947789

Springer Cham Heidelberg New York Dordrecht London  
© Springer International Publishing Switzerland 2016

This work is subject to copyright. All rights are reserved by the Publisher, whether the whole or part of the material is concerned, specifically the rights of translation, reprinting, reuse of illustrations, recitation, broadcasting, reproduction on microfilms or in any other physical way, and transmission or information storage and retrieval, electronic adaptation, computer software, or by similar or dissimilar methodology now known or hereafter developed.

The use of general descriptive names, registered names, trademarks, service marks, etc. in this publication does not imply, even in the absence of a specific statement, that such names are exempt from the relevant protective laws and regulations and therefore free for general use.

The publisher, the authors and the editors are safe to assume that the advice and information in this book are believed to be true and accurate at the date of publication. Neither the publisher nor the authors or the editors give a warranty, express or implied, with respect to the material contained herein or for any errors or omissions that may have been made.

Printed on acid-free paper

Springer International Publishing AG Switzerland is part of Springer Science+Business Media  
([www.springer.com](http://www.springer.com))

*to Milena*



# Preface

Recent evidence suggests that quantum mechanics is relevant in photosynthesis, magnetoreception, enzymatic catalytic reactions, olfactory reception, photoreception, genetics, electron transfer in proteins, and evolution, to mention a few. It has become evident that certain organisms can harness some of the quantum-mechanical features for a biological advantage over competitors. On the other hand, the standard DNA template-replication paradigm is not able to explain neither the long-term storage of the genetic information nor the evolution of genetic material through generations. Classical/quantum information theory provides the limits, known as channel capacity, beyond biological errors that cannot be corrected for. Any correction mechanism in communication systems has the limits on error correction capability. The DNA pol proofreading and DNA repair mechanisms are weak error correction concepts, far away from biological channel capacity, and as such are unable to explain the faithful preservation of the genetic information through the ages. The concepts from unequal error protection must be used to explain the faithful preservations of important genes through generations. However, this genetic stability is not absolute, regardless of genetic error correction mechanism. On the other hand, the imperfect stability in genetic material is also responsible for evolution. Without evolution, life will be in the same form as it initially appeared. There were also many attempts in an effort to explain the structure of genetic code and transfer of information from DNA to protein by using the concepts of classical information theory. However, given that many biological processes in organisms are quantum mechanics dependent, classical information theory is insufficient to provide proper answers to many open problems today. Moreover, given that Shannon (classical) entropy is just the special case of von Neumann (quantum) entropy, it appears that only quantum information theory efforts are relevant.

The key idea in this book is to describe various biological processes as communication processes, be they of classical, quantum, or hybrid nature. By using this approach, we describe the information flow from DNA to protein as the quantum communication channel problem. In this model, DNA replication, DNA to mRNA transcription, and mRNA to protein translations are considered as imperfect

processes subject to biological errors. We employ this model to describe both faithful preservation of genetic information and the evolution of genetic information from generation to generation. We then establish the connection between operator sum representation, used to model quantum biological channels, and quantum master equation (QME), widely used in quantum biology to describe various processes listed above, in particular photosynthesis, magnetoreception, and photoreception, and demonstrate that QME is just the Markovian approximation of the operator sum representation. This indicates that the quantum channel model description given by operator sum representation and the QME description are equivalent to each other (under the Markovian approximation) and can be interchangeably used to simplify the description of quantum biological process. The particular use of representation is dictated by the biological problem at hand. Therefore, our approach essentially integrates quantum information theory (QIT) and currently existing quantum biology (QB) approaches, and as such it can be called the *quantum biological information theory*.

The book *Quantum Biological Information Theory* is a self-contained, tutorial-based introduction to quantum information theory and quantum biology. It serves as a single-source reference to the topic for researchers in bioengineering, communications engineering, electrical engineering, applied mathematics, biology, computer science, and physics. The book provides all the essential principles of the quantum biological information theory required to describe the quantum information transfer from DNA to proteins, the sources of genetic noise and genetic errors, as well as their effects. For additional details on the book, an interested reader is referred to the introduction chapter and contents.

The unique features of the book include:

- It integrates quantum information and quantum biology concepts.
- The book does not require the prior knowledge of quantum mechanics.
- The book does not require any prerequisite material except basic concepts of vector algebra at undergraduate level.
- The book does not require prior knowledge in genetics or cell biology.
- This book offers in-depth discussion of the quantum biological channel modeling, quantum biological channel capacity calculation, quantum models of aging, quantum models of evolution, quantum models on tumor and cancer development, quantum modeling of bird navigation compass, quantum aspects of photosynthesis, and quantum biological error correction.
- The successful reader of the book will be well prepared for further study in this area and will be qualified to perform independent research.

Finally, the author would like to thank Charles Glaser, Jeffrey Taub, and Nicole Lowary of Springer US for their tremendous effort in organizing the logistics of the book including editing and promotion, which is indispensable to make this book happen.

Tucson, AZ

Ivan B. Djordjevic

# Contents

<b>1</b>	<b>Introduction</b>	1
1.1	Quantum Biology Perspective	1
1.2	Quantum Information Theory and Biology	7
1.3	Organization of the Book	13
1.4	Concluding Remarks	15
	References	16
<b>2</b>	<b>Quantum Information Theory Fundamentals</b>	21
2.1	State Vectors, Operators, Projection Operators, and Density Operators	21
2.1.1	State Vectors and Operators	22
2.1.2	Projection Operators	23
2.1.3	Photon, Spin-½ Systems, and Hadamard Gate	24
2.1.4	Density Operators	26
2.2	Measurements, Uncertainty Relations, and Dynamics of a Quantum System	29
2.2.1	Measurements	29
2.2.2	Uncertainty Principle	32
2.2.3	Time-Evolution Schrödinger Equation	33
2.3	Quantum Information Processing (QIP) Fundamentals	36
2.3.1	Superposition Principle, Quantum Parallelism, Quantum Gates, and QIP Basics	37
2.3.2	No-Cloning Theorem and Distinguishing the Quantum States	42
2.3.3	Quantum Entanglement	44
2.3.4	Operator Sum Representation	46
2.3.5	Decoherence Effects, Depolarization, and Amplitude Damping Channel Models	48
2.4	Classical (Shannon) and Quantum (von Neumann) Entropies	52

2.5	Holevo Information, Accessible Information, and Holevo Bound . . . . .	53
2.6	Schumacher's Noiseless Quantum Coding Theorem and Holevo–Schumacher–Westmoreland Theorem . . . . .	54
2.6.1	Schumacher's Noiseless Quantum Coding Theorem and Quantum Compression . . . . .	54
2.6.2	Holevo–Schumacher–Westmoreland Theorem and Channel Coding . . . . .	59
2.7	Quantum Error-Correction Concepts . . . . .	64
2.8	Hydrogen-Like Atoms and Beyond . . . . .	67
2.9	Concluding Remarks . . . . .	72
	References . . . . .	72
<b>3</b>	<b>Fundamentals of Biological Thermodynamics, Biomolecules, Cellular Genetics, and Bioenergetics . . . . .</b>	<b>75</b>
3.1	Biological Thermodynamics . . . . .	75
3.1.1	The First Law of Thermodynamics, Perfect Gas, Enthalpy of the System . . . . .	76
3.1.2	Gibbs–Boltzmann Distribution Law, Second Law of Thermodynamics, and Third Law of Thermodynamics . . . . .	78
3.1.3	Biochemical Reaction Energetics . . . . .	83
3.2	Biomolecules . . . . .	87
3.2.1	Amino Acids, Peptides, and Proteins . . . . .	90
3.2.2	Carbohydrates and Corresponding Polymers . . . . .	104
3.2.3	Lipids, Phospholipids, Membranes, and Vesicles . . . . .	108
3.2.4	Nucleic Acids, Nucleosides, and Nucleotides . . . . .	111
3.3	Cellular Genetics . . . . .	115
3.3.1	DNA Structure and DNA Replication Process . . . . .	115
3.3.2	Genetic Code, RNA Molecules, Transcription, and Translation . . . . .	118
3.3.3	Gene Anatomy and Regulation of Gene Expression . . . . .	122
3.4	Mutations, Evolution, and DNA Repair . . . . .	128
3.5	Bioenergetics of the Cell . . . . .	134
3.6	Concluding Remarks . . . . .	140
	References . . . . .	141
<b>4</b>	<b>Quantum Information Theory and Quantum Mechanics-Based Biological Modeling and Biological Channel Capacity Calculation . . . . .</b>	<b>143</b>
4.1	Introduction . . . . .	143
4.2	Quantum Biological Channel Models Suitable for Study of Quantum Information Transfer from DNA to Proteins . . . . .	144

4.3	Sources of Genetic Errors and Genetic Noise: A Quantum-Mechanical Perspective . . . . .	156
4.4	Quantum Biological Channel Capacity Evaluation . . . . .	166
4.5	Quantum Modeling of Bird Navigation Compass . . . . .	170
4.6	Quantum Aspects of Photosynthesis . . . . .	175
4.7	Concluding Remarks . . . . .	191
	References . . . . .	192
<b>5</b>	<b>Quantum-Mechanical Modeling of Mutations, Aging, Evolution, Tumor, and Cancer Development</b> . . . . .	197
5.1	Quantum-Mechanical and Quantum Mechanics-Like Models for Mutations and Evolution . . . . .	197
5.2	Markovian Chain-Like Quantum-Mechanical Modeling of Mutations and Aging . . . . .	207
5.3	Classical, Semiclassical, and Quantum Modeling of Tumor and Cancer Development . . . . .	222
5.4	Concluding Remarks . . . . .	232
	References . . . . .	233
<b>6</b>	<b>Classical and Quantum Error-Correction Coding in Genetics</b> . . . . .	237
6.1	Classical/Quantum Information Theory in Genetics and Evolution . . . . .	238
6.2	Classical/Quantum Error-Correction Coding in Genetics and Evolution . . . . .	244
6.3	Topological Codes . . . . .	256
6.4	Subsystem Codes . . . . .	259
6.5	Nonbinary Quantum Stabilizer Codes . . . . .	261
6.6	Classical/Quantum DNA Error Correction Robust to Tumor and Cancer Introducing Mutation Errors . . . . .	264
6.7	Concluding Remarks . . . . .	265
	References . . . . .	266

# Chapter 1

## Introduction

**Abstract** This chapter is devoted to both historical perspective of quantum biology and the most relevant research topics in quantum biology. We start the chapter with an overview of Schrödinger's ideas on the relevance of quantum mechanics to biological processes and link his order-from-disorder principle to the second principle of thermodynamics applied to living organisms. After that, we describe the relevance of quantum mechanics in photosynthesis, magnetoreception, enzymatic catalytic reactions, olfactory reception, photoreception, genetics, electron transfer in proteins, and evolution, to mention a few. We then describe the generic quantum channel model describing the information flow from DNA to protein. In this model, DNA replication, DNA to mRNA transcription, and mRNA to protein translations are considered as imperfect processes subject to biological errors. The use of this model to describe the evolution of genetic information from generation to generation is described as well. We then describe the basics of quantum information theory (QIT) and show that Shannon (classical) entropy is just the special case of von Neumann (quantum) entropy. We then establish connection between operator sum representation used in QIT and quantum master equation (QME) used in quantum biology and show that QME is just a Markovian approximation of operator sum representation. This indicates that the quantum channel model description given by operator sum representation and QME description are equivalent to each other (for Markovian approximation) and can be interchangeably used to easier describe a particular biological process. The next section of the chapter is devoted to the organization of the book, with detailed description of each chapter. The final section summarizes the chapter.

### 1.1 Quantum Biology Perspective

In 1944, Erwin Schrödinger published a nonfiction science book entitled *What Is Life?* [1, 2]. This book was based on a series of public lectures he delivered in February 1943, under the auspices of the Dublin Institute for Advanced Studies at Trinity College, Dublin. In the first chapter of his book, Schrödinger introduces the “order-from-disorder” principle and explains that most physical laws on a large

scale originate from the chaos on a small scale. He uses the diffusion as an illustrative example to show that it can be modeled as a highly ordered process, although it is caused by random movement of atoms or molecules. In Chaps. 2 and 3, Schrödinger summarizes the hereditary mechanism known at the time when the book was written. Interestingly enough, he describes the important role of mutations in evolution and predicts that the hereditary information storage material, now known as DNA, must be simultaneously small in size but permanent in time. In Chap. 4, he connects the mutations to the quantum jumps (leaps). In the same chapter, he explains that stability of molecules, being composed of atoms, should be contributed to the quantum mechanics. In Chap. 5, Schrödinger introduces the concept “aperiodic crystal,” which contains the genetic information in its configuration of covalent chemical bonds and does not repeat itself. This aperiodic structure allows us to encode an almost infinite number of possibilities with a small number of basic units, now known as nucleotides. In Chap. 7, he connects the “order-from-disorder” principle to the second law of thermodynamics, according to which *the entropy of the universe for spontaneous processes is always positive*. He claims that a living organism is able to avoid the decay to thermodynamical equilibrium by homeostatically maintaining negative change in entropy. This interpretation was used later in Davydov’s *Biology and Quantum Mechanics* [3] to conclude that quantum mechanics is most relevant to isolated systems in pure states and as such has nothing to do with biological systems that are at thermal equilibrium in statistical states. However, as we will show in Chap. 3, the second law of thermodynamics can be written as follows:

$$\Delta S = \Delta S_{\text{system}} + \Delta S_{\text{environment}} > 0$$

where with  $\Delta S_{\text{system}}$  we denoted the entropy of the system, while with  $\Delta S_{\text{environment}}$  we denoted the entropy of the environment (surrounding). This interpretation of the second thermodynamics law is consistent with all types of systems: open, closed, and isolated ones. Even though that for biological system  $\Delta S_{\text{system}} < 0$ , due to the increase of order inside of a biological system, the overall entropy of the system and environment is always positive. Schrödinger further discusses determinism, free will, and the mystery of human consciousness, which is still a subject of intensive debates these days [4, 5].

Based on the above, we conclude that Schrödinger is not only one of the founders of quantum mechanics but also the founder of what is called today quantum biology (QB), even though some basic ideas on DNA structure and importance of mutations can be found in papers by Muller, such as [6]. Moreover, Watson and Crick were most probably inspired by Schrödinger’s book, in addition to the paper by Chargaff et al. [7], when proposing the DNA structure in their famous papers [8, 9]. In addition to explaining the DNA structure, Watson and Crick suggested that point mutation might be caused by tautomeric forms of nucleic acids [9]. This idea was later studied in a series of papers [10–14], and it is a subject of interest even these days [15–19]. In several recent publications [20–30], it has become clear that both Darwinian type of evolution (random mutations followed by

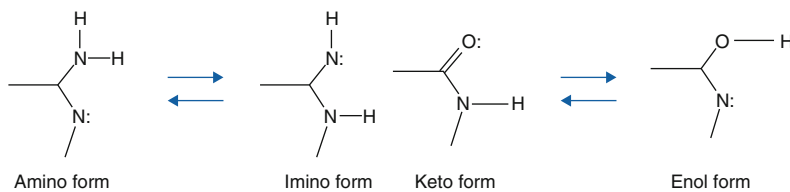
selection process) [31] and Lamarckian type of evolution (selected mutations beneficial to the organism) [32] are important. For low stress levels, the spontaneous mutations seem to be a dominant source to evolution, suggesting that the Darwinian evolution mode is more relevant. On the other hand, for strong stress levels, the adaptive mutations dominate, indicating that the Lamarckian mechanism is more relevant in this regime. The modernized Lamarckian mechanism, which can also be called neo-Lamarckism, can be described as follows: environmental factors introduce genomic changes, the mutations are targeted to specific genes, and the mutations provide the adaptation to the original cause. Clearly, this mechanism is well aligned with the adaptive mutation mechanism discussed in [33–35]. Based on current trends, we can recognize two trends in quantum evolution: (1) quantum evolution on a *genome level* [20, 21] and (2) quantum evolution on the *cellular level* (QECL) [26]. When genome-level evolution combines both Darwinian and Lamarckian principles, it is commonly referred to as the *epigenetic evolution*. The QECL is introduced by Ogryzko's research team [26]. It is well known that the state space of a composite system can be represented in terms of the tensor product of states of individual systems. The interaction with environment helps the biological composite system to suppress the most of exotic states and yield to the *preferred state* of the biological system. Therefore, in this interpretation, the environmentally induced decoherence is beneficial to the biological system.

There exists a growing evidence that *migration birds* can sense the direction of the gyromagnetic field based on chemical reaction whose product yields are dependent on the orientation of the reactants within the field [36–51]. Given that the magnetic field is very weak, between 30 and 70  $\mu\text{T}$ , the magnetoreception mechanism can only detect the angle between the magnetic field lines and the Earth's surface. This indicates that the migration birds can only distinguish between a pole and the equator, but cannot distinguish between north and south poles, which is sufficient for migration purpose. In addition to migration birds, the butterfly, the fruit fly, and other animals can also sense the direction. There exist different models to explain the magnetoreception, including very exotic ones, but it appears that radical pair (RP) magnetoreception mechanism [42] provides the most reasonable explanation.

The photosynthetic apparatus of prokaryotes is composed of three functional modules: (1) *receptor pigments*, organized into *light-harvesting* (LH) antennas' system (responsible for the photon absorption and transfer of absorbed energy to the reaction centers), (2) *the photosynthesis reaction center* (RC) (responsible for transformation of absorbed electromagnetic energy into the chemical energy), and (3) *the photosynthetic electron transport system* (responsible for the electron transport and accumulation of energy into ATP molecules). The pigments involved and precise photosynthetic apparatus differ from organism to organism [52–55]. Purple bacteria have a single RC and the photosynthetic apparatus is mainly located in so-called chromatophores, the lipid vesicles of 30–60 nm in diameter. The photosynthesis apparatus of cyanobacteria, algae, and plants employ two RCs operating in a series, known as photosystem II (PS II) and photosystem I (PS I), and are based on chlorophylls (absorbing pigment molecules) randomly arranged.

In prokaryotes, the RC and electron transport system are localized into cytoplasmic membrane (CPM). In cyanobacteria and prochlorophytes, the RC and electron transport system can also be located into thylakoid membranes (stacks of parallel sheets close to the CPM with a low packing density, which provides space for the external LH antennae). The localization of pigments in prokaryotes also varies. In purple bacteria, the pigments are located in the CPM. In green bacteria, the pigments are located in a specialized photosynthetic antenna complex known as a *chlorosome* (organizational rod units connected to the membrane but not being part of it). The fast excitation transfer along the spiral layer expedites the interrod transfer to bacteriochlorophyll (BChl) *a* to the baseplates. The energy is further transferred to reaction center through the Fenna–Matthews–Olson (FMO) complex, exhibiting almost perfect efficiency. The FMO complex is composed of a protein backbone, which contains a hydrophobic pocket holding seven strongly coupled BChl molecules, each with electronic transition near 800 nm (so-called  $Q_y$  transition) [56]. These seven states get coupled to one another electrostatically by dipole–dipole interaction. The purpose of the FMO complex is to maximize the efficiency of a single-excitation transport to the RC. The rate at which excitation leaves the target molecule to reach the RC is in the order of THz. On the other hand, BChl fluorescence relaxation time is about 1 ns. Clearly, the excitation rate is faster than the relaxation rate. Consequently, quantum effects are important here to enable such a fast excitation rate. It has been found in [56–58] that the coherence time is  $\leq 300$  fs at room temperature, which is more than enough for quantum excitation transfer. The protein scaffold can be modeled as the environment (bath, ambient) of harmonic oscillators with Gaussian fluctuations. The interaction of coherent excitation states and thermal (ambient) environment causes the level-broadening effect, which allows an easy escape from the local minima. The authors in [59] have shown numerically that such organization of the FMO complex is optimal (for green sulfur bacteria) with respect to variations in reorganization energy and environmental correlation time changes.

The point mutations are caused by tautomeric forms of nucleic acids, as claimed by many authors [10–17]. There exist two main forms of tautomerism: (1) *amino-imino* tautomerism and (2) *keto-enol* tautomerism given respectively by [11]:



The amino and keto forms are considered as standard forms, as shown in Fig. 1.1. Namely, the genome, representing the ensemble of genetic codewords, is prerecorded in DNA sequence by using the nucleotide alphabet composed of four symbols: adenine (A), guanine (G), cytosine (C), and thymine (T). The pairing of

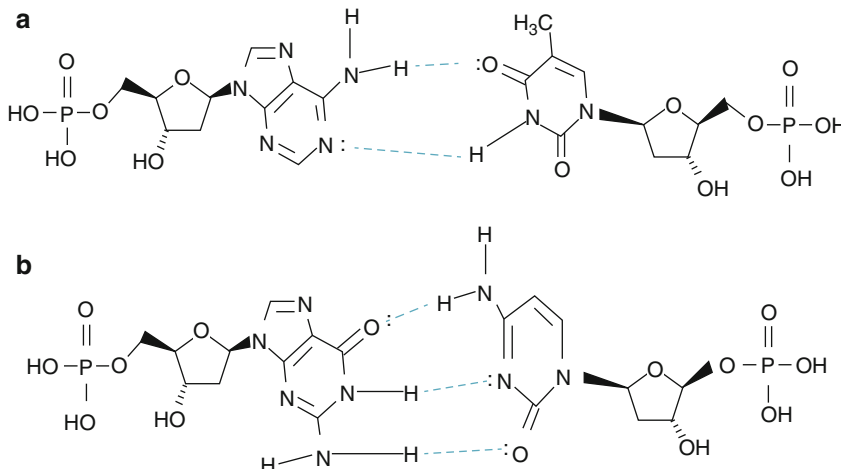
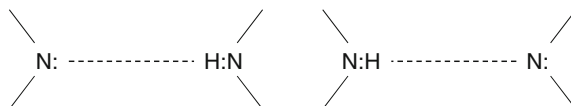


**Fig. 1.1** Standard nucleic acids' pairing rule: (a) A = T pairing and (b) G≡C pairing

nucleotides is specific to T = A and C ≡ G combinations, with “—” representing the hydrogen bond (H-bond). To determine the exact probability of occurrence of a tautomeric form, we can use the *double-well* model and tunneling effect in a fashion similar to that first described in [11]. By close inspection of Fig. 1.1, we can see that H-bonds in standard forms are asymmetric. Further, the protons have two equilibrium positions, for instance:



The principles of quantum mechanics indicate that the proton can move between these two equilibrium positions. The proton *probability density* can be determined as  $\rho(x, t) = |\psi(x, t)|^2$ , where  $\psi(x, t)$  is the corresponding *wave function*. Therefore, with certain probability, the proton can move in classically “forbidden” tautomeric states.

In order to determine the rate of many *enzymatic catalytic reactions*, the corresponding rate-determination step very often involves the tunneling of a proton, hydride, or hydrogen atom [60, 61]. Additionally, in the so-called proton-coupled electron transfer, important in many biological processes, the simultaneous proton and electron transfer from opposite sides takes place [61, 62]. The quantum effects in such enzymes provide the quantum energy correction of the activation energy, toward lower levels of energy, improving, therefore, the catalytic rates. The intrinsic kinetic isotope effect (KIE) in enzyme catalytic reactions is used as a measure of nuclear quantum tunneling effects [61, 63]. The large value of KIE (such as H/D

KIEs close to 100 in monooxygenase [61]) indicates the presence of quantum tunneling effects.

The similar concept can be applied to the *long-range electron transfer* [61]. In photosynthesis and aerobic respiration, the long-range electron flow between distant redox-active cofactors is a very common effect. Interestingly enough, experimental findings by Gray and Winkler [64] indicate that long-range electron transfer in proteins occurs in single-step tunneling rather than multistage hopping. The existence of specific channels for electron transfers in protein through covalent, hydrogen, and van der Waals bonds has been found by applying the pathway approach [65]. Some authors claims that in order to facilitate the electron transfer, proteins provide efficient conduction pathways [66]. There is also a discussion that quantum interferences among distinct pathways can play an important role in some proteins [67].

There exist many theories to explain the *olfactory reception* (the sense of smell). Two of them are predominant: (1) the shape theory of olfaction [68, 69] and (2) vibrational theory of olfaction [70–72]. In the shape theory of olfaction, the activation of corresponding sensory cells in invertebrates is dependent on molecular size, molecular shape, and functional groups. The key idea in this model is a lock-and-key mechanism by which a scent molecule fits into olfactory receptors, which distinguishes different smells. However, it was found in [70–72] that molecules of similar shape can smell quite differently. In the vibrational theory of smell, a molecule's smell character is determined by its vibrational frequency. The key idea behind the quantum version of the vibrational theory [72] is that a phonon-assisted tunneling of an electron between two receptor sides via the odorant enables the high precision of olfaction system. A recent experiment by Franco et al. [73] has found that *Drosophila melanogaster* can distinguish hydrogen and deuterium in odorants although being identically shaped isotopes, which disproves the shape theory of olfaction. Nevertheless, the vibrational theory still faces a fierce criticism by some authors (see [74] and references therein).

Biological *photoreceptors* contain chromophores, which absorb certain wavelengths of the visible-light spectrum and transmit/reflect others. In particular, transmembrane protein rhodopsin contains a retinal molecule that undergoes photoisomerization upon the light absorption [75–77]. The photoisomerization process is ultrafast (duration is shorter than 200 fs) with high quantum yield and clearly represents a quantum-mechanical effect. The photoisomerization triggers a protein conformational change; a series of enzymes get activated resulting in hydrolysis of cyclic guanosine monophosphate, which closes the  $\text{Na}^+$  ion channels. The hyperpolarization such obtained generates an electrical pulse that is further transferred to a nerve cell.

We have arrived to the point to define the QB topics, based on the above discussion. The widest definition of quantum biology would be to relate it to biological phenomena that make explicit use quantum-mechanical principles to either carry out the process or attain functionality. This was the main focus of *International Journal of Quantum Chemistry: Quantum Biology Symposium Series*, which is now discontinued. Initially, researchers focused their attention on applying

the quantum mechanics to study biological processes. However, in recent book [60], the authors have reduced QB topics to excited electronic states and corresponding dynamics, long-range tunneling effect through barriers, interference effects, and related biological processes. The goal was to provide new emerging insights from a quantum-mechanical perspective. However, with such an approach, the intramolecular forces (hydrogen bonds and van der Waals forces), predominant in defining the DNA structure and protein structures and responsible for membrane formation and enzyme–substrate associations, to mention a few, are completely left out. In this book instead, we prefer to draw a QB boundary somewhere in between these two extremes.

## 1.2 Quantum Information Theory and Biology

The use of both classical and quantum information theory (QIT) as well as error correction to describe the genome preservation and biological evolution is getting momentum, which can be judged by a number of recent papers related to these problems [78–84]. There were also many attempts in an effort to explain the structure of genetic code and transfer of information from DNA to protein by using the concepts of quantum mechanics (QM) [22, 85]. For instance, the general quantum-mechanical model to describe the transfer of information from DNA to protein by using the QIT is proposed by Karafyllidis [85]. However, given the high complexity of the problem, the determination of *quantum biological channel capacity* was still an open problem, until recently [19].

In this book, we develop the quantum biological channel models suitable for study of quantum information transfer from DNA to proteins. The quantum channel models with memory and without memory will be described. The quantum genetic noise will be described in terms of tautomeric nucleic base-pair formation, the concept developed by Löwdin [11] and briefly discussed in the previous section. By using the Holevo–Schumacher–Westmoreland (HSW) theorem [86], we will use the proposed models to determine the quantum biological channel capacity of various biological channels. The developed quantum channel models will also be used to describe the DNA to protein transfer based on quantum error-correction concepts. The quantum biological channel modeling will be followed by the development of quantum-mechanical models of aging and evolution. The concepts from both classical and quantum information theories will be used to describe the evolution of biological channel capacity through generations. In order to do so, several classical and quantum biological channel models will be employed including Markovian classical and Markovian-like quantum model, hybrid quantum-classical model, multilevel symmetric channel model, and Kimura model-based Markovian process. In order to describe the reliable long-time storage of genetic information in DNA, the use of unequal error protection (UEP) coding will be studied. Several classes of both classical and quantum error-correction codes suitable for UEP on a cellular level will be described. The following classes of

quantum codes suitable to either protect information flow from DNA to protein or preserve the genetic material stored in DNA will be described: stabilizer codes, topological codes, subsystem codes, and nonbinary stabilizer codes. We will also study the process of creation of tumors and cancer using the concepts from classical/QIT. Further, the bird navigation process and photosynthesis will be described. Finally, we will discuss the possible use of both classical and quantum error-correction concepts to improve tolerance to tumor and cancer introducing errors. Additional details on the organization of the book will be provided in incoming section. In the rest of this section, we briefly describe some important concepts from the book, with details to be found in incoming chapters.

The key idea in this book is to describe various biological processes as communication processes, be of classical, quantum, or hybrid nature. As an illustration, using the language of communication engineering, the purpose of a biological genetic system is to transport the information related to protein synthesis, contained in a DNA, and deliver it to the protein (destination) reliably. In Fig. 1.2a, we describe the generic quantum biological model suitable to study the flow of information from DNA to protein. The process of transcription is interpreted as

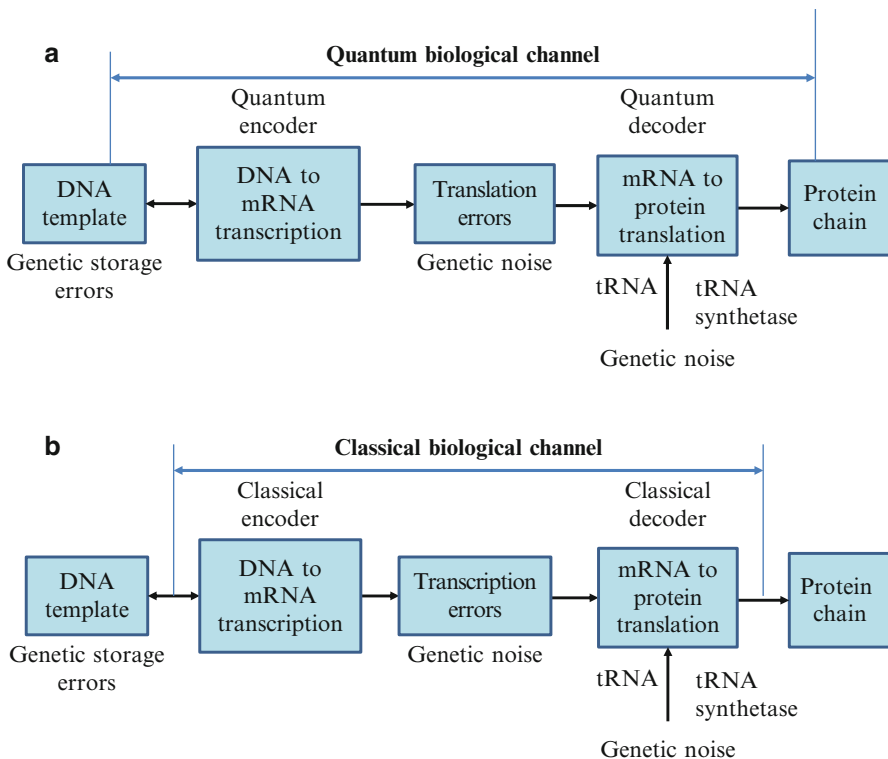


**Fig. 1.2** (a) Generic quantum channel model describing the information flow from DNA to protein. (b) Corresponding classical biological channel model

encoding; the various errors introduced during replication, transcription, or translation are considered as a source of genetic noise, while the process of translation is interpreted as decoding. For convenience, the corresponding classical biological channel model is shown in Fig. 1.2b. The key difference with respect to the model due to Yockey [78] and others [80, 82] is that here we assume that the DNA encoder is subject to DNA storage errors, while the decoder is subject to translation errors, so that the biological channel has been extended to include the DNA encoder and decoder (performing translation from mRNA to protein). The process of translation is also prone to errors, which can also be contributed to the genetic noise. Therefore, all errors introduced in any stage shown in Fig. 1.2a are called “genetic noise.” The transcription, DNA point mutations, insertions, deletions, and translation can all be interpreted as the quantum channel. It is assumed that genetic noise introduces random errors, which can be classified into several broad categories. The first types of errors, “storage errors,” occur in DNA itself as it is an imperfect storage of genetic information. The second types of errors are introduced during the DNA replication process. The third types of errors, transcription errors, are introduced during DNA to mRNA transcription process. The fourth types of errors, translation errors, are introduced during the translation process. Therefore, the key difference with respect to communication systems, where both encoders and decoders are implemented from perfect gates; in biological systems, DNA replication, DNA to mRNA transcription, and mRNA to protein translations are imperfect processes. Once more, this difference requires redefining the channel model, as it is done in Fig. 1.2. To describe the various genetic noises introducing processes, we can use either the quantum channel models or concepts from quantum mechanics, in particular the quantum master equation (QME). To show that these two approaches are equivalent to each other, we need briefly to review some basic concepts from the QIT.

In quantum mechanics, the primitive undefined concepts are *physical system*, *observable*, and *state*. A physical system is any sufficiently isolated quantum object, say an electron, a photon, or a molecule. An observable will be associated with a measurable property of a physical system, say energy or z-component of the spin. The condition of a quantum-mechanical system is completely specified by its *state vector*  $|\psi\rangle$  in a Hilbert space  $H$  (a vector space [86] on which a positive-definite scalar product is defined) over the field of complex numbers. Any state vector  $|\alpha\rangle$ , also known as a *ket*, can be expressed in terms of basis vectors  $|\phi_n\rangle$  by

$$|\alpha\rangle = \sum_{n=1}^{\infty} a_n |\phi_n\rangle.$$

An *observable*, such as momentum and spin, can be represented by an *operator*, say  $A$ . An operator acts on a ket from the left,  $(A) \cdot |\alpha\rangle = A |\alpha\rangle$ , which results in another ket. An operator  $A$  is said to be *Hermitian* if

$$A^\dagger = A, \quad A^\dagger = (A^T)^*.$$

The Hermitian conjugate of a ket  $|\alpha\rangle$  is denoted by  $\langle\alpha|$  and called the “bra.” The space dual to ket space is known as *bra space*. The *scalar (inner) product* of two state vectors  $|\alpha\rangle = \sum_n a_n |\phi_n\rangle$  and  $|\beta\rangle = \sum_n b_n |\phi_n\rangle$  is defined by

$$\langle\beta|\alpha\rangle = \sum_{n=1}^{\infty} a_n b_n^*.$$

Let the large number of quantum systems of the same kind be prepared, each in one of a set of states  $|\phi_n\rangle$ , and let the fraction of the system being in state  $|\phi_n\rangle$  be denoted by probability  $P_n$  ( $n = 1, 2, \dots$ ):

$$\langle\phi_m|\phi_n\rangle = \delta_{mn}, \quad \sum_n P_n = 1$$

Therefore, this ensemble of quantum states represents a classical *statistical mixture* of kets. The probability of obtaining  $\xi_n$  from the measurement of observable  $\Xi$  will be

$$\text{Pr}(\xi_k) = \sum_{n=1}^{\infty} P_n |\langle\xi_k|\phi_n\rangle|^2 = \sum_{n=1}^{\infty} P_n \langle\xi_k|\phi_n\rangle \langle\phi_n|\xi_k\rangle = \langle\xi_k|\rho|\xi_k\rangle,$$

where the operator  $\rho$  is known as a *density operator* and it is defined by

$$\rho = \sum_{n=1}^{\infty} P_n |\phi_n\rangle \langle\phi_n|.$$

The expected value of density operator is given by

$$\langle\rho\rangle = \sum_{k=1}^{\infty} \xi_k \text{Pr}(\xi_k) = \sum_{k=1}^{\infty} \xi_k \langle\xi_k|\rho|\xi_k\rangle = \sum_{k=1}^{\infty} \langle\xi_k|\rho\Xi|\xi_k\rangle = \text{Tr}(\rho\Xi)$$

In QIT, the density matrix can be used to determine the amount of information conveyed by the quantum state, i.e., to compute the von Neumann entropy:

$$S = \text{Tr}(\rho \log \rho) = - \sum_i \lambda_i \log_2 \lambda_i,$$

where  $\lambda_i$  are the eigenvalues of the density matrix. The corresponding Shannon entropy can be calculated by

$$H = - \sum_i p_i \log_2 p_i,$$

where  $p_i$  is the probability of selecting the  $i$ -th vector from an ensemble of orthogonal vectors. So the Shannon (classical) entropy is just a special case of the von Neumann (quantum) entropy, when the density matrix is diagonal.

Let the composite system  $C$  be composed of quantum register  $Q$  and environment  $E$ . This kind of system can be modeled as a closed quantum system. Because the composite system is closed, its dynamic is unitary, and the final state is specified by a unitary operator  $U$  as follows  $U(\rho \otimes \varepsilon_0)U^\dagger$ , where  $\rho$  is a density operator of the initial state of quantum register  $Q$  and  $\varepsilon_0$  is the initial density operator of the environment  $E$ . The reduced density operator of  $Q$  upon interaction  $\rho_f$  can be obtained by tracing out the environment:

$$\rho_f = \text{Tr}_E[U(\rho \otimes \varepsilon_0)U^\dagger] \equiv \xi(\rho)$$

The transformation (mapping) of initial density operator  $\rho$  to the final density operator  $\rho_f$ , denoted as  $\xi : \rho \rightarrow \rho_f$ , given by the equation above, is often called the *superoperator* or *quantum operation*. The final density operator can be expressed in the so-called operator sum representation as follows:

$$\rho_f = \sum_k E_k \rho E_k^\dagger, \quad (1.1)$$

where  $E_k$  are known as the Kraus operators for the superoperator satisfying the normalization condition  $\sum_k E_k E_k^\dagger = I$ . Clearly, in the absence of environment, the superoperator becomes  $U\rho U^\dagger$ , which is nothing else but a conventional time-evolution quantum operation.

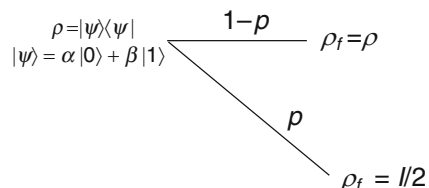
As an illustration, we described briefly the depolarization channel [86]. The *depolarizing channel*, as shown in Fig. 1.3, with probability  $1-p$  leaves the qubit as it is, while with probability  $p$  moves the initial state into  $\rho_f = I/2$  that maximizes the von Neumann entropy  $S(\rho) = -\text{Tr } \rho \log \rho = 1$ .

Under Markovian assumption, we can write

$$\rho(t + \delta t) = \rho(t) + O(\delta t) = E_0 \rho E_0^\dagger + \sum_{k=1,2,\dots} E_k \rho E_k^\dagger, \quad (1.2)$$

where

**Fig. 1.3** Depolarizing channel model representation using density operator description



$$E_0 = I + O(\delta t) = I + (K - jH)\delta t + o(\delta t) \quad \text{and} \quad E_k = L_k \sqrt{\delta t} + O(\sqrt{\delta t}); \quad (1.3)$$

with  $H$  and  $K$  being the Hermitian operators. From the normalization condition, we have that

$$\sum_{k=0,1,\dots} E_k E_k^\dagger = I = I + 2K\delta t + \sum_{k=1,2,\dots} L_k^\dagger L_k \delta t + o(\delta t), \quad (1.4)$$

which indicates that

$$K = -0.5 \sum_{k=1,2,\dots} L_k^\dagger L_k. \quad (1.5)$$

As  $\delta t \rightarrow 0$ , the (1.2), after the substitution of (1.5) into (1.3) and then (1.3) into (1.2), becomes

$$\frac{\partial \rho}{\partial t} = [-jH, \rho] + \sum_{k=1,2,\dots} \left[ L_k \rho L_k^\dagger - 0.5 \left\{ L_k^\dagger L_k, \rho \right\} \right], \quad (1.6)$$

where we use  $\{A, B\} = AB + BA$  to denote the anticommutator. Therefore, the QME (1.6) is just the Markovian approximation of the operator sum representation (1.1). (For simplicity, we omitted the reduced Planck constant  $\hbar = h/2\pi$  from discussion above.) In other words, for Markovian approximation, the quantum channel model description given by operator sum representation and QME description are equivalent to each other and will be both used throughout the book. The particular use of representation is dictated by the biological problem at hand. Therefore, our approach essentially integrates QIT and currently existing QB approaches, and as such, it can be called the *quantum biological information theory*.

Before concluding this section, we return to the quantum biology at the cellular model [26, 87] introduced above, as it nicely establishes connection between QIT discussed above and biology processes. Namely, it is well known that the state space of a composite system can be represented in terms of the tensor product of states of individual systems. The state of the macroscopic system can then be represented as the following entangled state (the state that cannot be written as a tensor product):

$$|\psi\rangle = a_1 \left( |\psi_1^{(1)}\rangle |\psi_2^{(1)}\rangle \dots \right) + \dots + a_i \left( |\psi_1^{(i)}\rangle |\psi_2^{(i)}\rangle \dots \right) + \dots$$

The density matrix describing the interaction of the system  $S$  and the environment  $E$  can be represented as

$$\rho = |\psi_{ES}\rangle \langle \psi_{ES}|.$$

By tracing out the environmental degrees of freedom, we obtain the state of the system after interaction with environment:

$$\rho_S = \text{Tr}_E |\psi_{ES}\rangle\langle\psi_{ES}|.$$

For instance, for the environmental basis  $\{|e_i\rangle\}$ , the reduced density operator states can be written as [87]

$$\rho_S = \sum a_i a_j^* \langle e_i | e_j \rangle |s_i\rangle\langle s_j|,$$

which will in general contain off-diagonal system terms  $|s_i\rangle\langle s_j|$ . The dynamic evolution of composite environment-quantum system (ES) can lead to rapid separation of different quantum states S, and off-diagonal term can vanish in time due to averaging effect, resulting in decoherence. In physics, the environment is typically homogenous, while in biology, it is quite opposite. The environment helps to suppress most of the exotic states and yields to the *preferred state* of the biological system. This environmentally induced decoherence is, therefore, beneficial to the biological system. Since the environment changes all the time, we need to observe several environments, say  $E_0, E_1, \dots, E_i, \dots$ . The effect of each environment  $E_i$  on the biological system can be represented by a unique set of preferred basis states  $\{|s_i^{(j)}\rangle\}$ . Let the reduced density operator of the biological system after interaction with environment  $E_0$  be denoted as  $\rho_{S,0}$ . The corresponding preferred basis states will be  $\{|s_0^{(j)}\rangle\}$ . If the environment changes to  $E_i$  ( $i \neq 0$ ), the corresponding set of preferred basis states will be  $\{|s_i^{(j)}\rangle\}$ . Providing that the corresponding environmental basis states are orthogonal, the change of the environment can be represented by the following mapping of preferred biological states:

$$\rho_{S,0} \xrightarrow{E_0 \rightarrow E_i} \rho_{S,i}.$$

Clearly, with this interpretation, the decoherence represents the positive force for adaptive mutation and evolution.

### 1.3 Organization of the Book

The book is organized as follows. After the Introduction, Chap. 2 provides an overview of the basic concepts of quantum information processing (QIP) and QIT. The following topics from quantum information processing are described in Sects. 2.1–2.3: state vectors, operators, density operators, measurements and dynamics of a quantum system, superposition principle, quantum parallelism, no-cloning theorem, and entanglement. The following concepts from QIT are described in Sects. 2.4–2.6: Holevo information, accessible information, Holevo bound, Shannon entropy and von Neumann entropy, Schumacher's noiseless quantum coding theorem, and HSW theorem. Section 2.7 is devoted to the quantum error-correction concepts. Finally, Sect. 2.8 is related to the hydrogen-like atoms (and beyond).

In Chap. 3, we describe the basics of biological thermodynamics (Sect. 3.1), biomolecules (Sect. 3.2), cellular genetics (Sect. 3.3), mutations and evolution (Sect. 3.4), and bioenergetics (Sect. 3.5). The following biomolecules are described: amino acids, peptides, proteins, carbohydrates, and corresponding polymers; nucleic acid, nucleosides, and nucleotides; and phospholipids. Regarding the cell dynamics, the following topics are described: DNA structure, the genetic code, gene anatomy, DNA synthesis and repair, transcription, and translation. Regarding the energetics of the cell, we describe the universal forms of energy (ATP and proton motive force) and the metabolism of the organism. We also discuss the relationship between genetics and evolution.

Chapter 4 is devoted to the quantum biological channel models suitable for study of quantum information transfer from DNA to proteins and corresponding channel capacity calculations. It is organized as follows. In Sect. 4.2, the quantum biological channel models suitable for study of quantum information transfer from DNA to proteins are described. The sources of genetic noise and genetic errors are also described in the same section. Various sources of genetic errors and genetic noise are studied in Sect. 4.3 using quantum-mechanical formalism. The quantum biological channel capacity evaluation is further described in Sect. 4.4. Section 4.5 is devoted to the use of quantum-mechanical concepts to describe the bird navigation compass. Finally, the quantum-mechanical aspects of photosynthesis are discussed in Sect. 4.6.

In Chap. 5, we describe the quantum-mechanical models to accurately describe the process of creation spontaneous, induced, and adaptive mutations. These models are then used in Sect. 5.1 to describe the processes of evolution and aging. The various theories of quantum evolution and epievolution are studied as well. We describe the Markovian chain-like classical and quantum-mechanical modeling of mutations and aging in Sect. 5.2. In the same section, the hybrid quantum-classical biological channel model with memory is described as well. In Sect. 5.3, various classical, semiclassical, and quantum models of cancer development are studied.

The main subject of Chap. 6 is on the use of classical/QIT and coding in genetics and evolution. Section 6.1 is related to various concepts ranging from classical to quantum information theories to describe the evolution of biological channel capacity through generations. In order to do so, several classical and quantum biological channel models are employed including Markovian classical and Markovian-like quantum model, hybrid quantum-classical model, multilevel symmetric channel model, and Kimura model-based Markovian process. In order to describe the reliable long-time storage of genetic information in DNA, in Sect. 6.2, the use of UEP coding is advocated. Several classes of error-correction codes suitable for UEP on a cellular level are described including nested coding, multilevel coding, rate-adaptive coding, and generalized LDPC coding. The use of concepts of constrained coding to describe the genetic information flow from DNA to proteins is also studied in the same section as well as joint constrained and error-correction coding. After that, the use of quantum error-correction concepts to deal with environmental errors including canonical quantum error-correction and

stabilizer codes is briefly described. In Sect. 6.3, the topological codes are described that might be relevant to biological processes as they only involve the local qubits in encoding process. In Sect. 6.4, the subsystem codes are described. The key idea behind subsystem codes is to decompose the quantum code as the tensor product of two subsystems, exon subsystem  $A$  and intron subsystem  $B$ , and we are concerned with correcting errors only on the exon subsystem, while subsystem  $B$  is used to absorb environmental errors in addition to storing the generalized parity qubits. In Sect. 6.5, we describe the use of nonbinary quantum stabilizer codes to deal with nucleobase substitution errors, both random and burst errors. In Sect. 6.6, we discuss the possible use of both classical and quantum error-correction concepts to improve tolerance to tumor and cancer introducing errors.

## 1.4 Concluding Remarks

This chapter has been devoted to both historical perspective of quantum biology and the most relevant research topics in quantum biology at the same time. In Sect. 1.1, we first have provided an overview of Schrödinger's ideas on relevance of quantum mechanics to biological processes and have linked his order-from-disorder principle to the second principle of thermodynamics applied to living organisms. In the same section, we have described the relevance of quantum mechanics in photosynthesis, magnetoreception, enzymatic catalytic reactions, olfactory reception, photoreception, genetics, electron transfer in proteins, and evolution. Further, we have discussed possible definitions of quantum biology. In Sect. 1.2, we have described the generic quantum channel model for the information flow from DNA to protein. In this model, DNA replication, DNA to mRNA transcription, and mRNA to protein translations have been interpreted as imperfect processes subject to biological errors. The use of this model to describe the evolution of genetic information from generation to generation has been discussed as well. We further have described the basics of QIT and have shown that Shannon (classical) entropy is just the special case of von Neumann (quantum) entropy. We have established the connection between operator sum representation used in QIT and QME, used in quantum biology. It has been shown that QME is just a Markovian approximation of operator sum representation. We have shown that the quantum channel model description given by operator sum representation and QME description are equivalent to each other (for Markovian approximation). Section 1.3 has been devoted to detailed description of the organization of the book.

## References

1. Schrödinger E (1944) What is life? The physical aspect of the living cell. Based on lectures delivered under the auspices of the Dublin Institute for Advanced Studies at Trinity College, Dublin, Feb 1943
2. Schrödinger E (1948) What is life? The physical aspect of the living cell. Cambridge University Press, Cambridge
3. Davydov AS (1981) Biology and quantum mechanics. Pergamon, New York
4. Hameroff S, Hagan S, Tuszyński JA (2002) Quantum computation in brain microtubules: decoherence and biological feasibility. *Phys Rev E Stat Nonlin Soft Matter Phys* 65 (6 Pt 1):061901
5. Behrman EC, Gaddam K, Steck JE, Skinner SR (2006) Microtubules as a quantum Hopfield network. In: Tuszyński JA (ed) The emerging physics of consciousness. Springer, New York, pp 351–370
6. Muller HJ (1922) Variation due to change in the individual gene. *Am Nat* 56:32–50
7. Chargaff E, Zamenhof S, Green C (1950) Composition of human desoxypentose nucleic acid. *Nature* 165:756–757
8. Watson JD, Crick FH (1953) Molecular structure of nucleic acids: a structure for deoxyribose nucleic acid. *Nature* 171(4356):737–738
9. Watson JD, Crick FHC (1953) Genetical implications of the structure of deoxyribonucleic acid. *Nature* 171:964–967
10. Rein R, Harris FE (1965) Studies of hydrogen-bonded systems. Potential-energy surface, tunneling, and tautomeric equilibria in the H-N···N and O···H-N bonds of the Guanine-cytosine base pair. *J Chem Phys* 43:4415–4421
11. Löwdin PO (1966) Quantum genetics and the aperiodic solid: some aspects on the biological problems of heredity, mutations, aging, and tumors in view of the quantum theory of the DNA molecule. In: Löwdin PO (ed) Advances in quantum chemistry, vol 2. Academic, New York, pp 213–360
12. Lunell S, Sperber G (1967) Study of the hydrogen bonding in the Adenine-Thymine, Adenine-Cytosine, and Guanine-thymine base pairs. *J Chem Phys* 46(6):2119–2124
13. Parker BR, van Every J (1971) Quantum tunneling in DNA. *Chem Phys Lett* 8:94–99
14. Tolpygo KB, Olkhovskaya IP (1972) Proton transitions in the hydrogen bonds of the DNA base pairs. *Chem Phys Lett* 16:550–554
15. Villani G (2005) Theoretical investigation of hydrogen transfer mechanism in the adenine-thymine base pair. *Chem Phys* 316:1–8
16. Villani G (2006) Theoretical investigation of hydrogen transfer mechanism in the guanine-cytosine base pair. *Chem Phys* 324:438–446
17. Villani G (2012) Theoretical investigation of the hydrogen atom transfer in the hydrated A–T base pair. *Chem Phys* 394:9–16
18. Fu L-Y, Wang G-Z, Ma B-G, Zhang H-Y (2011) Exploring the common molecular basis for the universal DNA mutation bias: revival of Löwdin mutation model. *Biochem Biophys Res Commun* 409:367–371
19. Djordjevic IB (2012) Quantum biological channel modeling and capacity calculation. *Life* 2:377–391
20. McFadden J, Al-Khalili J (1999) A quantum mechanical model of adaptive mutation. *Biosystems* 50:203–211
21. McFadden J (2000) Quantum evolution. W.W. Norton, New York
22. Ogryzko VV (2008) Erwin Schrödinger, Francis Crick and epigenetic stability. *Biol Direct* 3:15
23. Koonin EV, Wolf YI (2009) Is evolution Darwinian or/and Lamarckian? *Biol Direct* 4:42
24. Jablonka E, Raz G (2009) Transgenerational epigenetic inheritance: prevalence, mechanisms, and implications for the study of heredity and evolution. *Q Rev Biol* 84:131–176

25. Asano M, Basieva I, Khrennikov A, Ohya M, Tanaka Y (2013) A model of epigenetic evolution based on theory of open quantum systems. *Syst Synth Biol* 7:161–173
26. Bordorano M, Ogryzko V (2013) Quantum biology at the cellular level-elements of the research program. *Biosystems* 112:11–30
27. Khrennikov A (2011) Quantum-like model of processing of information in the brain based on classical electromagnetic field. *Biosystems* 105:250–262
28. Koonin EV, Wolf YI (2012) Evolution of microbes and viruses: a paradigm shift in evolutionary biology? *Front Cell Infect Microbiol* 2:119
29. Sollars V, Lu X, Xiao L, Wang X, Garfinkel MD, Ruden DM (2003) Evidence for an epigenetic mechanism by which HSP90 acts as a capacitor for morphological evolution. *Nat Genet* 33:70–74
30. Russel PJ (2011) *iGenetics: a molecular approach*, 3rd edn. Pearson Benjamin Cummings, San Francisco
31. Darwin C (1859) *On the origin of species*. Murray, London
32. Lamarck JB (1809) *Zoological philosophy: exposition with regard to the natural history of animals*. Dentu, Paris (in French)
33. Foster PL (1993) Adaptive mutation: the uses of adversity. *Ann Rev Microbiol* 47:467–504
34. Rosenberg SM (2001) Evolving responsibly: adaptive mutation. *Nat Rev Genet* 2:504–515
35. Roth JR, Kugelberg E, Reams AB, Kofoid E, Andersson DI (2006) Origin of mutations under selection: the adaptive mutation controversy. *Ann Rev Microbiol* 60:477–501
36. Wiltschko W (1968) Über den Einfluss statischer Magnetfelder auf die Zugorientierung der Rotkehlchen (*Erythacus rubecula*). *Z Tierpsychol* 25:537–558
37. Elmen S, Wiltschko W, Demong N, Wiltschko R (1976) Magnetic direction finding: evidence for its use in migratory indigo buntings. *Science* 193:505–508
38. Wiltschko R, Wiltschko W (2006) Magnetoreception. *Bioessays* 28:157–168
39. Wiltschko W, Wiltschko R (2005) Magnetic orientation and magnetoreception in birds and other animals. *J Comp Physiol A* 191:675–693
40. Ritz T, Adem S, Schulten K (2000) A model for photoreceptor-based magnetoreception in birds. *Biophys J* 78:707–718
41. Ritz T, Dommer DH, Phillips JB (2002) Shedding light on vertebrate magnetoreception. *Neuron* 34:503–506
42. Brocklehurst B (2002) Magnetic fields and radical reactions: recent developments and their role in nature. *Chem Soc Rev* 31:301–311
43. Johnsen S, Lohmann KJ (2005) The physics and neurobiology of magnetoreception. *Nat Rev Neurosci* 6:703–712
44. Mouritsen H, Ritz T (2005) Magnetoreception and its use in bird navigation. *Curr Opin Neurobiol* 15:406–414
45. Johnsen S, Lohmann KJ (2008) Magnetoreception in animals. *Phys Today* 61:29–35
46. Rodgers CT, Hore PJ (2009) Chemical magnetoreception in birds: the radical pair mechanism. *Proc Natl Acad Sci U S A* 106:353–360
47. Wiltschko R, Wiltschko W (2014) Sensing magnetic directions in birds: radical pair processes involving cryptochrome. *Biosensors* 4:221–242
48. Nießner C, Denzau S, Stappert K, Ahmad M, Peichl L, Wiltschko W, Wiltschko R (2013) Magnetoreception: activated cryptochrome 1a concurs with magnetic orientation in birds. *J R Soc Interface* 10:20130638. doi:[10.1098/rsif.2013.0638](https://doi.org/10.1098/rsif.2013.0638)
49. Müller P, Ahmad M (2011) Light-activated cryptochrome reacts with molecular oxygen to form a flavin-superoxide radical pair consistent with magnetoreception. *J Biol Chem* 286:21033–21040
50. Maeda K, Henbest KB, Cintolesi F, Kuprov I, Rodgers CT, Liddell PA, Gust D, Timmel CR, Hore PJ (2008) Chemical compass model of avian magnetoreception. *Nature* 453:387–390
51. Solov'yov IA, Ritz T, Schulten K, Hore PJ (2014) A chemical compass for bird navigation. In: Mohseni M, Engel GS, Plenio MB (eds) *Quantum effects in biology*. Cambridge University Press, Cambridge, pp 218–236

52. Blankenship RE (2002) Molecular mechanisms of photosynthesis. Blackwell Science, Oxford
53. Bozo J (2007) Bioenergetics: basic principles. Gradjevinska Knjiga, Zrenjanin, Serbia (in Serbian)
54. Cogdell RJ, Gardiner AT, Hashimoto H, Brotosudarmo THP (2008) A comparative look at the first few milliseconds of the light reactions of photosynthesis. *Photochem Photobiol Sci* 7:1150–1158
55. Lambert N, Chen Y-N, Cheng Y-C, Li C-M, Chen G-Y, Franco Nori F (2013) Quantum biology. *Nat Phys* 9:10–18
56. Engel GS (2014) Direct observation of quantum coherence. In: Mohseni M, Engel GS, Plenio MB (eds) *Quantum effects in biology*. Cambridge University Press, Cambridge, pp 144–158
57. Lee H, Cheng Y-C, Fleming GR (2007) Coherence dynamics in photosynthesis: protein protection of excitonic coherence. *Science* 316:1462–1465
58. Panitchayangkoon G et al (2011) Direct evidence of quantum transport in photosynthetic light-harvesting complexes. *Proc Natl Acad Sci U S A* 108:20908–20912
59. Shabani A, Mohseni M, Rabitz H, Lloyd S (2012) Efficient estimation of energy transfer efficiency in light-harvesting complexes. *Phys Rev E* 86:011915
60. Mohseni M, Omar Y, Engel GS, Plenio MB (eds) (2014) *Quantum effects in biology*. Cambridge University Press, Cambridge
61. Fleming GR, Scholes GD, Cheng Y-C (2011) Quantum effects in biology. *Proc Chem* 3:38–57
62. Huynh MHV, Meyer TJ (2007) Proton-coupled electron transfer. *Chem Rev* 107:5004–5064
63. Kohen A (2003) Kinetic isotropic effects as probes for hydrogen tunneling, couple motion and dynamics contribution to enzyme catalysis. *Prog React Kinet Mech* 28:119–156
64. Gray HB, Winkler JR (2005) Long-range electron transfer. *Proc Natl Acad Sci U S A* 102:3534–3539
65. Onuchic JN, Beratan DN, Winkler JR, Gray HB (1992) Pathway analysis of protein electron-transfer reactions. *Annu Rev Biophys Biomol Struct* 21:349–377
66. Skourtis SS, Waldeck DH, Beratan DN (2010) Fluctuations in biological and bioinspired electron-transfer reactions. *Annu Rev Phys Chem* 61:461–485
67. Regan J, Dibilio A, Langen R, Skov L, Winkler JR, Gray HB, Onuchic JN (1995) Electron tunneling in azurin: the coupling across a beta-sheet. *Chem Biol* 2:489–496
68. Guillot M (1948) Physiologie des sensations—Sur la relation entre l'odeur et la structure moleculaire. *C R Hebd Seances Acad Sci* 226:1472–1474 (in French)
69. Amoore JE (1967) Specific anosmia: a clue to the olfactory code. *Nature* 214:1095–1098
70. Dyson GM (1938) The scientific basis of odour. *Chem Ind* 57:647–651
71. Wright RH (1966) Odour and molecular vibration. *Nature* 209:571–572
72. Turin L (1996) A spectroscopic mechanism for primary olfactory reception. *Chem Senses* 21:773–791
73. Franco MI, Turin L, Mershin A, Skoulakis EMC (2011) Molecular vibration-sensing component in *Drosophila melanogaster* olfaction. *Proc Natl Acad Sci U S A* 108:3797–3802
74. Vosshall LB (2015) Laying a controversial smell theory to rest. *Proc Natl Acad Sci U S A* 112:6525–6526
75. Schoenlein RW, Peteanu L, Mathies RA, Shank C (1991) The first step in vision: femtosecond isomerization of rhodopsin. *Science* 254:412–415
76. Ben-Nun M, Molnar F, Lu H, Phillips JC, Martínez TJ, Schulten K (1998) Quantum dynamics of the femtosecond photoisomerization of retinal in bacteriorhodopsin. *Faraday Discuss* 110:447–462
77. Polli D et al (2010) Conical intersection dynamics of the primary photoisomerization event in vision. *Nature* 467:440–443
78. Yockey HP (1974) An application of information theory to the Central Dogma and the Sequence Hypothesis. *J Theor Biol* 46:369–406
79. Forsdyke DR (1981) Are introns in-series error-detecting sequences? *J Theor Biol* 93:861–866
80. Barbieri M (2003) *The organic codes*. Cambridge University Press, Cambridge

81. Yockey HP (2005) Information theory, evolution and the origin of life. Cambridge University Press, New York
82. Battaï G (2008) Information theory and error-correcting codes in genetics and biological evolution. In: Barbieri M (ed) Introduction to biosemiotics. Springer, Dordrecht, pp 299–345
83. Faria LCB, Rocha ASL, Kleinschmidt JH, Palazzo R, Silva-Filho MC (2010) DNA sequences generated by BCH codes over GF(4). *Electron Lett* 46:203–204
84. Battaï G (2014) Barbieri's organic codes enable error correction of genomes. *Biosemiotics* 7:259–277
85. Karafyllidis IG (2008) Quantum mechanical model for information transfer from DNA to protein. *Biosystems* 93:191–198
86. Djordjevic IB (2012) Quantum information processing and quantum error correction: an engineering approach. Elsevier, Amsterdam
87. Ogryzko V On two quantum approaches to adaptive mutations in bacteria. <http://arxiv.org/ftp/arxiv/papers/0805/0805.4316.pdf>

# Chapter 2

## Quantum Information Theory Fundamentals

**Abstract** In this chapter, we provide the basic concepts of quantum information processing and quantum information theory. The following topics from quantum information processing will be covered: state vectors, operators, density operators, measurements, dynamics of a quantum system, superposition principle, quantum parallelism, no-cloning theorem, and entanglement. The following concepts from quantum information theory will be provided: Holevo information, accessible information, Holevo bound, Shannon entropy and von Neumann entropy, Schumacher's noiseless quantum coding theorem, and Holevo–Schumacher–Westmoreland theorem.

### 2.1 State Vectors, Operators, Projection Operators, and Density Operators

In quantum mechanics, the primitive undefined concepts are *physical system*, *observable*, and *state* [1–15]. A physical system is any sufficiently isolated quantum object, say an electron, a photon, or a molecule. An observable will be associated with a measurable property of a physical system, say energy or z-component of the spin. The state of a physical system is a trickier concept in quantum mechanics compared to classical mechanics. The problem arises when considering composite physical systems. In particular, states exist, known as *entangled states*, for bipartite physical systems in which neither of the subsystems is in a definite state. Even in cases where physical systems can be described as being in a state, two classes of states are possible: pure and mixed.

### 2.1.1 State Vectors and Operators

The condition of a quantum-mechanical system is completely specified by its *state vector*  $|\psi\rangle$  in a Hilbert space  $H$  (a vector space [16] on which a positive-definite scalar product is defined) over the field of complex numbers. Any state vector  $|\alpha\rangle$ , also known as a **ket**, can be expressed in terms of basis vectors  $|\phi_n\rangle$  by

$$|\alpha\rangle = \sum_{n=1}^{\infty} a_n |\phi_n\rangle. \quad (2.1)$$

An **observable**, such as momentum and spin, can be represented by an **operator**, say  $A$ , in the vector space of question. Quite generally, an operator acts on a ket from the left:  $(A) \cdot |\alpha\rangle = A |\alpha\rangle$ , which results in another ket. An operator  $A$  is said to be *Hermitian* if

$$A^\dagger = A, \quad A^\dagger = (A^T)^*. \quad (2.2)$$

Suppose that the Hermitian operator  $A$  has a discrete set of eigenvalues  $a^{(1)}, \dots, a^{(n)}, \dots$ . The associated eigenvectors (eigenkets)  $|a^{(1)}\rangle, \dots, |a^{(n)}\rangle, \dots$  can be obtained from

$$A |a^{(n)}\rangle = a^{(n)} |a^{(n)}\rangle. \quad (2.3)$$

The Hermitian conjugate of a ket  $|\alpha\rangle$  is denoted by  $\langle\alpha|$  and called the “bra.” The space dual to ket space is known as **bra** space. There exists a one-to-one correspondence, dual correspondence (D.C.), between a ket space and a bra space:

$$\begin{aligned} |\alpha\rangle &\xleftrightarrow{\text{D.C.}} \langle\alpha| \\ |a^{(1)}\rangle, |a^{(2)}\rangle, \dots &\xleftrightarrow{\text{D.C.}} \langle a^{(1)}|, \langle a^{(2)}|, \dots \\ |\alpha\rangle + |\beta\rangle &\xleftrightarrow{\text{D.C.}} \langle\alpha| + \langle\beta| \\ c_\alpha |\alpha\rangle + c_\beta |\beta\rangle &\xleftrightarrow{\text{D.C.}} c_\alpha^* \langle\alpha| + c_\beta^* \langle\beta|. \end{aligned} \quad (2.4)$$

The *scalar (inner) product* of two state vectors  $|\phi\rangle = \sum_n a_n |\phi_n\rangle$  and  $|\psi\rangle = \sum_n b_n |\phi_n\rangle$  is defined by

$$\langle\psi|\phi\rangle = \sum_{n=1}^{\infty} a_n b_n^*. \quad (2.5)$$

### 2.1.2 *Projection Operators*

The eigenkets  $\{|\xi^{(n)}\rangle\}$  of operator  $\Xi$  form the basis so that arbitrary ket  $|\psi\rangle$  can be expressed in terms of eigenkets by

$$|\psi\rangle = \sum_{n=1}^{\infty} c_n |\xi^{(n)}\rangle. \quad (2.6)$$

By multiplying (2.6) with  $\langle \xi^{(n)}|$  from the left, we obtain

$$\langle \xi^{(n)} | \psi \rangle = \sum_{j=1}^{\infty} c_j \langle \xi^{(n)} | \xi^{(j)} \rangle = c_n \langle \xi^{(n)} | \xi^{(n)} \rangle + \sum_{j=1, j \neq n}^{\infty} c_j \langle \xi^{(n)} | \xi^{(j)} \rangle. \quad (2.7)$$

Since the eigenkets  $\{|\xi^{(n)}\rangle\}$  form the basis, the principle of orthonormality is satisfied  $\langle \xi^{(n)} | \xi^{(j)} \rangle = \delta_{nj}$ ,  $\delta_{nj} = \begin{cases} 1, & n = j \\ 0, & n \neq j \end{cases}$  so that (2.7) becomes

$$c_n = \langle \xi^{(n)} | \psi \rangle. \quad (2.8)$$

By substituting (2.8) into (2.6), we obtain

$$|\psi\rangle = \sum_{n=1}^{\infty} \langle \xi^{(n)} | \psi \rangle |\xi^{(n)}\rangle = \sum_{n=1}^{\infty} |\xi^{(n)}\rangle \langle \xi^{(n)} | \psi \rangle. \quad (2.9)$$

Because  $|\psi\rangle = I|\psi\rangle$  from (2.9), it is clear that

$$\sum_{n=1}^{\infty} |\xi^{(n)}\rangle \langle \xi^{(n)}| = I, \quad (2.10)$$

and the relation above is known as the *completeness relation*. The operators under summation in (2.10) are known as *projection operators*  $P_n$ :

$$P_n = |\xi^{(n)}\rangle \langle \xi^{(n)}|, \quad (2.11)$$

which satisfy the relationship  $\sum_{n=1}^{\infty} P_n = I$ . It is easy to show that the ket (2.6) with  $c_n$  determined by (2.8) is of unit length:

$$\langle \psi | \psi \rangle = \sum_{n=1}^{\infty} \langle \psi | \xi^{(n)} \rangle \langle \xi^{(n)} | \psi \rangle = \sum_{n=1}^{\infty} |\langle \psi | \xi^{(n)} \rangle|^2 = 1. \quad (2.12)$$

The following theorem is an important theorem that will be used often throughout the chapter.

It can be shown that the eigenvalues of a Hermitian operator  $A$  are real, and the eigenkets are orthogonal:

$$\langle a^{(m)} | a^{(n)} \rangle = \delta_{nm}. \quad (2.13)$$

For the proof of this claim, an interested reader is referred to [1].

### 2.1.3 Photon, Spin-½ Systems, and Hadamard Gate

**Photon.** The  $x$ - and  $y$ -polarizations of the photon can be represented by

$$|E_x\rangle = \begin{pmatrix} 1 \\ 0 \end{pmatrix} \quad |E_y\rangle = \begin{pmatrix} 0 \\ 1 \end{pmatrix}.$$

On the other hand, the right and left circular polarizations can be represented by

$$|E_R\rangle = \frac{1}{\sqrt{2}} \begin{pmatrix} 1 \\ j \end{pmatrix} \quad |E_L\rangle = \frac{1}{\sqrt{2}} \begin{pmatrix} 1 \\ -j \end{pmatrix}.$$

The  $45^\circ$  polarization ket can be represented as follows:

$$|E_{45^\circ}\rangle = \cos\left(\frac{\pi}{4}\right) |E_x\rangle + \sin\left(\frac{\pi}{4}\right) |E_y\rangle = \frac{1}{\sqrt{2}} (|E_x\rangle + |E_y\rangle) = \frac{1}{\sqrt{2}} \begin{pmatrix} 1 \\ 1 \end{pmatrix}.$$

The bras corresponding to the left and right polarization can be written as

$$\langle E_R | = \frac{1}{\sqrt{2}} (1 \quad -j) \quad \langle E_L | = \frac{1}{\sqrt{2}} (1 \quad j).$$

It can be easily verified that the left and right states are orthogonal and that the right polarization state is of unit length:

$$\langle E_R | E_L \rangle = \frac{1}{2} (1 \quad -j) \begin{pmatrix} 1 \\ -j \end{pmatrix} = 0 \quad \langle E_R | E_R \rangle = \frac{1}{2} (1 \quad -j) \begin{pmatrix} 1 \\ j \end{pmatrix} = 1.$$

The completeness relation is clearly satisfied because

$$|E_x\rangle\langle E_x| + |E_y\rangle\langle E_y| = \begin{pmatrix} 1 \\ 0 \end{pmatrix} (1 \quad 0) + \begin{pmatrix} 0 \\ 1 \end{pmatrix} (0 \quad 1) = \begin{pmatrix} 1 & 0 \\ 0 & 1 \end{pmatrix} = I_2.$$

An arbitrary polarization state can be represented by

$$|E\rangle = |E_R\rangle\langle E_R|E\rangle + |E_L\rangle\langle E_L|E\rangle.$$

For example, for  $E = E_x$ , we obtain

$$|E_x\rangle = |E_R\rangle\langle E_R|E_x\rangle + |E_L\rangle\langle E_L|E_x\rangle.$$

For the photon spin operator  $S$  matrix representation, we have to solve the following eigenvalue equation:

$$S|\psi\rangle = \lambda|\psi\rangle.$$

The photon spin operator satisfies  $S^2 = I$  so that we can write

$$|\psi\rangle = S^2|\psi\rangle = S(S|\psi\rangle) = S(\lambda|\psi\rangle) = \lambda S|\psi\rangle = \lambda^2|\psi\rangle.$$

It is clear from the previous equation that  $\lambda^2 = 1$  so that the corresponding eigenvalues are  $\lambda = \pm 1$ . By substituting the eigenvalues into the eigenvalue equation, we obtain that corresponding eigenkets are the left and the right polarization states:

$$S|E_R\rangle = |E_R\rangle \quad S|E_L\rangle = -|E_L\rangle.$$

The photon spin represented in  $\{|E_x\rangle, |E_y\rangle\}$  basis can be obtained by

$$S \doteq \begin{pmatrix} S_{xx} & S_{xy} \\ S_{yx} & S_{yy} \end{pmatrix} = \begin{pmatrix} \langle E_x | S | E_x \rangle & \langle E_x | S | E_y \rangle \\ \langle E_y | S | E_x \rangle & \langle E_y | S | E_y \rangle \end{pmatrix} = \begin{pmatrix} 0 & -j \\ j & 0 \end{pmatrix}.$$

**Spin-1/2 Systems.** The  $S_z$  basis in spin-1/2 systems can be written as  $\{|E_z; +\rangle, |E_z; -\rangle\}$ , where the corresponding basis kets represent the spin-up and spin-down states. The eigenvalues are  $\{\hbar/2, -\hbar/2\}$ , and the corresponding eigenket–eigenvalue relation is

$S_z|S_z; \pm\rangle = \pm\frac{\hbar}{2}|S_z; \pm\rangle$ , where  $S_z$  is the spin operator that can be represented in the basis above as follows:

$$S_z = \sum_{i=+, -} \sum_{j=+, -} |i\rangle\langle j| \underbrace{S_z|i\rangle}_{i\frac{\hbar}{2}|i\rangle} \langle j| = \sum_{i=+, -} i\frac{\hbar}{2}|i\rangle\langle i| = \frac{\hbar}{2}(|+\rangle\langle +| - |-\rangle\langle -|).$$

The matrix representation of spin-½ systems is obtained by

$$|S_z; +\rangle = \begin{pmatrix} \langle S_z; +|S_z; +\rangle \\ \langle S_z; -|S_z; +\rangle \end{pmatrix} \doteq \begin{pmatrix} 1 \\ 0 \end{pmatrix} \quad |S_z; -\rangle \doteq \begin{pmatrix} 0 \\ 1 \end{pmatrix}$$

$$S_z \doteq \begin{pmatrix} \langle S_z; +|S_z|S_z; +\rangle & \langle S_z; +|S_z|S_z; -\rangle \\ \langle S_z; -|S_z|S_z; +\rangle & \langle S_z; -|S_z|S_z; -\rangle \end{pmatrix} = \frac{\hbar}{2} \begin{pmatrix} 1 & 0 \\ 0 & -1 \end{pmatrix}.$$

**Hadamard Gate.** The matrix representation of Hadamard operator (gate) is given by

$$H = \frac{1}{\sqrt{2}} \begin{bmatrix} 1 & 1 \\ 1 & -1 \end{bmatrix}.$$

It can easily be shown that the Hadamard gate is Hermitian and unitary as follows:

$$H^\dagger = \frac{1}{\sqrt{2}} \begin{bmatrix} 1 & 1 \\ 1 & -1 \end{bmatrix} = H$$

$$H^\dagger H = \frac{1}{\sqrt{2}} \begin{bmatrix} 1 & 1 \\ 1 & -1 \end{bmatrix} \frac{1}{\sqrt{2}} \begin{bmatrix} 1 & 1 \\ 1 & -1 \end{bmatrix} = \begin{bmatrix} 1 & 0 \\ 0 & 1 \end{bmatrix} = I.$$

The eigenvalues for Hadamard gate can be obtained from  $\det(H - \lambda I) = 0$  to be  $\lambda_{1,2} = \pm 1$ . By substituting the eigenvalues into the eigenvalue equation, namely,  $H|\Psi_{1,2}\rangle = \pm|\Psi_{1,2}\rangle$ , the corresponding eigenkets are obtained as follows:

$$|\Psi_1\rangle = \begin{bmatrix} \frac{1}{\sqrt{4 - 2\sqrt{2}}} \\ \frac{1}{\sqrt{2\sqrt{2}}} \end{bmatrix} \quad |\Psi_2\rangle = \begin{bmatrix} \frac{1}{\sqrt{4 + 2\sqrt{2}}} \\ -\frac{1}{\sqrt{2\sqrt{2}}} \end{bmatrix}.$$

#### 2.1.4 Density Operators

Let the large number of quantum systems of the same kind be prepared, each in one of a set of states  $|\phi_n\rangle$ , and let the fraction of the system being in state  $|\phi_n\rangle$  be denoted by probability  $P_n$  ( $n = 1, 2, \dots$ ):

$$\langle \phi_m | \phi_n \rangle = \delta_{mn}, \quad \sum_n P_n = 1. \quad (2.14)$$

Therefore, this ensemble of quantum states represents a classical *statistical mixture* of kets. The probability of obtaining  $\xi_n$  from the measurement of  $\Xi$  will be

$$\Pr(\xi_k) = \sum_{n=1}^{\infty} P_n |\langle \xi_k | \phi_n \rangle|^2 = \sum_{n=1}^{\infty} P_n \langle \xi_k | \phi_n \rangle \langle \phi_n | \xi_k \rangle = \langle \xi_k | \rho | \xi_k \rangle, \quad (2.15)$$

where the operator  $\rho$  is known as a *density operator*, and it is defined by

$$\rho = \sum_{n=1}^{\infty} P_n |\phi_n \rangle \langle \phi_n|. \quad (2.16)$$

The expected value of density operator is given by

$$\langle \rho \rangle = \sum_{k=1}^{\infty} \xi_k \Pr(\xi_k) = \sum_{k=1}^{\infty} \xi_k \langle \xi_k | \rho | \xi_k \rangle = \sum_{k=1}^{\infty} \langle \xi_k | \rho \Xi | \xi_k \rangle = \text{Tr}(\rho \Xi). \quad (2.17)$$

The density operator *properties* can be summarized as follows:

1. The density operator is Hermitian ( $\rho^+ = \rho$ ), with the set of orthonormal eigenkets  $|\phi_n\rangle$  corresponding to the nonnegative eigenvalues  $P_n$  and  $\text{Tr}(\rho) = 1$ .
2. Any Hermitian operator with nonnegative eigenvalues and trace 1 may be considered as a density operator.
3. The density operator is positive definite:  $\langle \psi | \rho | \psi \rangle \geq 0$  for all  $|\psi\rangle$ .
4. The density operator has the property  $\text{Tr}(\rho^2) \leq 1$ , with equality iff one of the prior probabilities is 1, and all the rest 0:  $\rho = |\phi_n\rangle \langle \phi_n|$ , and the density operator is then a projection operator.
5. The eigenvalues of a density operator satisfy  $0 \leq \lambda_i \leq 1$ .

The proof of these properties is quite straightforward, and the proof is left as a homework problem. When  $\rho$  is the projection operator, we say that it represents the system in a *pure state*; otherwise, with  $\text{Tr}(\rho^2) < 1$ , it represents a *mixed state*. A mixed state in which all eigenkets occur with the same probability is known as a *completely mixed state* and can be represented by

$$\rho = \sum_{k=1}^{\infty} \frac{1}{n} |\phi_n\rangle \langle \phi_n| = \frac{1}{n} I \Rightarrow \text{Tr}(\rho^2) = \frac{1}{n} \Rightarrow \frac{1}{n} \leq \text{Tr}(\rho^2) \leq 1. \quad (2.18)$$

If the density matrix has off-diagonal elements different from zero, we say that it exhibits the *quantum interference*, which means that state term can interfere with each other. Let us observe the following pure state:

$$\begin{aligned} |\psi\rangle &= \sum_{i=1}^n \alpha_i |\xi_i\rangle \Rightarrow \rho = |\psi\rangle \langle \psi| = \sum_{i=1}^n |\alpha_i|^2 |a_i\rangle \langle a_i| + \sum_{i=1}^n \sum_{j=1, j \neq i}^n \alpha_i \alpha_j^* |\xi_i\rangle \langle \xi_j| \\ &= \sum_{i=1}^n \langle \xi_i | \rho | \xi_i \rangle |\xi_i\rangle \langle \xi_i| + \sum_{i=1}^n \sum_{j=1, j \neq i}^n \langle \xi_i | \rho | \xi_j \rangle |\xi_i\rangle \langle \xi_j|. \end{aligned} \quad (2.19)$$

The first term in (2.19) is related to the probability of the system being in state  $|a_i\rangle$ , and the second term is related to the quantum interference. It appears that the off-diagonal elements of a mixed state will be zero, while these of pure state will be nonzero. Notice that the existence of off-diagonal elements is base dependent; therefore, to check for purity, it is a good idea to compute  $\text{Tr}(\rho^2)$  instead.

In the quantum information theory, the density matrix can be used to determine the amount of information conveyed by the quantum state, i.e., to compute the von Neumann entropy:

$$S = \text{Tr}(\rho \log \rho) = -\sum_i \lambda_i \log_2 \lambda_i, \quad (2.20)$$

where  $\lambda_i$  are the eigenvalues of the density matrix. The corresponding Shannon entropy can be calculated by

$$H = -\sum_i p_i \log_2 p_i, \quad (2.21)$$

where  $p_i$  is the probability of selecting the  $i$ th vector from an ensemble of orthogonal vectors.

Suppose now that  $S$  is a *bipartite composite system* with component subsystems  $A$  and  $B$ . For example, the subsystem  $A$  can represent the quantum register  $Q$  and subsystem  $B$  the environment  $E$ . The composite system can be represented by  $AB = A \otimes B$ , where  $\otimes$  stands for the tensor product. If the dimensionality of Hilbert space  $H_A$  is  $m$  and the dimensionality of Hilbert space  $H_B$  is  $n$ , then the dimensionality of Hilbert space  $H_{AB}$  will be  $mn$ . If  $|\alpha\rangle \in A$  and  $|\beta\rangle \in B$ , then  $|\alpha\rangle|\beta\rangle = |\alpha\rangle \otimes |\beta\rangle \in AB$ . If the operator  $A$  acts on kets from  $H_A$  and the operator  $B$  on kets from  $H_B$ , then the action of  $AB$  on  $|\alpha\rangle|\beta\rangle$  can be described as follows:

$$(AB)|\alpha\rangle|\beta\rangle = (A|\alpha\rangle)(B|\beta\rangle). \quad (2.22)$$

The norm of state  $|\psi\rangle = |\alpha\rangle|\beta\rangle \in AB$  is determined by

$$\langle \psi | \psi \rangle = \langle \alpha | \alpha \rangle \langle \beta | \beta \rangle. \quad (2.23)$$

Let  $\{|\alpha_i\rangle\}$  ( $\{|\beta_i\rangle\}$ ) be a basis for the Hilbert space  $H_A$  ( $H_B$ ) and let  $E$  be an ensemble of physical systems  $S$  described by the density operator  $\rho$ . The *reduced density operator*  $\rho_A$  for subsystem  $A$  is defined to be the partial trace of  $\rho$  over  $B$ :

$$\rho_A = \text{Tr}_B(\rho) = \sum_j \langle \beta_j | \rho | \beta_j \rangle. \quad (2.24)$$

Similarly, the *reduced density operator*  $\rho_B$  for subsystems  $B$  is defined to be the partial trace of  $\rho$  over  $A$ :

$$\rho_B = \text{Tr}_A(\rho) = \sum_i \langle \alpha_i | \rho | \alpha_i \rangle. \quad (2.25)$$

## 2.2 Measurements, Uncertainty Relations, and Dynamics of a Quantum System

### 2.2.1 Measurements

Each measurable physical quantity—observable (such as position, momentum, or angular momentum) is associated with a Hermitian operator that has a complete set of eigenkets. According to P. A. Dirac, “A measurement always causes the system to jump into an eigenstate of the dynamical variable that is being measured [11].” The Dirac’s statement can be formulated as the following *postulate*: an exact measurement of an observable with operator  $A$  always yields as a result one of the eigenvalues  $a^{(n)}$  of  $A$ . Thus, the measurement changes the state, with the measurement system “thrown into” one of its eigenstates, which can be represented by:  $|\alpha\rangle \xrightarrow{A \text{ measurement}} |a^{(j)}\rangle$ . If before measurement the system was in state  $|\alpha\rangle$ , the probability that the result of a measurement will be the eigenvalue  $a^{(i)}$  is given by

$$\Pr(a^{(i)}) = \left| \langle a^{(i)} | \alpha \rangle \right|^2. \quad (2.26)$$

Since at least one of the eigenvalues must occur as the result of the measurements, these probabilities satisfy

$$\sum_i \Pr(a^{(i)}) = \sum_i \left| \langle a^{(i)} | \alpha \rangle \right|^2 = 1. \quad (2.27)$$

The expected value of the outcome of the measurement of  $A$  is given by

$$\langle A \rangle = \sum_i a^{(i)} \Pr(a^{(i)}) = \sum_i a^{(i)} \left| \langle a^{(i)} | \alpha \rangle \right|^2 = \sum_i a^{(i)} \langle \alpha | a^{(i)} \rangle \langle a^{(i)} | \alpha \rangle. \quad (2.28)$$

By applying the eigenvalue equation  $a^{(i)}|a^{(i)}\rangle = A|a^{(i)}\rangle$ , (2.28) becomes

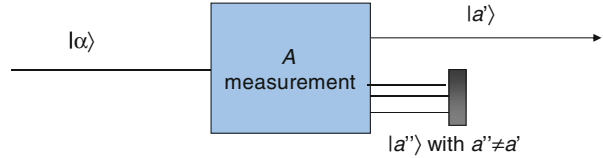
$$\langle A \rangle = \sum_i \langle \alpha | A | a^{(i)} \rangle \langle a^{(i)} | \alpha \rangle. \quad (2.29)$$

By using further the completeness relation  $\sum_i |a^{(i)}\rangle \langle a^{(i)}| = I$ , we obtain the expected value of the measurement of  $A$  to be simply

$$\langle A \rangle = \langle \alpha | A | \alpha \rangle. \quad (2.30)$$

In various situations, like initial state preparations for quantum information processing (QIP) applications, we need to select one particular outcome of the measurement. This procedure is known as the *selective measurement* (or filtration) and it can be conducted as shown in Fig. 2.1.

**Fig. 2.1** The illustration of the concept of a selective measurement (filtration)



The result of the selective measurement can be interpreted as applying the *projection operator*  $P_{a'}$  to  $|\alpha\rangle$  to obtain

$$P_{a'}|\alpha\rangle = |a'\rangle\langle a'|\alpha\rangle. \quad (2.31)$$

The probability that the outcome of the measurement of observable  $\Xi$  with eigenvalues  $\xi^{(n)}$  lies between  $(a, b)$  is given by

$$\begin{aligned} \Pr(\xi \in R(a, b)) &= \sum_{\xi^{(n)} \in R(a, b)} \left| \langle \xi^{(n)} | \alpha \rangle \right|^2 = \sum_{\xi^{(n)} \in R(a, b)} \langle \alpha | \xi^{(n)} \rangle \langle \xi^{(n)} | \alpha \rangle \\ &= \langle \alpha | P_{ab} | \alpha \rangle = \langle P_{ab} \rangle, \end{aligned} \quad (2.32)$$

where with  $P_{ab}$  we denoted the following projection operator:

$$P_{ab} = \sum_{\xi^{(n)} \in R(a, b)} |\xi^{(n)}\rangle\langle \xi^{(n)}|. \quad (2.33)$$

It can straightforwardly be shown that the projection operator  $P_{ab}$  satisfies

$$P_{ab}^2 = P_{ab} \Leftrightarrow P_{ab}(P_{ab} - I) = 0. \quad (2.34)$$

Therefore, the eigenvalues of projection operator  $P_{ab}$  are either 0 (corresponding to the “false proposition”) or 1 (corresponding to the “true proposition”), and it is of high importance in *quantum detection theory* [2].

In terms of projection operators, the state of the system after the measurement is given by

$$|\alpha\rangle \xrightarrow{A \text{ measurement}} \frac{1}{\sqrt{\langle \alpha | P_j | \alpha \rangle}} P_j |\alpha\rangle, \quad P_j = |a^{(j)}\rangle\langle a^{(j)}|. \quad (2.35)$$

In case operator  $A$  has the same eigenvalue  $a_i$  for the following eigenkets  $\{|a_i^{(j)}\rangle\}_{j=1}^{d_i}$ , with corresponding characteristic equation

$$A |a_i^{(j)}\rangle = a_i |a_i^{(j)}\rangle; \quad j = 1, \dots, d_i, \quad (2.36)$$

we say that eigenvalue  $a_i$  is *degenerate* of order  $d_i$ . The corresponding probability of obtaining the measurement result  $a_i$  can be found by

$$\Pr(a_i) = \sum_{j=1}^{d_i} \left| \langle a_i^{(j)} | \alpha \rangle \right|^2. \quad (2.37)$$

The projective measurements can be generalized as follows. Let the set of measurement operators be given by  $\{M_m\}$ , where index  $m$  stands for possible measurement result, satisfying the property  $\sum_m M_m^\dagger M_m = I$ . The probability of finding the measurement result  $m$ , given the state  $|\psi\rangle$ , is given by

$$\Pr(m) = \langle \psi | M_m^\dagger M_m | \psi \rangle. \quad (2.38)$$

After the measurement, the system will be left in following state:

$$|\psi_f\rangle = \frac{M_m |\psi\rangle}{\sqrt{\langle \psi | M_m^\dagger M_m | \psi \rangle}}. \quad (2.39)$$

For projective measurements, clearly  $M_m = P_m = |a^{(m)}\rangle\langle a^{(m)}|$ , and from the property above, we obtain

$$\sum_m M_m^\dagger M_m = \sum_m |a^{(m)}\rangle \underbrace{\langle a^{(m)}|}_{1} \langle a^{(m)}| = \sum_m |a^{(m)}\rangle \langle a^{(m)}| = \sum_m P_m = I, \quad (2.40)$$

which is the completeness relationship. The probability of obtaining the  $m$ , the result of the measurement, will be then

$$\Pr(m) = \text{Tr}(P_m^\dagger P_m \rho) = \text{Tr}(P_m \rho) = \text{Tr}\left(|a^{(m)}\rangle\langle a^{(m)}| \rho\right) = \langle a^{(m)} | \rho | a^{(m)} \rangle. \quad (2.41)$$

Another important type of measurement is known as a *positive operator-valued measure* (POVM). A POVM consists of the set of operators  $\{E_m\}$ , where each operator  $E_m$  is positive semidefinite, i.e.,  $\langle \psi | E_m | \psi \rangle \geq 0$ , satisfying the relationship

$$\sum_m E_m = I. \quad (2.42)$$

The POVM can be constructed from generalized measurement operators  $\{M_m\}$  by setting  $E_m = M_m^\dagger M_m$ . The probability of obtaining the  $m$ th result of measurements is given by  $\text{Tr}(E_m \rho)$ . The POVM concept is in particular suitable to situations when the measurements are not repeatable. For instance, by performing the measurement on a photon, it can be destroyed so that the repeated measurements are not possible.

### 2.2.2 Uncertainty Principle

Let  $A$  and  $B$  be two operators, which in general do not commute, i.e.,  $AB \neq BA$ . The quantity  $[A, B] = AB - BA$  is called the *commutator* of  $A$  and  $B$ , while the quantity  $\{A, B\} = AB + BA$  is called the *anticommutator*. Two observables  $A$  and  $B$  are said to be **compatible** when their corresponding operators commute:  $[A, B] = 0$ . Two observables  $A$  and  $B$  are said to be *incompatible* when  $[A, B] \neq 0$ . If in the set of operators  $\{A, B, C, \dots\}$  all operators commute in pairs, namely,  $[A, B] = [A, C] = [B, C] = \dots = 0$ , we say the set is a *complete set of commuting observables* (CSCO).

If two observables, say  $A$  and  $B$ , are to be measured simultaneously and exactly on the same system, the system after the measurement must be left in the state  $|a^{(n)}; b^{(n)}\rangle$  that is an eigenstate of both observables:

$$A|a^{(n)}; b^{(n)}\rangle = a^{(n)}|a^{(n)}; b^{(n)}\rangle, \quad B|a^{(n)}; b^{(n)}\rangle = b^{(n)}|a^{(n)}; b^{(n)}\rangle. \quad (2.43)$$

This will be true only if  $AB = BA$  or equivalently the commutator  $[A, B] = AB - BA = 0$ ; that is when two operators *commute* as shown below:

$$\begin{aligned} AB|a^{(n)}; b^{(n)}\rangle &= A(B|a^{(n)}; b^{(n)}\rangle) = Ab^{(n)}|a^{(n)}; b^{(n)}\rangle = b^{(n)} \cdot A|a^{(n)}; b^{(n)}\rangle \\ &= a^{(n)}b^{(n)}|a^{(n)}; b^{(n)}\rangle \\ BA|a^{(n)}; b^{(n)}\rangle &= a^{(n)}b^{(n)}|a^{(n)}; b^{(n)}\rangle \Rightarrow AB = BA. \end{aligned} \quad (2.44)$$

When two operators do not commute, they cannot be simultaneously measured with the complete precision. Given an observable  $A$ , we define the operator  $\Delta A = A - \langle A \rangle$ , and the corresponding expectation value of  $(\Delta A)^2$  that is known as the *dispersion* of  $A$ :

$$\langle (\Delta A)^2 \rangle = \langle A^2 - 2A\langle A \rangle + \langle A \rangle^2 \rangle = \langle A^2 \rangle - \langle A \rangle^2. \quad (2.45)$$

Then, for any state, the following inequality is valid:

$$\langle (\Delta A)^2 \rangle \langle (\Delta B)^2 \rangle \geq \frac{1}{4} |\langle [\Delta A, \Delta B] \rangle|^2, \quad (2.46)$$

which is known as **the Heisenberg uncertainty principle** [1, 4, 17–26].

*Example* The commutation relation for coordinate  $X$  and momentum  $P$  observables is given by  $[X, P] = j\hbar$ . By substituting this commutation relation into (2.46), we obtain

$$\langle X^2 \rangle \langle P^2 \rangle \geq \frac{\hbar^2}{4}.$$

If we observe a large ensemble of  $N$  independent systems, all of them are in the state  $|\psi\rangle$ . On some systems,  $X$  is measured, and on some systems,  $P$  is measured. The uncertainty principle asserts that for none state the product of dispersions (variances) cannot be less than  $\hbar^2/4$ .

### 2.2.3 Time-Evolution Schrödinger Equation

Time-evolution operator  $U(t, t_0)$  transforms the initial ket at time instance  $t_0$ ,  $|\alpha, t_0\rangle$ , into the final ket at the time instance  $t$  by

$$|\alpha, t_0; t\rangle = U(t, t_0)|\alpha, t_0\rangle. \quad (2.47)$$

This time-evolution operators must satisfy the following two properties:

1. *Unitary property*:  $U^\dagger(t, t_0)U(t, t_0) = I$ .
2. *Composition property*:  $U(t_2, t_0) = U(t_2, t_1)U(t_1, t_0)$ ,  $t_2 > t_1 > t_0$ .

Following (2.47), the action of infinitesimal time-evolution operator  $U(t_0 + dt, t_0)$  can be described by

$$|\alpha, t_0; t_0 + dt\rangle = U(t_0 + dt, t_0)|\alpha, t_0\rangle. \quad (2.48)$$

The following operator satisfies all propositions above, when  $dt \rightarrow 0$ :

$$U(t_0 + dt, t_0) = 1 - j\Omega dt, \quad \Omega^\dagger = \Omega \quad (2.49)$$

where the operator  $\Omega$  is related to the Hamiltonian  $H$  by  $H = \hbar\Omega$  and the Hamiltonian eigenvalues correspond to the energy  $E = \hbar\omega$ . For the infinitesimal time-evolution operator  $U(t_0 + dt, t_0)$ , we can derive the time-evolution equation as follows. The starting point in derivation is the composition property:

$$U(t + dt, t_0) = U(t + dt, t)U(t, t_0) = \left(1 - \frac{j}{\hbar}H dt\right)U(t, t_0). \quad (2.50)$$

Equation (2.50) can be rewritten into the following form:

$$\lim_{dt \rightarrow 0} \frac{U(t + dt, t_0) - U(t, t_0)}{dt} = -\frac{j}{\hbar}HU(t, t_0), \quad (2.51)$$

and, by taking the partial derivative definition into account, (2.51) becomes

$$j\hbar \frac{\partial}{\partial t} U(t, t_0) = HU(t, t_0), \quad (2.52)$$

and this equation is known as **Schrödinger equation for time-evolution operator**.

The Schrödinger equation for a state ket [1, 4, 17–26] can be obtained by applying the time-evolution operator on initial ket:

$$j\hbar \frac{\partial}{\partial t} U(t, t_0) |\alpha, t_0\rangle = HU(t, t_0) |\alpha, t_0\rangle, \quad (2.53)$$

which based on (2.52) can be rewritten as

$$j\hbar \frac{\partial}{\partial t} |\alpha, t_0; t\rangle = H|\alpha, t_0; t\rangle. \quad (2.54)$$

For *conservative systems*, for which the Hamiltonian is time invariant, we can easily solve (2.54) to obtain

$$U(t, t_0) = e^{-\frac{j}{\hbar}H(t-t_0)}. \quad (2.55)$$

The time evolution of kets in conservative systems can therefore be described by applying (2.55) in (2.47), which yields to

$$|\alpha(t)\rangle = e^{-\frac{j}{\hbar}H(t-t_0)} |\alpha(t_0)\rangle. \quad (2.56)$$

Therefore, the operators do not explicitly depend on time and this concept is known as the *Schrödinger picture*.

In the *Heisenberg picture*, on the other hand, the state vector is independent of time, but operators depend on time:

$$A(t) = e^{\frac{j}{\hbar}H(t-t_0)} A e^{-\frac{j}{\hbar}H(t-t_0)}. \quad (2.57)$$

The time-evolution equation in Heisenberg picture is given by

$$j\hbar \frac{dA(t)}{dt} = [A(t), H] + j\hbar \frac{\partial A(t)}{\partial t}. \quad (2.58)$$

The density operator  $\rho$ , representing the statistical mixture of states, is independent on time in the Heisenberg picture. The expectation value of a measurement of an observable  $\Xi(t)$  at time instance  $t$  is given by

$$\begin{aligned} E_t[\Xi] &= \text{Tr}[\rho \Xi(t)] \\ E_t[\Xi] &= \text{Tr}[\rho(t) \Xi], \quad \rho(t) = e^{\frac{j}{\hbar}H(t-t_0)} \rho e^{-\frac{j}{\hbar}H(t-t_0)}. \end{aligned} \quad (2.59)$$

*Example* The Hamiltonian for a two-state system is given by

$$H = \begin{bmatrix} \omega_1 & \omega_2 \\ \omega_2 & \omega_1 \end{bmatrix}.$$

The basis for this system is given by  $\{|0\rangle = [1 \ 0]^T, |1\rangle = [0 \ 1]^T\}$ :

- (a) Determine the eigenvalues and eigenkets of  $H$ , and express the eigenkets in terms of basis.
- (b) Determine the time evolution of the system described by the Schrödinger equation

$$j\hbar \frac{\partial}{\partial t} |\psi\rangle = H|\psi\rangle, \quad |\psi(0)\rangle = |0\rangle.$$

To determine the eigenkets of  $H$ , we start from the characteristic equation  $\det(H - \lambda I) = 0$  and find that eigenvalues are  $\lambda_{1,2} = \omega_1 \pm \omega_2$ . The corresponding eigenvectors are

$$|\lambda_1\rangle = \frac{1}{\sqrt{2}} \begin{bmatrix} 1 \\ 1 \end{bmatrix} = \frac{1}{\sqrt{2}}(|0\rangle + |1\rangle) \quad |\lambda_2\rangle = \frac{1}{\sqrt{2}} \begin{bmatrix} 1 \\ -1 \end{bmatrix} = \frac{1}{\sqrt{2}}(|0\rangle - |1\rangle).$$

We now have to determine the time evolution of arbitrary ket  $|\psi(t)\rangle = [\alpha(t)\beta(t)]^T$ . The starting point is the Schrödinger equation:

$$\begin{aligned} j\hbar \frac{\partial}{\partial t} |\psi\rangle &= j\hbar \begin{bmatrix} \dot{\alpha}(t) \\ \dot{\beta}(t) \end{bmatrix}, \\ H|\psi\rangle &= \begin{bmatrix} \omega_1 & \omega_2 \\ \omega_2 & \omega_1 \end{bmatrix} \begin{bmatrix} \alpha(t) \\ \beta(t) \end{bmatrix} = \begin{bmatrix} \omega_1\alpha(t) + \omega_2\beta(t) \\ \omega_2\alpha(t) + \omega_1\beta(t) \end{bmatrix} \\ &\Rightarrow j\hbar \begin{bmatrix} \dot{\alpha}(t) \\ \dot{\beta}(t) \end{bmatrix} = \begin{bmatrix} \omega_1\alpha(t) + \omega_2\beta(t) \\ \omega_2\alpha(t) + \omega_1\beta(t) \end{bmatrix}. \end{aligned}$$

By substitution of  $\alpha(t) + \beta(t) = \gamma(t)$  and  $\alpha(t) - \beta(t) = \delta(t)$ , we obtain the ordinary set of differential equations

$$j\hbar \frac{d\gamma(t)}{dt} = (\omega_1 + \omega_2)\gamma(t) \quad j\hbar \frac{d\delta(t)}{dt} = (\omega_1 - \omega_2)\delta(t),$$

whose solution is  $\gamma(t) = C \exp\left(\frac{\omega_1 + \omega_2}{j\hbar} t\right)$  and  $\delta(t) = D \exp\left(\frac{\omega_1 - \omega_2}{j\hbar} t\right)$ . From the initial state  $|\psi(0)\rangle = |0\rangle = [1 \ 0]^T$ , we obtain the unknown constants  $C = D = 1$  so that state time evolution is given by

$$|\psi(t)\rangle = \exp\left(-\frac{j}{\hbar}\omega_1 t\right) \begin{bmatrix} \cos\left(\frac{\omega_2 t}{\hbar}\right) \\ -j \sin\left(\frac{\omega_2 t}{\hbar}\right) \end{bmatrix}.$$

## 2.3 Quantum Information Processing (QIP) Fundamentals

*Fundamental features* of QIP are different from that of classical computing and can be summarized into three: (1) linear superposition, (2) quantum parallelism, and (3) entanglement. Below we provide some basic details of these features:

1. *Linear superposition.* Contrary to the classical bit, a quantum bit or *qubit* can take not only two discrete values 0 and 1 but also *all* possible *linear combinations* of them. This is a consequence of a fundamental property of quantum states: it is possible to construct a *linear superposition* of quantum state  $|0\rangle$  and quantum state  $|1\rangle$ .
2. *Quantum parallelism.* The *quantum parallelism* is a possibility to perform a large number of operations in parallel, which represents the key difference from classical computing. Namely, in classical computing, it is possible to know what the internal status of the computer is. On the other hand, because of the no-cloning theorem, it is not possible to know the current state of the quantum computer. This property has led to the development of the Shor factorization algorithm, which can be used to crack the Rivest–Shamir–Adleman (RSA) encryption protocol. Some other important quantum algorithms include the Grover search algorithm, which is used to perform a search for an entry in an unstructured database; the quantum Fourier transform, which is a basis for a number of different algorithms; and Simon’s algorithm. The quantum computer is able to encode all input strings of length  $N$  simultaneously into a single computation step. In other words, the quantum computer is able simultaneously to pursue  $2^N$  classical paths, indicating that the quantum computer is significantly more powerful than the classical one.
3. *Entanglement.* At a quantum level, it appears that two quantum objects can form a single entity, even when they are well separated from each other. Any attempt to consider this entity as a combination of two independent quantum objects, given by tensor product of quantum states, fails, unless the possibility of signal propagation at superluminal speed is allowed. These quantum objects that cannot be decomposed into tensor product of individual independent quantum objects are called *entangled* quantum objects. Given the fact that arbitrary quantum states cannot be copied, which is the consequence of the no-cloning theorem, the communication at superluminal speed is not possible, and as consequence, the entangled quantum states cannot be written as the tensor product of independent quantum states. Moreover, it can be shown that the amount of information contained in an entangled state of  $N$  qubits grows exponentially instead of linearly, which is the case for classical bits.

In incoming subsections, we describe these fundamental features with more details.

### 2.3.1 Superposition Principle, Quantum Parallelism, Quantum Gates, and QIP Basics

We say that the allowable states  $|\mu\rangle$  and  $|\nu\rangle$  of the quantum system satisfy the *superposition principle* if their linear superposition  $\alpha|\mu\rangle + \beta|\nu\rangle$ , where  $\alpha$  and  $\beta$  are the complex numbers ( $\alpha, \beta \in C$ ), is also allowable quantum state. Without loss of generality, we typically observe the computational basis composed of the orthogonal canonical states  $|0\rangle = \begin{bmatrix} 1 \\ 0 \end{bmatrix}$ ,  $|1\rangle = \begin{bmatrix} 0 \\ 1 \end{bmatrix}$ , so that the quantum bit, also known as *qubit*, lies in a two-dimensional Hilbert space  $H$ , isomorphic to the  $C^2$  space, and can be represented as

$$|\psi\rangle = \alpha|0\rangle + \beta|1\rangle = \begin{pmatrix} \alpha \\ \beta \end{pmatrix}; \quad \alpha, \beta \in C; \quad |\alpha|^2 + |\beta|^2 = 1. \quad (2.60)$$

If we perform the measurement of a qubit, we will get  $|0\rangle$  with probability  $|\alpha|^2$  and  $|1\rangle$  with probability of  $|\beta|^2$ . Measurement changes the state of a qubit from a superposition of  $|0\rangle$  and  $|1\rangle$  to the specific state consistent with the measurement result. If we parameterize the probability amplitudes  $\alpha$  and  $\beta$  as follows:

$$\alpha = \cos\left(\frac{\theta}{2}\right), \quad \beta = e^{i\phi} \sin\left(\frac{\theta}{2}\right), \quad (2.61)$$

where  $\theta$  is a polar angle and  $\phi$  is an azimuthal angle, we can geometrically represent the qubit by the Bloch sphere (or the Poincaré sphere for the photon) as illustrated in Fig. 2.2. Bloch vector coordinates are given by  $(\cos\phi \sin\theta, \sin\phi \sin\theta, \cos\theta)$ . This Bloch vector representation is related to computational basis (CB) by

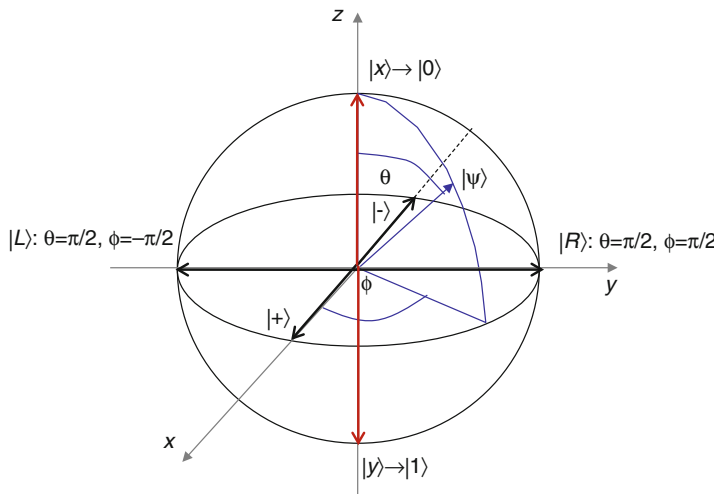


Fig. 2.2 Bloch (Poincaré) sphere representation of the single qubit

$$|\psi(\theta, \phi)\rangle = \cos(\theta/2)|0\rangle + e^{i\phi} \sin(\theta/2)|1\rangle \doteq \begin{pmatrix} \cos(\theta/2) \\ e^{i\phi} \sin(\theta/2) \end{pmatrix}, \quad (2.62)$$

where  $0 \leq \theta \leq \pi$  and  $0 \leq \phi < 2\pi$ . The north and south poles correspond to computational  $|0\rangle$  ( $|x\rangle$ -polarization) and  $|1\rangle$  ( $|y\rangle$ -polarization) basis kets, respectively. Other important bases are the *diagonal basis*  $\{|+\rangle, |-\rangle\}$ , very often denoted as  $\{|/\rangle, |\\\rangle\}$ , related to CB by

$$|+\rangle = |\diagup\rangle = \frac{1}{\sqrt{2}}(|0\rangle + |1\rangle), \quad |-\rangle = |\diagdown\rangle = \frac{1}{\sqrt{2}}(|0\rangle - |1\rangle), \quad (2.63)$$

and the *circular basis*  $\{|R\rangle, |L\rangle\}$ , related to the CB as follows:

$$|R\rangle = \frac{1}{\sqrt{2}}(|0\rangle + j|1\rangle), \quad |L\rangle = \frac{1}{\sqrt{2}}(|0\rangle - j|1\rangle). \quad (2.64)$$

The pure qubit states lie on the Bloch sphere, while the mixed qubit states lie in the interior of the Bloch sphere. The maximally mixed state  $I/2$  ( $I$  denotes the identity operator) lies in the center of the Bloch sphere. The orthogonal states are antipodal. From Fig. 2.2, we see that CB, diagonal basis, and circular bases are  $90^\circ$  apart from each other, and we often say that these three bases are mutually *conjugate bases*. These bases are used as three pairs of signal states for the six-state quantum key distribution (QKD) protocol. Another important basis used in QKD and for eavesdropping is the *Breidbart basis* given by  $\{\cos(\pi/8)|0\rangle + \sin(\pi/8)|1\rangle, -\sin(\pi/8)|0\rangle + \cos(\pi/8)|1\rangle\}$ .

The superposition principle is the key property that makes quantum parallelism possible. To see this, let us juxtapose  $n$  qubits lying in  $n$  distinct two-dimensional Hilbert spaces  $H_0, H_1, \dots, H_{n-1}$  that are isomorphic to each other. In practice, this means the qubits have been prepared separately, without any interaction, which can be mathematically described by the tensor product

$$|\psi\rangle = |\psi_0\rangle \otimes |\psi_1\rangle \otimes \cdots \otimes |\psi_{n-1}\rangle \in H_0 \otimes H_1 \otimes \cdots \otimes H_{n-1}. \quad (2.65)$$

Any arbitrary basis can be selected as the computational basis for  $H_i$ ,  $i = 0, 1, \dots, n-1$ . However, for ease of exposition, we assume the computational basis to be  $|0_i\rangle$  and  $|1_i\rangle$ . Consequently, we can represent the  $i$ th qubit as  $|\psi_i\rangle = \alpha_i|0_i\rangle + \beta_i|1_i\rangle$ . Introducing a further assumption,  $\alpha_i = \beta_i = 2^{-1/2}$ , without loss of generality, we now have

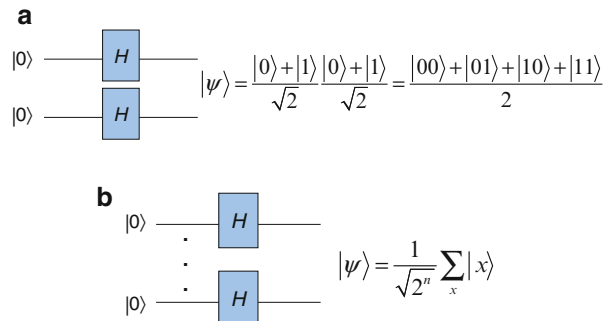
$$|\psi\rangle = \prod_{i=0}^{n-1} \frac{1}{\sqrt{2}}(|0_i\rangle + |1_i\rangle) = 2^{-n/2} \sum_{\mathbf{x}} |\mathbf{x}\rangle, \quad \mathbf{x} = x_0x_1 \cdots x_{n-1}, x_j \in \{0, 1\}. \quad (2.66)$$

This composite quantum system is called the ***n*-qubit register**, and as can be seen from the equation above, it represents a superposition of  $2^n$  quantum states that exist simultaneously! This is an example of quantum parallelism. In the classical realm, a linear increase in size corresponds roughly to a linear increase in processing power.

**Fig. 2.3** The Walsh–Hadamard transform: (a) on two qubits and (b) on  $n$  qubits. The action of the Hadamard gate

$H$  on computational basis kets is given by:

$$H|0\rangle = 2^{-1/2}(|0\rangle + |1\rangle) \text{ and } H|1\rangle = 2^{-1/2}(|0\rangle - |1\rangle)$$



In the quantum world, due to the power of quantum parallelism, a linear increase in size corresponds to an exponential increase in processing power. The downside, however, is the accessibility to this parallelism. Remember that superposition collapses the moment we attempt to measure it. The quantum circuit to create the superposition state above, in other words Walsh–Hadamard transform, is shown in Fig. 2.3. Therefore, the Walsh–Hadamard transform on  $n$  ancilla qubits in state  $|00\dots 0\rangle$  can be implemented by applying the Hadamard operators (gates)  $H$ , whose action is described in Fig. 2.3, on ancillary qubits.

More generally, a linear operator (gate)  $B$  can be expressed in terms of eigenkets  $\{|a^{(n)}\rangle\}$  of a Hermitian operator  $A$ . The *operator*  $B$  is associated with a *square matrix* (albeit infinite in extent), whose elements are

$$B_{mn} = \langle a^{(m)} | B | a^{(n)} \rangle, \quad (2.67)$$

and can explicitly be written as

$$B \doteq \begin{pmatrix} \langle a^{(1)} | B | a^{(1)} \rangle & \langle a^{(1)} | B | a^{(2)} \rangle & \dots \\ \langle a^{(2)} | B | a^{(1)} \rangle & \langle a^{(2)} | B | a^{(2)} \rangle & \dots \\ \vdots & \vdots & \ddots \end{pmatrix}, \quad (2.68)$$

where we use the notation  $\doteq$  to denote that operator  $B$  is represented by the matrix above. Very important single-qubit gates are Hadamard gate  $H$ , the phase shift gate  $S$ , the  $\pi/8$  (or  $T$ ) gate, controlled-NOT (or CNOT) gate, and Pauli operators  $X, Y, Z$ . The Hadamard gate  $H$ , phase shift gate,  $T$  gate, and CNOT gate have the following matrix representation in CB  $\{|0\rangle, |1\rangle\}$ :

$$H \doteq \frac{1}{\sqrt{2}} \begin{bmatrix} 1 & 1 \\ 1 & -1 \end{bmatrix}, \quad S \doteq \begin{bmatrix} 1 & 0 \\ 0 & j \end{bmatrix}, \quad T \doteq \begin{bmatrix} 1 & 0 \\ 0 & e^{j\pi/4} \end{bmatrix}, \quad \text{CNOT} \doteq \begin{bmatrix} 1 & 0 & 0 & 0 \\ 0 & 1 & 0 & 0 \\ 0 & 0 & 0 & 1 \\ 0 & 0 & 1 & 0 \end{bmatrix}. \quad (2.69)$$

The Pauli operators, on the other hand, have the following matrix representation in CB:

$$X \doteq \begin{bmatrix} 0 & 1 \\ 1 & 0 \end{bmatrix}, \quad Y \doteq \begin{bmatrix} 0 & -j \\ j & 0 \end{bmatrix}, \quad Z \doteq \begin{bmatrix} 1 & 0 \\ 0 & -1 \end{bmatrix}. \quad (2.70)$$

The action of Pauli gates on an arbitrary qubit  $|\psi\rangle = \alpha|0\rangle + \beta|1\rangle$  is given as follows:

$$\begin{aligned} X(\alpha|0\rangle + \beta|1\rangle) &= \alpha|1\rangle + \beta|0\rangle, & Y(\alpha|0\rangle + \beta|1\rangle) &= j(\alpha|1\rangle - \beta|0\rangle), \\ Z(\alpha|0\rangle + \beta|1\rangle) &= \alpha|0\rangle - \beta|1\rangle. \end{aligned} \quad (2.71)$$

So the action of  $X$  gate is to introduce the bit flip, the action of  $Z$  gate is to introduce the phase flip, and the action of  $Y$  gate is to simultaneously introduce the bit and phase flips.

Several important single-, double-, and triple-qubit gates are shown in Fig. 2.4. The action of a single-qubit gate is to apply the operator  $U$  on qubit  $|\psi\rangle$ , which results in another qubit. The controlled- $U$  gate conditionally applies the operator  $U$  on target qubit  $|\psi\rangle$ , when the control qubit  $|c\rangle$  is in the  $|1\rangle$ -state. One particularly important controlled- $U$  gate is CNOT gate. This gate flips the content of target qubit  $|t\rangle$  when the control qubit  $|c\rangle$  is in  $|1\rangle$ -state. The purpose of SWAP gate is to interchange the positions of two qubits, and it can be implemented by using three CNOT gates as shown in Fig. 2.4d. Finally, the Toffoli gate represents the generalization of CNOT gate, where two control qubits are used.

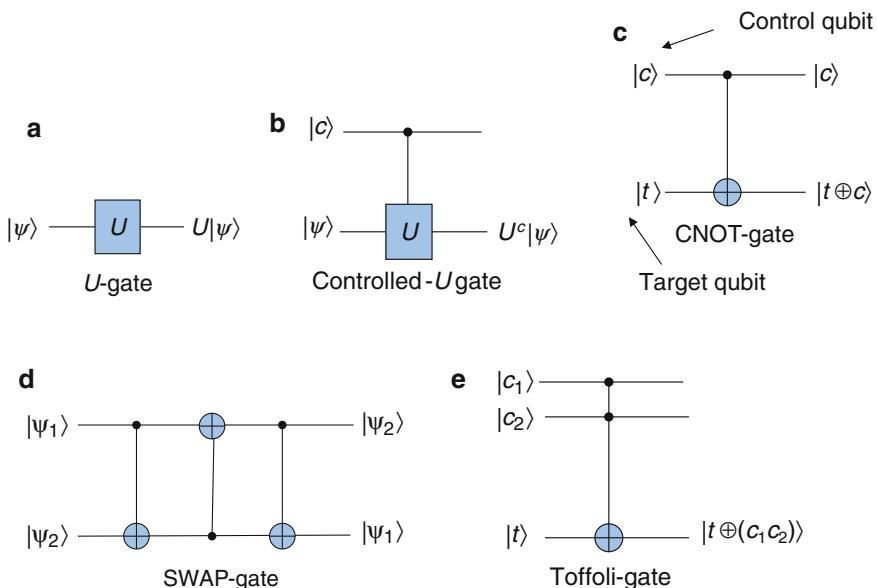
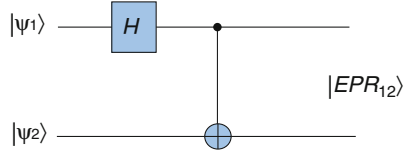


**Fig. 2.4** Important quantum gates and their action: (a) single-qubit gate, (b) controlled- $U$  gate, (c) CNOT gate, (d) SWAP gate, and (e) Toffoli gate

**Fig. 2.5** Bell state (EPR pairs) preparation circuit



The minimum set of gates that can be used to perform arbitrary quantum computation algorithm is known as the *universal set of gates*. The most popular sets of universal quantum gates are  $\{H, S, \text{CNOT}, \text{Toffoli}\}$  gates,  $\{H, S, \pi/8 (\text{T}), \text{CNOT}\}$  gates, Barenco gate, and Deutsch gate. By using these universal quantum gates, more complicated operations can be performed. As an illustration, in Fig. 2.5, the Bell state [Einstein–Podolsky–Rosen (EPR) pairs] preparation circuit is shown, which is of high importance in quantum teleportation and QKD applications.

So far, single-, double-, and triple-qubit quantum gates have been considered. An arbitrary quantum state of  $K$  qubits has the form  $\sum_s \alpha_s |s\rangle$ , where  $s$  runs over all binary strings of length  $K$ . Therefore, there are  $2^K$  complex coefficients, all independent except for the normalization constraint:

$$\sum_{s=00\dots00}^{11\dots11} |\alpha_s|^2 = 1. \quad (2.72)$$

For example, the state  $\alpha_{00}|00\rangle + \alpha_{01}|01\rangle + \alpha_{10}|10\rangle + \alpha_{11}|11\rangle$  (with  $|\alpha_{00}|^2 + |\alpha_{01}|^2 + |\alpha_{10}|^2 + |\alpha_{11}|^2 = 1$ ) is the general 2-qubit state (we use  $|00\rangle$  to denote the tensor product  $|0\rangle \otimes |0\rangle$ ). The multiple qubits can be **entangled** so that they cannot be decomposed into two separate states. For example, the Bell state or EPR pair  $(|00\rangle + |11\rangle)/\sqrt{2}$  cannot be written in terms of tensor product  $|\psi_1\rangle |\psi_2\rangle = (\alpha_1|0\rangle + \beta_1|1\rangle) \otimes (\alpha_2|0\rangle + \beta_2|1\rangle) = \alpha_1\alpha_2|00\rangle + \alpha_1\beta_2|01\rangle + \beta_1\alpha_2|10\rangle + \beta_1\beta_2|11\rangle$ , because it would require  $\alpha_1\alpha_2 = \beta_1\beta_2 = 1/\sqrt{2}$ , while  $\alpha_1\beta_2 = \beta_1\alpha_2 = 0$ , which a priori has no reason to be valid. This state can be obtained by using circuit shown in Fig. 2.5, for two-qubit input state  $|00\rangle$ . We will return to the concept of entanglement in Sect. 2.3.3.

The quantum parallelism can now be introduced more formally as follows. The QIP device, denoted as  $QIP$ , implemented on a quantum register maps the input string  $i_1, \dots, i_N$  to the output string  $O_1(i), \dots, O_N(i)$ :

$$\begin{pmatrix} O_1(i) \\ \vdots \\ O_N(i) \end{pmatrix} = U(QIP) \begin{pmatrix} i_1 \\ \vdots \\ i_N \end{pmatrix}; \quad (i)_{10} = (i_1, \dots, i_N)_2. \quad (2.73)$$

The CB states are denoted by

$$|i_1, \dots, i_N\rangle = |i_1\rangle \otimes \dots \otimes |i_N\rangle; \quad i_1, \dots, i_N \in \{0, 1\}. \quad (2.74)$$

The linear superposition allows us to form the following  $2N$ -qubit state:

$$|\psi_{\text{in}}\rangle = \left[ \frac{1}{\sqrt{2^N}} \sum_i |i_1, \dots, i_N\rangle \right] \otimes |0 \dots 0\rangle, \quad (2.75)$$

and upon the application of quantum operation  $U(QIP)$ , the output can be represented by

$$|\psi_{\text{out}}\rangle = U(QIP)|\psi_{\text{in}}\rangle = \frac{1}{\sqrt{2^N}} \sum_i |i_1, \dots, i_N\rangle \otimes |O_1(i), \dots, O_N(i)\rangle. \quad (2.76)$$

The QIP circuit (or a quantum computer) has been able to encode all input strings generated by  $QIP$  into  $|\psi_{\text{out}}\rangle$ ; in other words, it has simultaneously pursued  $2^N$  classical paths. This ability of a QIP circuit to encode multiple computational results into a quantum state in a single quantum computational step is known as **quantum parallelism**, as mentioned earlier.

### 2.3.2 No-Cloning Theorem and Distinguishing the Quantum States

Just like in quantum parallelism, the quantum superposition is also the key concept behind our inability to clone arbitrary quantum states. To see this, let us think of a quantum copier that takes as input an arbitrary quantum state and outputs two copies of that state, resulting in a clone of the original state. For example, if the input state is  $|\psi\rangle$ , then the output of the copier is  $|\psi\rangle|\psi\rangle$ . For an arbitrary quantum state, such a copier raises a fundamental contradiction. Consider two arbitrary states  $|\psi\rangle$  and  $|\chi\rangle$  that are inputted to the copier. When they are inputted individually, we expect to get  $|\psi\rangle|\psi\rangle$  and  $|\chi\rangle|\chi\rangle$ . Now consider a superposition of these two states given by

$$|\varphi\rangle = \alpha|\psi\rangle + \beta|\chi\rangle. \quad (2.77)$$

Based on the above description that the quantum copier clones the original state, we expect the output,

$$\begin{aligned} |\varphi\rangle|\varphi\rangle &= (\alpha|\psi\rangle + \beta|\chi\rangle)(\alpha|\psi\rangle + \beta|\chi\rangle) \\ &= \alpha^2|\psi\rangle|\psi\rangle + \alpha\beta|\psi\rangle|\chi\rangle + \alpha\beta|\chi\rangle|\psi\rangle + \beta^2|\chi\rangle|\chi\rangle. \end{aligned} \quad (2.78)$$

On the other hand, the linearity of quantum mechanics, as evidenced by the Schrodinger wave equation, tells us that the quantum copier can be represented by a unitary operator that performs the cloning. If such a unitary operator were to act on

the superposition state  $|\varphi\rangle$ , the output would be a superposition of  $|\psi\rangle|\psi\rangle$  and  $|\chi\rangle|\chi\rangle$ , that is,

$$|\varphi'\rangle = \alpha|\psi\rangle|\psi\rangle + \beta|\chi\rangle|\chi\rangle. \quad (2.79)$$

As is clearly evident, the difference between previous two equations leads to contradiction mentioned above. As a consequence, there is no unitary operator that can clone  $|\varphi\rangle$ . We therefore, formulate the no-cloning theorem as follows.

*No-cloning Theorem.* No quantum copier exists that can clone an arbitrary quantum state.

This result raises a related question: do there exist some specific states for which cloning is possible? The answer to this question is (surprisingly) yes. Remember, a key result of quantum mechanics is that unitary operators preserve probabilities. This implies that inner (dot) products  $\langle\varphi|\varphi\rangle$  and  $\langle\varphi'|\varphi'\rangle$  should be identical. The inner products  $\langle\varphi|\varphi\rangle$  and  $\langle\varphi'|\varphi'\rangle$  are, respectively, given by

$$\begin{aligned} \langle\varphi|\varphi\rangle &= (\langle\psi|\alpha^* + \langle\chi|\beta^*)(\alpha|\psi\rangle + \beta|\chi\rangle) \\ &= |\alpha|^2\langle\psi|\psi\rangle + |\beta|^2\langle\chi|\chi\rangle + \alpha^*\beta\langle\psi|\chi\rangle + \alpha\beta^*\langle\chi|\psi\rangle \\ \langle\varphi'|\varphi'\rangle &= (\langle\psi|\langle\psi|\alpha^* + \langle\chi|\langle\chi|\beta^*)(\alpha|\psi\rangle|\psi\rangle + \beta|\chi\rangle|\chi\rangle) \\ &= |\alpha|^2|\langle\psi|\psi\rangle|^2 + |\beta|^2|\langle\chi|\chi\rangle|^2 + \alpha^*\beta|\langle\psi|\chi\rangle|^2 + \alpha\beta^*|\langle\chi|\psi\rangle|^2. \end{aligned} \quad (2.80)$$

We know that  $\langle\psi|\psi\rangle = \langle\chi|\chi\rangle = 1$ . Therefore, the discrepancy lies in the cross terms. Specifically, to avoid the contradiction that resulted in the no-cloning theorem, we require that  $|\langle\psi|\chi\rangle|^2 = \langle\psi|\chi\rangle$ . This condition can only be satisfied when the states are orthogonal. Thus cloning is possible only for mutually orthogonal states. It is, however, important to remember a subtle point here. Even if we have a mutually orthogonal set of states, we need a quantum copier (or unitary operator) specifically for those states. If the unitary operator is specific to a different set of mutually orthogonal states, cloning would fail. It would seem that the no-cloning theorem would prevent us from exploiting the richness of quantum mechanics. It turns out that this is not the case. A key example is the QKD that with very high probability guarantees secure communication.

Not only that non-orthogonal quantum states cannot be cloned, they also cannot be reliably distinguished. There is no measurement device we can create that can reliably distinguish non-orthogonal states. This fundamental result plays an important role in quantum cryptography. Its proof is based on contradiction. Let us assume that the measurement operator  $M$  is the Hermitian operator (with corresponding eigenvalues  $m_i$  and corresponding projection operators  $P_i$ ) of an observable  $\mathfrak{M}$ , which allows unambiguously to distinguish between two non-orthogonal states  $|\psi_1\rangle$  and  $|\psi_2\rangle$ . The eigenvalue  $m_1$  ( $m_2$ ) unambiguously identifies the state  $|\psi_1\rangle$  ( $|\psi_2\rangle$ ) as the premeasurement state. We know that for projection operators the following properties are valid:

$$\begin{aligned} \langle \psi_1 | P_1 | \psi_1 \rangle &= 1 & \langle \psi_2 | P_2 | \psi_2 \rangle &= 1 \\ \langle \psi_1 | P_2 | \psi_1 \rangle &= 0 & \langle \psi_2 | P_1 | \psi_2 \rangle &= 0. \end{aligned} \quad (2.81)$$

Since  $|\psi_1\rangle$  and  $|\psi_2\rangle$  are non-orthogonal states,  $\langle \psi_1 | \psi_2 \rangle \neq 0$ , and  $|\psi_2\rangle$  can be represented in terms of  $|\psi_1\rangle$  and another state  $|\chi\rangle$  that is orthogonal to  $|\psi_1\rangle$  ( $\langle \psi_1 | \chi \rangle = 0$ ) as follows:

$$|\psi_2\rangle = \alpha|\psi_1\rangle + \beta|\chi\rangle. \quad (2.82)$$

From the projection operator properties, listed above, we can conclude the following:

$$\begin{aligned} 0 &= \langle \psi_1 | P_2 | \psi_1 \rangle \stackrel{P_2^2 = P_2}{=} \langle \psi_1 | P_2 P_2 | \psi_1 \rangle = \|P_2|\psi_1\rangle\|^2 \Rightarrow P_2|\psi_1\rangle = 0 \\ 1 &= \langle \psi_2 | P_2 | \psi_2 \rangle = \langle \psi_2 | P_2 P_2 | \psi_2 \rangle = (\alpha^* \langle \psi_1 | + \beta^* \langle \chi |)(\alpha P_2 |\psi_1\rangle + \beta P_2 |\chi\rangle) = |\beta|^2 \langle \chi | P_2 | \chi \rangle. \end{aligned} \quad (2.83)$$

Now we use the completeness relationship

$$1 = \langle \chi | \chi \rangle = \langle \chi | \sum_i^J P_i | \chi \rangle = \sum_i \langle \chi | P_i | \chi \rangle \stackrel{\langle \chi | P_i | \chi \rangle \geq 0}{\geq} \langle \chi | P_2 | \chi \rangle. \quad (2.84)$$

By combining the previous two equations, we obtain

$$1 = \langle \psi_2 | P_2 | \psi_2 \rangle \leq |\beta|^2 \Rightarrow |\beta|^2 = 1, \quad (2.85)$$

indicating that the probability of finding of  $|\psi_2\rangle$  in  $|\chi\rangle$  is 1. Therefore, we conclude that  $|\psi_2\rangle = |\chi\rangle$ , which is a contradiction. Therefore, indeed, *it is impossible to unambiguously distinguish non-orthogonal quantum states*.

### 2.3.3 Quantum Entanglement

Let  $|\psi_0\rangle, \dots, |\psi_{n-1}\rangle$  be  $n$  qubits lying in the Hilbert spaces  $H_0, \dots, H_{n-1}$ , respectively, and let the state of the joint quantum system lying in  $H_0 \otimes \dots \otimes H_{n-1}$  be denoted by  $|\psi\rangle$ . The qubit  $|\psi\rangle$  is then said to be entangled if it cannot be written in the product state form

$$|\psi\rangle = |\psi_0\rangle \otimes |\psi_1\rangle \otimes \dots \otimes |\psi_{n-1}\rangle. \quad (2.86)$$

Important examples of two-qubit states are *Bell states*, also known as *EPR states* (pairs):

$$\begin{aligned} |B_{00}\rangle &= \frac{1}{\sqrt{2}}(|00\rangle + |11\rangle), & |B_{01}\rangle &= \frac{1}{\sqrt{2}}(|01\rangle + |10\rangle), \\ |B_{10}\rangle &= \frac{1}{\sqrt{2}}(|00\rangle - |11\rangle), & |B_{11}\rangle &= \frac{1}{\sqrt{2}}(|01\rangle - |10\rangle). \end{aligned} \quad (2.87)$$

The  $n$ -qubit ( $n > 2$ ) analogs of Bell states will be now briefly reviewed. One popular family of entangled multiqubit states is Greenberger–Horne–Zeilinger (GHZ) states:

$$|\text{GHZ}\rangle = \frac{1}{\sqrt{2}}(|00\cdots 0\rangle \pm |11\cdots 1\rangle). \quad (2.88)$$

Another popular family of multiqubit entangled states is known as  $W$  states:

$$|W\rangle = \frac{1}{\sqrt{N}}(|00\cdots 01\rangle + |00\cdots 10\rangle + \cdots + |01\cdots 00\rangle + |10\cdots 00\rangle). \quad (2.89)$$

The  $W$  state of  $n$  qubits represents a superposition of single-weighted CB states, each occurring with probability amplitude of  $N^{-1/2}$ .

For a bipartite system, we can elegantly verify whether or not the qubit  $|\psi\rangle$  is a product state or an entangled one, by Schmidt decomposition [1, 7]. The *Schmidt decomposition theorem* states that a pure state  $|\psi\rangle$  of the composite system  $H_A \otimes H_B$  can be represented as

$$|\psi\rangle = \sum_i c_i |i_A\rangle |i_B\rangle, \quad (2.90)$$

where  $|i_A\rangle$  and  $|i_B\rangle$  are orthonormal basis of the subsystems  $H_A$  and  $H_B$ , respectively, and  $c_i \in \mathfrak{R}^+$  ( $\mathfrak{R}^+$  is the set of nonnegative real numbers) are *Schmidt coefficients* that satisfy the following condition  $\sum_i c_i^2 = 1$ . For the proof of the theorem, please refer to [1]. The Schmidt coefficients can be calculated from the partial density matrix  $\text{Trace}_B(|\psi\rangle\langle\psi|)$ . A corollary of the Schmidt decomposition theorem is that a pure state in a composite system is a product state if and only if the Schmidt rank is 1 and is an entangled state if and only if the Schmidt rank is greater than one.

As an illustration, let us verify if the Bell state  $|B_{11}\rangle$  is an entangled one. We first determine the density matrix:

$$\begin{aligned} \rho &= |\psi\rangle\langle\psi| = \frac{1}{\sqrt{2}}(|01\rangle - |10\rangle)\frac{1}{\sqrt{2}}(\langle 01| - \langle 10|) \\ &= \frac{1}{2}(|01\rangle\langle 01| - |01\rangle\langle 10| - |10\rangle\langle 01| + |10\rangle\langle 10|). \end{aligned}$$

By tracing out the subsystem  $B$ , we obtain

$$\begin{aligned}\rho_A &= \text{Trace}_B(|\psi\rangle\langle\psi|) = \langle 0_B|\psi\rangle\langle\psi|0_B\rangle + \langle 1_B|\psi\rangle\langle\psi|1_B\rangle \\ &= \frac{1}{2}(|1\rangle\langle 1| + |0\rangle\langle 0|) = \frac{1}{2}I.\end{aligned}$$

The eigenvalues are  $c_1 = c_2 = 1/2$ , and the Schmidt rank is 2 indicating that the Bell state  $|B_{11}\rangle$  is an entangled state.

### 2.3.4 Operator Sum Representation

Let the composite system  $C$  be composed of quantum register  $Q$  and environment  $E$ . This kind of system can be modeled as a closed quantum system. Because the composite system is closed, its dynamic is unitary, and final state is specified by a unitary operator  $U$  as follows:  $U(\rho \otimes \varepsilon_0)U^\dagger$ , where  $\rho$  is a density operator of initial state of quantum register  $Q$  and  $\varepsilon_0$  is the initial density operator of the environment  $E$ . The reduced density operator of  $Q$  upon interaction  $\rho_f$  can be obtained by tracing out the environment:

$$\rho_f = \text{Tr}_E[U(\rho \otimes \varepsilon_0)U^\dagger] \equiv \xi(\rho). \quad (2.91)$$

The transformation (mapping) of initial density operator  $\rho$  to the final density operator  $\rho_f$ , denoted as  $\xi : \rho \rightarrow \rho_f$ , given by (2.91), is often called the *superoperator* or *quantum operation*. The final density operator can be expressed in the so-called operator sum representation as follows:

$$\rho_f = \sum_k E_k \rho E_k^\dagger, \quad (2.92)$$

where  $E_k$  are the operation elements for the superoperator. Clearly, in the absence of environment, the superoperator becomes  $U\rho U^\dagger$ , which is nothing else but a conventional time-evolution quantum operation.

The operator sum representation can be used in the classification of quantum operations into two categories: (1) *trace preserving* when  $\text{Tr } \xi(\rho) = \text{Tr } \rho = 1$  and (2) *non-trace preserving* when  $\text{Tr } \xi(\rho) < 1$ . Starting from the trace-preserving condition

$$\text{Tr } \rho = \text{Tr } \xi(\rho) = \text{Tr} \left[ \sum_k E_k \rho E_k^\dagger \right] = \text{Tr} \left[ \rho \sum_k E_k E_k^\dagger \right] = 1, \quad (2.93)$$

we obtain

$$\sum_k E_k E_k^\dagger = I. \quad (2.94)$$

For non-trace-preserving quantum operation, (2.93) is not satisfied, and informally we can write  $\sum_k E_k E_k^\dagger < I$ .

If the *environment dimensionality is large enough*, it can be found in pure state,  $\epsilon_0 = |\phi_0\rangle\langle\phi_0|$ , and the corresponding superoperator becomes

$$\begin{aligned} \xi(\rho) &= \text{Tr}_E[U(\rho \otimes \epsilon)U^\dagger] = \sum_k \langle\phi_k| (U\rho \otimes \epsilon U^\dagger) |\phi_k\rangle \\ &= \sum_k \langle\phi_k| \left( U\rho \otimes \left( \underbrace{|\phi_0\rangle\langle\phi_0|}_{\epsilon} \right) U^\dagger \right) |\phi_k\rangle \\ &= \sum_k \underbrace{\langle\phi_k|U|\phi_0\rangle}_{E_k} \rho \underbrace{\langle\phi_0|U^\dagger|\phi_k\rangle}_{E_k^\dagger} \\ &= \sum_k E_k \rho E_k^\dagger, \quad E_k = \langle\phi_k|U|\phi_0\rangle. \end{aligned} \quad (2.95)$$

The  $E_k$  operators in operator sum representation are known as *Kraus operators*.

As an illustration, let us consider bit-flip and phase-flip channels. Let the composite system be given by  $|\phi_E\rangle|\psi_Q\rangle$ , wherein the initial state of environment is  $|\phi_E\rangle = |0_E\rangle$ . Let further the quantum subsystem  $Q$  interacts to the environment  $E$  by the Pauli- $X$  operator:

$$U = \sqrt{1-p}I \otimes I + \sqrt{p}X \otimes X, \quad 0 \leq p \leq 1. \quad (2.96)$$

Therefore, with probability  $1-p$ , we leave the quantum system untouched, while with probability  $p$  we apply Pauli- $X$  operator to both quantum subsystem and the environment. By applying the operator  $U$  on environment state, we obtain

$$U|\phi_E\rangle = \sqrt{1-p}I \otimes I|0_E\rangle + \sqrt{p}X \otimes X|0_E\rangle = \sqrt{1-p}|0_E\rangle I + \sqrt{p}|1_E\rangle X. \quad (2.97)$$

The corresponding Kraus operators are given by

$$E_0 = \langle 0_E|U|\phi_E\rangle = \sqrt{1-p}I, \quad E_1 = \langle 1_E|U|\phi_E\rangle = \sqrt{p}X. \quad (2.98)$$

Finally, the operator sum representation is given by

$$\xi(\rho) = E_0 \rho E_0^\dagger + E_1 \rho E_1^\dagger = (1-p)\rho + pX\rho X. \quad (2.99)$$

In similar fashion, the Kraus operators for the phase-flip channel are given by

$$E_0 = \langle 0_E|U|\phi_E\rangle = \sqrt{1-p}I, \quad E_1 = \langle 1_E|U|\phi_E\rangle = \sqrt{p}Z, \quad (2.100)$$

and the corresponding operator sum representation is

$$\xi(\rho) = E_0\rho E_0^\dagger + E_1\rho E_1^\dagger = (1 - p)\rho + pZ\rho Z. \quad (2.101)$$

### 2.3.5 Decoherence Effects, Depolarization, and Amplitude Damping Channel Models

Quantum computation works by manipulating quantum interference effect. The quantum interference, a manifestation of coherent superposition of quantum states, is the cornerstone behind all quantum information tasks such as quantum computation and quantum communication. A major source of problem is our inability to prevent our quantum system of interest from interacting with the surrounding environment. This interaction results in an entanglement between the quantum system and the environment leading to decoherence. To understand this system–environment entanglement and decoherence better, let us consider a qubit described by density state (matrix)  $\rho = \begin{bmatrix} a & b \\ c & d \end{bmatrix}$  interacting with the environment, described by the following three states:  $|0_E\rangle$ ,  $|1_E\rangle$ , and  $|2_E\rangle$ . Without loss of generality, we assume that environment was initially in state  $|0_E\rangle$ . The unitary operator introducing the entanglement between the quantum system and the environment is defined as

$$\begin{aligned} U|0\rangle|0_E\rangle &= \sqrt{1-p}|0\rangle|0_E\rangle + \sqrt{p}|0\rangle|1_E\rangle \\ U|0\rangle|0_E\rangle &= \sqrt{1-p}|1\rangle|0_E\rangle + \sqrt{p}|1\rangle|2_E\rangle. \end{aligned} \quad (2.102)$$

The corresponding Kraus operators are given by

$$E_0 = \sqrt{1-p}I, \quad E_1 = \sqrt{p}|0\rangle\langle 0|, \quad E_2 = \sqrt{p}|1\rangle\langle 1|. \quad (2.103)$$

The operator sum representation is given by

$$\xi(\rho) = E_0\rho E_0^\dagger + E_1\rho E_1^\dagger + E_2\rho E_2^\dagger = \begin{bmatrix} a & (1-p)b \\ (1-p)c & d \end{bmatrix}. \quad (2.104)$$

By applying these quantum operation  $n$ -times, the corresponding final state would be

$$\rho_f = \begin{bmatrix} a & (1-p)^n b \\ (1-p)^n c & d \end{bmatrix}. \quad (2.105)$$

If the probability  $p$  is expressed as  $p = \gamma\Delta t$ , we can write  $n = t/\Delta t$  and in limit we obtain

$$\lim_{\Delta t \rightarrow 0} (1 - p)^n = (1 - \gamma\Delta t)^{t/\Delta t} = e^{-\gamma t}. \quad (2.106)$$

Therefore, the corresponding operator sum representation as  $n$  tends to plus infinity is given by

$$\xi(\rho) = \begin{bmatrix} a & e^{-\gamma t}b \\ e^{-\gamma t}c & d \end{bmatrix}. \quad (2.107)$$

Clearly, the terms  $b$  and  $c$  go to zero as  $t$  increases, indicating that the relative phase in the original state of the quantum system is lost, and the corresponding channel model is known as the *phase damping* channel model.

In the above example, we have considered the coupling between a single-qubit quantum system and the environment and discussed the resulting loss of interference or coherent superposition. In general, for multiple qubit systems, decoherence also results in loss of coupling between the qubits. In fact, with increasing complexity and size of the quantum computer, the decoherence effect becomes worse. Additionally, the quantum system lies in some complex Hilbert space where there are infinite variations of errors that can cause decoherence.

A more general example of dephasing is the depolarization. The *depolarizing channel*, as shown in Fig. 2.6, with probability  $1 - p$  leaves the qubit as it is, while with probability  $p$  moves the initial state into  $\rho_f = I/2$  that maximizes the von Neumann entropy  $S(\rho) = -\text{Tr } \rho \log \rho = 1$ . The properties describing the model can be summarized as follows:

1. Qubit errors are independent.
2. Single-qubit errors ( $X, Y, Z$ ) are equally likely.
3. All qubits have the same single-error probability  $p/4$ .

The Kraus operators  $E_i$  of the channel should be selected as follows:

$$E_0 = \sqrt{1 - 3p/4}I; \quad E_1 = \sqrt{p/4}X; \quad E_2 = \sqrt{p/4}Y; \quad E_3 = \sqrt{p/4}Z. \quad (2.108)$$

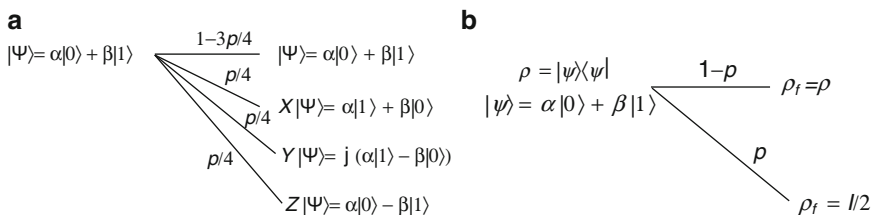


**Fig. 2.6** Depolarizing channel model: (a) Pauli operator description and (b) density operator description

The action of depolarizing channel is to perform the following mapping:  $\rho \rightarrow \xi(\rho) = \sum_i E_i \rho E_i^\dagger$ , where  $\rho$  is the initial density operator. Without loss of generality, we will assume that initial state was pure  $|\psi\rangle = a|0\rangle + b|1\rangle$  so that

$$\begin{aligned}\rho &= |\psi\rangle\langle\psi| = (a|0\rangle + b|1\rangle)(\langle 0|a^* + \langle 1|b^*) \\ &= |a|^2 \begin{bmatrix} 1 & 0 \\ 0 & 0 \end{bmatrix} + ab^* \begin{bmatrix} 0 & 1 \\ 0 & 0 \end{bmatrix} + a^*b \begin{bmatrix} 0 & 0 \\ 1 & 0 \end{bmatrix} + |b|^2 \begin{bmatrix} 0 & 0 \\ 0 & 1 \end{bmatrix} \\ &= \begin{bmatrix} |a|^2 & ab^* \\ a^*b & |b|^2 \end{bmatrix}.\end{aligned}\quad (2.109)$$

The resulting quantum operation can be represented using operator sum representation as follows:

$$\begin{aligned}\xi(\rho) &= \sum_i E_i \rho E_i^\dagger = \left(1 - \frac{3p}{4}\right)\rho + \frac{p}{4}(X\rho X + Y\rho Y + Z\rho Z) \\ &= \left(1 - \frac{3p}{4}\right) \begin{bmatrix} |a|^2 & ab^* \\ a^*b & |b|^2 \end{bmatrix} + \frac{p}{4} \begin{bmatrix} 0 & 1 \\ 1 & 0 \end{bmatrix} \begin{bmatrix} |a|^2 & ab^* \\ a^*b & |b|^2 \end{bmatrix} \begin{bmatrix} 0 & 1 \\ 1 & 0 \end{bmatrix} \\ &\quad + \frac{p}{4} \begin{bmatrix} 1 & 0 \\ 0 & -1 \end{bmatrix} \begin{bmatrix} |a|^2 & ab^* \\ a^*b & |b|^2 \end{bmatrix} \begin{bmatrix} 1 & 0 \\ 0 & -1 \end{bmatrix} + \frac{p}{4} \begin{bmatrix} 0 & -j \\ j & 0 \end{bmatrix} \begin{bmatrix} |a|^2 & ab^* \\ a^*b & |b|^2 \end{bmatrix} \begin{bmatrix} 0 & -j \\ j & 0 \end{bmatrix} \\ &= \left(1 - \frac{3p}{4}\right) \begin{bmatrix} |a|^2 & ab^* \\ a^*b & |b|^2 \end{bmatrix} + \frac{p}{4} \begin{bmatrix} |b|^2 & a^*b \\ ab^* & |a|^2 \end{bmatrix} + \frac{p}{4} \begin{bmatrix} |a|^2 & -ab^* \\ -a^*b & |b|^2 \end{bmatrix} + \frac{p}{4} \begin{bmatrix} |b|^2 & -a^*b \\ -ab^* & |a|^2 \end{bmatrix} \\ &= \begin{bmatrix} \left(1 - \frac{p}{2}\right)|a|^2 + \frac{p}{2}|b|^2 & (1-p)ab^* \\ (1-p)a^*b & \frac{p}{2}|a|^2 + \left(1 - \frac{p}{2}\right)|b|^2 \end{bmatrix} \\ &= \begin{bmatrix} (1-p)|a|^2 + \frac{p}{2}(|a|^2 + |b|^2) & (1-p)ab^* \\ (1-p)a^*b & \frac{p}{2}(|a|^2 + |b|^2) + (1-p)|b|^2 \end{bmatrix}.\end{aligned}\quad (2.110)$$

Since  $|a|^2 + |b|^2 = 1$ , the operator sum representation can be written as

$$\xi(\rho) = \sum_i E_i \rho E_i^\dagger = (1-p) \begin{bmatrix} |a|^2 & ab^* \\ a^*b & |b|^2 \end{bmatrix} + \frac{p}{2}I = (1-p)\rho + \frac{p}{2}I. \quad (2.111)$$

The first line in (2.110) corresponds to the model shown in Fig. 2.6a, and the last line (see also (2.111)) corresponds to the model shown in Fig. 2.6b. It is clear from (2.109) and (2.111) that  $\text{Tr } \xi(\rho) = \text{Tr } (\rho) = 1$  meaning that the superoperator is trace preserving. Notice that the depolarizing channel model in some other books/papers can slightly be differently defined.

In the rest of this subsection, we describe the amplitude damping channel model. In certain quantum channels, the errors  $X$ ,  $Y$ , and  $Z$  do not occur with the same probability. In amplitude damping channel, the operation elements are given by

$$E_0 = \begin{pmatrix} 1 & 0 \\ 0 & \sqrt{1-\varepsilon^2} \end{pmatrix}, \quad E_1 = \begin{pmatrix} 0 & \varepsilon \\ 0 & 0 \end{pmatrix}. \quad (2.112)$$

The *spontaneous emission* is an example of a physical process that can be modeled using the amplitude damping channel model. If  $|\psi\rangle = a|0\rangle + b|1\rangle$  is the initial qubit state ( $\rho = \begin{bmatrix} |a|^2 & ab^* \\ a^*b & |b|^2 \end{bmatrix}$ ), the effect of amplitude damping channel is to perform the following mapping:

$$\begin{aligned} \rho \rightarrow \xi(\rho) &= E_0 \rho E_0^\dagger + E_1 \rho E_1^\dagger = \begin{pmatrix} 1 & 0 \\ 0 & \sqrt{1-\varepsilon^2} \end{pmatrix} \begin{bmatrix} |a|^2 & ab^* \\ a^*b & |b|^2 \end{bmatrix} \begin{pmatrix} 1 & 0 \\ 0 & \sqrt{1-\varepsilon^2} \end{pmatrix} \\ &\quad + \begin{pmatrix} 0 & \varepsilon \\ 0 & 0 \end{pmatrix} \begin{bmatrix} |a|^2 & ab^* \\ a^*b & |b|^2 \end{bmatrix} \begin{pmatrix} 0 & 0 \\ \varepsilon & 0 \end{pmatrix} \\ &= \begin{pmatrix} |a|^2 & ab^* \sqrt{1-\varepsilon^2} \\ a^*b \sqrt{1-\varepsilon^2} & |b|^2(1-\varepsilon^2) \end{pmatrix} + \begin{pmatrix} |b|^2 \varepsilon^2 & 0 \\ 0 & 0 \end{pmatrix} \\ &= \begin{pmatrix} |a|^2 + \varepsilon^2 |b|^2 & ab^* \sqrt{1-\varepsilon^2} \\ a^*b \sqrt{1-\varepsilon^2} & |b|^2(1-\varepsilon^2) \end{pmatrix}. \end{aligned} \quad (2.113)$$

Probabilities  $P(0)$  and  $P(1)$  that  $E_0$  and  $E_1$  occur are given by

$$\begin{aligned} P(0) &= \text{Tr}(E_0 \rho E_0^\dagger) = \text{Tr} \begin{pmatrix} |a|^2 & ab^* \sqrt{1-\varepsilon^2} \\ a^*b \sqrt{1-\varepsilon^2} & |b|^2(1-\varepsilon^2) \end{pmatrix} = 1 - \varepsilon^2 |b|^2 \\ P(1) &= \text{Tr}(E_1 \rho E_1^\dagger) = \text{Tr} \begin{pmatrix} |b|^2 \varepsilon^2 & 0 \\ 0 & 0 \end{pmatrix} = \varepsilon^2 |b|^2. \end{aligned} \quad (2.114)$$

The corresponding amplitude damping channel model is shown in Fig. 2.7.

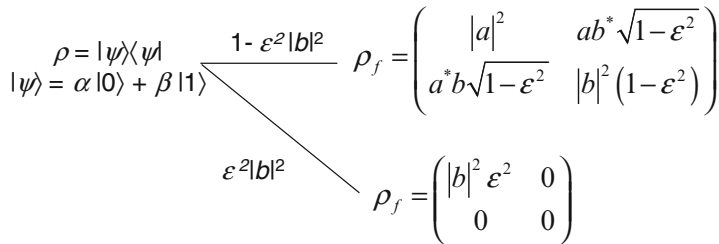


**Fig. 2.7** Amplitude damping channel model

## 2.4 Classical (Shannon) and Quantum (von Neumann) Entropies

Let us observe a classical discrete memoryless source with the alphabet  $X = \{x_1, x_2, \dots, x_N\}$ . The symbols from the alphabet are emitted by the source with probabilities  $P(X = x_n) = p_n$ ,  $n = 1, 2, \dots, N$ . The amount of information carried by the  $k$ th symbol is related to the uncertainty that is resolved when this symbol occurs, and it is defined as  $I(x_n) = \log(1/p_n) = -\log(p_n)$ , where the logarithm is to the base 2. The classical (Shannon) entropy is defined as the measure of the average amount of information per source symbol [27, 28]:

$$H(X) = E[I(x_n)] = \sum_{n=1}^N p_n I(x_n) = \sum_{n=1}^N p_n \log_2 \left( \frac{1}{p_n} \right). \quad (2.115)$$

The Shannon entropy satisfies the following inequalities:

$$0 \leq H(X) \leq \log N = \log |X|. \quad (2.116)$$

Let  $Q$  be a quantum system with the state described by the density operator  $\rho_x$ . The probability that the output  $\rho_x$  is obtained is given by  $p_x = P(x)$ . The quantum source is, therefore, described by the ensemble  $\{\rho_x, p_x\}$ , characterized by the mixed density operator  $\rho = \sum_{x \in X} p_x \rho_x$ . Then the *quantum (von Neumann) entropy* is defined as

$$S(\rho) = -\text{Tr}(\rho \log \rho) = -\sum_{\lambda_i} \lambda_i \log \lambda_i, \quad (2.117)$$

where  $\lambda_i$  are eigenvalues of  $\rho$ . When all quantum states are pure and mutually orthogonal, then von Neumann entropy equals the Shannon entropy as in that case  $p_i = \lambda_i$ . As an illustration, in Fig. 2.8, we provide an interpretation of quantum representation of the classical information.

Two different preparations  $P^{(i)}$  and  $P^{(j)}$ , with  $H(X^{(i)}) \neq H(X^{(j)})$  ( $i \neq j$ ), can generate the same  $\rho$  and hence have the same von Neumann entropy  $S(\rho)$  because the states of the two preparations may not be physically distinguishable from each other.

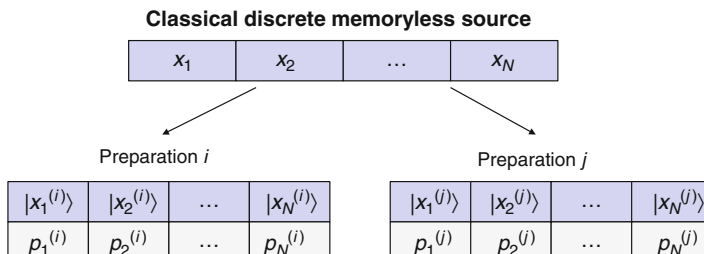


**Fig. 2.8** The illustration of quantum representation of the classical information

## 2.5 Holevo Information, Accessible Information, and Holevo Bound

A classical discrete memoryless channel (DMC) is described by the set of transition probabilities

$$p(y_k|x_j) = P(Y = y_k|X = x_j); \quad 0 \leq p(y_k|x_j) \leq 1 \quad (2.118)$$

satisfying the condition  $\sum_k p(y_k|x_j) = 1$ . The conditional entropy of  $X$ , given  $Y = y_k$ , is related to the uncertainty of the channel input  $X$  by observing the channel output  $y_k$ , and it is defined as

$$H(X|Y = y_k) = \sum_j p(x_j|y_k) \log \left[ \frac{1}{p(x_j|y_k)} \right], \quad (2.119)$$

where

$$p(x_j|y_k) = p(y_k|x_j) p(x_j) / p(y_k), \quad p(y_k) = \sum_j p(y_k|x_j) p(x_j). \quad (2.120)$$

The amount of uncertainty remaining about the channel input  $X$  after the observing channel output  $Y$  can be then determined by

$$\begin{aligned} H(X|Y) &= \sum_k H(X|Y = y_k) p(y_k) \\ &= \sum_k p(y_k) \sum_j p(x_j|y_k) \log \left[ \frac{1}{p(x_j|y_k)} \right]. \end{aligned} \quad (2.121)$$

Therefore, the amount of uncertainty about the channel input  $X$  that is resolved by observing the channel input would be the difference  $H(X) - H(X|Y)$ , and this difference is known as the mutual information  $I(X, Y)$  (also known as transinformation) [29, 30]. In other words,

$$I(X, Y) = H(X) - H(X|Y) = \sum_j p(x_j) \sum_k p(y_k|x_j) \log \left[ \frac{p(y_k|x_j)}{p(y_k)} \right]. \quad (2.122)$$

The mutual information can also be defined between any two random variables  $X$  and  $Y$ . In this case, the mutual information is related to the amount information that  $Y$  has about  $X$  in average, namely,  $I(X;Y) = H(X) - H(X|Y)$ . In other words, it represents the amount of uncertainty about  $X$  that is resolved given that we know  $Y$ .

In the quantum information theory, we can provide a similar interpretation of Holevo information. The *Holevo information*  $\chi$  for the ensemble of states  $\{\rho_x, p_x\}$

corresponds to the average reduction in quantum entropy given that we know how  $\rho$  was prepared, namely,  $\rho = \sum_x p_x \rho_x$ , and it is defined as

$$\chi = S(\rho) - \sum_x p_x S(\rho_x). \quad (2.123)$$

Holevo information is upper bounded by Shannon entropy, namely,  $\chi \leq H(X)$ .

Maximum of the mutual information over all generalized POVM measurement schemes  $M_y$ , denoted as  $H(X:Y)$ , is known as *accessible information*, and it is officially defined as

$$H(X : Y) = \max_{M_y} I(X; Y). \quad (2.124)$$

If the quantum states are pure and mutually orthogonal, instead of POVM we consider projective measurements such that  $p(y|x) = \text{Tr}(M_y \rho_x) = \text{Tr}(P_y \rho_x) = 1$ , iff  $x = y$  and zero otherwise. In that case,  $H(X:Y) = H(X)$  and Bob (receiver) is able accurately to estimate the information sent by Alice (transmitter). If the states are non-orthogonal, the accessible information is bounded by

$$H(X : Y) \leq S(\rho) \leq H(X). \quad (2.125)$$

When  $\rho_x$  states are mixed states, the accessible information is bounded by the Holevo information

$$H(X : Y) \leq \chi. \quad (2.126)$$

Since the Holevo information is upper bounded by the Shannon entropy, we can write

$$H(X : Y) \leq \chi \leq H(X). \quad (2.127)$$

Therefore, it is impossible for Bob to completely recover the classical information, characterized by  $H(X)$ , which Alice has sent him over the quantum channel!

## 2.6 Schumacher's Noiseless Quantum Coding Theorem and Holevo–Schumacher–Westmoreland Theorem

### 2.6.1 Schumacher's Noiseless Quantum Coding Theorem and Quantum Compression

Consider a classical source  $X$  that generates symbols 0 and 1 with probabilities  $p$  and  $1 - p$ , respectively. The probability of output sequence  $x_1, \dots, x_N$  is given by

$$p(x_1, \dots, x_N) = p \sum_i x_i (1-p) \sum_i (1-x_i) \xrightarrow{N \rightarrow \infty} p^{Np} (1-p)^{N(1-p)}. \quad (2.128)$$

By taking the logarithm of this probability, we obtain

$$\log p(x_1, \dots, x_N) \approx Np \log p + N(1-p) \log(1-p) = -NH(X). \quad (2.129)$$

Therefore, the probability of occurrence of the so-called typical sequence is  $p(x_1, \dots, x_N) \approx 2^{-NH(X)}$ , and in average,  $NH(X)$  bits are needed to represent any typical sequence, which is illustrated in Fig. 2.9a. We denoted the typical set by  $T(N, \varepsilon)$ . Clearly, not much of the information will be lost if we consider  $2^{NH(X)}$  typical sequences, instead of  $2^N$  possible sequences, in particular for large  $N$ . This observation can be used in data compression. Namely, with  $NH(X)$  bits, we can enumerate all typical sequences. If the source output is a typical sequence, it will be represented with  $NH(X)$  bits. On the other hand, when atypical sequence gets generated by the source, we will assign a fixed index to it resulting in compression loss. However, as  $N \rightarrow \infty$ , the probability of occurrence of atypical sequence will tend to zero resulting in arbitrary small information loss.

Let us now extend this concept to nonbinary sources. The law of large numbers [27] applied to a nonbinary source with i.i.d. outputs  $X_1, \dots, X_N$  claims that as  $N \rightarrow \infty$ , the expected value of the source approaches the true value  $E(X)$  in probability sense. In other words,

$$P\left(\left|\frac{1}{N} \sum_i X_i - E(X)\right| \leq \varepsilon\right) > 1 - \delta \quad (2.130)$$

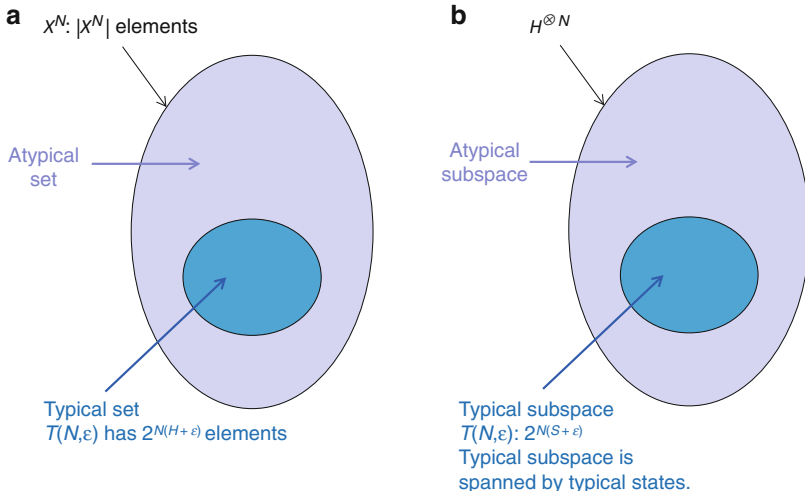


**Fig. 2.9** The illustration of typical set (a) and typical subspace (b)

for sufficiently large  $N$  and  $\varepsilon, \delta > 0$ . Based on the discussion for the typical set, we can write

$$-N[H(X) + \varepsilon] \leq \log P(x_1, \dots, x_N) \leq -N[H(X) - \varepsilon]. \quad (2.131)$$

Since  $P[T(N, \varepsilon)] > 1 - \delta$ , the size of typical set, denoted as  $|T(N, \varepsilon)|$ , will be bounded by

$$(1 - \varepsilon)2^{N[H(X) - \varepsilon]} \leq |T(N, \varepsilon)| \leq 2^{N[H(X) + \varepsilon]}. \quad (2.132)$$

Suppose now that a compression rate  $R$  is larger than  $H(X)$ , say  $R > H(X) + \varepsilon$ . Then based on the discussion above, the total number of typical sequences is bounded by

$$|T(N, \varepsilon)| \leq 2^{N[H(X) + \varepsilon]} \leq 2^{NR}, \quad (2.133)$$

and the probability of occurrence of typical sequence is lower bounded by  $1 - \delta$ , where  $\delta$  is arbitrary small.

The source encoding strategy can be described as follows. Let us divide the set of all sequences generated by the source into typical and atypical sets as shown in Fig. 2.9a. From the equation above, it is clear that sequences in the typical set can be represented by at most  $NR$  bits. If an atypical sequence occurs, we assign to it a fixed index. As  $N$  tends to infinity, the probability for this event to occur tends to zero, indicating that we can encode and decode typical sequences reliably. On the other hand, when  $R < H(X)$ , we can encode maximum  $2^{NR}$  typical sequences, labeled as  $T_R(N, \varepsilon)$ . Since the probability of occurrence of typical sequence is upper bounded by  $2^{-N[H(X) - \varepsilon]}$ , the typical sequences in  $T_R(N, \varepsilon)$  will occur with probability  $2^{N[R - H(X) + \varepsilon]}$ , which tends to zero as  $N$  tends to infinity, indicating that the reliable compression scheme does not exist in this case. With this, we have just proved the Shannon's source coding theorem, which can be formulated as follows.

**Shannon's Source Coding Theorem.** For an i.i.d. source  $X$ , the reliable compression method exists for  $R > H(X)$ . If, on the other hand,  $R < H(X)$ , then no reliable compression scheme exists.

Consider now a quantum source emitting a pure state  $|\psi_x\rangle$  with probability  $p_x$ , described in terms of the mixed density operator

$$\rho = \sum_x p_x |\psi_x\rangle \langle \psi_x|. \quad (2.134)$$

The quantum message comprises  $N$  quantum source outputs, independent of each other, so that

$$\rho_{\otimes N} = \rho \otimes \dots \otimes \rho. \quad (2.135)$$

The mixed density operator can be expressed in terms of eigenkets as

$$\rho = \sum_{\alpha} \lambda_{\alpha} |\lambda_{\alpha}\rangle\langle\lambda_{\alpha}|. \quad (2.136)$$

The *typical state* is a state  $|\lambda_1\rangle \dots |\lambda_N\rangle$  for which  $\lambda_1 \dots \lambda_N$  is a typical sequence satisfying the following inequality for sufficiently large  $N$ :

$$P\left(\left|\frac{1}{N} \log \left(\frac{1}{P(\lambda_1)P(\lambda_2)\dots P(\lambda_N)}\right) - S(\rho)\right| \leq \varepsilon\right) > 1 - \delta. \quad (2.137)$$

The projector on a typical subspace is given by

$$P_T = \sum_{\lambda} |\lambda_1\rangle\langle\lambda_1| \otimes \dots \otimes |\lambda_N\rangle\langle\lambda_N|. \quad (2.138)$$

The *projection* of the quantum message on the typical subspace is determined by

$$P_T \rho_{\otimes N}. \quad (2.139)$$

The probability of the projections is given by its trace. By using the projection operator, we can separate the total Hilbert space into typical and atypical subspaces, as illustrated in Fig. 2.9b. The probability that the state of the quantum message lies in the typical subspace is given by

$$P(P_T \rho_{\otimes N}) > 1 - \delta. \quad (2.140)$$

The bounds for the typical subspace  $T_{\lambda}(N, \varepsilon)$ , following a similar methodology as for typical sequences, can be determined as

$$(1 - \varepsilon) 2^{N[S(\rho) - \varepsilon]} \leq |T_{\lambda}(N, \varepsilon)| \leq 2^{N[S(\rho) + \varepsilon]}. \quad (2.141)$$

Now we are in a position to formulate the corresponding *compression procedure*. Define the projector on the typical subspace  $P_T$  and its complement projecting on orthogonal subspace  $P_T^{\perp} = I - P_T$  ( $I$  is the identity operator) with corresponding outcomes 0 and 1. For compression purposes, we perform the measurements using two orthogonal operators with outputs denoted as 1 and 0, respectively. If the outcome is 1, we know that the message is in a typical state, and we do nothing further. If, on the other hand, the outcome is 0, we know that it belongs to atypical subspace and numerate it as a *fixed* state from the typical subspace. Given that the probability of this to happen can be made as small as possible for large  $N$ , we can compress the quantum message without the loss of information. We shall now formulate the Schumacher's source coding theorem, the quantum information theory equivalent to the Shannon's source coding theorem. For derivation, an interested reader is referred to [1].

**Schumacher's Source Coding Theorem.** Let  $\{|\psi_x\rangle, p_x\}$  be an i.i.d. quantum source. If  $R > S(\rho)$ , then there exists a reliable compression scheme of rate  $R$  for this source. Otherwise, if  $R < S(\rho)$ , then no reliable compression scheme of rate  $R$  exists.

In the formulation of the Schumacher's source coding theorem, we used the concept of reliable compression, without formally introducing it. We say that the compression is reliable if the corresponding *entanglement fidelity* tends to 1 for large  $N$ :

$$\begin{aligned} F(\rho_{\otimes N}; D^N \circ C^N) &\xrightarrow[N \rightarrow \infty]{} 1; \quad \rho_{\otimes N} = |\psi_{\otimes N}\rangle\langle\psi_{\otimes N}|, \quad \langle\psi_{\otimes N}| \\ &= |\psi_{x_1}\rangle \otimes \cdots \otimes |\psi_{x_N}\rangle \end{aligned} \quad (2.142)$$

where we used  $D^N$  and  $C^N$  to denote the decompression and compression operations, respectively, defined as the following mappings:

$$D^N : H_c^N \rightarrow H^N, \quad C^N : H^N \rightarrow H_c^N, \quad (2.143)$$

where  $H_c^N$  is  $2^{NR}$ -dimensional subspace of  $H^N$ . The entanglement fidelity  $F$  represents the measure of the preservation of entanglement before and after performing the trace-preserving quantum operation. There exist different definitions of fidelity. Let  $\rho$  and  $\sigma$  be two density operators. Then the fidelity can be defined as

$$F(\rho, \sigma) = \text{Tr}\left(\sqrt{\rho^{1/2}\sigma\rho^{1/2}}\right). \quad (2.144)$$

For two pure states with density operators  $\rho = |\psi\rangle\langle\psi|$ ,  $\sigma = |\phi\rangle\langle\phi|$ , the corresponding fidelity will be

$$\begin{aligned} F(\rho, \sigma) &= \text{Tr}\left(\sqrt{\rho^{1/2}\sigma\rho^{1/2}}\right) \stackrel{\rho^2 = \rho}{=} \text{Tr}\left(\sqrt{|\psi\rangle\langle\psi|(|\phi\rangle\langle\phi|)|\psi\rangle\langle\psi|}\right) \\ &= \text{Tr}\left(\underbrace{|\psi\rangle\langle\psi|}_{|\langle\phi|\psi\rangle|^2} \underbrace{|\phi\rangle\langle\phi|}_{|\langle\phi|\psi\rangle|^2} \right)^{1/2} = |\langle\phi|\psi\rangle| \underbrace{\text{Tr}(|\psi\rangle\langle\psi|)}_1 = |\langle\phi|\psi\rangle| \end{aligned} \quad (2.145)$$

where we used the property of the density operators for pure states  $\rho^2 = \rho$  (or equivalently  $\rho = \rho^{1/2}$ ). Clearly, for pure states, the fidelity corresponds to the square root of probability of finding the system in state  $|\phi\rangle$  if it is known to be prepared in state  $|\psi\rangle$  (and vice versa). Since fidelity is related to the probability, it ranges between 0 and 1, with 0 indicating that there is no overlap and 1 meaning that the states are identical. The following *properties* of fidelity hold:

1. The symmetry property:

$$F(\rho, \sigma) = F(\sigma, \rho). \quad (2.146)$$

2. The fidelity is invariant under unitary operations:

$$F(U\rho U^\dagger, U\sigma U^\dagger) = F(\rho, \sigma). \quad (2.147)$$

3. If  $\rho$  and  $\sigma$  commute, the fidelity can be expressed in terms of eigenvalues of  $\rho$ , denoted as  $r_i$ , and  $\sigma$ , denoted as  $s_i$ , as follows:

$$F(\rho, \sigma) = \sum_i (r_i s_i)^{1/2}. \quad (2.148)$$

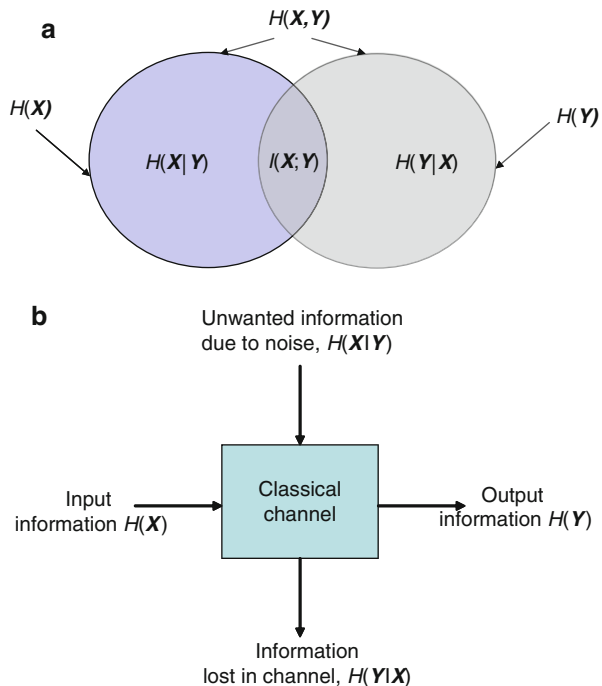
### 2.6.2 Holevo–Schumacher–Westmoreland Theorem and Channel Coding

We have already introduced the concept of mutual information  $I(X, Y)$  in Sect. 2.5, where we defined it as  $I(X, Y) = H(X) - H(Y|X)$ .  $H(X)$  represents the uncertainty about the channel input  $X$  before observing the channel output  $Y$ , while  $H(X|Y)$  denotes the conditional entropy or the amount of uncertainty remaining about the channel input after the channel output has been received. Therefore, the mutual information represents the amount of information (per symbol) that is conveyed by the channel. In other words, it represents the uncertainty about the channel input that is resolved by observing the channel output. The mutual information can be interpreted by means of a Venn diagram shown in Fig. 2.10a. The left circle represents the entropy of channel input, the right circle represents the entropy of channel output, and the mutual information is obtained in intersection of these two circles. Another interpretation due to Ingels [28] is shown in Fig. 2.10b. The mutual information, i.e., the information conveyed by the channel, is obtained as the output information minus information lost in the channel. One important figure of merit the classical channel is the *channel capacity*, which is obtained by maximization of mutual information  $I(X, Y)$  over all possible input distributions:

$$C = \max_{\{p(x_i)\}} I(X; Y). \quad (2.149)$$

The classical channel encoder accepts the message symbols and adds redundant symbols according to a corresponding prescribed rule. The channel coding is the act of transforming of a length- $K$  sequence into a length- $N$  codeword. The set of rules specifying this transformation are called the *channel code*, which can be represented as the following mapping:

**Fig. 2.10** Interpretation of the mutual information: (a) using Venn diagrams and (b) using the approach due to Ingels



$$C : M \rightarrow X, \quad (2.150)$$

where  $C$  is the channel code,  $M$  is the set of information sequences of length  $K$ , and  $X$  is the set of codewords of length  $N$ . The decoder exploits these redundant symbols to determine which message symbol was actually transmitted. The concept of classical channel coding is introduced in Fig. 2.11. An important class of channel codes is the class of *block codes*. In an  $(N, K)$  *block code*, the channel encoder accepts information in successive  $K$ -symbol blocks and adds  $N - K$  redundant symbols that are algebraically related to the  $K$  message symbols, thus producing an overall encoded block of  $N$  symbols ( $N > K$ ), known as a *codeword*. If the block code is *systematic*, the information symbols stay unchanged during the encoding operation, and the encoding operation may be considered as adding the  $N - K$  generalized parity checks to  $k$  information symbols. The code rate of the code is defined as  $R = K/N$ .

In order to determine the error-correction capability of the linear block code, we have to introduce the concepts of Hamming distance and Hamming weight. The Hamming distance  $d(x_1, x_2)$  between two codewords  $x_1$  and  $x_2$  is defined as the number of locations in which these two vectors differ. The Hamming weight  $\text{wt}(x)$  of a codeword vector  $x$  is defined as the number of nonzero elements in the vector. The minimum distance  $d_{\min}$  of a linear block code is defined as the smallest Hamming distance between any pair of code vectors in the code space. Since the

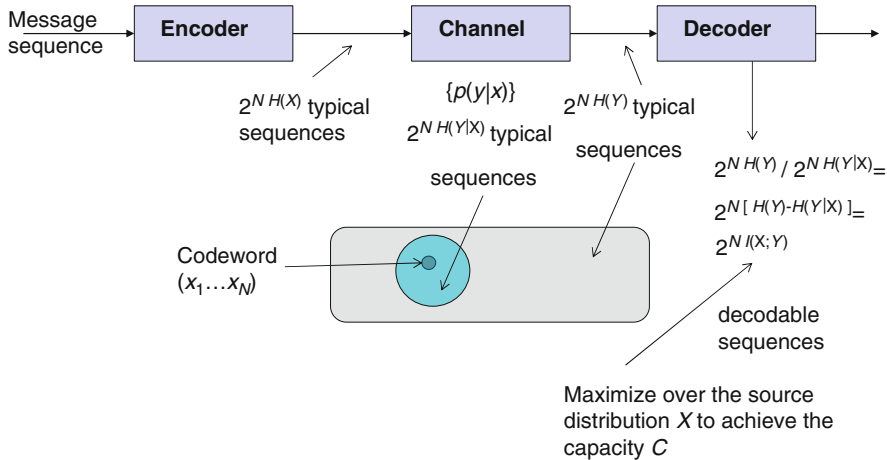


**Fig. 2.11** The illustration of classical channel coding and Shannon capacity theorem derivation

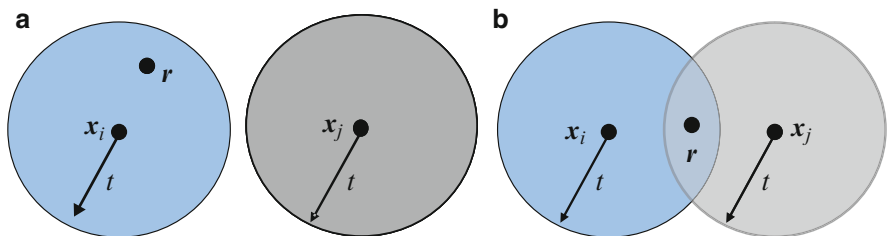


**Fig. 2.12** The illustration of Hamming distance: (a)  $d(\mathbf{x}_i, \mathbf{x}_j) \geq 2t + 1$  and (b)  $d(\mathbf{x}_i, \mathbf{x}_j) < 2t + 1$

zero vector is also a codeword, the minimum distance of a linear block code can be defined as the smallest Hamming weight of the nonzero code vectors in the code. The codewords can be represented as points in  $N$ -dimensional space, as shown in Fig. 2.12. Decoding process can be visualized by creating the spheres of radius  $t$  around codeword points. The received word vector  $\mathbf{r}$  in Fig. 2.12a will be decoded as a codeword  $\mathbf{x}_i$  because its Hamming distance  $d(\mathbf{x}_i, \mathbf{r}) \leq t$  is closest to the codeword  $\mathbf{x}_i$ . On the other hand, in the example shown in Fig. 2.12b, the Hamming distance satisfies relation  $d(\mathbf{x}_i, \mathbf{x}_j) \leq 2t$ , and the received vector  $\mathbf{r}$  that falls in intersection area of two spheres cannot be uniquely decoded.

Therefore,  $(N, K)$  linear block code of minimum distance  $d_{\min}$  can correct up to  $t$  errors if and only if  $t \leq \lfloor 1/2(d_{\min} - 1) \rfloor$  or  $d_{\min} \geq 2t + 1$  (where  $\lfloor \cdot \rfloor$  denotes the largest integer smaller or equal to the enclosed quantity). If we are only interested in detecting  $e_d$  errors, then the minimum distance should be  $d_{\min} \geq e_d + 1$ . However, if we are interested in detecting  $e_d$  errors and correcting  $e_c$  errors, then the minimum distance should be  $d_{\min} \geq e_d + e_c + 1$ .

Shannon has shown that if  $R < C$ , we can construct  $2^{NR}$  length- $N$  codewords that can be sent over the (classical) channel with maximum probability of error

approaching zero for large  $N$ . In order to prove this claim, we introduce the concept of jointly typical sequences. Two length- $N$  sequences  $\mathbf{x}$  and  $\mathbf{y}$  are jointly typical sequences if they satisfy the following set of inequalities:

$$P\left(\left|\frac{1}{N}\log\left(\frac{1}{P(\mathbf{x})}\right) - H(X)\right| \leq \varepsilon\right) > 1 - \delta \quad (2.151)$$

$$P\left(\left|\frac{1}{N}\log\left(\frac{1}{P(\mathbf{y})}\right) - H(Y)\right| \leq \varepsilon\right) > 1 - \delta \quad (2.152)$$

$$P\left(\left|\frac{1}{N}\log\left(\frac{1}{P(\mathbf{x}, \mathbf{y})}\right) - H(X, Y)\right| \leq \varepsilon\right) > 1 - \delta \quad (2.153)$$

where  $P(\mathbf{x}, \mathbf{y})$  denotes the joint probability of the two sequences and  $H(X, Y)$  is their joint entropy.

For an length- $N$  input codeword randomly generated according to the probability distribution of a source  $X$ , the number of random input sequences is approximately  $2^{NH(X)}$ , and the number of output typical sequences is approximately  $2^{NH(Y)}$ . Furthermore, the total number of input and output sequences that are jointly typical is  $2^{NH(X,Y)}$ . Therefore, the total pairs of sequences that are simultaneously  $\mathbf{x}$ -typical,

$$\underbrace{N[H(X) + H(Y) - H(X, Y)]}_{I(X, Y)} = 2^{NI(X, Y)},$$

$\mathbf{y}$ -typical, and also jointly typical are  $2^{NI(X, Y)}$ , where  $I(X, Y)$  is the mutual information between  $X$  and  $Y$ , as illustrated in Fig. 2.11(bottom). These are the maximum number of codeword sequences that can be distinguished. One way of seeing this is to consider a single codeword. For this codeword, the action of the channel, characterized by the conditional probability  $P(\mathbf{y}|\mathbf{x})$ , defines the Hamming sphere in which this codeword can lie after the action of the channel. The size of this Hamming sphere is approximately  $2^{NH(Y|X)}$ . Given that the total number of output typical sequences is approximately  $2^{NH(Y)}$ , if we desire to have no overlap between two Hamming spheres, the maximum number of codewords we can consider is given by  $2^{NH(X)}/2^{NH(Y|X)} = 2^{NI(X, Y)}$ . To increase this number, we need to maximize  $I(X, Y)$  over the distribution of  $X$ , as we do not have a control over the channel. This maximal mutual information is referred to as the capacity of the channel. If we have a rate  $R < C$ , then Shannon's noisy channel coding theorem tells us that we can construct  $2^{NR}$  length- $N$  codewords that can be sent over the channel with maximum probability of error approaching zero for large  $N$ . Now we can formally formulate Shannon channel coding theorem as follows [1].

**Shannon's Channel Coding Theorem.** Let us consider the transmission of  $2^{N(C - \varepsilon)}$  equiprobable messages. Then there exists a classical channel coding scheme of rate  $R < C$  in which the codewords are selected from all  $2^N$  possible words such that the decoding error probability can be made arbitrary small for sufficiently large  $N$ .

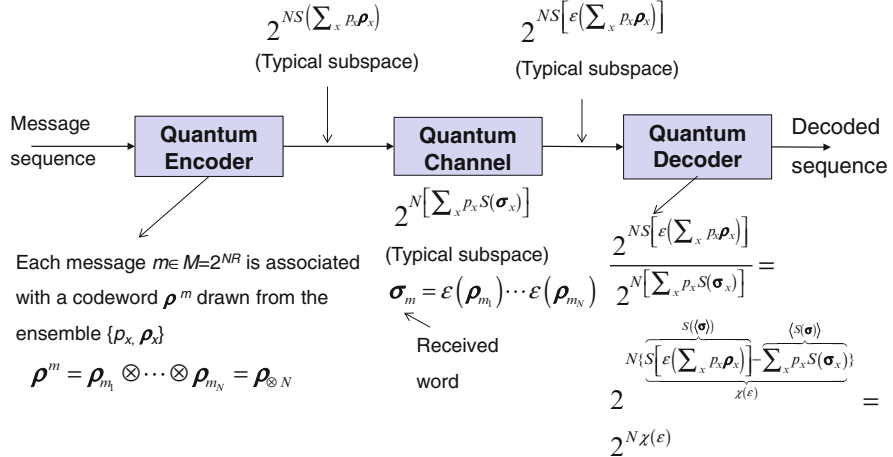


**Fig. 2.13** The illustration of quantum channel coding and HSW theorem derivation

Now we consider the communication over the quantum channel, as illustrated in Fig. 2.13. The quantum encoder for each message  $m$  out of  $M = 2^{NR}$  generates a product state codeword  $\rho^m$  drawn from the ensemble  $\{p_x, \rho_x\}$  as follows:

$$\rho^m = \rho_{m_1} \otimes \cdots \otimes \rho_{m_N} = \rho_{\otimes N}. \quad (2.154)$$

This quantum codeword is sent over the quantum channel described by the trace-preserving quantum operation  $\epsilon$ , resulting in the received quantum word:

$$\sigma_m = \epsilon(\rho_{m_1}) \otimes \epsilon(\rho_{m_2}) \otimes \cdots \otimes \epsilon(\rho_{m_N}). \quad (2.155)$$

Bob performs the measurement on received state using the POVM measurement operators  $\{M_m\}$  in order to decode Alice's message. The probability of successful decoding is given by  $p_m = \text{Trace}(\sigma_m M_m)$ . The goal is to maximize the transmission rate over the quantum channel so that the probability of decoding error is arbitrarily small. The von Neumann entropy associated with the quantum encoder would be  $S(\rho) = S\left(\sum_x p_x \rho_x\right)$ , while the dimensionality of the typical subspace of quantum encoder is given by  $2^{NS\left(\sum_x p_x \rho_x\right)}$ . On the other hand, the dimensionality of the quantum subspace characterizing the quantum channel is given by  $2^{N\left[\sum_x p_x S(\sigma_x)\right]}$ . The quantum channel perturbs the quantum codeword transmitted over the quantum channel by performing the trace-preserving quantum operation so that the entropy at the channel output can be written as  $S\left[e\left(\sum_x p_x \rho_x\right)\right]$ , while the dimensionality of the corresponding subspace is given by

$2^{NS[\epsilon(\sum_x p_x \rho_x)]}$ . The number of decodable codewords would be then

$$\frac{2^{NS[\epsilon(\sum_x p_x \rho_x)]}}{2^N[\sum_x p_x S(\sigma_x)]} = 2^N \left\{ \underbrace{S[\epsilon(\sum_x p_x \rho_x)]}_{\chi(\epsilon)} - \underbrace{\sum_x p_x S(\sigma_x)}_{\langle S(\sigma) \rangle} \right\} = 2^{N\chi(\epsilon)}. \quad (2.156)$$

In order to maximize the number of decodable codewords, we need to perform the optimization of  $\chi(\epsilon)$  over  $p_x$  and  $\rho_x$ , which represents the simplified derivation of the Holevo–Schumacher–Westmoreland (HSW) theorem, which can be formulated as follows [1].

**Holevo–Schumacher–Westmoreland (HSW) Theorem.** Let us consider the transmission of a codeword  $\rho^m$  drawn from the ensemble  $\{p_x, \rho_x\}$  over the quantum channel, characterized by the trace-preserving quantum operation  $\epsilon$ , with the rate  $R < C(\epsilon)$ , where  $C(\epsilon)$  is the product state capacity defined as

$$\begin{aligned} C(\epsilon) &= \max_{\{p_x, \rho_x\}} \chi(\epsilon) = \max_{\{p_x, \rho_x\}} [S(\langle \sigma \rangle) - \langle S(\sigma) \rangle] \\ &= \max_{\{p_x, \rho_x\}} \left[ S \left[ \epsilon \left( \sum_x p_x \rho_x \right) \right] - \sum_x p_x S(\epsilon(\rho_x)) \right], \end{aligned} \quad (2.157)$$

where the maximization of  $\chi(\epsilon)$  is performed over  $p_x$  and  $\rho_x$ . Then there exists a coding scheme that allows reliable error-free transmission over the quantum channel.

## 2.7 Quantum Error-Correction Concepts

The QIP relies on delicate superposition states, which are sensitive to interactions with environment, resulting in decoherence. Moreover, the quantum gates are imperfect and the use of quantum error-correction coding (QECC) is necessary to enable the fault-tolerant computing and to deal with quantum errors. QECC is also essential in quantum communication and quantum teleportation applications. The elements of quantum error-correction codes are shown in Fig. 2.14a. The  $(N, K)$  QECC code performs the encoding of the quantum state of  $K$  qubits, specified by  $2^K$  complex coefficients  $\alpha_s$ , into a quantum state of  $N$  qubits, in such a way that errors can be detected and corrected, and all  $2^K$  complex coefficients can be perfectly restored, up to the global phase shift. Namely, from quantum mechanics, we know that two states  $|\psi\rangle$  and  $e^{i\theta}|\psi\rangle$  are equal up to a *global phase shift* as the results of measurement on both states are the same. A quantum error correction consists of

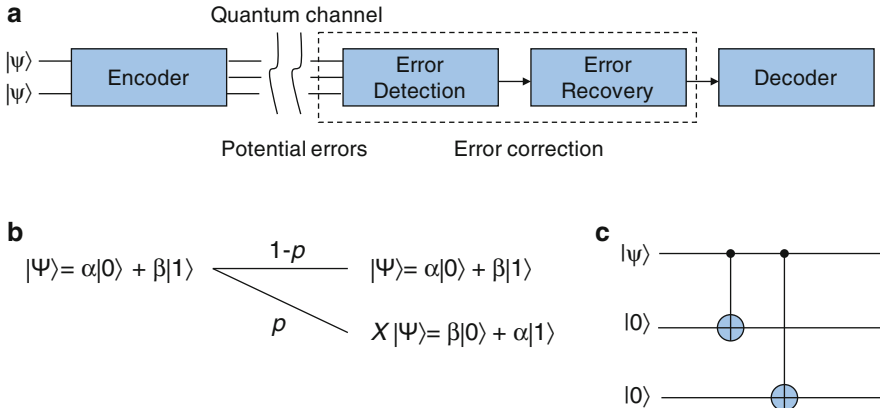


**Fig. 2.14** (a) A quantum error-correction principle. (b) Bit-flipping channel model. (c) Three-qubit flip code encoder

four major steps: encoding, error detection, error recovery, and decoding, as shown in Fig. 2.14a. The sender (Alice) encodes quantum information in state  $|\psi\rangle$  with the help of local ancilla qubits  $|0\rangle$  and then sends the encoded qubits over a noisy quantum channel (say free-space optical channel or optical fiber). The receiver (Bob) performs multiqubit measurement on all qubits to diagnose the channel error and performs a recovery unitary operation  $R$  to reverse the action of the channel. The quantum error correction is essentially more complicated than classical error correction. Difficulties for quantum error correction can be summarized as follows: (1) the no-cloning theorem indicates that it is impossible to make a copy of an arbitrary quantum state, (2) quantum errors are continuous and a qubit can be in any superposition of the two bases states, and (3) the measurements destroy the quantum information. The quantum error-correction principles will be more evident after a simple example given below.

Assume we want to send a single qubit  $|\psi\rangle = \alpha|0\rangle + \beta|1\rangle$  through the quantum channel in which during transmission the transmitted qubit can be flipped to  $X|\psi\rangle = \beta|0\rangle + \alpha|1\rangle$  with probability  $p$ . Such a quantum channel is called a *bit-flip channel* and it can be described as shown in Fig. 2.14b. A three-qubit flip code sends the same qubit three times and therefore represents the *repetition code* equivalent. The corresponding codewords in this code are  $|\bar{0}\rangle = |000\rangle$  and  $|\bar{1}\rangle = |111\rangle$ . The three-qubit flip code encoder is shown in Fig. 2.14c. One input qubit and two ancillas are used at the input encoder, which can be represented by  $|\psi_{123}\rangle = \alpha|000\rangle + \beta|100\rangle$ . The first ancilla qubit (the second qubit at the encoder input) is controlled by the information qubit (the first qubit at encoder input) so that its output can be represented by  $\text{CNOT}_{12}(\alpha|000\rangle + \beta|100\rangle) = \alpha|000\rangle + \beta|110\rangle$  (if the control qubit is  $|1\rangle$  the target qubit gets flipped; otherwise it stays unchanged). The output of the first CNOT gate is used as input to the second CNOT gate in which the second ancilla qubit (the third qubit) is controlled by the information qubit (the first qubit) so that the corresponding encoder output is

obtained as  $\text{CNOT}_{13}(\alpha|000\rangle + \beta|110\rangle) = \alpha|000\rangle + \beta|111\rangle$ , which indicates that basis codewords are indeed  $|\bar{0}\rangle$  and  $|\bar{1}\rangle$ . With this code, we are capable to correct a single-qubit flip error, which occurs with probability  $(1-p)^3 + 3p(1-p)^2 = 1 - 3p^2 + 2p^3$ . Therefore, the probability of an error remaining uncorrected or wrongly corrected with this code is  $3p^2 - 2p^3$ . It is clear from Fig. 2.14c that three-qubit bit-flip encoder is a *systematic encoder* in which the information qubit is unchanged, and the ancilla qubits are used to impose the encoding operation and create the parity qubits (the output qubits 2 and 3).

Let us assume that a qubit flip occurred on the first qubit leading to received quantum word  $|\psi_r\rangle = \alpha|100\rangle + \beta|011\rangle$ . In order to identify the error, it is needed to perform the measurements on the following observables:  $Z_1Z_2$  and  $Z_2Z_3$ , where the subscript denotes the index of a qubit on which a given Pauli gate is applied. The result of the measurement is the eigenvalue  $\pm 1$ , and corresponding eigenvectors are two valid codewords, namely,  $|000\rangle$  and  $|111\rangle$ . The observables can be represented as follows:

$$\begin{aligned} Z_1Z_2 &= (|00\rangle\langle 11| + |11\rangle\langle 11|) \otimes I - (|01\rangle\langle 01| + |10\rangle\langle 10|) \otimes I \\ Z_2Z_3 &= I \otimes (|00\rangle\langle 11| + |11\rangle\langle 11|) - I \otimes (|01\rangle\langle 01| + |10\rangle\langle 10|). \end{aligned} \quad (2.158)$$

It can be showed that  $\langle\psi_r|Z_1Z_2|\psi_r\rangle = -1$ ,  $\langle\psi_r|Z_2Z_3|\psi_r\rangle = +1$ , indicating that an error occurred on either the first or second qubit but neither on the second nor third qubit. The intersection reveals that the first qubit was in error. By using this approach, we can create the three-qubit lookup table (LUT), given as Table 2.1.

Three-qubit flip code error detection and error-correction circuits are shown in Fig. 2.15. The results of measurements on ancillas (see Fig. 2.15a) will determine

**Table 2.1** The three-qubit flip code LUT

$Z_1Z_2$	$Z_2Z_3$	Error
+1	+1	/
+1	-1	$X_3$
-1	+1	$X_1$
-1	-1	$X_2$

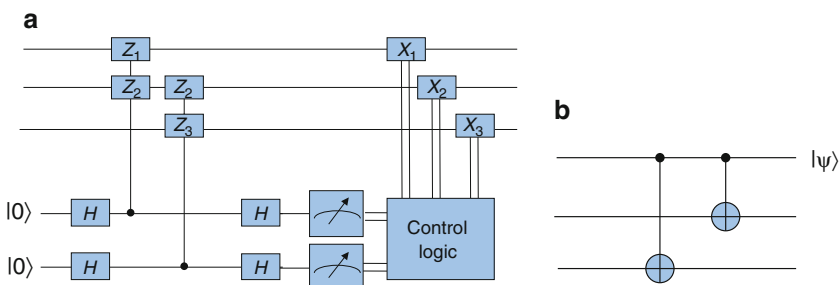


**Fig. 2.15** (a) Three-qubit flip code error detection and error-correction circuit. (b) Decoder circuit configuration

the error syndrome  $[\pm 1 \pm 1]$ , and based on LUT given by Table 2.1, we identify the error event and apply corresponding  $X_i$  gate on the  $i$ th qubit being in error, and the error gets corrected since  $X^2 = I$ . The control logic operation is described in Table 2.1. For example, if both outputs at the measurements circuits are  $-1$ , the operator  $X_2$  is activated. The last step is to perform decoding as shown in Fig. 2.15b by simply reversing the order of elements in corresponding encoder.

## 2.8 Hydrogen-Like Atoms and Beyond

At this point, it is convenient to establish *connection* between *wave quantum mechanics* and *matrix quantum mechanics*, as we will use the concept of the wave function in the rest of the section. In wave mechanics, the information about the state of a particle is described by the corresponding **wave function**  $\psi(x, t) = \langle x | \psi \rangle$ . The wave function gives the information about the location of the particle, namely, the magnitude squared of the wave functions  $|\psi(x, t)|^2$  is related to the *probability density function*. The probability of finding the particle within the interval  $x$  and  $x + dx$  is given by

$$dP(x, t) = |\psi(x, t)|^2 dx. \quad (2.159)$$

In wave quantum mechanics, the actions of the position  $X$  and the momentum  $P$  operators are defined by

$$X\psi(x, t) = x\psi(x, t) \quad P\psi(x, t) = -j\hbar \frac{\partial}{\partial x} \psi(x, t). \quad (2.160)$$

When we apply the commutator to the test wave function  $\psi(x, t)$ , we obtain

$$\begin{aligned} [X, P]\psi(x, t) &= (XP - PX)\psi(x, t) = XP\psi(x, t) - PX\psi(x, t) \\ &= -j\hbar x \frac{\partial}{\partial x} \psi(x, t) + j\hbar \frac{\partial}{\partial x} (X\psi(x, t)) \\ &= -j\hbar x \frac{\partial}{\partial x} \psi(x, t) + j\hbar \frac{\partial}{\partial x} (x\psi(x, t)) \\ &= -j\hbar x \frac{\partial}{\partial x} \psi(x, t) + j\hbar \left( \psi(x, t) + x \frac{\partial}{\partial x} \psi(x, t) \right) = j\hbar \psi(x, t), \end{aligned} \quad (2.161)$$

indicating, therefore, that  $[X, P] = j\hbar$ , which was used in the section on uncertainty principle.

A hydrogen atom is a bound system, consisting of a proton and a neutron, with potential given by

$$V(r) = -\frac{1}{4\pi\epsilon_0} \frac{e^2}{r}, \quad (2.162)$$

where  $e$  is an electron charge. Therefore, the potential is only function of radial coordinate, and because of spherical symmetry, it is convenient to use the spherical coordinate system in which the Laplacian is defined by

$$\nabla^2 = \frac{1}{r^2} \frac{\partial}{\partial r} \left( r^2 \frac{\partial}{\partial r} \right) + \frac{1}{r^2 \sin \theta} \frac{\partial}{\partial \theta} \left( \sin \theta \frac{\partial}{\partial \theta} \right) + \frac{1}{r^2 \sin^2 \theta} \frac{\partial^2}{\partial \phi^2}. \quad (2.163)$$

The angular momentum operator  $L^2$  in spherical coordinates is given by

$$L^2 = -\hbar^2 \left[ \frac{1}{\sin \theta} \frac{\partial}{\partial \theta} \left( \sin \theta \frac{\partial}{\partial \theta} \right) + \frac{1}{\sin^2 \theta} \frac{\partial^2}{\partial \phi^2} \right]. \quad (2.164)$$

The Hamiltonian can be written by

$$H = -\frac{\hbar^2}{2mr^2} \frac{\partial}{\partial r} \left( r^2 \frac{\partial}{\partial r} \right) + \frac{1}{2mr^2} L^2 + V(r). \quad (2.165)$$

Because the operators  $L^2$  and  $L_z$  have the common eigenkets, the Hamiltonian leads to the following three equations:

$$\begin{aligned} H\Psi(r, \theta, \phi) &= E\Psi(r, \theta, \phi) \\ L^2\Psi(r, \theta, \phi) &= \hbar^2 l(l+1)\Psi(r, \theta, \phi) \\ L_z\Psi(r, \theta, \phi) &= m\hbar\Psi(r, \theta, \phi). \end{aligned} \quad (2.166)$$

With this problem, we can associate three quantum numbers: (1) the *principal quantum number*,  $n$ , corresponding to the energy (originating from Hamiltonian  $H$ ); (2) the *azimuthal quantum number*,  $l$ , representing the angular momentum (originating from  $L^2$ ); and (3) the *magnetic quantum number*,  $m$ , originating from  $L_z$ . In order to solve (2.166), we can use the method of separation of variables:  $\Psi(r, \theta, \phi) = R(r)\Theta(\theta)\Phi(\phi)$ . Since  $\Theta(\theta)\Phi(\phi)$  is related to the spherical harmonics  $\Theta(\theta)\Phi(\phi) = Y_l^m(\theta, \phi)$ , we are left with the radial equation to solve

$$-\frac{\hbar^2}{2mr} \frac{d^2}{dr^2} [rR_{nl}(r)] + \left[ \frac{l(l+1)\hbar^2}{2mr^2} + V(r) \right] R_{nl}(r) = ER_{nl}(r). \quad (2.167)$$

The spherical harmonics  $Y_l^m(\theta, \phi)$  are defined by

$$Y_l^m(\theta, \phi) = \begin{cases} (-1)^m \sqrt{\frac{(2l+1)(l-m)!}{4\pi(l+m)!}} P_l^m(\cos \theta) e^{im\phi}, & m > 0 \\ (-1)^{|m|} \sqrt{\frac{(2l+1)(l-|m|)!}{4\pi(l+m)!}} P_l^{|m|}(\cos \theta) e^{im\phi}, & m < 0 \end{cases}. \quad (2.168)$$

With  $P_l^m(x)$ , we denoted the associated Legendre polynomials

$$P_l^m(x) = (1-x^2)^{m/2} \frac{d^m}{dx^m} P_l(x), \quad (2.169)$$

where  $P_l(x)$  are the Legendre polynomials, defined by

$$P_l(x) = \frac{1}{2^l l!} \frac{d^l}{dx^l} [(x^2 - 1)^l]. \quad (2.170)$$

The Legendre polynomial can be determined recursively as follows:

$$(l+1)P_{l+1}(x) = (2l+1)xP_l(x) - lP_{l-1}(x); \quad P_0(x) = 1, \quad P_1(x) = x. \quad (2.171)$$

By substituting the Coulomb potential into the radial equation, we obtain

$$-\frac{\hbar^2}{2mr} \frac{d^2}{dr^2} [rR_{nl}(r)] + \left[ \frac{l(l+1)\hbar^2}{2mr^2} - \frac{1}{4\pi\epsilon_0} \frac{e^2}{r} \right] R_{nl}(r) = ER_{nl}(r). \quad (2.172)$$

The solution of radial equation can be written as

$$R_{nl}(r) = \sqrt{\left(\frac{2}{na_H}\right) \frac{(n-l-1)!}{2n[(n-1)!]^2}} e^{-r/2a_H} \left(\frac{r}{a_H}\right)^l L_{n+1}^{2l+1} \left(\frac{r}{a_H}\right), \quad (2.173)$$

where  $a_H$  is the first Bohr radius (the lowest energy orbit radius) ( $a_H = 0.0529$  nm) and  $L_{n+1}^{2l+1}(r/a_H)$  are the corresponding associated Laguerre polynomials, defined by

$$L_n^\alpha(x) = \frac{x^{-\alpha} e^x}{n!} \frac{d^n}{dx^n} (e^{-x} x^{n+\alpha}). \quad (2.174)$$

The radial portion of the wave function is typically normalized as follows:

$$\int_0^\infty r^2 |R(r)|^2 dr = 1. \quad (2.175)$$

The complete wave function is the product of radial wave function and spherical harmonics:

$$\Psi(r, \theta, \phi) = \sqrt{\left(\frac{2}{na_H}\right) \frac{(n-l-1)!}{2n[(n-1)!]^2}} e^{-r/2a_H} \left(\frac{r}{a_H}\right)^l L_{n+1}^{2l+1} \left(\frac{r}{a_H}\right) Y_l^m(\theta, \phi). \quad (2.176)$$

By substituting (2.168) and (2.173) into the wave function expression  $\Psi(r, \theta, \phi) = R(r)\Theta(\theta)\Phi(\phi)$ , we obtain

$$\Psi(\rho, \theta, \phi) = C_{n, l, m} e^{-\rho/2} (\rho)^l L_{n+1}^{2l+1}(\rho) P_l^{|m|}(\cos \theta) e^{im\phi}, \quad (2.177)$$

where  $\rho = r/a_H$  and  $C_{n, m, l}$  is the normalization constant obtained as product of normalization constants in (2.168) and (2.176). The energy levels in hydrogen atom are only functions on  $n$  and are given by

$$E_n = \frac{E_1}{n^2}, \quad E_1 = -\frac{m^2 e^4}{32\pi^2 \epsilon_0^2 \hbar^2} = -13.6 \text{ eV}. \quad (2.178)$$

Because the values that  $l$  can take are  $\{0, 1, \dots, n-1\}$ , while the values that  $m$  can take are  $\{-l, -l+1, \dots, l-1, l\}$ , and since the radial component is not a function of  $m$ , the number of states with the same energy (the total *degeneracy* of the energy level  $E_n$ ) is

$$2 \sum_{l=0}^{n-1} (2l+1) = 2n^2. \quad (2.179)$$

The states in which  $l=0, 1, 2, 3, 4$  are traditionally called *s*, *p*, *d*, *f*, and *g*, respectively. The simpler eigenfunctions of the hydrogen atom, by ignoring the normalization constant, are given in Table 2.2, which is obtained based on (2.177).

The results above applicable to many two-particle systems with attraction energy are reversely proportional to the distance between them, provided that parameters are properly chosen. For instance, if the charge of nucleus is  $Z$ , then in the calculations above, we need to substitute  $e^2$  by  $Ze^2$ . Examples include deuterium, tritium, ions that contain only one electron, positronium, and muonic atoms.

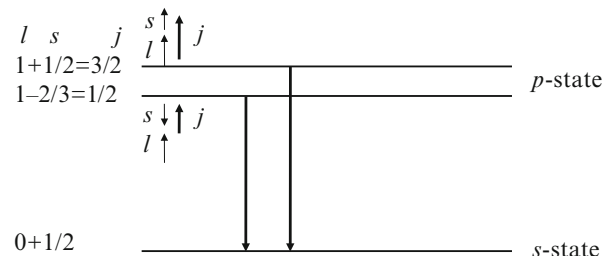
The total angular momentum of an electron  $j$  in an atom can be found as the vector sum of orbital angular momentum  $\mathbf{l}$  and spin  $\mathbf{s}$  as by

$$\mathbf{j} = \mathbf{l} + \mathbf{s}. \quad (2.180)$$

For a given value of azimuthal quantum number  $l$ , there exist two values of total angular momentum quantum number of an electron:  $j=l+1/2$  and  $j=l-1/2$ . Namely, as the electron undergoes orbital motion around the nucleus, it experiences the magnetic field, and this interaction is known as the spin-orbit interaction.

**Table 2.2** Hydrogen atom eigenfunctions

State	$n$	$l$	$m$	Eigenfunction
$1s$	1	0	0	$e^{-\rho/2}$
$2s$	2	0	0	$e^{-\rho/2}(1 - \rho)$
$2p$	2	1	-1	$e^{-\rho/2}\rho \begin{cases} \sin \theta e^{-j\phi} \\ \cos \theta \\ \sin \theta e^{j\phi} \end{cases}$
			0	
			1	
$3s$	3	0	0	$e^{-\rho/2}(\rho^2 - 4\rho + 2)$
$3p$	3	1	-1	$e^{-\rho/2}(\rho^2 - 2\rho) \begin{cases} \sin \theta e^{-j\phi} \\ \cos \theta \\ \sin \theta e^{j\phi} \end{cases}$
			0	
			1	
$3d$	3	2	-2	$e^{-\rho/2}\rho^2 \begin{cases} \sin^2 \theta e^{-j2\phi} \\ \sin \theta \cos \theta e^{-j\phi} \\ 1 - 3 \cos^2 \theta \\ \sin \theta \cos \theta e^{j\phi} \\ \sin^2 \theta e^{j2\phi} \end{cases}$
			-1	
			0	
			1	
			2	

**Fig. 2.16** Illustration of spin-orbit interaction

The result of this interaction is two states  $j = l + s$  and  $j = l - s$  with slightly different energies as shown in Fig. 2.16.

For atoms containing more than one electron, the total angular momentum  $\mathbf{J}$  is given by the sum of individual orbital momenta  $\mathbf{L} = \mathbf{l}_1 + \mathbf{l}_2 + \dots$  and spins  $\mathbf{S} = \mathbf{s}_1 + \mathbf{s}_2 + \dots$ , so that we can write

$$\mathbf{J} = \mathbf{L} + \mathbf{S}; \quad \mathbf{L} = l_1 + l_2 + \dots, \quad \mathbf{S} = s_1 + s_2 + \dots \quad (2.181)$$

This type of coupling is known as  $LS$  coupling. Another type of coupling, namely,  $JJ$  coupling, occurs when individual  $\mathbf{j}$ s add together to produce the resulting  $\mathbf{J}$ . The  $LS$  coupling typically occurs in the lighter elements, while  $JJ$  coupling typically occurs in heavy elements. In  $LS$  coupling, the magnitudes of  $\mathbf{L}$ ,  $\mathbf{S}$ , and  $\mathbf{J}$  are given by

$$|\mathbf{L}| = \hbar \sqrt{L(L+1)}, \quad |\mathbf{S}| = \hbar \sqrt{S(S+1)}, \quad |\mathbf{J}| = \hbar \sqrt{J(J+1)}, \quad (2.182)$$

where  $L$ ,  $S$ , and  $J$  are quantum numbers satisfying the following properties: (1)  $L$  is always a nonnegative integer, (2) the spin quantum number  $S$  is either integral or

half-integral depending whether the number of electrons is even or odd, and (3) the total angular momentum quantum number  $J$  is either integral or half-integral depending whether the number of electrons is even or odd, respectively. The *spectroscopic notation* of a state characterized by the quantum numbers  $L$ ,  $S$ , and  $J$  is as follows:

$$^{2S+1}L_J, \quad (2.183)$$

where the quantity  $2S+1$  is known as the *multiplicity* and determines the numbers of different  $J$ s for a given value of  $L$ . If  $L \ll S$ , different values of  $J$  are  $L+S, L+S-1, \dots, L-S$ , meaning that there are  $2S+1$  possible values for  $J$ . If, on the other hand,  $L < S$ , then the possible values of  $J$  are  $L+S, L+S-1, \dots, |L-S|$ , meaning only  $2L+1$  different values for  $J$  exist. The states in which  $L=0, 1, 2, 3, 4, 5, 6, 7, 8, \dots$  are traditionally called  $S, P, D, F, G, H, I, K, M, \dots$ , respectively. The states with multiplicity  $2S+1=0, 1, 2, 3, 4, 5$ , and 6 are typically called singlet, doublet, triplet, quartet, quintet, and sextet states, respectively.

## 2.9 Concluding Remarks

This chapter has provided an overview of the basic concepts of QIP and quantum information theory. The following topics from QIP have been described in Sects. 2.1–2.3: state vectors, operators, density operators, measurements, dynamics of a quantum system, superposition principle, quantum parallelism, no-cloning theorem, and entanglement. The following concepts from quantum information theory have been described in Sects. 2.4–2.6: Holevo information, accessible information, Holevo bound, Shannon entropy and von Neumann entropy, Schumacher’s noiseless quantum coding theorem, and Holevo–Schumacher–Westmoreland theorem. Section 2.7 has been elated to the quantum error-correction concepts. Finally, Sect. 2.8 is devoted to the hydrogen-like atoms (and beyond).

## References

1. Djordjevic IB (2012) Quantum information processing and quantum error correction: an engineering approach. Elsevier/Academic Press, Amsterdam
2. Helstrom CW (1976) Quantum detection and estimation theory. Academic, New York
3. Helstrom CW, Liu JWS, Gordon JP (1970) Quantum mechanical communication theory. Proc IEEE 58:1578–1598
4. Sakurai JJ (1994) Modern quantum mechanics. Addison-Wesley, Reading
5. Gaitan F (2008) Quantum error correction and fault tolerant quantum computing. CRC, Boca Raton
6. Baym G (1990) Lectures on quantum mechanics. Westview Press, New York
7. McMahon D (2007) Quantum computing explained. Wiley, Hoboken

8. McMahon D (2006) Quantum mechanics demystified. McGraw-Hill, New York
9. Nielsen MA, Chuang IL (2000) Quantum computation and quantum information. Cambridge University Press, Cambridge
10. Fleming S (2008) PHYS 570: quantum mechanics (Lecture notes). University of Arizona, Tucson
11. Dirac PAM (1958) Quantum mechanics, 4th edn. Oxford University Press, London
12. Peleg Y, Pnini R, Zaarur E (1998) Schaum's outline of theory and problems of quantum mechanics. McGraw-Hill, New York
13. Fowles GR (1989) Introduction to modern optics. Dover, New York
14. Scully MO, Zubairy MS (1997) Quantum optics. Cambridge University Press, Cambridge
15. Le Bellac M (2006) A short introduction to quantum information and quantum computation. Cambridge University Press, Cambridge
16. Pinter CC (2010) A book of abstract algebra. Dover, New York
17. Griffiths D (1995) Introduction to quantum mechanics. Prentice-Hall, Englewood Cliffs
18. Zettili N (2001) Quantum mechanics, concepts and applications. Wiley, New York
19. Von Neumann J (1955) Mathematical foundations of quantum mechanics. Princeton University Press, Princeton
20. Jauch JM (1968) Foundations of quantum mechanics. Addison-Wesley, Reading
21. Peres A (1995) Quantum theory: concepts and methods. Kluwer, Boston
22. Goswami A (1996) Quantum mechanics. McGraw-Hill, New York
23. Jammer M (1974) Philosophy of quantum mechanics. Wiley, New York
24. McWeeny R (2003) Quantum mechanics, principles and formalism. Dover, Mineola
25. Weyl H (1950) Theory of groups and quantum mechanics. Dover, New York
26. Liboff RL (1997) Introductory quantum mechanics. Addison-Wesley, Reading
27. Cover TM, Thomas JA (1991) Elements of information theory. Wiley, New York
28. Ingels FM (1971) Information and coding theory. Intext Educational Publishers, Scranton
29. Cvijetic M, Djordjevic IB (2013) Advanced optical communications and networks. Artech House, Boston
30. Djordjevic IB, Ryan W, Vasic B (2010) Coding for optical channels. Springer, New York

# Chapter 3

## Fundamentals of Biological Thermodynamics, Biomolecules, Cellular Genetics, and Bioenergetics

**Abstract** In this chapter, we describe the basics of biomolecules, cellular genetics, and bioenergetics. The chapter starts with the biological thermodynamics. The following biomolecules will be described: amino acids, peptides, proteins, carbohydrates, and corresponding polymers; nucleic acid, nucleosides, and nucleotides; and phospholipids. Regarding the cell dynamics, the following topics will be described: DNA structure, the genetic code, gene anatomy, DNA synthesis and repair, transcription, and translation. Regarding the energetics of the cell, we will discuss universal forms of energy, namely, ATP and proton motive force, and the metabolism of the organism. Full details on prokaryote organism metabolism regulation will be provided. Further, we will discuss the relationship between genetics and evolution.

### 3.1 Biological Thermodynamics

The systems can be classified into three generic categories: closed systems, open systems, and isolated systems. The *closed systems* are the systems only exchanging the energy (more precisely heat) with the surrounding (environment). On the other hand, the live systems are *open systems*, i.e., the systems exchanging both energy and matter with the surrounding (environment). Namely, the live systems take the nutrients (matter and energy) from the environment, perform the work and generate the heat, and finally release the waste products. No way can they be considered as the closed systems. On the other hand, the live systems frozen for experimental and research purposes can be considered as closed systems. We say that system is *isolated* if neither energy nor matter get exchanged with the surroundings. At this point, it is convenient to introduce the concepts of equilibrium and steady state. We say that system is in *equilibrium* when all relevant system parameters are time-invariant. On the other hand, we say that the system is in a *steady state* when the energy and/or matter enters the system and exits the system at the same rate.

When several systems are in physical contact, at equilibrium they will have the same temperature. This claim is sometimes referred to as the zeroth law of

thermodynamics. For instance, the adjacent cells are in close proximity of each other and will be in both thermal and hydraulic equilibrium.

### 3.1.1 The First Law of Thermodynamics, Perfect Gas, Enthalpy of the System

The *first law of thermodynamics* is related to the energy conservation law and can be stated as follows [1–8]: the energy in the universe can be neither created nor destroyed, it can only be transformed from one form to another. The *internal energy* of the system, denoted as  $U$ , is increased by the amount of heat  $\Delta Q$  added to it and decreased by the amount of work  $\Delta W$  performed by the system on the environment, so that we can write

$$\Delta U = \Delta Q - \Delta W, \quad (3.1)$$

where  $\Delta U$  is the change in the internal energy. Notice that (3.1) can also be written as  $\Delta U = \Delta Q + \Delta W$ , with  $\Delta W$  denoting now the work performed on the system. Depending on whether the heat has been released ( $\Delta Q < 0$ ) or absorbed ( $\Delta Q > 0$ ) by the system, the processes in the cell can be classified as either *exothermic* or *endothermic*, respectively.

For a given system very often we are able to define the corresponding *equation of state*, such as

$$\rho = \rho(P, T) \quad (3.2)$$

where  $\rho$  is the density of material,  $P$  denotes the pressure, and  $T$  denotes the temperature. This equation is applicable to fluids be in liquid or gaseous phase. In particular, for very *dilute gases*, it can be expressed in analytical form:

$$\rho = \frac{N}{V} m \quad (3.3)$$

$$\rho = \frac{P}{RT} \mathcal{M} \quad (3.4)$$

where  $N$  is the number of molecules,  $V$  is the volume in which gas is contained,  $m$  is the mass of single molecule, and  $\mathcal{M}$  is the chemical molecular weight (the molar mass). Equation (3.3) is applicable on molecular (microscopic) level, while (3.2) on macroscopic level. Since cell can contain  $10^{14}$  (and beyond) molecules, we can consider it as a macroscopic “object.” In this domain, the thermodynamic principles are applicable, while on molecular level, the concept of statistical physics, be classical or quantum, should be used instead. On macroscopic level, we can measure the temperature of the cell, the tension in the membrane, and the pressure

inside vacuole, to mention few. In (3.4), we use  $R$  to denote the universal gas constant defined as

$$R = 8.3145 \text{ J/(Kmol)}. \quad (3.5)$$

We can relate it to the Boltzmann's constant  $k = 1.381 \times 10^{-23} \text{ J/K}$  through the Avogadro's number  $\mathcal{A} = 6.023 \times 10^{23} \text{ mol}^{-1}$  as follows:

$$R = \mathcal{A}k. \quad (3.6)$$

Notice that in some books the universal constant is expressed in cal/(deg mol) as  $R = 1.987 \text{ cal/(K mol)}$ . Given that 1 cal = 4.184 J, it is trivial to establish the connection between the two. In similar fashion, given that 1 mol contains  $\mathcal{A}$  molecules, we can write

$$\mathcal{W} = \mathcal{A}m. \quad (3.7)$$

Now by equating (3.3) and (3.4), with the help of (3.6)–(3.7), we obtain

$$PV = NkT \quad (3.8)$$

$$P\mathcal{V} = RT, \quad (3.9)$$

where the (3.9) is derived from (3.8) by setting  $N = \mathcal{A}$  and  $\mathcal{V}$  denotes the molar volume. The molar volume is independent of the nature of the gas, and at 0 °C it equals  $\mathcal{V}_0 = 22.4 \text{ L/mol}$ . Equation (3.9) is valid for highly dilute gases, which are also known as *ideal* or *perfect gas*. The corresponding state equation for imperfect or real gases needs to be modified. The most popular generalization is due to van der Waals:

$$\left( P + \frac{a}{\mathcal{V}^2} \right) (\mathcal{V} - b) = RT, \quad (3.10)$$

where the term  $b$  is used to denote that compression beyond  $\mathcal{V} = b$  is not possible, while the term  $a/\mathcal{V}^2$  to denote the pressure needed to hold gas together at a given temperature  $T$ .

The heat content of the system can be expressed in terms of so-called enthalpy of the system, denoted as  $H$ , and defined as

$$H = U + PV. \quad (3.11)$$

Under the constant temperature and pressure conditions, which is common state of the cell, the change in enthalpy  $\Delta H$  will be caused by the change in internal energy

of the system  $\Delta U$  and work performed on the system  $P\Delta V$  (causing the volume change of  $\Delta V$ ) so that we can write

$$\Delta H = \Delta U + P\Delta V. \quad (3.12)$$

Since many biochemical reactions occur in solution, the change in volume can be neglected and we can write  $\Delta H = \Delta U$ .

### 3.1.2 Gibbs–Boltzmann Distribution Law, Second Law of Thermodynamics, and Third Law of Thermodynamics

Maxwell and Boltzmann first devised the statistical physics concepts and applied it to small identical particles moving independently from each other. Gibbs generalized this concept by applying it to large bodies with a complicated internal structure.

Let the ensemble of systems be described by states 1, 2, ... Let the number of systems being in these states be denoted respectively as  $N_1, N_2, \dots$ , and the corresponding energies be denoted as  $E_1, E_2, \dots$  The number of ways in which a given set of occupation numbers, denoted as  $N_i$ , can be realized is described by corresponding multinomial coefficients [8]:

$$M(N_1, N_2, \dots) = \frac{N!}{N_1! N_2! \dots}, \quad N = N_1 + N_2 + \dots \quad (3.13)$$

The measure of uncertainty of this ensemble of systems is called the *entropy* and can be defined as

$$S = \log M(N_1, N_2, \dots), \quad (3.14)$$

where the base in (quantum) information theory is typically 2, while the base in statistical physics is typically  $e$  ( $=2.718281828\dots$ ). For historical reasons, the entropy in statistical physics is always expressed in the same dimension as Boltzmann constant, so that we can also define the entropy as  $S = k \log M(N_1, N_2, \dots)$ . However, in this chapter, we will omit the Boltzmann's constant to be consistent with the previous chapter; see also [9]. To determine the distribution of a given set of occupation numbers, we perform the maximization of entropy subject to *occupation number (probability) constraint*:

$$N = \sum_i N_i, \quad (3.15)$$

and *energy constraint*:

$$E = \sum_i N_i E_i. \quad (3.16)$$

We can use the Lagrangian method and maximize the expression

$$\mathcal{L} = S(N_1, N_2, \dots) - \alpha \left( N - \sum_i N_i \right) - \beta \left( E - \sum_i N_i E_i \right), \quad (3.17)$$

where  $\alpha$  and  $\beta$  are Lagrangian multipliers. By using the Stirling's approximation  $\log n! = n \log n - n + O(\log n)$  ( $n \in \{N, N_i\}$ ), we can rewrite (3.17) as follows:

$$\begin{aligned} \mathcal{L} \cong & N \log N - N - \left( \sum_i N_i \log N_i - \sum_i N_i \right) - \alpha \left( N - \sum_i N_i \right) \\ & - \beta \left( E - \sum_i N_i E_i \right), \end{aligned} \quad (3.18)$$

where we assumed that log-function is to the base  $e$ . Now by differentiating with respect to  $N_i$  and setting that this derivative is zero, we obtain:

$$\log N_i + \alpha + \beta E_i = 0. \quad (3.19)$$

The solution for  $N_i$  is then

$$N_i = e^{-\alpha - \beta E_i}. \quad (3.20)$$

The probability of occupying state  $i$  with energy  $E_i$  can be determined as

$$p_i = p(E_i) = \frac{N_i}{N} = \frac{e^{-\alpha - \beta E_i}}{\sum_j e^{-\alpha - \beta E_j}} = \frac{e^{-\beta E_i}}{\sum_j e^{-\beta E_j}}, \quad (3.21)$$

which is a well-known Gibbs distribution. The nonnegative parameter  $\beta$ , known as inverse temperature, is related to temperature as  $\beta = 1/(kT)$ , so that we can rewrite (3.21) as follows:

$$p(E_i) = \frac{e^{-E_i/kT}}{\sum_j e^{-E_j/kT}}. \quad (3.22)$$

By interpreting  $E_i$  as the energy of a molecule in state  $i$ , we can rewrite (3.22) in terms of energy per mole  $E_{\text{mol},i}$  as

$$p(E_{\text{mol},i}) = \frac{e^{-E_{\text{mol},i}/RT}}{\sum_j e^{-E_{\text{mol},j}/RT}}. \quad (3.23)$$

The denominator in (3.21) is known as the *partition function*, denotes as  $F$ , and defined as  $F = \sum_j e^{-\beta E_j}$ . For continuous systems, we can drop the subscript and the corresponding distribution would be

$$p(E) = C_0 e^{-\beta E}, \quad C_0 = 1/F. \quad (3.24)$$

The parameter  $\beta$  would be  $1/kT$  for molecules and  $1/RT$  for moles. The biochemical reaction forward reaction rate  $r$  can be then defined as

$$\log r = -\beta E + \text{constant}, \quad \beta = \begin{cases} 1/kT, & \text{for molecules} \\ 1/RT, & \text{for moles} \end{cases}, \quad (3.25)$$

and this dependence is known as Arrhenius' law.

The average energy of the ensembles of systems, denoted as  $U$ , based on (3.21) can be determined as

$$U = \sum_i p(E_i)E_i = \frac{\sum_i E_i e^{-\beta E_i}}{\sum_j e^{-\beta E_j}}. \quad (3.26)$$

The entropy of an individual member of ensemble can be defined as  $S = N^{-1} \log M(N_1, N_2, \dots)$ , and by using the Stirling's approximation, we obtain [9]

$$\begin{aligned} S &\cong \left( N \log N - \sum_i N_i \log N_i \right) / N = - \sum_i (N_i/N) \log (N_i/N) \\ &= - \sum_i p_i \log p_i, \end{aligned} \quad (3.27)$$

indicating that thermodynamics entropy of an individual member of ensemble is equal to the Shannon entropy  $H = - \sum_i p_i \log p_i$ . In other words, the Shannon entropy is a Stirling's approximation of the thermodynamics entropy of an

individual member of ensemble, which has been noticed in [9] already. By substituting (3.21) into (3.27), we obtain

$$\begin{aligned}
 S &\cong -\sum_i p_i \log p_i = -\sum_i \frac{e^{-\beta E_i}}{F} \log \left( \frac{e^{-\beta E_i}}{F} \right) \\
 &= -\frac{1}{F} \sum_i e^{-\beta E_i} (-\beta E_i - \log F) = \beta \underbrace{\frac{\sum_i E_i e^{-\beta E_i}}{F}}_U + \log F = \beta U + \log F \\
 &= \frac{U}{T} + \log F.
 \end{aligned} \tag{3.28}$$

In (3.28), we redefined  $\beta$  as  $\beta = 1/T$ , as we omitted the factor  $k$  in the definition of entropy. This relationship establishes the connection between the energy of the system  $U$  and the entropy. The entropy defined by (3.27) has the same properties as the Shannon entropy  $0 \leq S \leq \log K$ , where  $K$  is the number of probability terms in (3.21). Clearly, the largest uncertainty (entropy) is obtained when  $\beta \rightarrow 0$ ; in this case, the Gibbs distribution becomes uniform. However, this case is not of practical interest as it requires infinitely large temperature. The entropy of two uncoupled systems is additive:

$$\begin{aligned}
 S &= -\sum_{i,j} p_i^{(1)} p_j^{(2)} \log p_i^{(1)} p_j^{(2)} = -\sum_{i,j} p_i^{(1)} p_j^{(2)} [\log p_i^{(1)} + \log p_j^{(2)}] \\
 &= -\sum_i p_i^{(1)} \log p_i^{(1)} - \sum_j p_j^{(2)} \log p_j^{(2)} = S^{(1)} + S^{(2)},
 \end{aligned} \tag{3.29}$$

where the superscripts (1) and (2) are used to denote uncoupled systems 1 and 2.

If we observe the ensemble of systems as a statistical mixture of quantum systems each occurring with probability  $p_i$ , we can describe it with corresponding density matrix, which is diagonal, in this particular example, with diagonal elements given by (3.21). For ensemble of systems described with nondiagonal density matrix  $\rho$ , the entropy can be defined as

$$S = -\text{Tr}[\rho \log \rho] = -\sum_i \lambda_i \log_2 \lambda_i, \tag{3.30}$$

where  $\lambda_i$  are the eigenvalues of the density matrix. Clearly, the thermodynamics entropy is related to the von Neumann entropy introduced in Chap. 2. As mentioned earlier, for historical reasons, the entropy in statistical physics is commonly expressed in the same dimension as Boltzmann constant so that (3.30) should be written as  $S = -k \text{Tr}[\rho \log \rho]$ . However, without loss of generality, we omitted the constant  $k$ , to easier establish the relationship between thermodynamics entropy and the von Neumann entropy. Therefore, the concepts of quantum information theory developed in Chap. 2 are directly applicable here.

The *second law of thermodynamics* can now be formulated as follows [8]: The entropy of the system, defined as  $S = -\text{Tr}[\rho \log \rho]$ , is larger for diagonal density matrix, with matrix elements given by Gibbs distribution  $\lambda_i = p_i = e^{-\beta E_i} / \sum_j e^{-\beta E_j}$ , than any other density matrix satisfying the same constraints:

$$\text{Tr}(\rho) = 1, \quad \text{Tr}(\rho \mathcal{H}) = U, \quad (3.31)$$

where  $\mathcal{H}$  denotes the corresponding Hamiltonian.

To prove this claim, let us consider another diagonal density matrix with diagonal elements being  $q_i (\neq p_i)$ . The corresponding entropy difference  $\Delta S$  would be

$$\Delta S = -\sum_i q_i \log q_i - \left( -\sum_i p_i \log p_i \right). \quad (3.32)$$

The corresponding probability and energy constraints are given by

$$\sum_i p_i = \sum_i q_i = 1, \quad \sum_i p_i U_i = \sum_i q_i U_i = U. \quad (3.33)$$

Let us now consider the summation of mixed term  $q_i \log p_i$  and take into account that distribution of  $p_i$  is Gibbs to obtain

$$\begin{aligned} \sum_i q_i \log p_i &= \sum_i q_i \log \left( \frac{e^{-\beta U_i}}{F} \right) = \sum_i q_i (-\beta U_i + \log F) = -\beta U + \log F \\ &= \sum_i p_i \log p_i \end{aligned} \quad (3.34)$$

Now by replacing  $\sum_i p_i \log p_i$  with  $\sum_i q_i \log p_i$ , the entropy difference becomes

$$\Delta S = -\sum_i (q_i \log q_i - q_i \log p_i) = -\sum_i q_i \log \left( \frac{q_i}{p_i} \right). \quad (3.35)$$

Since the function  $f(x) = x \log x - (x - 1)$  is positive for  $x \geq 0$ , except  $x = 1$ , we obtain

$$\Delta S = \sum_i p_i \frac{q_i}{p_i} \log \left( \frac{q_i}{p_i} \right) + \underbrace{\sum_i p_i \left( 1 - \frac{q_i}{p_i} \right)}_{=0} = \sum_i p_i \left[ \frac{q_i}{p_i} \log \left( \frac{q_i}{p_i} \right) - \left( \frac{q_i}{p_i} - 1 \right) \right] > 0 \quad (3.36)$$

Therefore, the difference in entropies is always positive. Based on this derivation, we can conclude that *the entropy of the universe for spontaneous processes is always positive*:

$$\Delta S = \Delta S_{\text{system}} + \Delta S_{\text{environment}} > 0 \quad (3.37)$$

where with  $\Delta S_{\text{system}}$  we denoted the entropy of the system, while with  $\Delta S_{\text{environment}}$  we denoted the entropy of the environment (surrounding). Notice that this interpretation of the second thermodynamics law is consistent with all types of systems: open, closed, and isolated ones.

The *third law of thermodynamics*, also known as *Nernst heat theorem*, is related to the entropy at absolute zero ( $T = -273.15$  °C). The zero-point entropy can be expressed as

$$S(0) = \log M(E_0), \quad (3.38)$$

where  $E_0$  is the ground state and  $M(E_0)$  is the multiplicity factor (degeneracy) of the ground state. Since the multiplicity factor of ground state at absolute zero ( $T = -273.15$  °C) must be 1, and  $\log 1 = 0$ , it appears that entropy at this temperature is zero.

The second and third thermodynamic laws can be combined into one single statement claiming that the *entropy of the universe is nonnegative*; in other words

$$\Delta S = \Delta S_{\text{system}} + \Delta S_{\text{environment}} \geq 0. \quad (3.39)$$

### 3.1.3 Biochemical Reaction Energetics

From (3.28) is evident that for isothermal processes (in which temperature does not change), the change of entropy  $\Delta S \cong \Delta U/T$ , where  $\Delta U$  is the change in internal energy due to the heat absorption. In other words,  $\Delta U \cong T\Delta S$ , and we can interpret  $\Delta S$  as the change in entropy due to the heat absorbed by the system. Since most of the biochemical reactions appear in solution, the change of volume is negligible, and the change of the heat content of the system (enthalpy)  $\Delta H$  would be the same as  $\Delta U$ . The difference between  $\Delta H$  and  $T\Delta S$  is typically denoted as  $\Delta G$ , where  $G$  is the Gibbs free energy defined as  $G = H - TS$ . Therefore, we can write

$$\Delta G = \Delta H - T \Delta S. \quad (3.40)$$

This equation indicates that out of the energy released by the biochemical reaction, only a portion of energy, so-called free energy, can be used to perform a certain work. This parameter ( $\Delta G$ ) can be used as a measure of spontaneity of the process, and the process at constant temperature and constant pressure is spontaneous when  $\Delta G \leq 0$ . The parameter  $\Delta G$  can also be used to classify the processes and biochemical reactions (at constant temperature and pressure) into three categories: (1) the *exergonic* for  $\Delta G < 0$ , (2) *endergonic* for  $\Delta G > 0$ , and (3) processes (reactions) being at equilibrium for  $\Delta G = 0$ . The exergonic processes are spontaneous and energetically favorable, as the energy of the products is lower than the energy of the reactants.

Let us now consider the following generic biochemical reaction:



where we use  $A$  and  $B$  to denote the reactants, while  $C$  and  $D$  the products. The corresponding concentrations are denoted as  $[A]^a$ ,  $[B]^b$ ,  $[C]^c$ , and  $[D]^d$ , respectively, where with  $a$ ,  $b$ ,  $c$ , and  $d$ , we denote the stoichiometries of the reactants. From Gibbs–Boltzmann law, given by (3.23), we can write

$$\frac{[C]^c [D]^d}{[A]^a [B]^b} = \frac{\exp[-(\text{The change of energy of products})/RT]}{\exp[-(\text{The change of energy of reactants})/RT]}. \quad (3.42)$$

By taking the logarithm of both sides of equation and rearranging, we obtain that the change of free energy for this biochemical reaction can be determined as

$$\Delta G = \Delta G^0 + RT \log \left\{ \frac{[C]^c [D]^d}{[A]^a [B]^b} \right\}, \quad (3.43)$$

where  $\Delta G^0$  denotes the Gibbs free energy of the *standard biological state*. Notice that the standard state in biochemistry is different from that in physics, and it is defined as the solute state, at room temperature of 25 °C and pressure of 101.325 kPa, in which the concentration of all components is 1 mol/L, except for  $H^+$  whose concentration is  $10^{-7}$ , corresponding to pH of 7. When the biochemical reaction is in equilibrium,  $\Delta G = 0$ , and we can determine  $\Delta G^0$  from (3.43) as

$$\Delta G^0 = -RT \log \left\{ \frac{[C]_{\text{eq}}^c [D]_{\text{eq}}^d}{[A]_{\text{eq}}^a [B]_{\text{eq}}^b} \right\} = -RT \log K_{\text{eq}}, \quad K_{\text{eq}} = \frac{[C]_{\text{eq}}^c [D]_{\text{eq}}^d}{[A]_{\text{eq}}^a [B]_{\text{eq}}^b} \quad (3.44)$$

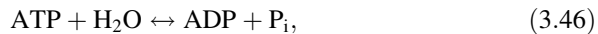
where  $K_{\text{eq}}$  denotes the equilibrium constant and the subscript eq is used to denote the concentrations at equilibrium. The temperature dependence of logarithm of the

equilibrium constant is linear in reverse temperature  $\beta = 1/T$ , and from (3.44) we obtain

$$\begin{aligned}\log K_{\text{eq}} &= -\frac{\Delta G^0}{RT} = -\frac{\Delta H^0 - T\Delta S^0}{RT} = -\frac{\Delta H^0}{R} \frac{1}{T} + \frac{\Delta S^0}{R} \\ &= -\frac{\Delta H^0}{R} \beta + \frac{\Delta S^0}{R},\end{aligned}\quad (3.45)$$

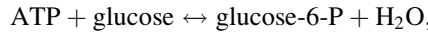
and this dependence is known as a *van't Hoff law* (isochore). In (3.45) we use the superscript 0 to denote the parameters of the standard state. Clearly, the slope of this straight line is given by  $-\Delta H^0/R$  and the intercept on  $\log K_{\text{eq}}$ -axis is given by  $\Delta S^0/R$ .

Very often in biological systems, several reactions occur simultaneously. In this situation, what matters is the total change of the free energy of all reactions. If some reactions are endergonic, they will still proceed if overall process involving all reactions is exergonic. The endergonic reactions are typically combined with the adenosine triphosphate (ATP) hydrolysis, given by



as the change in free energy during hydrolysis is about  $\Delta G^0 = -31.8 \text{ kJ/mol}$  ( $-7.6 \text{ kcal/mol}$ ), which is typically sufficient to overcome the endergonic character of another reaction. In (3.46), we use ADP to denote adenosine diphosphate and  $\text{P}_i$  to denote inorganic phosphate  $\text{HPO}_4^{2-}$ . The structures of ATP, ADP, and adenosine monophosphate (AMP) will be provided in Sect. 3.2.

*Example* As an illustration, the phosphorylation of glucose by inorganic phosphate ( $\text{P}_i$ ), given by  $\text{Glucose} + \text{P}_i \rightarrow \text{glucose-6-P} + \text{H}_2\text{O}$ , requires the free energy of  $+14 \text{ kJ/mol}$ . Such reaction will not proceed spontaneously. When this reaction is combined with ATP hydrolysis, we obtain



and the overall change in free energy will be  $\Delta G^0 = +14 \text{ kJ/mol} - 31.8 \text{ kJ/mol} = -17.8 \text{ kJ/mol}$ . Clearly, the overall process is exergonic, and the phosphorylation reaction will go forward.

This concept of biochemical processes energetics is also applicable to *redox reactions*: the oxidation reactions, in which a substance dons electrons, and the reduction reactions, in which a substance serves as an acceptor of electrons. Let us observe the following generic redox reaction:



The change in free energy for this redox reaction is given by

$$\Delta G = \Delta G^0 + RT \log \left\{ \frac{[A]_{\text{Red}}[B]_{\text{Ox}}}{[A]_{\text{Ox}}[B]_{\text{Red}}} \right\}. \quad (3.48)$$

By dividing the both sides of (3.48) by  $-ne\mathcal{A}$ , where  $n$  is the number of electrons transferred during the redox reaction,  $e$  is an electron charge, and  $\mathcal{A}$  denotes Avogadro's number, we obtain the so-called *Nernst equation*:

$$E = E_0 - \frac{RT}{ne\mathcal{A}} \log \left\{ \frac{[A]_{\text{Red}}[B]_{\text{Ox}}}{[A]_{\text{Ox}}[B]_{\text{Red}}} \right\} = E_0 - \frac{RT}{nF} \log \left\{ \frac{[A]_{\text{Red}}[B]_{\text{Ox}}}{[A]_{\text{Ox}}[B]_{\text{Red}}} \right\}, \quad F = e\mathcal{A}, \quad (3.49)$$

where  $E$  denotes the *electromotive force*, defined as  $E = -\Delta G/(nF)$ , and  $F$  is a Faraday constant  $F = e\mathcal{A} = 96.485 \text{ kJ}/(\text{V mol})$ . At equilibrium,  $\Delta G = 0$ , and we can establish the relationship with equilibrium constant as follows:

$$\log K_{\text{eq}} = \frac{nF}{RT} E_0. \quad (3.50)$$

The Nernst equation can be used to determine the potential of ion of charge  $z$  across a membrane of the cell as follows:

$$E = \frac{RT}{zF} \log \left\{ \frac{[\text{ions outside cell}]}{[\text{ions inside cell}]} \right\}. \quad (3.51)$$

In thermodynamics equilibrium, the membrane potential must be the same as Nernst potential. However, when the cell is not in the equilibrium due to ion pump activity, the resting potential (the static membrane potential of quiescent cells)  $E_m$  can be determined using the so-called Goldman equation:

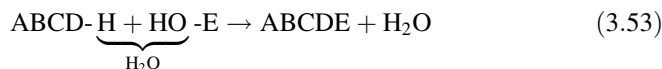
$$E_m = \frac{RT}{F} \log \left\{ \frac{\sum_i P_{A_i^-} [A_i^-]_{\text{in}} + \sum_j P_{M_j^+} [M_j^+]_{\text{out}}}{\sum_i P_{A_i^-} [A_i^-]_{\text{out}} + \sum_j P_{M_j^+} [M_j^+]_{\text{in}}} \right\}, \quad (3.52)$$

where with  $P_{\text{ion}}$  we denoted the permeability of ion  $\in \{A_i^-, M_j^+\}$ ,  $[\text{ion}]_{\text{in}}$  denotes the intracellular concentration of the ion, and  $[\text{ion}]_{\text{out}}$  denotes the extracellular concentration of the ion.

## 3.2 Biomolecules

In this section, we describe the fundamental building blocks—biomolecules of the cell [10–22]. This section has been written by having a nonbiologist reader in mind. It is well known that about 70 % of the weight of the living cell is composed of water, the rest are different *macromolecules*, representing the chains of monomers. The most common elements found in living organisms are carbon (C), hydrogen (H), nitrogen (N), oxygen (O), phosphorus (P), and sulfur (S). In terms of number of valence electrons, they can be placed in the following series: H has valence 1, O has valence 2, N 3, C 4, P 5, and S has the valence 6. Interestingly enough, except from P and S, the other elements from this list are leading elements of the corresponding group of elements in the periodic table of elements. Other life important elements include Na, K, Mg, Ca, Cl, Cr, Mn, Fe, Co, Cu, Zn, and Mo.

The macromolecules can be classified into several generic categories: proteins, carbohydrates, lipids, and nucleic acids. The macromolecules are polymers obtained by joining together simpler molecules called monomers. The corresponding reactions used to perform this polymerization are known as *condensation (dehydration) reactions*. Let ABCD-H be a polymer with reactive hydrogen end (–H), while E-OH be a monomer with hydroxyl ending group (–OH). The condensation reaction can be described as follows:



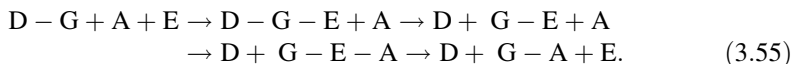
Clearly, the products of reaction are polymer ABCDE and the water molecule  $\text{H}_2\text{O}$ . Therefore, the macromolecules are formed by adding one monomer at the time to the growing chain of monomers until the process of polymerization is over. The monomers within the macromolecule are called by the name of building block followed by a keyword *residue*.

The reaction reverse to the condensation reaction is known as the *hydrolysis reaction* and involves disassembly of a given molecule in the presence of water. The ATP hydrolysis given by (3.46) is an illustrative example of hydrolysis reactions. Evidently, the hydrolysis reaction releases the energy to the environment. The hydrolysis reactions require high activation energy and do not occur without corresponding mediating enzymes. The activation energy is an energetic barrier needed to overcome for reaction to proceed. The purpose of enzymes is to overcome this barrier and speed up the reaction. On a basic level, a typical reaction carried out by the enzyme E on substrate S to create the product P can be described as



Two basic mechanisms by which the substrate binds with the enzyme E to create the *enzyme–substrate complex* ES are (1) lock-and-key and (2) induced fit mechanisms. In lock-and-key mechanism, the substrate binds to the site of exact

complementarity. On the other hand, in the induced fit mechanism, the enzyme introduces either stress or distortion of the substrate to enable the catalysis (reduction in the activation energy). The catalytic reaction then converts the substrate to the product P, which is still bound to the enzyme, as shown by (3.54). The product then dissociates from enzyme so that the enzyme gets unchanged during this process. As an illustration, let us consider the donor D and acceptor A and group G initially connected to donor as D–G. The reaction of migrating group G from donor to acceptor A in the presence of enzyme E can be described as follows:



Without the enzyme, the migration reaction will not proceed due to too high activation energy.

In what follows, instead of using standard representation for three-dimensional (3-D) molecules, we will use the Kyoto Encyclopedia of Genes and Genomes (KEGG) representation because it is more compact. In both KEGG and standard representations, the adenosine monophosphate (AMP) is described as shown in Fig. 3.1. In KEGG representation, shown in Fig. 3.1a, when the carbon atoms are not explicitly written, they are implicitly assumed to be in the corners of the structural formula. The bond shown by dashed arrow indicates that this bond is directed from the reader below the plane. On the other hand, the bond denoted by solid black arrows is directed from the plane toward the reader. Further, the hydrocarbon bonds can be omitted, and when omitted, they are implicitly assumed. Namely, it is well known

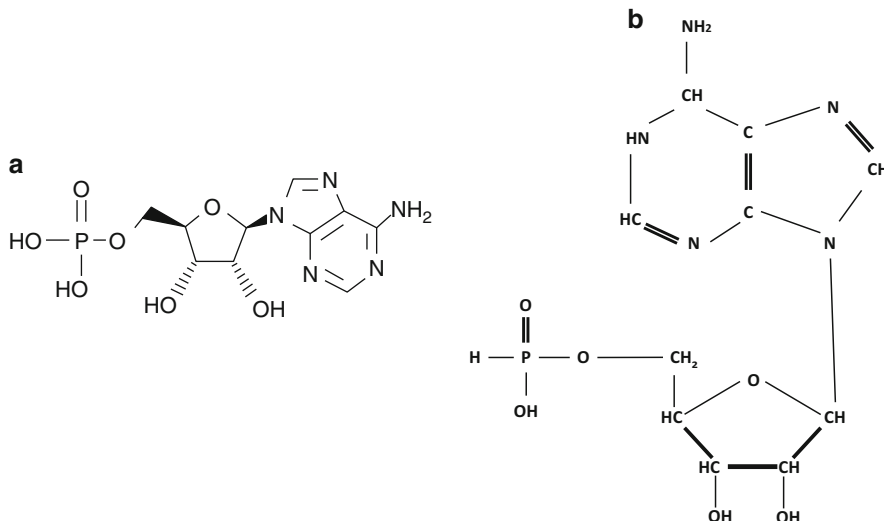


**Fig. 3.1** AMP in (a) KEGG representation, (b) standard (Haworth) representation

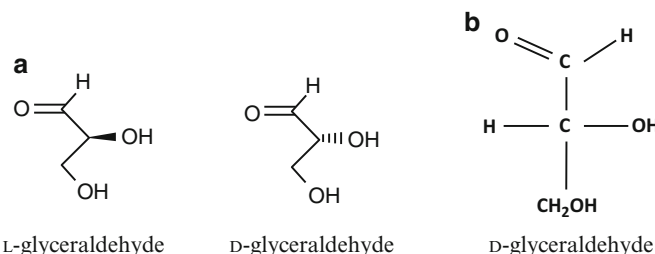


**Fig. 3.2** (a) L-glyceraldehyde and D-glyceraldehyde in KEGG representation and (b) standard (Fischer) representation of D-glyceraldehyde

that each carbon atom must have four bonds with neighboring atoms/functional groups. When the number of bonds is smaller than 4, we immediately know that the remaining ones are hydrocarbon bonds. In standard representation, shown in Fig. 3.1b, the ring structure is considered to be perpendicular to the plane of the paper, with tick line closer to the reader. Two hydroxyl groups are considered to be below the ring plane, while the purine group above the ring plane.

The molecules with the same chemical composition, but with different 3-D bond positioning, are known as *isomers*. In particular, the isomers that are mirror images of each other are known as *stereoisomers* and are optical active. Whenever a molecule has *chiral* (*asymmetric*) carbon atoms present, it will have different stereoisomers. A chiral carbon atom is connected to four different atoms or molecules. The carbohydrates contain many examples of stereoisomers. The three-carbon sugars L-glyceraldehyde and D-glyceraldehyde, with chemical formula  $C_3H_6O_3$ , are stereoisomers; they are mirror images of each other, and corresponding structural formulas (diagrams) in KEGG representation are shown in Fig. 3.2a.

For convenience, the Fischer (standard) representation of D-glyceraldehyde has been provided as well in Fig. 3.2b. In Fischer's representation, the horizontal bonds are considered to be in front of the plane (page), while the vertical bonds are considered to be behind the plane. The central carbon atom is connected to four different subunits (CHO, H, OH, and CH<sub>2</sub>OH), and it is, therefore, chiral. In KEGG representation, L (*levo*)-glyceraldehyde has the hydroxyl group connected to the chiral carbon atom above the plane (toward the reader), while in D (*dextro*)-glyceraldehyde the corresponding hydroxyl group is placed below the plane (away from the reader). These D- and L-forms could have different physical properties. For instance, the D-form rotates the polarized light clockwise, while the L-form counterclockwise. If a molecule has  $N$  chiral carbons, the number of stereoisomeric forms will be  $2^N$ .

### 3.2.1 Amino Acids, Peptides, and Proteins

In this subsection, we first describe the protein structure and then review their roles as (1) catalysts of biochemical reactions, (2) actuators to generate the motion, and (3) sensors to process the molecular signals.

The protein molecule is a linear chain of *amino acid residues*, with two neighboring amino acid residues linked via a *peptide bond*. The proteins of animals are composed of 20 amino acids. Each amino acid (AA) contains one amino group ( $-\text{NH}_2$ ), one carboxyl group ( $-\text{COOH}$ ), and one unique functional group (denoted as  $-\text{R}$ ), linked to the same carbon atom in  $\alpha$ -position, as shown in Fig. 3.3. This unique functional group, typically, determines the character (base or acid) of the amino acid. Two amino acids are linked together by the peptide bond, formed by the interaction of amino group from one AA with carboxyl group for the second AA and releasing one water molecule as shown in Fig. 3.4.

**Fig. 3.3** The generic structure of amino acids

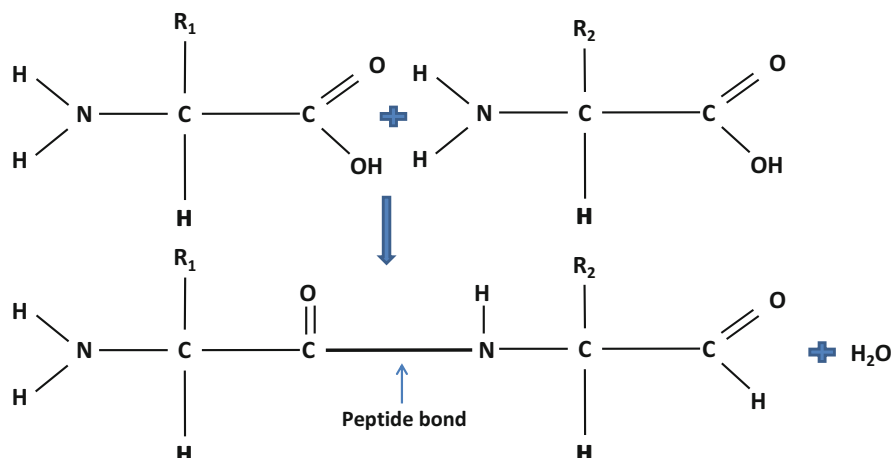
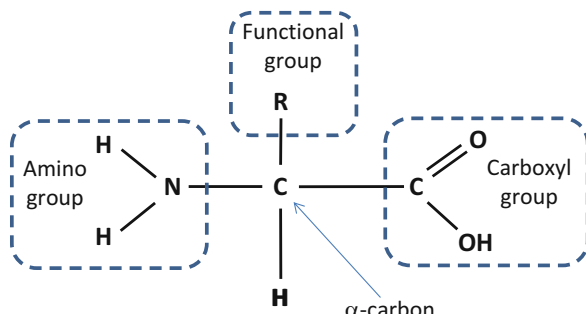


**Fig. 3.4** The creation of the peptide bond

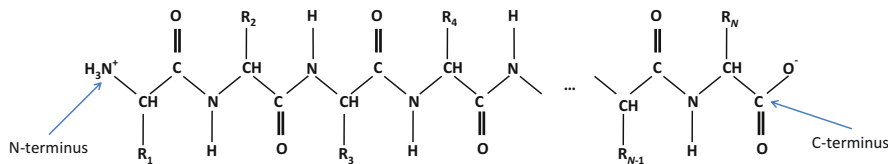


**Fig. 3.5** A generic polypeptide configuration

This carboxyl-amino linkage in organic chemistry is also known as the amide bond. Clearly, this peptide bond formation reaction is a dehydration (condensation) reaction. *Dipeptide* contains two amino residues as well as free amino and carboxyl groups, which are also known as N-terminus (N-terminal) and C-terminus (C-terminal), respectively. By linking up to 20 amino acids in similar fashion as shown in Fig. 3.4, the corresponding polymer is known as *oligopeptide*. Longer chain of amino acid residues is called the *peptide*. Finally, long chain of AA residues is called a protein or a polypeptide chain (it could even have 4000 AA residues). One generic example of peptide is shown in Fig. 3.5, with N-terminus and C-terminus being indicated. During protein synthesis, the polypeptide chain grows from N-terminus toward the C-terminus. Clearly, the key polypeptide chain contains series of three groups CH, CO, and NH, repeated periodically. The lateral chains of functional groups are linked to the CH portion of the chain.

Some amino acids can contain free amino or carboxyl groups, which gives a base or acid character of AA. The functional group could contain hydroxyl ( $-\text{OH}$ ) group or sulfur. Based on functional group, we can classify amino acids into several categories, as shown in Fig. 3.6. Glycine (Gly, G), alanine (Ala, A), valine (Val, V), leucine (Leu, L), and isoleucine (Ile, I) contain *aliphatic* functional group. The aspartic acid (Asp, D) and glutamate (Glu, E) contain *acid* functional group R. Histidine (His, H), lysine (Lys, K), and arginine (Arg, R) contain *basic* functional group. Asparagine (Asn, N) and glutamine (Gln, Q) contain *amide* functional group. Serine (Ser, S) and threonine (Thr, T) contain functional group with *hydroxyl* group. Cysteine (Cys, C) and methionine (Met, M) contain functional group with *sulfur*. Tyrosine (Tyr, Y), tryptophan (Trp, W), and phenylalanine (Phe, F) contain *aromatic* functional group. Finally, the proline (Pro, P) has a *cyclic* functional group. The functional group determines which AA is hydrophobic and which one is hydrophilic. For instance, alanine, leucine, methionine, phenylalanine, tyrosine, tryptophan, and valine are hydrophobic. On the other hand, arginine, asparagine, aspartate, glutamine, glutamate, histidine, isoleucine, lysine, serine, and threonine are hydrophilic. The proline is a very specific AA compared to other AAs, as it does not contain the amino group, but instead the imino group. The cyclic structure of proline changes the regular structure of polypeptide shown in Fig. 3.5. Namely, when the proline is inserted as the amid in the polypeptide chain, its nitrogen is not linked to any hydrogen, indicating that it cannot serve as the hydrogen bond donor, but instead can serve as the hydrogen bond acceptor. This changes the whole conformation structure of the peptide.

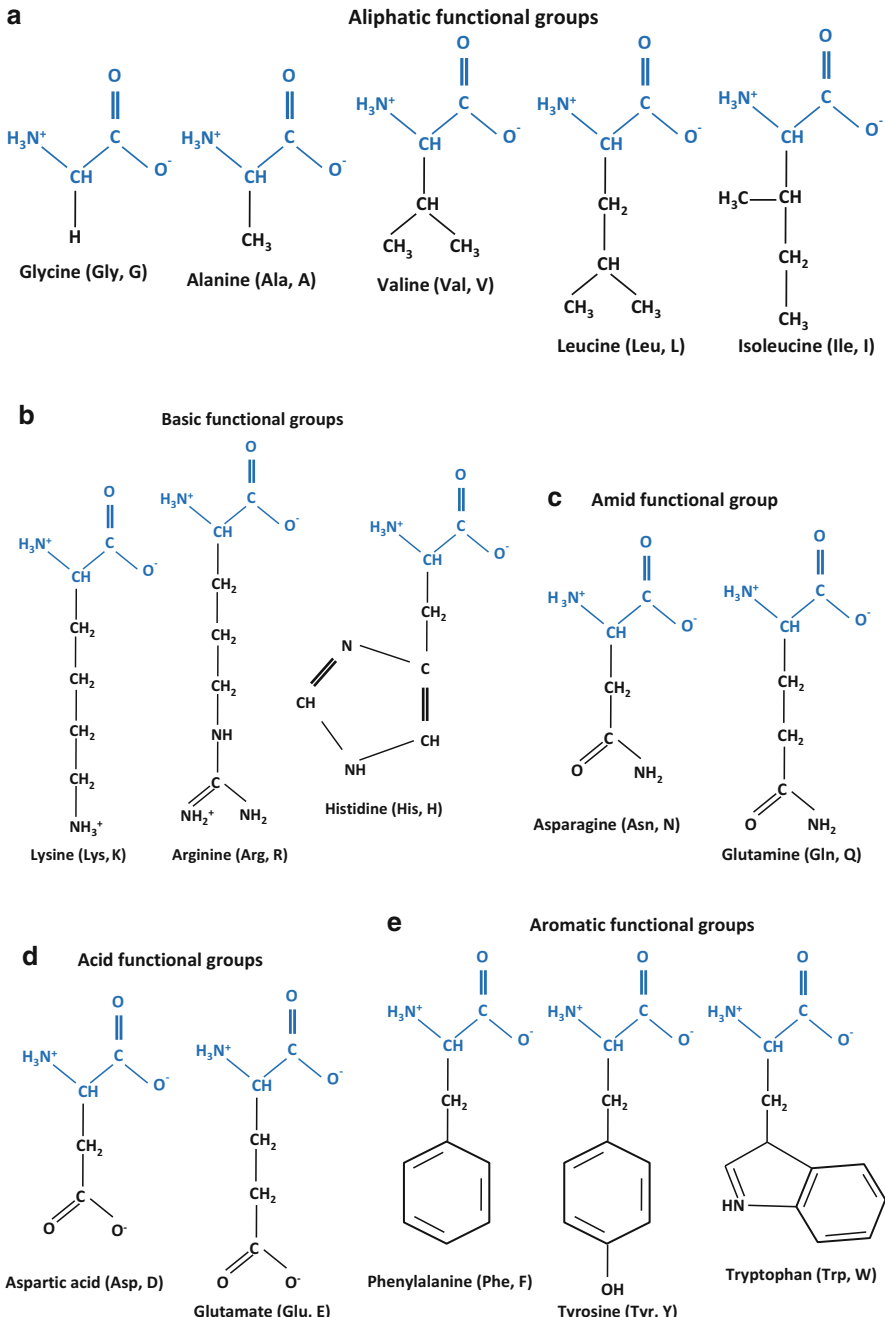


**Fig. 3.6** AAs classified based on functional group. AAs with (a) aliphatic functional group, (b) basic functional groups, (c) amid group, (d) acid functional groups, and (e) aromatic functional groups. AAs with (f) functional groups containing OH, (g) functional groups containing sulfur, and (h) cyclic functional group (proline). The portion of AA molecule common to all AAs is shown in blue characters, while functional groups are shown in black characters

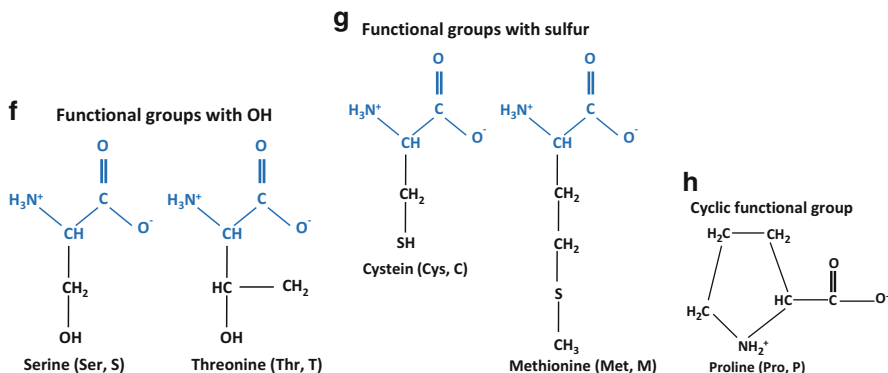
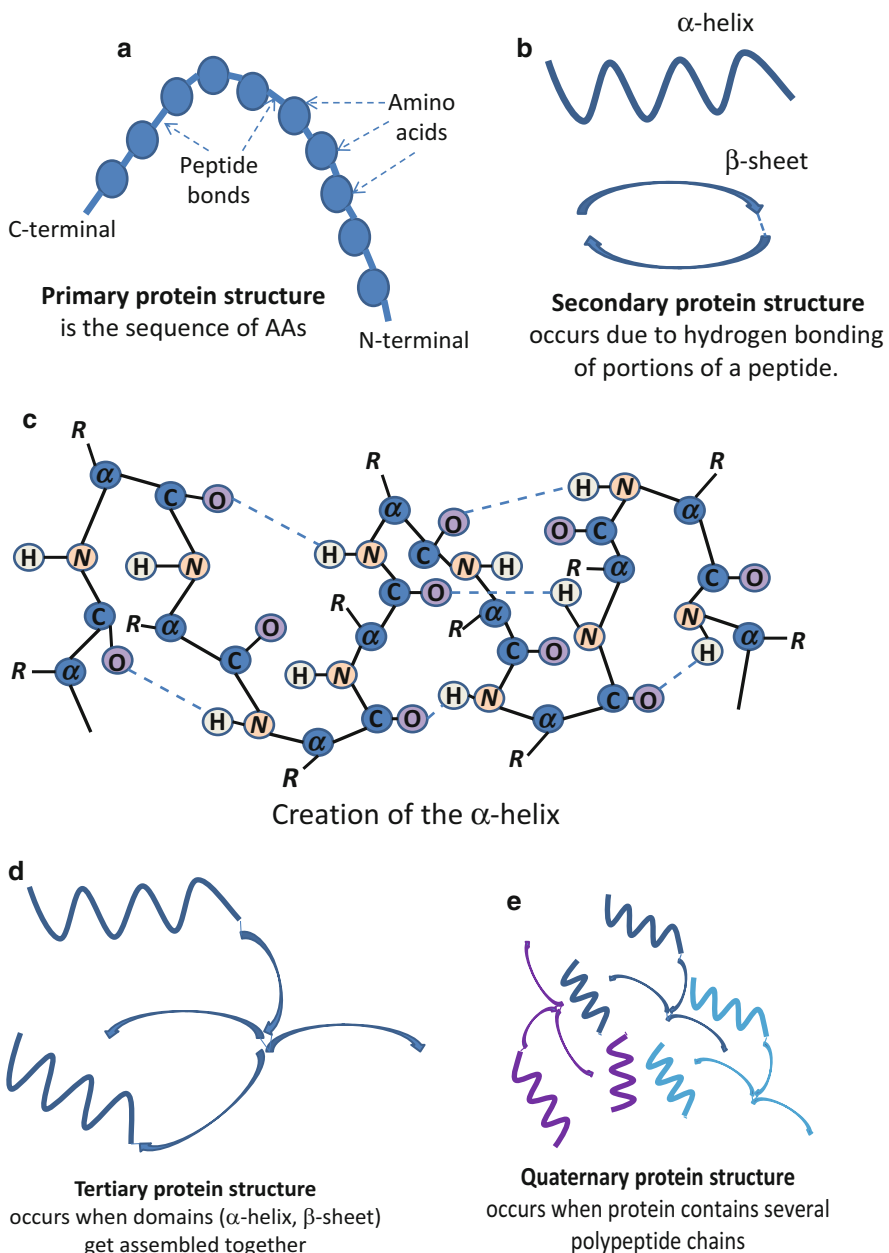


Fig. 3.6 (continued)

Amino acids with simple structures are more often found in polypeptides, such as alanine, glutamate, aspartic acid, leucine, and glycine. On the other hand, AAs with more complicated structure such as histidine, tryptophan, tyrosine, and phenylalanine are rarely used. The polypeptide structure, shown in Fig. 3.5, in other words the linear chain of amino acids, is commonly referred to as the *primary structure*.

The number of possible combinations of primary structure with 20 AAs is enormous. Let us say that the primary structure contains 20 AA residues. The number of possible combinations is  $20^{20} = 1.048 \times 10^{26}$ . However, the function of protein cannot be solely determined by amino acid analysis, which determines the percentage of AAs in a polypeptide. However, the sequence of AAs in the chain can give us more information about the function (role) of a particular polypeptide.

In a cell, the polypeptide chain (protein) forms several levels of high-order structures, known as secondary, tertiary, and quaternary structures, respectively, which is illustrated in Fig. 3.7. Given the close proximity of N–H and C = O bonds, as shown in Fig. 3.5, it is possible that N–H bond donates the hydrogen to the backbone group C = O, creating the hydrogen bond between N and O atoms. The most common hydrogen bonding is one in which the  $(i + 4)$ th backbone N–H group donates the hydrogen to the  $i$ th backbone C = O group in the peptide chain, as shown in Fig. 3.7c. The resulting secondary structure is known as  $\alpha$ -helix, as it has right-handed-coiled or spiral conformation. Interestingly enough, the  $\alpha$ -helix structure is very regular and can be predicted from the sequence of AA residues. However, the presence of proline violates this regular structure since the proline does not participate in the formation of the hydrogen bonds and prevents the spiraling. Therefore, due to the presence of proline, about 40–60 % of polypeptide could be of spiral structure, the rest would be just linear chain structure. Another common secondary structure is  $\beta$ -pleated sheet. The  $\beta$ -pleated sheets get created when polypeptides lie parallel to each other, forming the flat sheets. It is also possible to be created by hydrogen bonding of subunits involved in peptide bonds. The  $\beta$ -sheet is shown by an arrow in a typical protein graph.



**Fig. 3.7** Protein structure levels: (a) the primary structure, (b) the secondary protein structure, (c) illustration of the creation of  $\alpha$ -helix, (d) tertiary structure, and (e) quaternary protein structure

The spiral conformation of the polypeptide shortens the length of otherwise linear polypeptide and places the remote portions of the polypeptide in close proximity. This allows the interaction of different portions of the polypeptide, also known as the *tertiary structure*. The tertiary structure, therefore, represents the 3-D conformation of the polypeptide, typically determined by disulfide (S–S) bonds. In other words, the tertiary structure is composed of several secondary structure elements, known as *domains*, assembled together by inter-helix bonds such as hydrogen bonds and van der Waals forces.

For instance, when the lateral portions of the polypeptide across each other contain the cysteine residues under certain conditions, the oxidation of sulfhydryl (–SH) groups is possible, creating the covalent disulfide bonds. For instance, the enzyme ribonuclease (RNase), which catalyzes the degradation of RNA into smaller subunits, contains eight cysteine residues with four disulfide bonds Cys26-Cys84, Cys58-110, Cys40-95, and Cys65-72. The first two disulfide bonds (26-84 and 58-110) are key for the conformational folding. The cleavage of disulfide bonds can be performed by reduction reaction. There are 105 combinations in which the disulfide bond can be recreated by oxidation [5]. Only one corresponds to the native conformation state, indicating that the native conformation is the most energetically favorable. Moreover, this example also confirms that for higher-order structures, the interaction among lateral portions of the polypeptide chain is relevant.

The proteins containing multiple polypeptide chains exhibit an additional structure, the *quaternary structure*. The individual polypeptides are called subunits, and their spatial arrangement describes the protein quaternary structure. In order to create such a structure, the hydrogen bonds, ionic bonds, and hydrophobic interactions among subunits are involved.

The higher-order protein structure of protein, and at the same time the corresponding function, can be modified by the so-called phosphorylation. The phosphorylation is the modification by which a phosphate group ( $\text{PO}_4^-$ ) is added to a specific AA residue, to activate the molecule. By using this modification, the energy level of affected molecule is increased, promoting the subsequent biochemical reaction.

A certain number of proteins have been used as building blocks in membranes and other structures in the cell. The most important role of proteins is the enzyme function to catalyze the biochemical reactions. Other roles of proteins include signaling and sensing roles as well as they have the role in generating a motion.

One of the most important roles of the proteins is to catalyze the biochemical reactions that is to serve as the enzymes. At each particular time instance, there might be thousands of different biochemical reactions being in progress in the cell. Without the enzymes, the progress of these processes would be to slow due to high activation energy. The *activation energy* is the smallest energy required for a biochemical reaction to proceed, and this energy is typically used to break the bonds within the molecule. The number of molecules being active  $n_{E_a}$  (having the activation energy  $E_a$ ) follows the Gibbs–Boltzmann law as shown in section on

biological thermodynamics, namely,  $n_{E_a} = n_0 \exp(-E_a/RT)$ , where  $n_0$  is the total number of molecules. The larger the activation energy is, the smaller the number of active molecules is. With the help of enzyme, the activation energy gets reduced, and the rate of biochemical reaction gets increased. In other words, the rate constant of biochemical reaction, denoted as  $c$ , is related to the activation energy as follows:

$$c = C \exp(-E_a/RT), \quad (3.56)$$

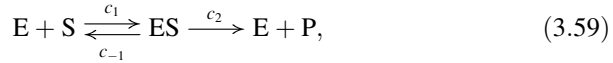
where  $C$  is the normalization constant. More accurate expression is given by

$$c = (kT/h) \exp(-\Delta G_{ES_a}/RT), \quad (3.57)$$

where  $k$  and  $h$  are Boltzmann and Plank constants, respectively, and  $\Delta G_{ES_a}$  is the activation energy of the ES-complex. Since the change in Gibbs free energy is related to the change in enthalpy and entropy by  $\Delta G = \Delta H - T\Delta S$ , we can also write

$$c = (kT/h) \exp(-\Delta H_{ES_a}/RT) \exp(\Delta S_{ES_a}/R). \quad (3.58)$$

Let us now return to the catalyzed biochemical reaction (3.54), which has been rewritten here to facilitate the explanations:



where we use  $c_i$  ( $i \in \{1, -1, 2\}$ ) to denote the rate constant of reaction  $i$ . As mentioned earlier, the enzyme  $E$  binds to the substrate  $S$  to create the enzyme–substrate complex  $ES$ . The rate constant of this reaction is  $c_1$ , while the constant rate of opposite reaction is  $c_{-1}$ . The creation of  $ES$ -complex is a spontaneous process, leading to the reduction of free energy. The bonds in  $ES$ -complex are weak ( $\leq 40$  kJ/mol), and the substrate molecule can easily dissociate from the complex. On the other hand, the interactions within the complex change the intramolecular forces of the substrate. The conformation of the substrate molecules get changed to become product molecules, which does not fit the complex very well anymore and  $EP$  complex dissociates, creating the product  $P$  and leaving enzyme  $E$  molecules unchanged. The rate constant of this reaction is denoted by  $c_2$ . In equilibrium, we can define the equilibrium constant of  $c_{-1}$ -process by  $K_S = [E][S]/[ES]$ . The total concentration of  $E$  and  $S$  at any time instance can be determined from initial conditions:

$$[E]_0 = [E] + [ES], \quad [S]_0 = [S] + [ES] + [P]. \quad (3.60)$$

Typically the initial concentration of substrate is much larger than concentration of enzyme ( $[S]_0 \gg [E]_0$ ), and we can write  $[S] \cong [S]_0$ , so that the equilibrium constant  $K_S$  can be written as

$$K_S \cong \frac{([E]_0 - [ES])[S]_0}{[ES]} = \left( \frac{[E]_0}{[ES]} - 1 \right) [S]_0. \quad (3.61)$$

By rearranging, we can express the concentration of the ES-complex by

$$[ES] \cong \frac{[E]_0}{1 + \frac{K_S}{[S]_0}} = \frac{[E]_0 [S]_0}{K_S + [S]_0}. \quad (3.62)$$

The rate of creation of product P would be now

$$v_0 = c_2[ES] = c_2 \frac{[E]_0 [S]_0}{K_S + [S]_0} = \frac{V[S]_0}{K_S + [S]_0}, \quad (3.63)$$

where  $V = c_2[E]_0$  and represents the maximum possible product rate, at saturation. Namely, when  $[S] \gg K_S$ ,  $v_0$  tends to  $V$ . On the other hand, when  $K_S \rightarrow [S]_0/2$ ,  $v_0 \rightarrow V/2$ , and  $K_S$  can be interpreted as the substrate concentration for which the product rate is half of the maximum possible. Equation (3.63) is known as *Michaelis–Menten* equation (law).

Enzyme reactions can be categorized as follows: (1) hydrolysis reactions in which chemical bonds get broken in the presence of water, (2) condensation reactions in which two molecules get covalently bonded, (3) group transfer in which group of atoms get transferred between two molecules, (4) isomerization in which group of atoms get transferred within the same molecule, and (5) redox reactions in which several protons get transferred from one molecule to another.

Let us now consider the *steady-state regime* in which the formation and dissociation of the complex ES is constant over time, i.e.,  $[ES] = \text{const}$  [7, 18]. The corresponding first derivative of  $[ES]$  would be zero then. To determine product rate in this regime, we start with time-evolution equations of concentration of S, E, ES, and P as follows:

$$\begin{aligned} \frac{d[E]}{dt} &= c_{-1}[ES] + c_2[ES] - c_1[E][S], & \frac{d[S]}{dt} &= c_{-1}[ES] - c_1[E][S], \\ \frac{d[ES]}{dt} &= c_1[E][S] - c_{-1}[ES] - c_2[ES], \\ \frac{d[P]}{dt} &= c_2[ES]. \end{aligned} \quad (3.64)$$

By setting  $d[ES]/dt = 0$ , and solving for  $c_2[ES]$ , we obtain the following equation for the rate of product:

$$v = \frac{d[P]}{dt} = c_2[ES] = c_1[E][S] - c_{-1}[ES] = -\frac{d[S]}{dt}. \quad (3.65)$$

In other words, the rate at which the concentration of product increases is equal to the rate at which the concentration of substrate decreases. By summing up  $d[E]/dt$

and  $d[ES]/dt$  rates from (3.64), we obtain zero. In other words,  $d([E] + [ES])/dt = 0$ , an indication that the total concentration of enzyme be in free state  $[E]$  or in ES-complex  $[ES]$  is constant, which we can denote as  $[E]_0$ . Since the enzyme just catalyzes the reaction but does not change, the total concentration of enzyme does not change. The concentration of enzyme in free state  $[E]$  can then be expressed as

$$[E] = [E]_0 - [ES]. \quad (3.66)$$

By substituting (3.66) into (3.65) and by solving for  $[ES]$ , we obtain

$$[ES] = \frac{[E]_0[S]}{\underbrace{\frac{c_2 + c_{-1}}{c_1} + [S]}_K} = \frac{[E]_0[S]}{K + [S]}. \quad (3.67)$$

Finally, since the rate of concentration of product  $v = d[P]/dt = c_2[ES]$ , we obtain

$$v = \frac{d[P]}{dt} = c_2[ES] = c_2 \frac{[E]_0[S]}{K + [S]} = \frac{V[S]}{K + [S]}, \quad V = c_2[E]_0, \quad (3.68)$$

which is clearly Michaelis–Menten equation. Therefore, in both equilibrium and steady-state regimes, the Michaelis–Menten law is applicable. By taking reciprocals of both sides of Michaelis–Menten equation, we obtain

$$\frac{1}{v} = \frac{K}{V} \frac{1}{[S]} + \frac{1}{V}, \quad (3.69)$$

which is a linear equation with slope  $K/V$  and the intercept on  $v^{-1}$ -axis is given by  $1/V$ . Equation (3.69) is sometimes called Lineweaver–Burk equation. Both functions, Michaelis–Menten and Lineweaver–Burk, have been shown in Fig. 3.8.

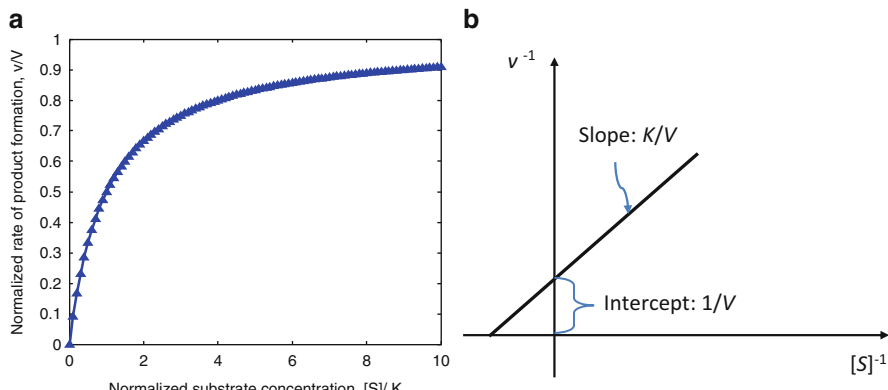
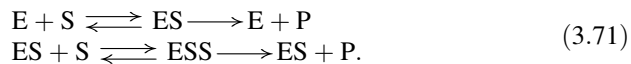


**Fig. 3.8** Enzyme kinetics: (a) Michaelis–Menten law and (b) Lineweaver–Burk representation

When an enzyme has multiple binding sites, the enzyme kinetics is more complicated. In particular, when the binding of multiple substrates is *cooperative*, the corresponding dependence is sigmoidal [19]:

$$v = \frac{d[P]}{dt} = \frac{V[S]^n}{K^n + [S]^n}, \quad (3.70)$$

and the corresponding dependence is known as *Hill function*. For  $[S] < K$ , the rate of product formation is slower than for Michaelis–Menten law. However, for  $[S] > K$ , the rate of product formation is much faster than in Michaelis–Menten law, as illustrated in Fig. 3.9. As an illustration, for  $n = 2$ , there will be two binding sites for the same substrate, and the enzyme reactions can be described as follows:



The enzyme can be in several forms: free enzyme with both binding sites unoccupied; the enzyme with one binding site occupied with substrate, denoted as ES; and the enzyme with both binding sites occupied with a substrate, denoted as ESS.

The rate of enzyme reaction can be changed by changing the efficiency of the enzyme mechanism or changing the concentration of enzyme. Since the product of the enzyme-catalyzed reaction resides in the active site, its presence in certain threshold concentration can inhibit the reaction, and such inhibition is known as the *product inhibition*. Various mechanisms of enzyme inhibition can be classified as (1) competitive inhibition, (2) uncompetitive (anticompetitive) inhibition, and (3) mixed inhibition.

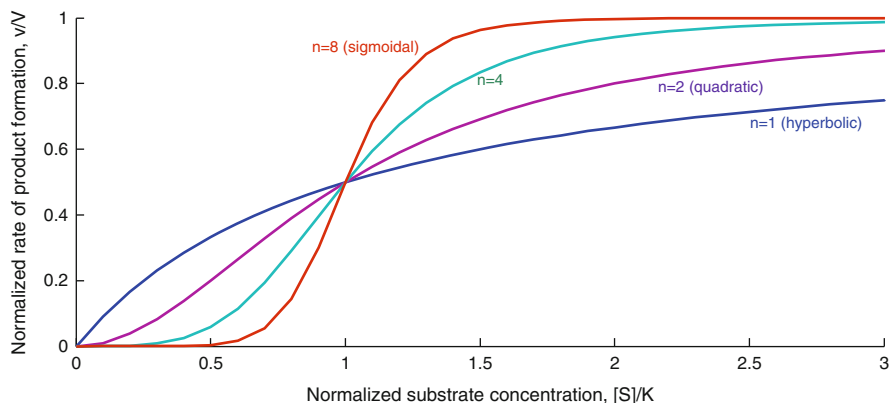
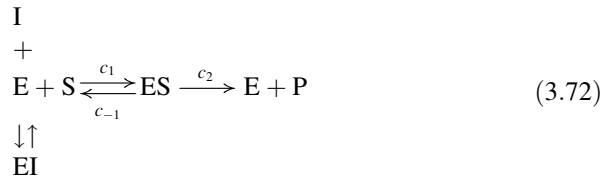


**Fig. 3.9** Product of formation rate versus substrate concentration for different number of binding sites  $n$

In *competitive inhibition*, the inhibitor I competes with the substrate for binding to the enzyme, and this reaction can be described as follows:



where the rate constants in inhibitor–enzyme reaction are the same as in enzyme–substrate reaction. In other words,  $\text{E} + \text{I} \xrightleftharpoons[c_{-1}]{c_1} \text{EI}$ . The corresponding rate equations relevant for the determination of the rate of product formation are

$$\frac{d[\text{I}]}{dt} = c_{-1}[\text{EI}] - c_1[\text{E}][\text{I}], \tag{3.73}$$

$$\frac{d[\text{ES}]}{dt} = c_1[\text{E}][\text{S}] - (c_{-1} + c_2)[\text{ES}], \tag{3.74}$$

$$\frac{d[\text{P}]}{dt} = c_2[\text{ES}]. \tag{3.75}$$

The total concentration of enzyme in either free or complex state must be constant, so that we can write

$$[\text{E}]_0 = [\text{E}] + [\text{ES}] + [\text{EI}]. \tag{3.76}$$

In steady-state regime, the formation and dissociation of the complex ES as well as inhibitor I must be constant over time, so that we can write  $d[\text{ES}]/dt = 0$  and  $d[\text{I}]/dt = 0$ . From (3.73), we therefore obtain

$$[\text{EI}] = \frac{c_1}{c_{-1}}[\text{E}][\text{I}], \tag{3.77}$$

while from (3.74)

$$c_1[\text{E}][\text{S}] = (c_2 + c_{-1})[\text{ES}]. \tag{3.78}$$

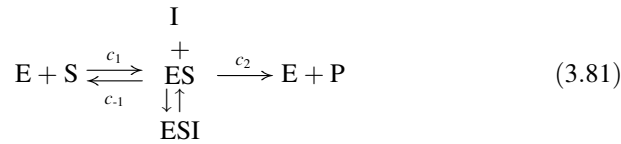
By substituting (3.77) into (3.76), solving for [E], and then substituting it in (3.78), we obtain

$$[\text{ES}] = \frac{[\text{E}]_0[\text{S}]}{(1 + c_1[\text{I}])\left(\frac{[\text{S}]}{1 + c_1[\text{I}]} + \frac{c_2 + c_{-1}}{c_1}\right)}, \quad c_1 = \frac{c_1}{c_{-1}}. \tag{3.79}$$

The rate of product formation is then

$$v = c_2[\text{ES}] = \frac{\overbrace{c_2[\text{E}]_0[\text{S}]}^V}{[\text{S}] + (1 + c_1[\text{I}])\underbrace{\frac{c_2 + c_{-1}}{c_1}}_K} = \frac{V[\text{S}]}{[\text{S}] + (1 + c_1[\text{I}])K}. \quad (3.80)$$

In *uncompetitive inhibition*, the inhibitor I binds to the ES-complex instead and corresponding reaction can be described as



The corresponding rate equations, relevant for the determination of the rate of product formation, are

$$\frac{d[\text{I}]}{dt} = c_{-1}[\text{ESI}] - c_1[\text{ES}][\text{I}], \quad (3.82)$$

$$\frac{d[\text{ES}]}{dt} = c_1[\text{E}][\text{S}] - (c_{-1} + c_2)[\text{ES}], \quad (3.83)$$

$$\frac{d[\text{P}]}{dt} = c_2[\text{ES}]. \quad (3.84)$$

The total concentration of enzyme in either free or complex state must be constant, so that we can write

$$[\text{E}]_0 = [\text{E}] + [\text{ES}] + [\text{ESI}]. \quad (3.85)$$

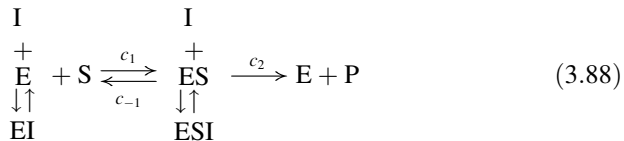
In steady-state regime, the formation and dissociation of the complex ES as well as inhibitor I must be constant over time, so that we can write  $d[\text{ES}]/dt = 0$  and  $d[\text{I}]/dt = 0$ . From (3.73), we therefore obtain

$$[\text{ESI}] = \underbrace{\frac{c_1}{c_{-1}}}_{C_{\text{II}}} [\text{ES}][\text{I}] = c_{\text{II}}[\text{ES}][\text{I}]. \quad (3.86)$$

By substituting (3.86) into (3.85), expressing  $[\text{E}]$ , and substituting it in (3.83), we obtain the following expression for the rate of product formation:

$$v = c_2[\text{ES}] = \frac{\overbrace{c_2[\text{E}]_0[\text{S}]}^V}{\underbrace{\frac{c_2 + c_{-1}}{c_1} + (1 + c_{\text{II}}[\text{I}])[\text{S}]}_K} = \frac{V[\text{S}]}{K + (1 + c_{\text{II}}[\text{I}])[\text{S}]} \quad (3.87)$$

In *mixed inhibition*, the inhibitor I binds to both free enzyme E- and ES-complex, so that the corresponding reaction can be written as



By generalizing the expressions (3.80) and (3.87), we obtain the rate of product formation in mixed inhibition as follows:

$$v = c_2[\text{ES}] = \frac{V[\text{S}]}{(1 + c_{\text{I}}[\text{I}])K + (1 + c_{\text{II}}[\text{I}])[\text{S}]} \quad (3.89)$$

In Lineweaver–Burk representation, the reciprocal of product rate can be written in the following form:

$$\frac{1}{v} = \frac{K}{V}(1 + c_{\text{I}}[\text{I}])\frac{1}{[\text{S}]} + \frac{1}{V}(1 + c_{\text{II}}[\text{I}]). \quad (3.90)$$

If we consider the concentration of inhibitor [I] as a parameter, the dependence of  $1/v$  versus  $1/[\text{S}]$  is still linear, with the slope  $(K/V)(1 + c_{\text{I}}[\text{I}])$  and  $v^{-1}$ -axis intercept being  $(1 + c_{\text{II}}[\text{I}])/V$ .

Many enzymes have multiple binding sites, and the product rate can be described using Hill kinetics (3.70) rather than Michaelis–Menten kinetics. In Hill kinetics, the binding of multiple substrates on an enzyme is *cooperative*. Namely, after binding a substrate molecule at one site, the other substrate molecule can bind at another site. When the interaction between two remote binding sites is indirect, in the sense that binding of one substrate molecule at one site can affect the binding activity at another site, we call this interaction allosteric, and an enzyme exhibiting this property is called *allosteric enzyme*. Allosteric enzymes typically catalyze the reactions at the beginning of a metabolic process or at branch points of metabolic pathways. The allosteric enzyme has two centers: catalytic (active) center and control (regulatory, allosteric) center. Catalytic activity of the allosteric enzyme can be modified by binding the regulator molecule also known as control center effector. The effector could be the final product or substrate. When effector binding at one site increases the binding activity at another site, we call it the *activator*. On the other hand, when the effector decreases the activity at catabolic center, it is called the inhibitor. The simplest form of regulation of a metabolic pathway is the

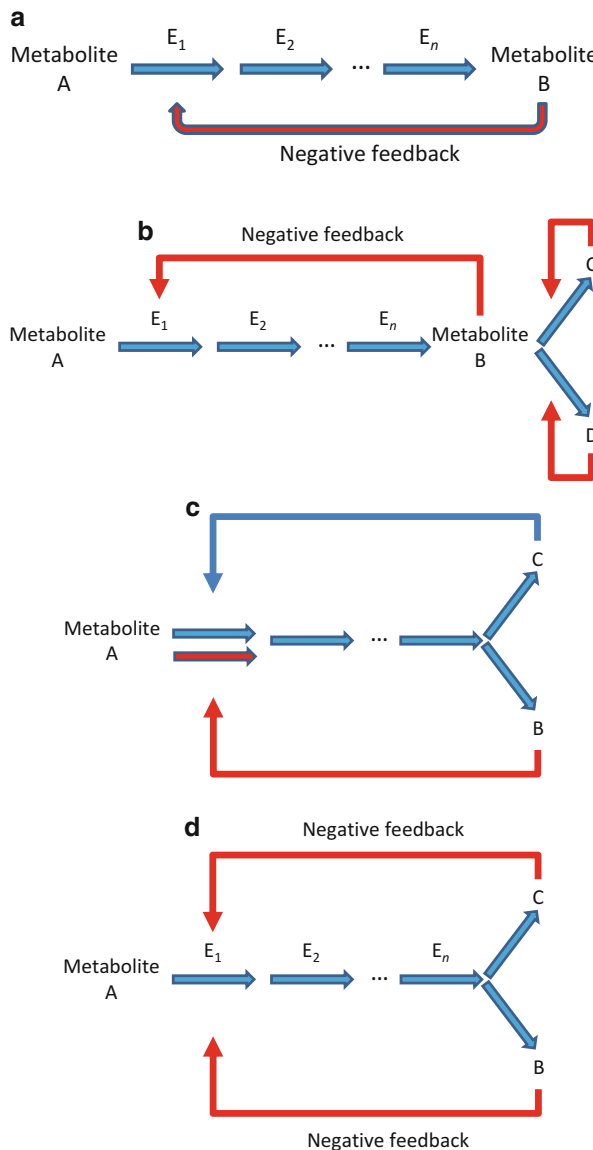


**Fig. 3.10** Feedback inhibition in a metabolic process: (a) simple feedback inhibition, (b) sequential inhibition, (c) multivalent feedback inhibition, and (d) cooperative feedback inhibition

inhibition by the final product (end-product inhibition), which is illustrated in Fig. 3.10. This control mechanism is known as *feedback inhibition* or *negative feedback control*. Several versions of negative feedback control have been listed including simple feedback inhibition (Fig. 3.10a), sequential inhibition (Fig. 3.10b), multivalent feedback inhibition (Fig. 3.10c), and cooperative feedback inhibition

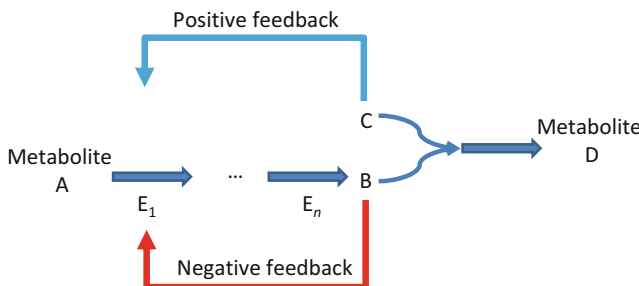


**Fig. 3.11** Feedback control in a branched metabolic pathway

(Fig. 3.10d). In simple feedback inhibition, as the concentration of the product B increases, it inhibits the activity of the first enzyme, and the rate of synthesis will decrease. For instance, the synthesis of L-isoleucine from L-threonine can be explained using this mechanism (for  $n = 4$ ). The enzyme  $E_1$  is an allosteric enzyme, and in syntheses of L-isoleucine, it is known as threonine deaminase. This enzyme gets exclusively inhibited by the isoleucine (as the final product). In sequential feedback inhibition (Fig. 3.10b), each end product controls the enzyme immediately after the branch point leading to that product. In multivalent inhibition (Fig. 3.10c), several products in a concert inhibit the activity of the first enzyme. If only one is present, it will not change the activity of the enzyme. In cooperative inhibition (Fig. 3.10d), the inhibition of activity of products is higher than it could be predicted from individual products at the same concentration.

In addition to negative feedback mechanisms shown in Fig. 3.10, we can also define cumulative inhibition and additive inhibition. In cumulative inhibition, the end products can separately inhibit the target enzyme. Finally, in additive inhibition, the end products bind to the target enzyme in a mutually exclusive manner, while the inhibition action is additive.

The feedback control in a branched metabolic pathway is more complicated as shown in Fig. 3.11. When  $[B] \gg [C]$ , it will inhibit the activity of enzyme  $E_1$ . On the other hand, when  $[C] \gg [B]$ , it will activate synthesis of product B.

### 3.2.2 Carbohydrates and Corresponding Polymers

The carbohydrates, as its name suggests, are composed of carbon, hydrogen, and oxygen atoms; and their generic chemical formula can be written as  $C_m(H_2O)_n$ , where  $m$  and  $n$  are positive integers. The carbohydrates provide the energy needed for biochemical processes to proceed. Some of carbohydrates have also been used as the building blocks in various organisms ranging from bacteria to plants. The carbohydrates are composed of basic monomer units known as *monosaccharides*. Three-carbon monosaccharide D-glyceraldehyde, already discussed in Fig. 3.2, often occurs as an intermediate product in various biochemical reactions involving the food processing.

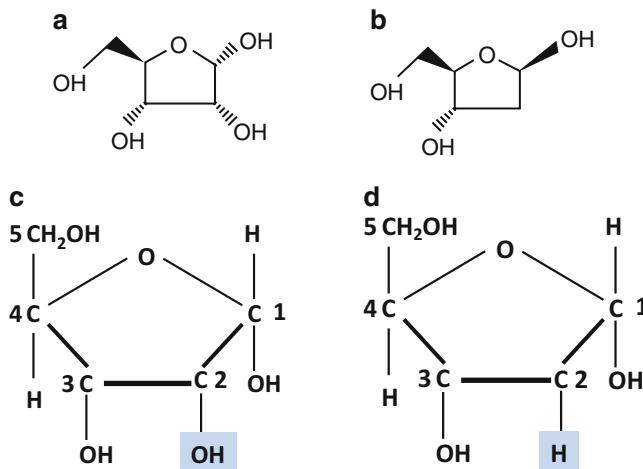


**Fig. 3.12** The five-carbon sugars participating in building of nucleic acids in KEGG notation: (a) D-ribose and (b) D-deoxyribose. The five-carbon sugars participating in building of nucleic acids in standard representation: (c) D-ribose and (d) D-deoxyribose

Five-carbon monosaccharides, such as D-ribose and D-deoxyribose, are basic nucleoside building blocks of nucleic acids. Namely, nucleic acids are polymers composed of monomers known as nucleotides. The nucleotides are further composed of three subunits: (1) 5-carbon (pentose) sugar molecule (ribose or deoxyribose), (2) a nitrogenous basis (pyrimidine or purine), and (3) a phosphate group. In deoxyribonucleic acid (DNA), the 5-carbon sugar D-deoxyribose is used, while in ribonucleic acid (RNA), the 5-carbon sugar D-ribose is used instead. The ribose is a pentose with chemical formula  $C_5H_{10}O_5$  and linear formula  $H-(C=O)-(CHOH)_4-H$ . The molecular formula for D-ribose is shown in Fig. 3.12a, in KEGG notation. On the other hand, the deoxyribose (or more precise 2-deoxyribose) is a pentose with linear formula  $H-(C=O)-(CH_2)-(CHOH)_3-H$ . As its name suggests, it is a deoxy sugar derived from the ribose by removing one oxygen atom, as shown in Fig. 3.12b. Clearly, ribose and deoxyribose differ by only one oxygen atom that is missing on the second carbon atom in deoxyribose observed clockwise from the oxygen atom. To see this better, in Fig. 3.12c, d, we provide the corresponding standard (Haworth) representation, in which the difference is clearly indicated. In the same figure, we provide the typical enumeration of carbon atoms.

Regarding the six-carbon sugars, the most common are D-glucose (grape sugar), D-mannose (fruit sugar, a common constituent of glycoproteins), and D-galactose (a constituent of lactose (milk sugar)). These six-carbon sugars are shown in Fig. 3.13. Two versions of glucose,  $\alpha$ - and  $\beta$ -versions, differ only in the placement of  $-H$  and  $-OH$  attached to carbon atom 1. Given the fact the four carbon atoms are chiral, there exist 16 stereoisomers.

Two monosaccharides can be involved in a condensation reaction to create a *disaccharide* molecule, as illustrated in Fig. 3.14 where the creation of maltose is shown through 1-4 glycosidic bond. The most abundant disaccharide sugars are

**Fig. 3.13** The common six-carbon sugars:  
**(a)** D-glucose, **(b)** D-mannose, and  
**(c)** D-galactose

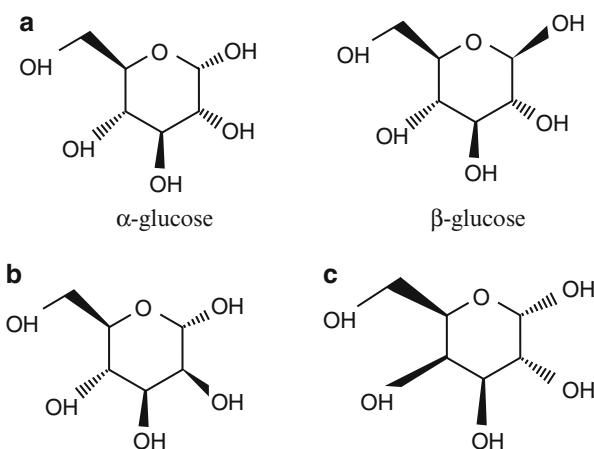
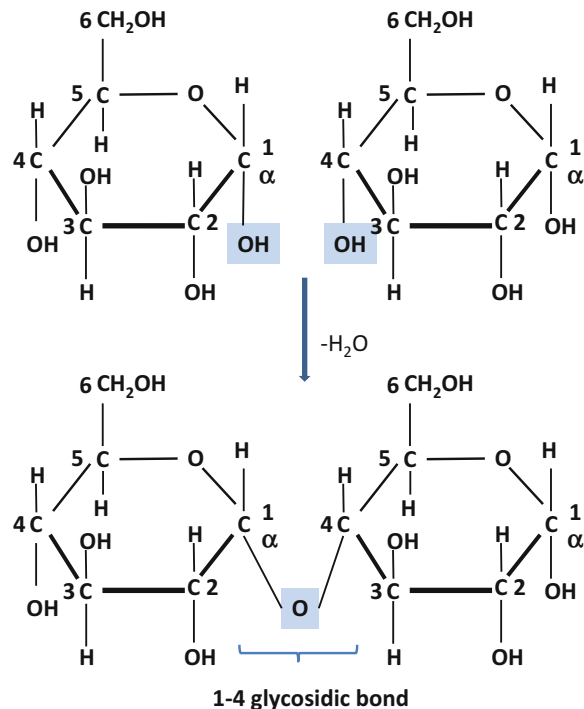


**Fig. 3.14** Illustration of condensation reaction for the formation of disaccharide maltose from two monosaccharides through 1-4 glycosidic bond



sucrose (table sugar) and lactose (milk sugar), whose structure is shown in Fig. 3.15. Trisaccharides and tetrasaccharides can be formed in a similar fashion from three and four monosaccharides, respectively, and are commonly referred to as *oligosaccharides*. The large chains of monosaccharide residues are known as *polysaccharides*.

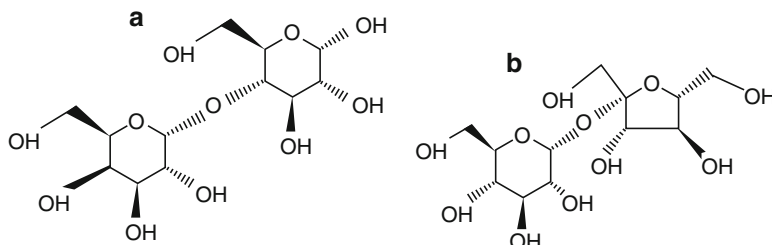


Fig. 3.15 The structure of lactose (a) and sucrose (b)

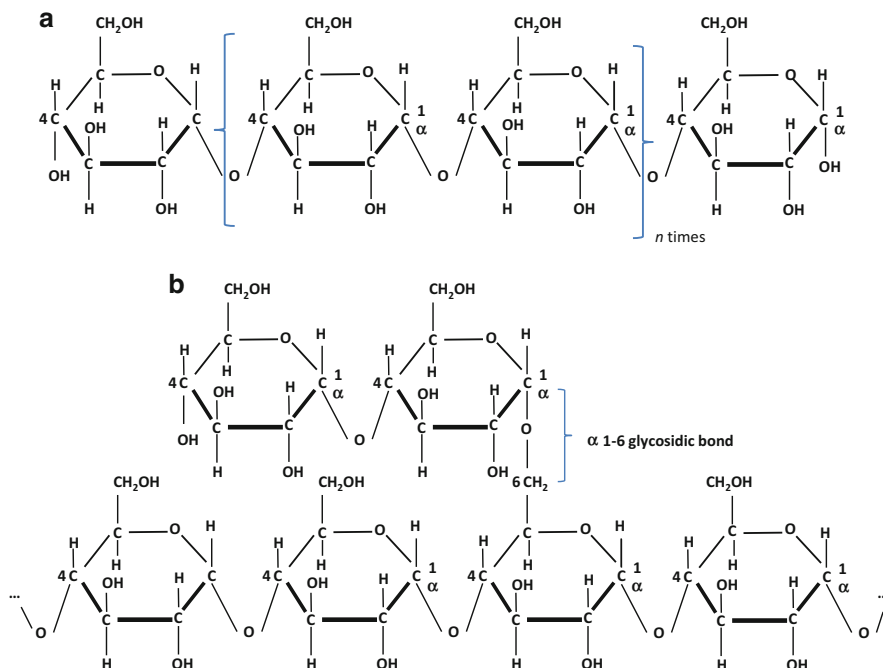
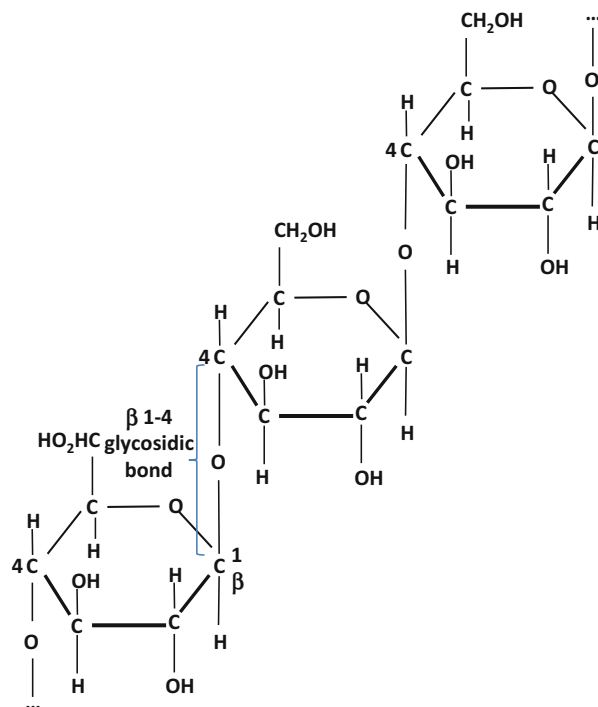


Fig. 3.16 The structure of amylose (a) and amylopectin (b)

The most abundant polysaccharides found in nature are *starch* and *cellulose*. In humans (and other animals), the most important polysaccharide is *glycogen*, which is also known as animal starch. The starch consists of two types of molecules: the amylose (20–25 %) and branched amylopectin (75–80 %). The glycogen is essentially a more branched version of the amylopectin. The structures of amylose and amylopectin are shown in Fig. 3.16. The amylose is composed of glucose monomers linked mainly by  $\alpha$  1–4 bonds, as shown in Fig. 3.16a. The amylopectin (see Fig. 3.16b) is highly branched polymer of glucose found in plants. The main chain of amylopectin is similar to amylose and represents the chain of glucose monomers linked by  $\alpha$  1–4 bonds. Branching in amylopectin takes place with  $\alpha$  1–6 bonds that occur in every

**Fig. 3.17** The structure of the cellulose



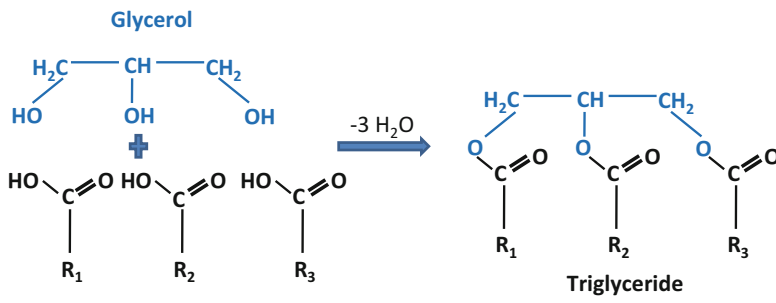
24–30 glucose units. In glycogen chain, on the other hand, one out of every 12 glucose monomers is connected to a second monomer in  $\alpha$  1–6 bond.

The cellulose is a polysaccharide that consists of a linear chain  $n$   $\beta$  1–4 linked glucose units, as illustrated in Fig. 3.17, where  $n$  is in the order of several hundred to many thousands. Another important polymer is chitin, which is an amino sugar, and forms long straight chains having structural roles, in particular in insects.

### 3.2.3 Lipids, Phospholipids, Membranes, and Vesicles

Lipids represent fatty acid esters of glycerol. Based on number of fatty acids linked to the glycerol, we can classify them into mono-, di-, and triglycerides. Triglycerides serve as the storage of biological energy. The process of formation of triglycerides is illustrated in Fig. 3.18. Namely, one molecule of glycerol and three fatty acid molecules are involved in a condensation reaction in which a triglyceride is formed and three molecules of water are released. Depending on whether triglycerides contain intrachain double bonds or not, they can be classified as either unsaturated or saturated, as shown in Fig. 3.19.

The existence of double bonds can be recognized by the presence of “kinks,” which prevent tight intermolecular packaging of triglycerides. This is the main reason



Three fatty acid molecules

**Fig. 3.18** The illustration of the formation of triglyceride through a condensation reaction of glycerol and three fatty acid molecules.  $R_i$  ( $i = 1, 2, 3$ ) denote fatty acid residues that are nonpolar and as such hydrophobic

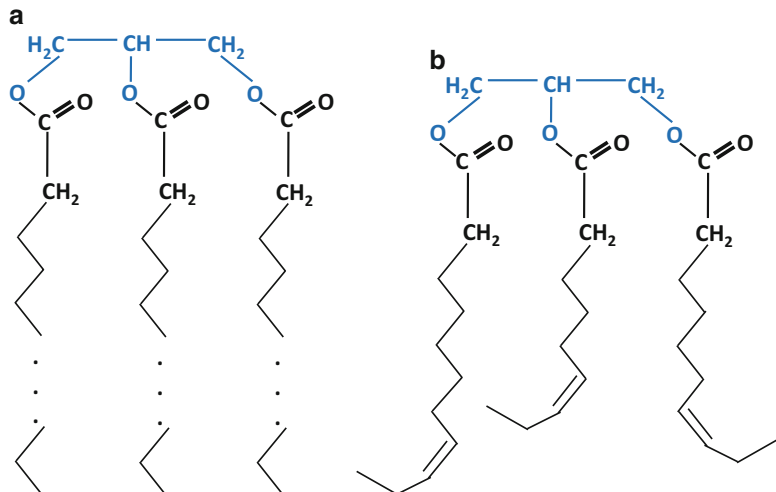
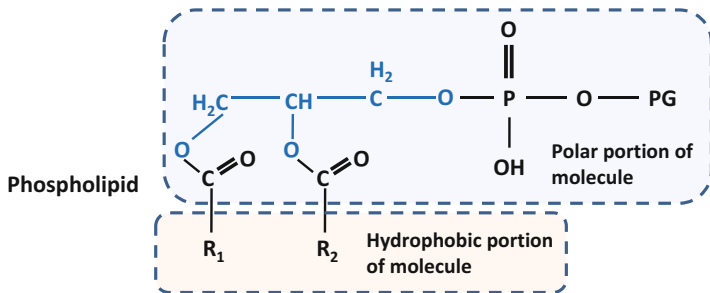


Fig. 3.19 Saturated (a) and unsaturated (b) triglycerides

why unsaturated triglycerides (as well as short triglycerides) are liquid at the room temperature. On the other hand, saturated triglycerides are solid at room temperature.

When two molecules of fatty acids and one molecule of phosphoric acid are involved in a condensation reaction with glycerol, the *phospholipid* gets formed, whose generic chemical formula is shown in Fig. 3.20. Clearly, the phospholipid molecule is bimodal, having both a hydrophobic ( $R_1$  and  $R_2$  groups) and hydrophilic (PG) parts of molecule, and in water phospholipid molecules get oriented toward  $H_2O$  molecules by polar groups. Such associations are known as *micelles* and are shown in Fig. 3.21a. In addition to spherical aggregations, the laminar bilayer *membranes* can also be formed as shown in Fig. 3.21b. The phospholipid bilayer of spheroidal shape is known as a *vesicle*, which is shown in Fig. 3.22a. An artificially prepared vesicle is commonly referred to as a *liposome*. The vesicles can contain different types of



**Fig. 3.20** Generic phospholipid structure. PG denotes the polar group originating from serine, choline, ethanolamine, or inositol.  $R_1$  and  $R_2$  denote hydrocarbon chains originating from fatty acids, which are nonpolar (and therefore hydrophobic)

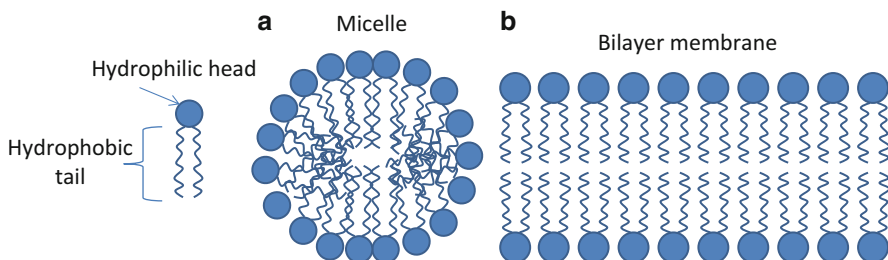


**Fig. 3.21** Associations of phospholipids in water: (a) micelle and (b) bilayer membrane

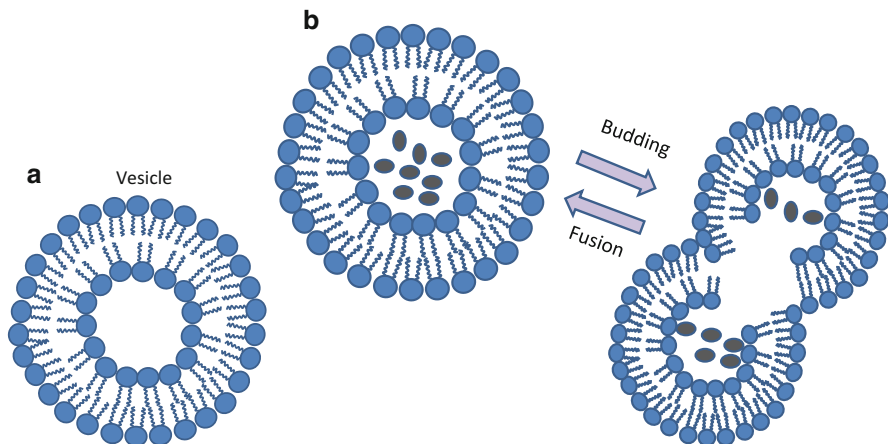


**Fig. 3.22** The vesicle made from phospholipid bilayer (a) and fusion/budding of the vesicles (b)

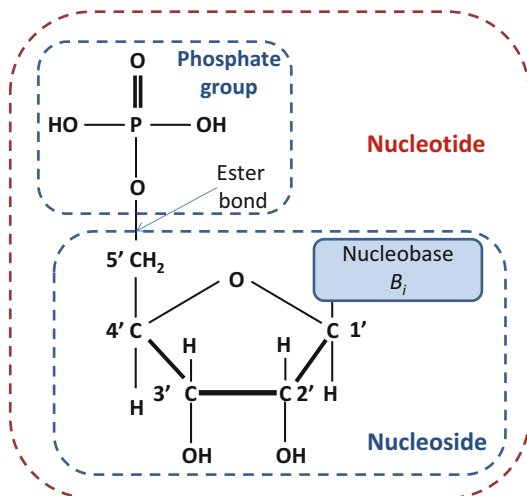
molecules and can localize the biochemical reactions. The vesicles very often function as molecule carriers. Namely, the vesicle encapsulates different molecules, and the motor proteins transport the vesicles to different locations within the cell. A vesicle can be embedded into channel proteins so that the molecules that are not permeable to

the phospholipid bilayer can be transported inside of the vesicle. Once the vesicle is transported to the desired location in the cell, it can be incorporated to the specific organelle through process known as *fusion*, which is illustrated in Fig. 3.22b. The opposite process of separating a set of molecules into two subsets of molecules is known as *budding*, and it is illustrated in Fig. 3.22b as well.

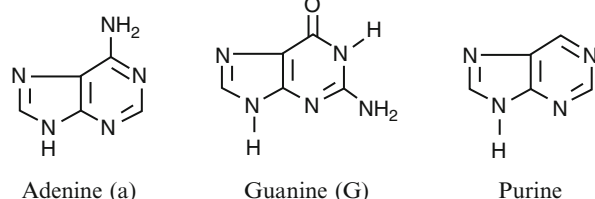
### 3.2.4 Nucleic Acids, Nucleosides, and Nucleotides

Nucleic acids are polymers of basic units (monomers) known as nucleotides [20, 21]. *Nucleotides*, as shown in Fig. 3.23, are composed of a nitrogenous base (nucleobase), a five-carbon sugar (pentose), and one phosphate group. The nucleobase together with a pentose is often called a *nucleoside*. In ribonucleic acid (RNA), the five-carbon sugar participating in its formation is D-ribose, as shown in Fig. 3.23. On the other hand, in deoxyribonucleic acid (DNA), the five-carbon sugar D-deoxyribose is used instead, as shown in Fig. 3.12b, in which OH-group of D-ribose linked to the 2' carbon atom is replaced by H-atom. In either RNA or DNA, four bases participate. Two of them, *adenine* (A) and *guanine* (G), are derived from heterocyclic amino base *purine* as shown in Fig. 3.24. In DNA, the

**Fig. 3.23** The generic structure of a nucleotide



**Fig. 3.24** Purine bases: adenine (A) and guanine (G)



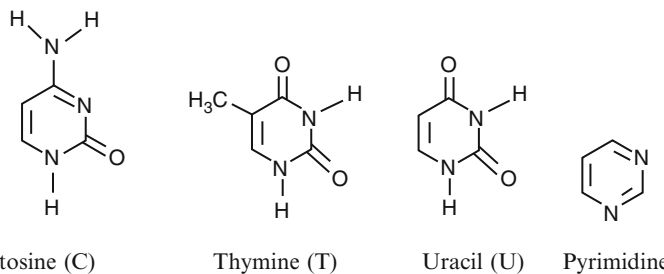


**Fig. 3.25** Pyrimidine bases: cytosine (C), thymine (T), and uracil (U)

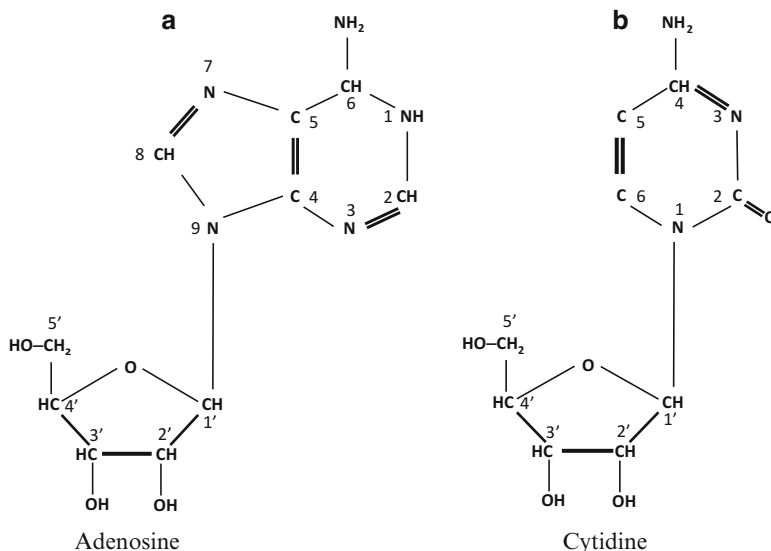


**Fig. 3.26** Illustrating the creation of nucleosides: (a) adenosine and (b) cytidine

bases derived from *pyrimidine*, namely, *cytosine* (C) and *thymine* (T), participate. On the other hand, in RNA pyrimidine base *uracil* (U) is used instead of thymine. All three pyrimidine bases, C, T, and U, are shown in Fig. 3.25.

The creation of nucleosides can be explained as follows. In adenosine, the bond between the nucleobase and the pentose is established between carbon atom 1' of pentose and nitrogen atom 9 of purine base adenine as illustrated in Fig. 3.26a. On the other hand, in cytidine, the bond between the nucleobase and the pentose of cytosine is established between carbon atom 1' of pentose and nitrogen atom 1 of pyrimidine base as illustrated in Fig. 3.26b. The creation of guanine, thymidine, and uridine can be explained in a similar fashion.

By establishing the ester bond between 5' carbon atom of adenosine and phosphorous acid, we obtain the adenosine monophosphate as shown in Fig. 3.27a. The ATP, shown in Fig. 3.27b, is created from AMP by establishing two phosphoric-anhydride

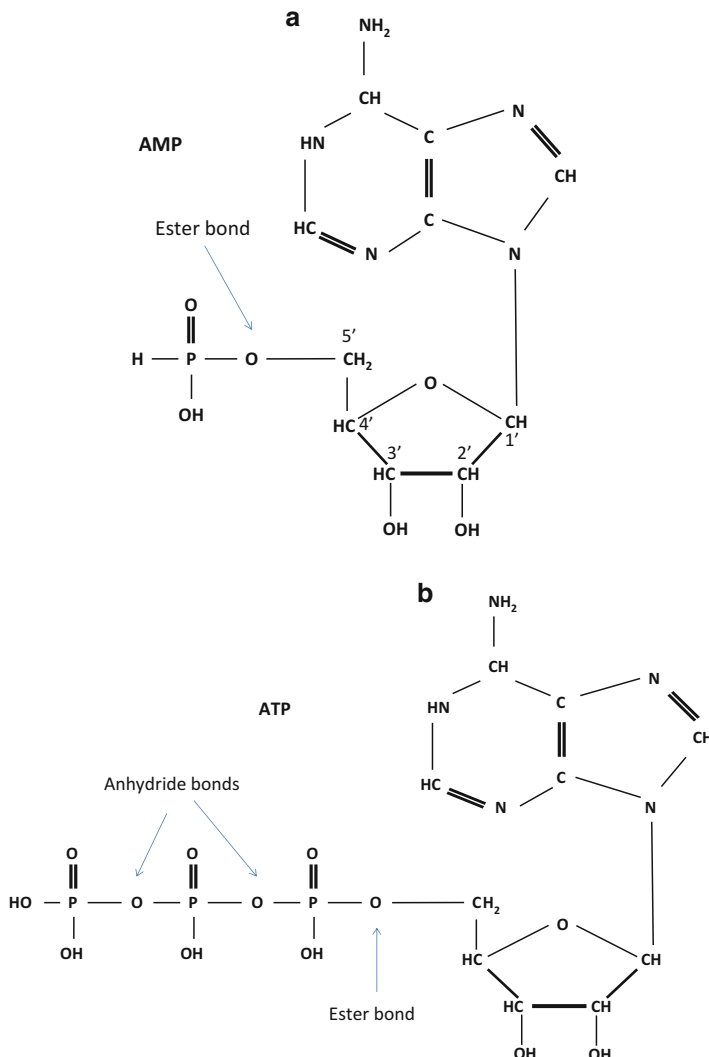
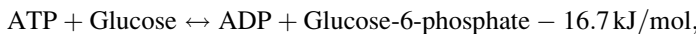


**Fig. 3.27** Illustrating the creation of nucleotides: (a) adenosine monophosphate (AMP) and (b) adenosine triphosphate (ATP)

bonds, which are well-known high-energy phosphate bonds. The energy released by hydrolysis of esters is  $\sim 12.6 \text{ kJ/mol}$ , while the energy released by hydrolysis of anhydride bonds in ATP is  $\sim 31.4 \text{ kJ/mol}$ . This is the reason why ATP, and other nucleotide triphosphates, has a central role in metabolic reactions. As an illustration, the glucose is an inert molecule. However, when coupled with ATP, it undergoes the following reaction:



in which about  $16.7 \text{ kJ/mol}$  of energy is released.

The creation of other nucleotides, such as GMP, TMP, and CMP, can be explained in fashion similar to that from Fig. 3.27a.

The primary structure of nucleic acids can be explained with the help of Fig. 3.28. The hydroxyl group of the 3'-rd carbon atom in deoxyribose interacts with the phosphorous group of the next nucleotide, and two nucleotides get interlinked by an ester bond. The phosphorous group creates the second ester

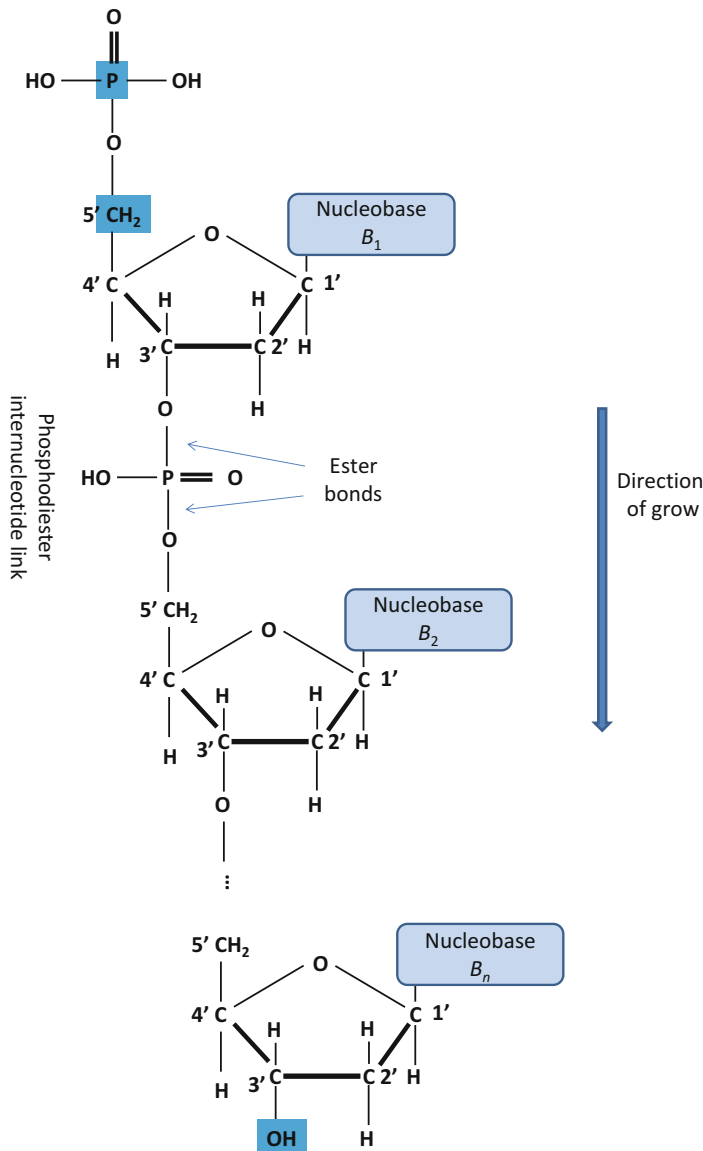


**Fig. 3.28** Illustrating the primary structure (the backbone) of nucleic acids.  $B_i \in \{A, G, C, T\}$

bond with the 5' carbon atom of the next nucleotide. Therefore, two nucleotides get interlinked by phosphodiester internucleotide link. The process of interlinking continues until the last (the  $n$ th) nucleotide gets interlinked. Clearly, the hydroxyl group connected to the  $n$ th nucleotide's 3' carbon atom is not connected to the next nucleotide, and this end is known as 3' end. On the other hand, the phosphorous group connected to 5' carbon atom of the first nucleotide is not connected to any other nucleotide, and this end is known as 5' end. This two ends give the sense of direction to the nucleic acid. By convention the sequence of nucleobases that compose the nucleic acid is listed from 5' end to 3' end.

### 3.3 Cellular Genetics

#### 3.3.1 DNA Structure and DNA Replication Process

In cells two DNA molecules, commonly referred to as *DNA strands*, typically ensemble together to form a double-helix structure, which is made up by applying the *base-pairing rules* [20–33]. In base-pairing rules [20, 21], T and A make one base pair, while C and G make another base pair. The base pairs are stabilized by hydrogen bonds. There are two hydrogen bonds in T=A pair and three hydrogen bonds in C≡G pair, as illustrated in Fig. 3.29.

Two DNA strands are aligned in antiparallel fashion, with one strand running in the 5' to 3' direction and the other strand in 3' to 5' direction (see Fig. 3.30). We say that two strands are *complementary* when DNA bases in one strand form the base pairs (according to the base-pairing rule) with nucleobases from the other strand, which is illustrated in Fig. 3.30.

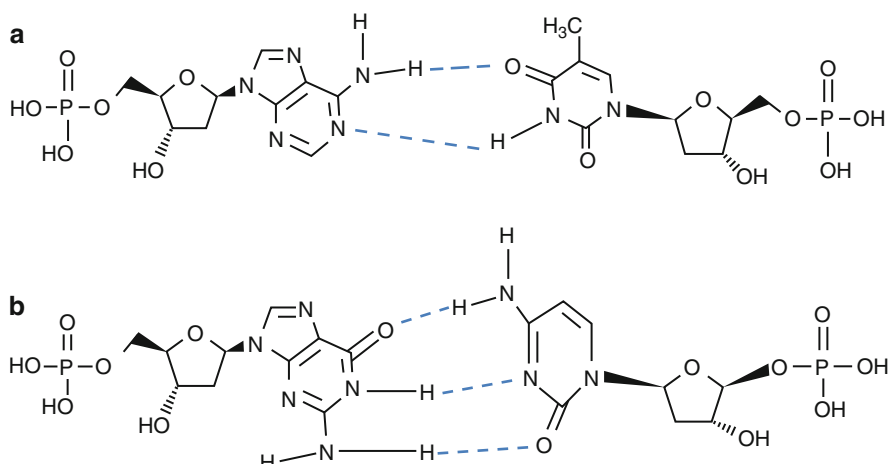


**Fig. 3.29** DNA base-pair formation through H-bonds: (a) A-T pair and (b) G-C pair

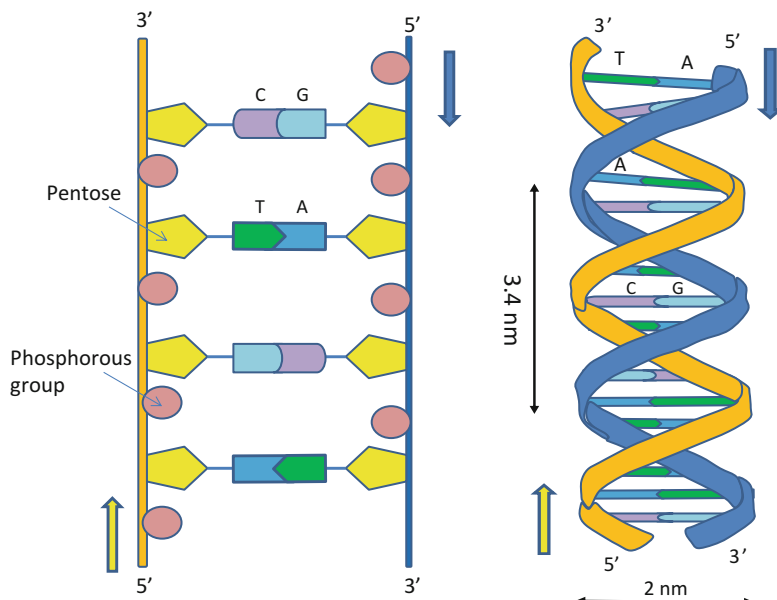
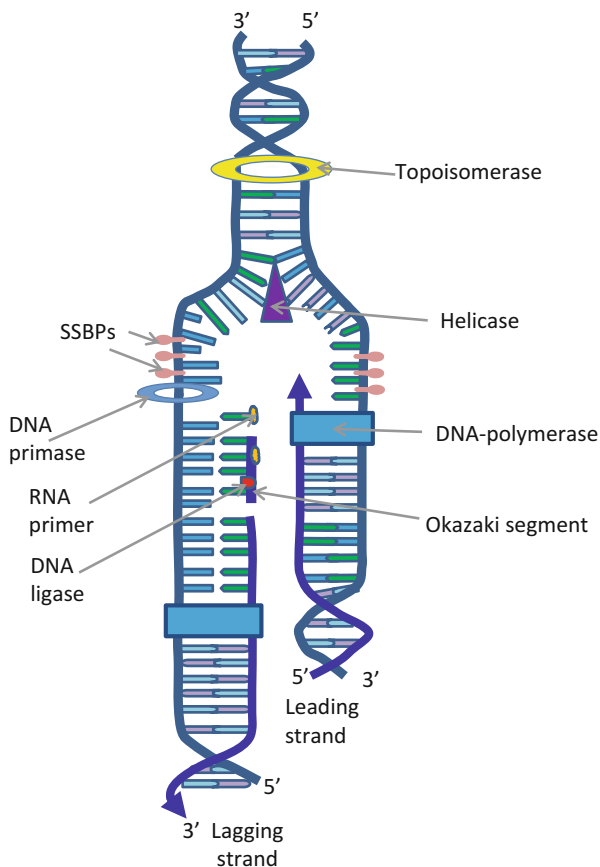


**Fig. 3.30** Illustrating the structure of DNA: (left) coupling of two DNA strands and base-pairing rules and (right) DNA double-helix structure

The diameter of double-helix structure is  $\sim 2$  nm, while the period of helix turn is  $\sim 3.4$  nm and contains 10 base pairs. This model of DNA is known as B-form and dominates under low ionic strength and high degree of hydration. On the other hand, A-form dominates under low hydration condition. In A-form the number of residues per helix turn is 11. Both A- and B-forms have the right direction of helical rotation. The regions of the helix dominated by CG base pairs can exist in so-called Z-form, containing 12 base pairs per helix turn and having left direction of helical rotation.

In the cell division, during the replication process, two DNA strands get separated first, and this separation process is commonly referred to as *denaturation*. This process occurs as the result of action of ATP-dependent helicases, which unwinds the DNA double-helix. The denaturation can also occur due to heating process, when high temperature fluctuations break up the weak hydrogen bonds. The point when 50 % of the DNA molecule exists as the single strand is known as the melting temperature. When thermally melted DNA is cooled-down, the complementary strands will create the base pairs in proper order, and the process is known as annealing, hybridization, or renaturation. The hybridization process can be messed up if the cooling is performed too fast.

**Fig. 3.31** Illustrating the DNA replication process (the arrows indicate the direction of growth for leading and lagging strands, in both cases 5' to 3' direction). *Helicase* enzyme used to separate strands of a DNA double-helix, *DNA ligase* facilitates the joining of DNA strands together by catalyzing the formation of a phosphodiester bond, *DNA primase* enzyme involved in the replication of DNA, *Primer* a strand of nucleic acid serving as a starting point in DNA synthesis, *Topoisomerase* enzymes that regulate the overwinding/underwinding of DNA to prevent the halting of the DNA replication process because of tension, *SSBPs* single-strand binding proteins prevent reannealing (recreation of double-helix) and stabilize the strands (keep them open until replication is completed)



The *DNA replication process* [12–17] is illustrated in Fig. 3.31. The two strands of double-helix get separated first. In the second phase, each strand's complementary DNA sequence is recreated with the help of DNA polymerase. Since DNA polymerases can only extend a DNA strand in a 5' to 3' direction, as shown in Fig. 3.28, different mechanisms are adopted to replicate the antiparallel strands of the double-helix. Phosphodiester links get formed between 3' and 5' carbon atoms of corresponding nucleotides with the help of DNA polymerase. For the leading strand, the new nucleotides get added as the DNA helix opens up in 5' to 3' direction continuously. However, for the lagging strand, the starting point is 3' end, and nucleotides cannot be added in 3' to 5' direction. Instead, we need to wait for DNA helix to open up for 100–200 nucleotides and start creating the complement daughter strand in 5' to 3' direction. Clearly, the lagging strand can only be synthesized in segments of 100–200 nucleotides, and these segments are known

as Okazaki fragments. DNA polymerase will later on perform the splicing of different Okazaki fragments together. During the replication process, the nucleobases of the old strand dictate which nucleobases will appear on the newly synthesized strand. Therefore, in every double-helix, one DNA strand originates from the parental chain and the other one is a newly replicated strand.

### 3.3.2 *Genetic Code, RNA Molecules, Transcription, and Translation*

Like DNA, RNA molecule is a chain of four different types of nucleotides. Typically, RNA molecules are single-stranded chains of nucleotides. The base-pairing rules still apply, but with one difference compared to DNA molecules. Instead of thymine (T) used in DNA, in RNA, the nucleobase uracil (U) is used. Therefore, A–U is the first base pair, and G–C is the second base pair. Because RNA molecule is single stranded, it is possible that RNA molecule folds to create local loops and hairpins. RNA molecules play a key role in protein synthesis. DNA and RNA actually control all biochemical processes in the cell by regulating the gene expression. A *gene* is a unit of genetic information stored in the sequence of nucleotides in DNA, containing the information about either a single peptide or an RNA molecule synthesis. The whole genetic material of an organism is called the *genome*. The genome includes both the genes and noncoding sequences in DNA/RNA. The genome of eukaryotic cells is composed of linear DNA molecules, each forming a chromosome with corresponding proteins. The genome in human diploid cells is composed of DNA molecules, making up 46 chromosomes. Chromosome represents an efficient way to store the genes. In human body, there exist ~25,000 chromosomes. The length of genes varies from 1000 base pairs (bp) to several hundred thousand bp. The gene expression is described by the so-called central dogma of molecular biology [24–33], composed of two processes: (1) *transcription* by which the DNA content is copied into corresponding *messenger RNA* (mRNA) molecule and (2) *translation* by which a peptide is synthesized using mRNA molecule as a template. A key role in translation process is performed by *transfer RNA* (tRNA) molecules, carrying the corresponding amino acids for protein synthesis. The process of translation is catalyzed by a large RNA–protein complex known as the *ribosome*, containing two catalytic sites to promote the biochemical reactions. The RNA molecules participating in creation of ribosome are known as *ribosomal RNA* (rRNA) molecules. The ribosomes, therefore, can be interpreted as “factories” for protein synthesis. The ribosome is typically 15–20 nm in size and is composed of rRNA and proteins. Each ribosome has three binding sites for tRNA: (1) *P (peptidyl) site* that holds tRNA carrying the growing polypeptide chain, (2) *A (aminoacyl) site* that holds the tRNA molecule carrying the amino acid to be attached to the polypeptide chain, and (3) *E (exit) site* is where discharged tRNA leaves the ribosome.

The nucleotide sequence of mRNA determines the sequence of amino acid residues of a polypeptide, whose synthesis it encodes. The corresponding mapping rule that maps a sequence of nucleotides in mRNA into a sequence of amino residues in corresponding polypeptide is called the *genetic code*. In genetic code, a sequence of three nucleotides, known as *codon*, encodes a single amino acid residue. Since the base of genetic code is 4, it is possible to encode up to  $4^3 = 64$  amino acid residues. Out of 64 codons, 61 are used to encode different amino acid residues, while the remaining three represent the STOP codons and these are UAA, UAG, and UGA. The START codon is AUG and encodes the methionine (Met, M). Therefore, every polypeptide starts with amino acid methionine. The genetic code is summarized in Table 3.1. Tryptophan (Trp, W), in addition to Met, is represented by single codon UGG. Other amino acids are represented by multiple codons. For instance, arginine (Arg, R) is represented by even six codons: CGU, CGC, CGA, CGG, AGA, and AGG. Leucine (Leu, L) and serine (Ser, S) are also represented by six codons each. Valine (Val, V), proline (Pro, P), threonine (Thr, T), alanine (Ala, A), and glycine (Gly, G) are represented with four codons each. Isoleucine (Ile, I) is represented by three codons and remaining amino acids by two codons each. The different codons representing the same amino acid are said to be synonymous. It is evident from Table 3.1 that in most of the codons, the first two characters specify the encoded amino acid. For instance, the first two characters CG specify the amino acid Arg. Further, if the third character is either U or C, while the first two characters are the same in both codons, then the corresponding codons represent the same amino acid. For instance, codons AGC and AGU represent amino acid Ser. Finally, it can be noticed that amino acids represented with codons having either U or C on the second nucleotide tend to be hydrophobic. Because in genetic codes the same amino acid can be represented by multiple codons, we say that genetic code is *degenerate*.

**Table 3.1** The standard genetic code

		The second nucleotide												The third nucleotide
		U		C		A		G		C		A		
The first nucleotide	U	UUU	Phe, F	UCU	Ser, S	UAU	Tyr, Y	UGU	Cys, C	U				
	U	UUC	Phe, F	UCC	Ser, S	UAC	Tyr, Y	UGC	Cys, C	C				
	U	UUA	Leu, L	UCA	Ser, S	UAA	STOP	UGA	STOP	A				
	U	UUG	Leu, L	UCG	Ser, S	UAG	STOP	UGG	Trp, W	G				
	C	CUU	Leu, L	CCU	Pro, P	CAU	His, H	CGU	Arg, R	U				
The first nucleotide	C	CUC	Leu, L	CCC	Pro, P	CAC	His, H	CGC	Arg, R	C				
	C	CUA	Leu, L	CCA	Pro, P	CAA	Gln, Q	CGA	Arg, R	A				
	C	CUG	Leu, L	CCG	Pro, P	CAG	Gln, Q	CGG	Arg, R	G				
	A	AUU	Ile, I	ACU	Thr, T	AAU	Asn, N	AGU	Ser, S	U				
The first nucleotide	A	AUC	Ile, I	ACC	Thr, T	AAC	Asn, N	AGC	Ser, S	C				
	A	AUA	Ile, I	ACA	Thr, T	AAA	Lys, K	AGA	Arg, R	A				
	A	AUG	Met, M, START	ACG	Thr, T	AAG	Lys, K	AGG	Arg, R	G				
	G	GUU	Val, V	GCU	Ala, A	GAU	Asp, D	GGU	Gly, G	U				
The first nucleotide	G	GUC	Val, V	GCC	Ala, A	GAC	Asp, D	GGC	Gly, G	C				
	G	GU	Val, V	GCA	Ala, A	GAA	Glu, E	GGA	Gly, G	A				
	G	GUG	Val, V	GCG	Ala, A	GAG	Glu, E	GGG	Gly, G	G				

There exist some organisms with slightly different genetic code that is provided in Table 3.1, which is known as a *standard* genetic code.

The process of *transcription* is catalyzed by RNA polymerase, which binds to the promoter region of the gene, and moves in 3' to 5' direction along template strand of DNA as illustrated in Fig. 3.32. RNA polymerase then starts reading the DNA template strand one nucleotide at the time. By applying the base-pairing rules, RNA polymerase takes a corresponding complementary nucleoside triphosphate, namely, ATP, UTP, GTP, and CTP, from the environment and produces corresponding nucleotide to be concatenated to the existing mRNA chain. Therefore, the nucleotides have been added to the 3' end of the growing mRNA molecule. The process of adding one nucleotide at the time continues until terminator point (STOP codon) is reached. In Fig. 3.32, we use  $B_i$  to denote the  $i$ th base ( $i = 1, 2, \dots, n$ ),  $B_i \in \{T, A, C, G\}$ , of the template DNA strand, and  $\bar{B}_i$  to denote the corresponding complement base. Notice that complement base for A in mRNA is U, not T. As an illustration of transcription process (from DNA to mRNA) and translation process (from mRNA to polypeptide), we provide the following example below:

DNA: 3' TAC CCC TTT CAA ... ATT 5'

mRNA: 5' AUG GGG UUU GUU ... UAA 5'

Encoded amino acids: Met Gly Phe Val ... STOP

The polypeptide synthesis in ribosome starts from the 5' end of mRNA and proceeds from the N-terminus of the polypeptide to the C-terminus, as illustrated in Fig. 3.33.

A specific type of tRNA binds on the start codon of mRNA (AUG) by matching anticodon–codon pair. Another type of tRNA binds to the next codon based on anticodon–codon pair. The ribosome then catalyzes the biochemical reaction to “splice” the current amino acid (AA) to the previous AA by establishing the peptide bond. The previous tRNA gets discharged and leaves the ribosome through E site, while we move one codon into 3' direction (of mRNA). The translation process continues, until the stop codon is found in mRNA (UAA, UAG, or UGA).

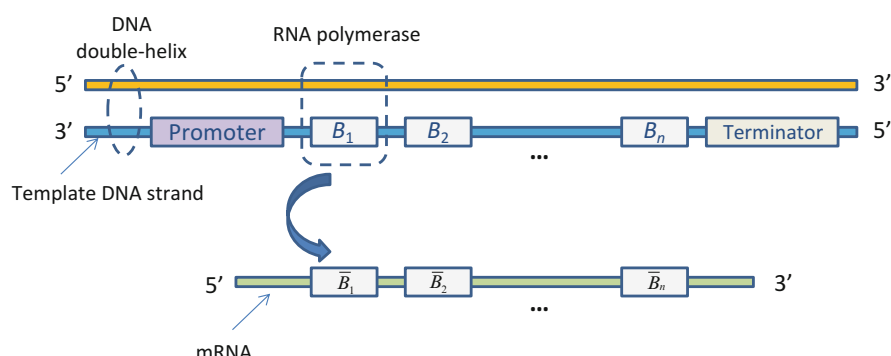


**Fig. 3.32** Illustrating the mRNA transcription process

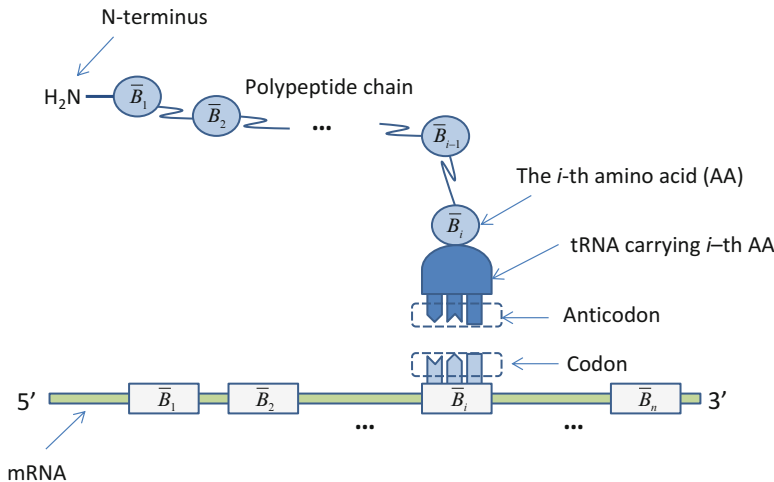
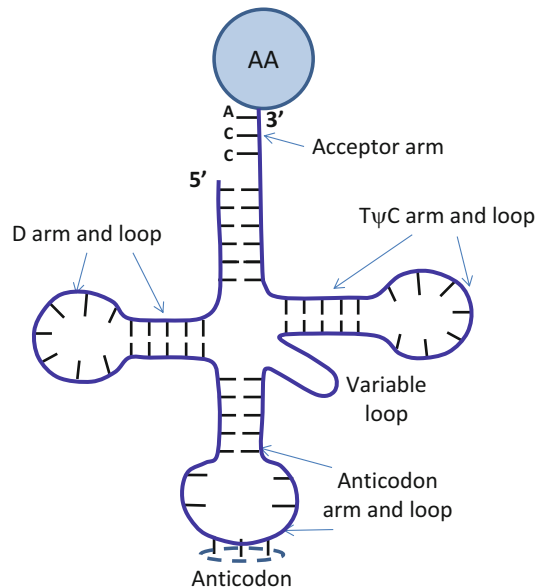


**Fig. 3.33** Illustrating the translation process

**Fig. 3.34** The secondary structure of tRNA. AA amino acid



Clearly, the main role of tRNA is to transport AA from cytoplasm amino acid “pool” to a ribosome. The structure of tRNA is illustrated in Fig. 3.34. The primary structure is defined by a sequence of nucleotides. The secondary structure is typically described by *cloverleaf structure* as shown in Fig. 3.34. The tertiary structure is derived from secondary by coaxial stacking of the helices into three-dimensional L-shape. The RNA molecule end with free OH-group represents the

acceptor arm end where a particular amino acid is bound. The anticodon arm has a three-nucleobase sequence binding to the complementary codon of mRNA, based on base-pairing rule. The D arm contains dihydrouracil and several purine bases. This is the loop where a particular enzyme can bind. The T $\psi$ C arm contains thymine–pseudouracil–cytosine (T $\psi$ C) triplet and represents the loop by which tRNA binds on ribosome. Each charged tRNA is matched with corresponding AA long before it reaches the ribosome. This matching is performed by the set of 20 aminoacyl-tRNA synthetases, which ensure that each tRNA carries the correct AA. (Some bacteria species might have less than 20 aminoacyl-tRNA synthetases indicating that the matching process could be more complicated than that described here.) The primary structure of tRNA contains  $\sim$ 10 bases that cannot be found in other RNA molecules, including thymine. These special bases often contain CH<sub>3</sub>-groups, which prevents tRNA from getting involved in pairing with other nucleobases.

### 3.3.3 Gene Anatomy and Regulation of Gene Expression

As indicated in previous section, the *gene* represents a unit of genetic information stored in the sequence of nucleotides in DNA, containing the information about either a single peptide or an RNA molecule synthesis. In other words, the gene is a sequence of nucleotides (nucleobases) containing the information for a single functional polypeptide synthesis. The genes can be found on both DNA strands. The gene in prokaryotes is different from that in eukaryotes. A typical prokaryotic gene is shown in Fig. 3.35a. Clearly, the prokaryotic DNA contains the continuous coding regions. The prokaryotic genes are clustered into subunits known as *operons*. Each operon consists of promoter, operator, coding regions, stop codon,

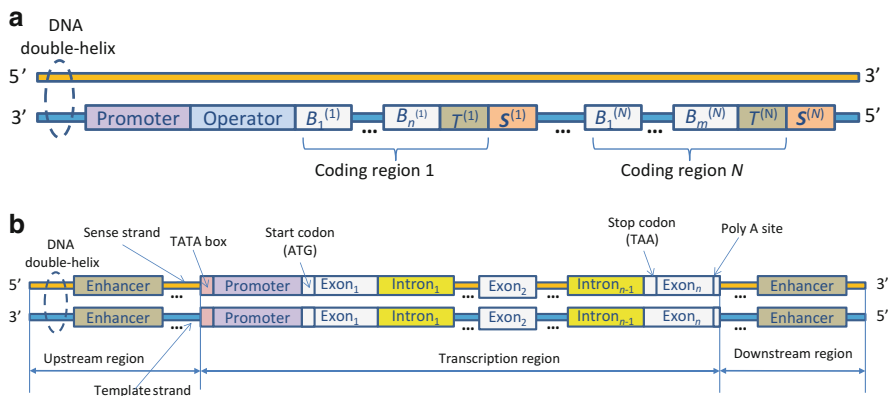


**Fig. 3.35** The gene anatomy: (a) a typical prokaryotic gene and (b) a typical eukaryotic gene. *T* terminator (stop codon), *S* spacing sequence

separators (short spacing regions between two neighboring coding regions), and control (regulatory) sequences (not shown in Fig. 3.35a).

Eukaryotic genes are more complicated as shown in Fig. 3.35b. The coding regions called *exons* are separated by noncoding segments called *introns*. The sense strand runs in 5' to 3' direction and contains the same sequences of nucleobases as in mRNA. The template strand runs in opposite direction and contains the complementary sequence, which will be used in transcription stage. The regulatory segment closest to the first exon is called *promoter*, while remote regulatory segments in either upstream or downstream directions are called *enhancers*. The transcription region starts with the start codon (ATG) corresponding to the mRNA starting codon (AUG). A common promoter sequence is known as TATA box, which corresponds to the sequence 5'-TATAAA, and it is located about 30 bp upstream of the start codon. Exons are typically 300 bp long and are uninterrupted by stop codons. On the other hand, the introns are not uninterrupted sequences of codons, and the corresponding nucleotides in primary RNA sequences are removed out before translation can take place. Interestingly enough, almost the entire eukaryotic gene is composed of the noncoding sequence (it could be even 98 %). The enhancer in the upstream direction (less frequently in downstream direction) contains sequences that control the initiation rate of transcription process. The transcription region typically ends after the stop codon, downstream of the Poly A site. It is believed that the role of Poly A site is to facilitate the transport of mRNA from nucleus to the cytoplasm. Namely, the transcribed Poly A sequence denotes the location at which the primary mRNA is cleaved.

Each eukaryotic gene can be classified into three categories depending which, out of three RNA polymerases, has been used. The genes for RNAs are transcribed by RNA polymerases I and II. On the other hand, the genes for proteins are transcribed by RNA polymerase II (pol II).

In prokaryotic cells, there exist three types of regulatory protein (enzyme) molecules affecting the expression of operons: (1) repressors, (2) activators, and (3) inducers. *Repressors* are either DNA- or RNA-binding proteins that inhibit the expression of a gene (or multiple genes) by binding to the operator region. A DNA-binding repressor prevents the attachment of RNA polymerase to the promoter, thus preventing transcription of the genes into messenger mRNA. On the other hand, the RNA-binding repressor binds to the mRNA and prevents translation of the mRNA into protein. The process of blocking the gene expression by DNA-binding protein is called *repression*. *Activator* is a protein that increases gene transcription rate. Typically, activators are DNA-binding proteins that bind to either enhancers or promoter-proximal elements. Finally, *inducer* is a particular molecule that starts gene expression and can bind to either repressor or activator. The process of facilitating the gene expression by small inducer molecules is called *induction*.

Now we describe the *end-product repression*, described by Jacob and Monod [22], and it is illustrated in Fig. 3.36. The regulator gene expresses the synthesis of inactive repressor. RNA polymerase binds on promoter and synthesis of the end product proceeds, as shown in Fig. 3.36a. Once the end product is abundant, one of

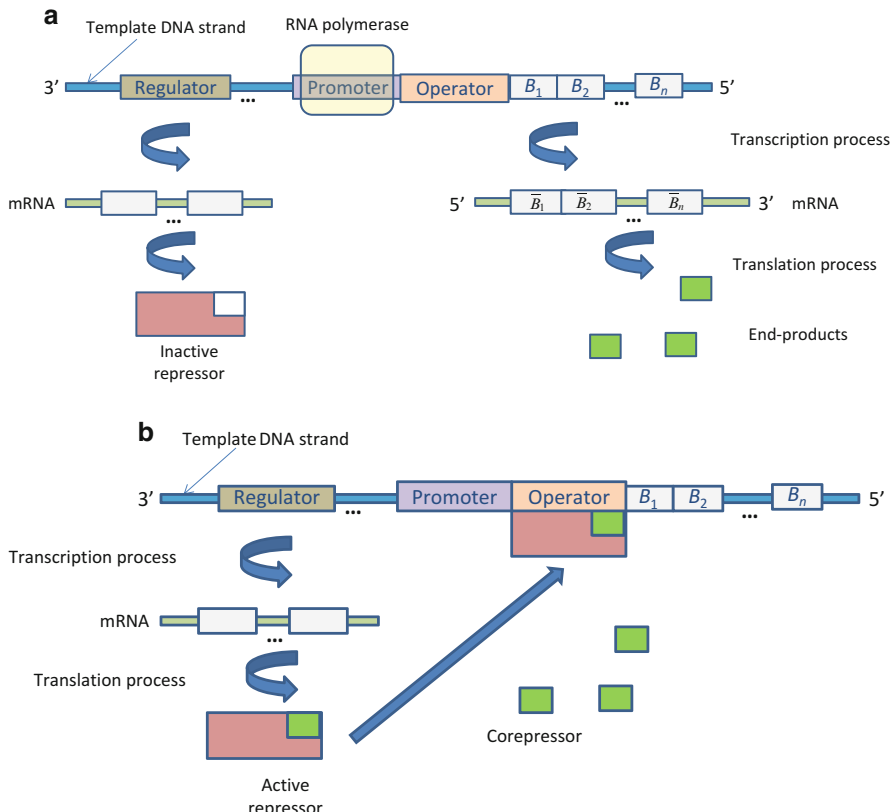


**Fig. 3.36** Illustration of end-product repression. **(a)** End-product synthesis stage: inactive repressor cannot bind to promoter and synthesis of end-product proceeds. **(b)** End-product repression stage: the end product serves as corepressor and creates the repressor–corepressor complex, which binds to the operator region of template DNA strand and prevents any transcription

its molecules binds on inactive repressor, serves as corepressor, and activates the repressor. The repressor now binds on operator and prevents further synthesis of the end product, as shown in Fig. 3.36b. Clearly, this is an example of negative feedback mechanism discussed earlier. The synthesis of tryptophan follows this strategy. The tryptophan molecule serves as the corepressor, while corresponding tryptophan repressor can be denoted as TrpR. The blocks  $B_1 – B_n$  correspond to the coding regions trpE–trpA. In eukaryotes, the corepressor is typically a protein instead, which binds to the so-called transcription factors.

Now we describe the protein synthesis by *induction*, which is illustrated in Fig. 3.37. The regulator gene expresses the synthesis of active repressor, which binds to the operator and covers the promoter, thus preventing the binding of the RNA polymerase, as shown in Fig. 3.37a. Therefore, the synthesis of a protein is blocked. In the presence of inducer, one of its molecules binds to the active repressor, serves as inhibitor, and deactivates the repressor. The deactivated repressor

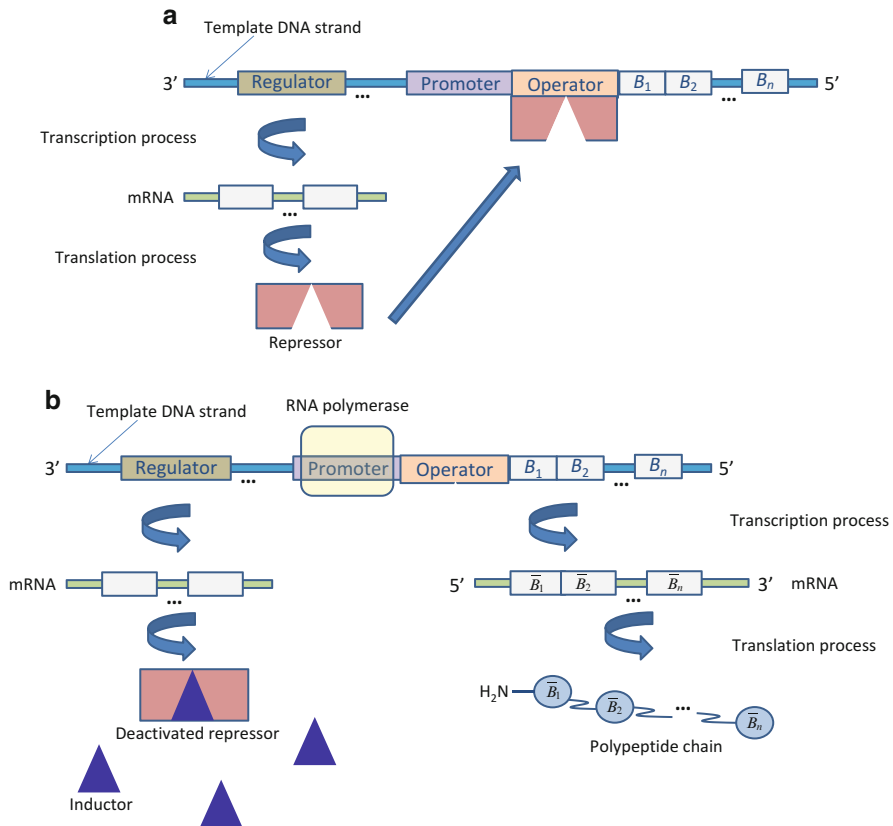


**Fig. 3.37** Illustration of protein synthesis by induction. (a) Regulator gene initiates the synthesis of repressor that binds on operator and blocks protein synthesis. (b) Inductor creates inductor-repressor complex; the repressor is deactivated and unbinds from operator. Protein synthesis is enabled now

now unbinds from operator and thus enabling the RNA polymerase binding on promoter, as shown in Fig. 3.37b. The process of protein synthesis is now enabled. Clearly, this is an example of positive feedback mechanism discussed earlier. The synthesis of enzymes needed for lactose catabolism follows this strategy.

We now move to description of *catabolite repression* mechanism. This mechanism allows bacteria to adapt quickly to a preferred source of energy first. The preferred source of energy is glucose rather than lactose. If both glucose and lactose are present, the glucose will be consumed first. Even though lactose is present, corresponding enzymes involved in catabolism of lactose will not be synthesized. Once the concentration of glucose falls below certain low threshold limit, the transcription of the corresponding lac operon (regulating the catabolism of lactose) will start. The catabolite repression mechanism is illustrated in Fig. 3.38. In the presence of glucose, the presence of inducer (lactose) is not sufficient for translation process to proceed, as illustrated in Fig. 3.38a. However, once glucose is

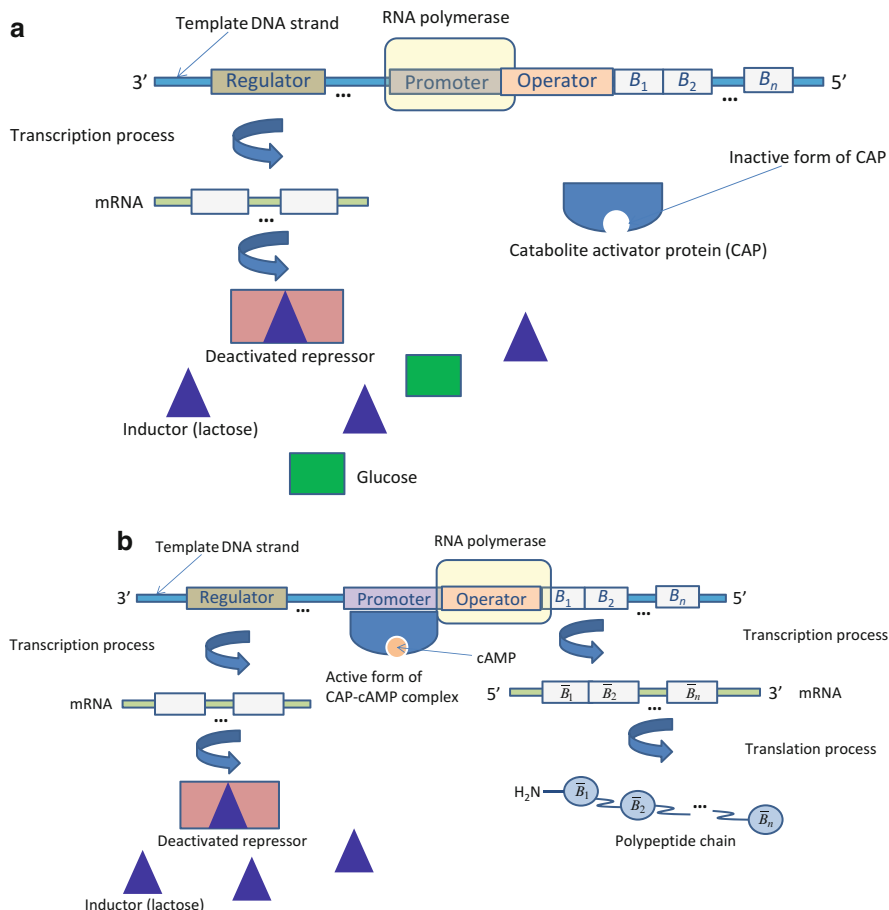
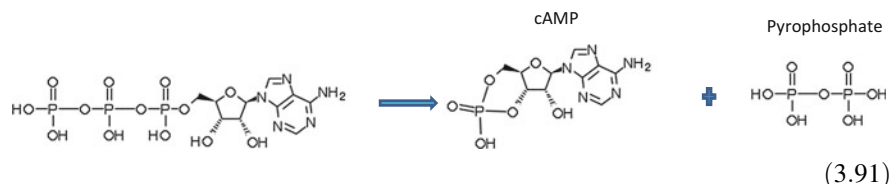


**Fig. 3.38** Illustration of catabolic repression mechanism. (a) In the presence of glucose, the inducer lactose is not sufficient to enable transcription of lac operon. Namely, the CAP is in inactive form and cannot bind to promoter for transcription of lac to proceed. (b) When lactose is the only source of energy, the cAMP concentration increases, and the complex CAP-cAMP is in active form and binds to promoter, while RNA polymerase binds to the operator. Protein synthesis is enabled now

consumed, adenylyl cyclase (located on the inner side of the plasma membrane) catalyzes the creation of cyclic AMP (cAMP) out of ATP as follows:



The synthesized cAMP creates CAP-cAMP complex, which binds to promoter, RNA polymerase binds to operator, and transcription process proceeds. As the concentration of glucose goes down, the adenylyl cyclase gets more active and cAMP concentration increases. In the presence of glucose, the activity of the adenylyl cyclase gets reduced, the concentration of cAMP goes down, and transcription of lac operon is blocked. The coding blocks  $B_1$ ,  $B_2$ , and  $B_3$  (for  $n = 3$ ) in Fig. 3.38 represent the genes lacZ, lacY, and lacA, respectively. The lacZ gene contains 3075 bp and encodes the synthesis of *β-galactosidase*, which is responsible for splitting the disaccharide lactose into monosaccharides glucose and galactose. The lacY gene contains 1254 bp and encodes the synthesis of *lactose permease*, which is responsible of pumping the lactose into the cell. Finally, the gene lacA contains 123 bp and encodes synthesis of *thiogalactoside transacetylase*, which is involved in degradation of small carbon compounds. The promoter is 84 bp long, while operator is 39 bp long. The spacing between lacZ and lacY genes is 52 bp, while the spacing between lacY and lacA genes is 66 bp. The gene responsible for synthesis for lac repressor (denoted as regulator in Fig. 3.38) is denoted as lacI, it is composed of 1081 bp, and it is located immediately next to the promoter in upstream direction.

The regulatory logic of eukaryotic genes is much more complicated than that of prokaryotic genes, and multiple regulatory sites have been involved in transcription process. Unlike prokaryotic cells, RNA polymerase requires so-called transcription factors to facilitate the transcription initiation phase. The *transcription factor* (TF) is protein that binds to a particular DNA subsequence and therefore affects the transcription rate. There are three types of regulatory proteins involved in turning the genes on: (1) *general transcription factors* (GTFs) that are required at every pol II promoter, (2) *DNA-binding transcription activators* that bind to enhancers to facilitate transcription process, and (3) *coactivators* that act independently by binding to other proteins rather than DNA. The pol II must be recruited to the promoter region to create a preinitiation complex. The creation of preinitiation complex begins by binding of TATA-binding protein (TBP) to the TATA box. TBP, which represents a part of larger TF complex called TFIID, then recruits pol II and other GTFs to the gene. The creation of preinitiation complex is still not enough for transcription process to begin. Namely, the interaction with positive regulators is needed. At enhancer site that can be thousands bp away from the promoter region, in upstream direction, transcription activators bind, while coactivators bind on activators instead. These activators then interact with proteins located at promoter side through intermediates. For this interaction to happen, the so-called DNA looping is required to bring enhancers that are thousands bp away in closer proximity of promoter region. DNA looping is enabled by nonhistone proteins, known as high-mobility group (HMG) proteins, which are abundant in chromatin. The activators bound to enhancer now can interact with preinitiation complex through a group of mediator proteins, and the gene expression is finally enabled. Evidently, two different genes can have the same promoter but different enhancers, resulting in so-called differential gene expression (depending on the cell function, etc.). Like prokaryotic cells, eukaryotic cells also have transcriptional repressors that bind to promoter and enhancer regions to block the transcription process. Based

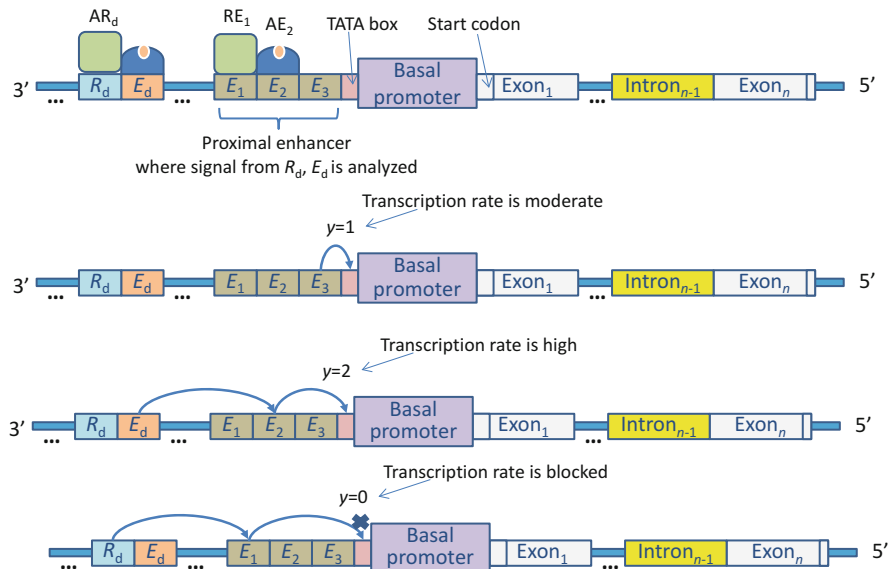


**Fig. 3.39** Illustration of regulatory logic of a typical development eukaryotic gene

on discussion above, it is obvious that regulatory logic of eukaryotic genes is much more complicated than that in prokaryotic genes. What is interesting to notice is that the combinational logic from computer science can be used to describe the control of the gene transcription process [23].

In what follows, we describe in Fig. 3.39 the conceptual diagram of a typical *eukaryotic gene regulatory logic*, which is based on [1, 24], and it is related to Endo 16 gene (of the sea urchin). The basal promoter (BP) is controlled by proximal enhancer module  $E_p$  composed of three sites ( $E_1$ ,  $E_2$ ,  $E_3$ ), distal enhancer  $E_d$ , and distal repressor  $R_d$ . The regulatory site  $E_3$  dominates the transcription when other sites are inactive (bound by corresponding repressors) and the transcription rate is moderate, which we denote by the output signal  $y = 1$ . When both enhancers  $E_d$  and  $E_2$  are active,  $E_2$  behaves as an active relay for  $E_d$ , which amplifies the signal from  $E_d$  and relays it to BP, so that the transcription rate is high. The corresponding output signal of proximal enhancer  $E$  is  $y = 2$ . Finally, when both sites  $R_d$  and  $E_1$  are occupied with corresponding TFs, the transcription process is repressed completely, and the output signal of region  $E$  is  $y = 0$ .

### 3.4 Mutations, Evolution, and DNA Repair

The information about organism characteristics is stored inside the DNA. The integrity and stability of DNA is essential for life. However, this stability is not absolute, but rather DNA is subject to either damage caused by environmental

source or random errors occurring in genetic storage material. Moreover, the DNA replication, transcription, and translation processes are imperfect. On the other hand, the instability in genetic material is also responsible for evolution. Without evolution, the life will be in the same form as it initially appeared. The various damages to DNA can be classified into two broad categories: (1) *endogenous* damage that is caused by an internal source and (2) *exogenous* damage that is caused by an external source. Interestingly enough, an individual cell can be subject of even one million DNA damages per day [16]. Due to various damages, the DNA spatial structure can be changed. The damages can be introduced to the single strand (SS) or double strand (DS). To deal with different damages, the cell has developed different mechanisms for DNA repair. Before we move to different mechanisms for DNA repair, we review the mutations.

Mutations represent the mistakes introduced in a cell's DNA. Mutations could be caused by mutagens and carcinogens or be caused by random mutations. The *mutagen* is a chemical substance or physical event that can cause the genetic mutations. On the other hand, the carcinogen could be a mutagen or any other source serving as an agent directly involved in causing the cancer. For instance, well-known carcinogens are tobacco and asbestos. The UV radiation can cause skin cancer due to excessive exposure to UV radiation (typically sunlight, but in certain situations, the tanning beds could be also responsible). The well-known endogenous mutagens are so-called reactive oxygen species (ROS), the chemically reactive molecules containing oxygen such as oxygen ions and peroxides. ROS can be formed either as a natural byproduct of the normal metabolism of oxygen or be caused by the environmental stress such as UV or heat exposure. When ROS levels increase dramatically, they can cause significant damage to the cell structures including DNA. Cumulatively, this effect is known as oxidative stress. ROS can also be generated by ionizing radiation. The ROS reacting with DNA can cause double-strand breaks and introduce nucleobase modifications. Well-known examples of exogenous mutagens include (1) *intercalators* such as EtBr whose molecule can get inserted between the planar nucleobases of DNA and deform the structure of DNA and (2) *base analogs* such as 5-bromouracil (5-BU) that pretends to be a nucleobase but acts differently. The 5-BU can replace uracil, but can have two different forms, keto and enol, which act differently. The keto form of BU pairs well with A, while enol form pairs well with G instead, introducing the mutations.

Mutations can be classified into two broad categories: (a) *gene mutations* causing low-scale mutations such as point mutations and (b) *chromosomal mutations* causing large-scale mutations. The chromosomal mutations can be related to either changes in chromosomal structure or changes in chromosome number. The mutations in chromosomal structure can be classified into several categories: (1) *chromosomal deletions* in which a section of a chromosome is missing, (2) *chromosomal duplication* in which a section of a chromosome is duplicated, (3) *chromosomal inversion* in which a section of chromosome is inverted, and (4) *chromosomal translocation* in which a section of a chromosome breaks off and reattaches to another nonhomologous chromosome. The mutations in chromosomal number (index) are of nondisjunction nature (chromosome pairs fail to

separate during meiosis) and are responsible for various syndromes. When the 21st chromosome pair has three chromosomes instead of two, this mutation is known as trisomy 21 and it is responsible for Down's syndrome. When Y-chromosome is missing, the corresponding syndrome is known as Turner's syndrome. Further, Klinefelter's syndrome corresponds to the set of symptoms resulting from either additional X-chromosome in males or additional Y-chromosome in females.

The criterion for classification is either based on observing DNA changes or protein product changes. When effects of DNA are used for classification, mutations could be either point mutations or frameshift mutations. In *point mutations*, one DNA nucleobase gets replaced by another one. *Frameshift mutations* can be classified as *insertion* and *deletion* mutations depending on whether a single nucleobase gets inserted or deleted, respectively. The frameshift mutations cause the problem in the reading of DNA sequence as all codons after the time-shift mutation are read incorrectly. The base substitutions can further be classified into *transition mutations* in which the type of base (purine or pyrimidine) gets preserved, *transversion mutations* in which the type of base gets changed, and *mispairing (mismatching) mutations* in which instead of conventional pairing rule, a different pairing rule is applied (either A–C or G–T). When the effects on protein are observed, the mutations can be classified into *nonsense mutations* in which the amino acid (AA) codon is mistaken for STOP codon and vice versa and *missense mutations* in which one AA gets replaced with another one. The missense mutation can further be classified into three categories: (1) *silent mutations* in which one codon gets changed to another codon representing the same AA, (2) *conservative mutations* in which one AA gets changed with another one of the same type, and (3) *non-conservative mutations* in which one AA gets changed with another one of different type.

The phenotype properties could be a result of mutation or recombination of genetic material. There exist three types of *genetic recombination* in bacteria: (1) conjugation, (2) transformation, and (3) transduction. In *conjugation*, the transfer of genetic material from one bacteria cell (donor cell) to another bacteria cell (acceptor) is performed through the direct physical contact through a specialized sex pilus (conjugation tube). In *transformation*, the bacterium takes the foreign DNA from the environment through plasma membrane and incorporates it in its own DNA. In *transduction*, the transfer of genetic material from donor cell to recipient cell is mediated by a virus that infects bacteria known as bacteriophage.

The prokaryotes are haploid; all genes are localized on one chromosome. It is possible that one cell can contain multiple copies of the same chromosome. For mutation to be inherited, it is necessary that it occurs on haploid chromosome or to be replicated on all instances of the chromosome. The speed of evaluation is directly proportional to the frequency of mutations. It is reasonable to assume that initially, at the beginning of biological evolution, mutations were more frequent than they are today thanks to the strong UV radiation and ionizing radiation. Moreover, the DNA repair mechanism in primitive forms of life was not that advanced. It is well known that mutations can be beneficial, neutral, or damaging to the cell. The mutation damaging to the cell gets eliminated through the natural

selection. The beneficial mutations, leading to the better adaptation to the varying environmental conditions, more effective growing mechanism, and reproduction, get inherited and contribute to the evolution. Notice that some of the damaging mutations can be reverted through the mechanism known as the *adaptive mutation* [31–33]. An important step in evolution is recombination of genetic material, which leads to new genes in genetic material of the population, similar as for mutations. However, the recombination has lower potential for evolution compared to mutations.

Regarding the *theory of evolution*, it has become evident that both Darwinian type of evolution (random mutations followed by selection process) [34] and Lamarckian type of evolution (selected mutations beneficial to the organism) [35] are important [36]. The modernized Lamarckian mechanism can be described as follows: environmental factors are introducing genomic changes, the mutations are targeted to specific genes, and the mutations provide the adaptation to the original cause. Clearly, this mechanism is well aligned with adaptive mutation mechanism mentioned above. The Darwinian mechanism of evaluation is less demanding as no specialized mechanism is required to direct the change of the relevant genomic locus and restrict it to the specific mutations. Based on mutation models we discussed, it appears that both mechanisms can contribute to the evolution. For low stress levels, the spontaneous mutations are dominant source to evolution, suggesting Darwinian evolution mode is more relevant. On the other hand, for strong stress levels, the adaptive mutations dominate, indicating that Lamarckian mechanism is more relevant in this regime.

We conclude this section with the discussion on *DNA repair mechanisms*. The DNA repair is a collection of processes by which cell identifies and corrects the damages introduced by either endogenous (internal) or exogenous (external) resources. Regardless of the source of damage or repair mechanism, the cell activates a highly coordinated chain of events in literature known as DNA damage response (DDR) [37], in which the cell senses the DNA damage, signals its presence, and mediates its repair. The vast majority of DNA modifications are endogenous in nature. The most common DNA modification is related to the loss of A or G due to spontaneous hydrolysis of the bond between purine nucleobase and deoxyribose, and this modification is known as *depurination*, and it is illustrated in Fig. 3.40a. Interestingly enough, the depurination occurs 5000–10,000 times a day in each human cell. Another type of internal DNA damage, which appears less frequently (about 100 times a day per human cell), is related to *deamination* and occurs due to collision of  $\text{H}_3\text{O}^+$  ions with amino group–cytosine bond leading to deamination and creation of uracil instead of cytosine, as illustrated in Fig. 3.40b.

Further, DNA can be damaged by ROS as discussed above. Nucleobases can be oxidized, hydrolyzed, or alkylated through interactions with ROS and free radicals. Finally, DNA replication process, although highly accurate, is still imperfect. Namely, DNA polymerase can insert incorrect nucleobase or repair enzymes could be themselves defective. DNA pol performs proofreading before adding the next nucleobase. Nevertheless, the process is imperfect and occasionally insertions, deletions, and mismatches can occur. UV light and mutagens/carcinogens can also

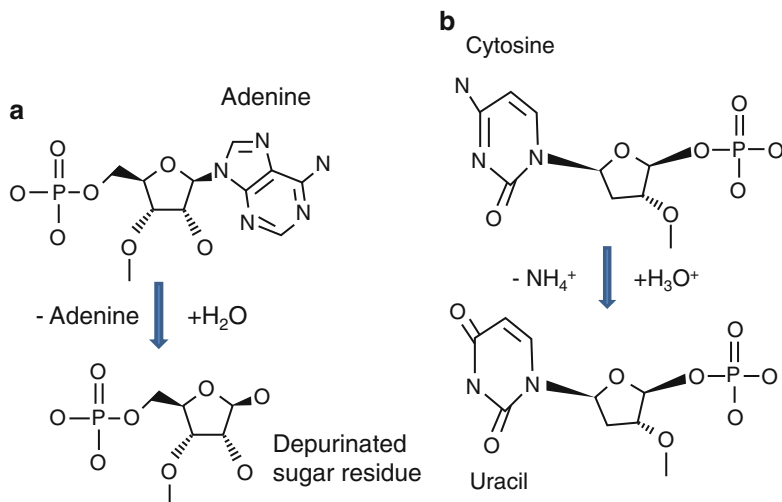


**Fig. 3.40** Illustration of depurination and deamination reactions: (a) depurination reaction and (b) deamination reaction

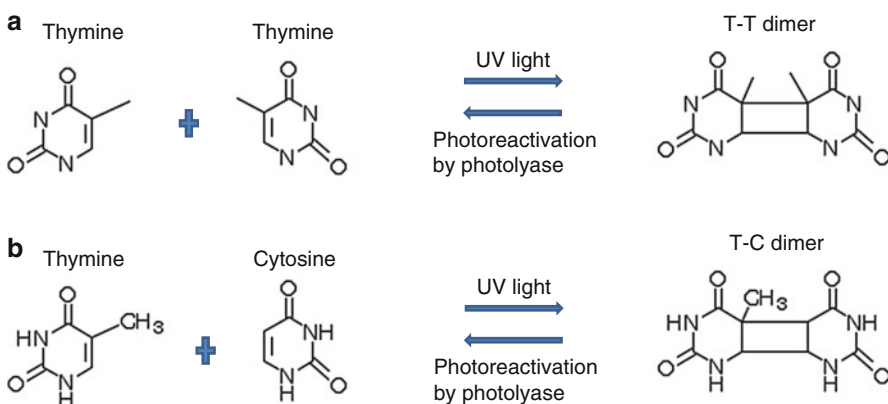


**Fig. 3.41** Illustration of creation of cyclobutane pyrimidine dimers by UV light: (a) thymine–thymine dimer and (b) thymine–cytosine dimer

cause damages to DNA as discussed above. For instance, the absorption of UV light can cause two thymine residues to get covalently bonded into thymine dimers. The cytosine–thymine dimer can similarly be formed as illustrated in Fig. 3.41. Different mutagens and ionizing radiation (such as X-rays and gamma rays) can also cause *double-strand breaks*, representing one of the most hazardous types of DNA damage.

Since the damage to DNA changes the actual spatial structure of DNA helix, it gets recognized by the cell. Once recognized, the DDR mechanism is initiated. Different DNA repair mechanisms can be classified into two broad categories:

single-strand (SS) repair mechanisms and double-strand (DS) repair mechanisms. SS repair mechanisms can further be categorized into the following categories:

1. Nucleotide excision repair (NER)
2. Base excision repair (BER) in which damaged or inappropriate nucleobases are removed and replaced
3. Mismatch repair (MMR) in which incorrectly paired (or unpaired) nucleobases are removed and replaced with correct ones

The NER mechanism is responsible in fixing pyrimidine dimer (T-T and T-C) damages. Namely, dimers introduce bends or kinks in DNA and can easily be recognized by the cell. In eukaryotic cells, the enzyme complex of at least 18 proteins is involved in NER. The particular enzymes, known as endonucleases, recognize the dimer and cut it out of the damaged DNA strand together with about 30 neighboring nucleotides. The gap such formed has been regenerated by DNA polymerase by inserting a proper base, and later on it has been sealed by DNA ligase. If the NER fails to fix the problem, the melanoma will occur on the skin. Defects in genes responsible for NER can cause the xeroderma pigmentosa (XP) disease, the condition in which the pyrimidine dimerization is not repaired. On the other hand, in bacteria (prokaryotes), the NER mechanism is conducted by only three enzymes UvrA, UvrB, and UvrC. Numerous organisms such as bacteria, fungi, plants, fruit flies, and frogs have another mechanism to repair the UV DNA damage known as *photoreactivation*. In photoreactivation, enzyme called photolyase binds pyrimidine dimer regions, and at the same time, the chromophore converts the light energy into chemical energy needed to reverse dimerization reaction, as indicated in Fig. 3.41.

BER mechanism is responsible for damages in nucleobases such as depurination or deamination. Since uracil is not part of the DNA, it has been recognized and removed by the repair enzyme known as (uracil-DNA) glycosidase. Apurinic/apyrimidinic (AP) endonuclease cuts the remaining phosphodiester bonds, the DNA pol inserts the proper base, and DNA ligase seals the new base to the remainder of DNA strand.

MMR mechanism is responsible for correction of errors occurred during the replication process, and not corrected by proofreading mechanism, such as mismatch errors as well as deletions and insertions. This mechanism is conducted by a group of proteins (MutS and MutL) that scan DNA and identify incorrectly paired bases or unpaired bases. The incorrect nucleotide is removed and DNA pol reattaches the correct nucleobase. In *E. coli*, the adenine requires a methyl group. The parental DNA strand will have methyl groups, while newly synthesized strand will lack them. The DNA pol will then use the parental DNA strand as template and remove the wrongly incorporated bases from the newly synthesized strand.

Regarding the *DS repair mechanisms*, they can be classified into three categories as well:

1. Nonhomologous end-joining (NHEJ)
2. Microhomology-mediated end-joining (MMEJ)
3. Homologous recombination (HR)

In NHEJ, the specialized enzyme known as DNA ligase IV employs overhanging pieces of DNA adjacent to the break to join and fill in the corresponding ends [25]. MMEJ operates by ligating the mismatched hanging strands of DNA, removing overhanging nucleotides and filling in the missing base pairs. When a break occurs, a homology of 5–25 complementary bp on both strands is identified and used as a template to align the strand with mismatched end. Once aligned, any overhanging bases or mismatched pairs are removed and any missing nucleotides are inserted. In HR repair, the homologous chromosome or sister chromatid itself is used as a template to perform the repairing.

The cell that has accumulated too many DNA damages and can no longer perform the DNA damage repair mechanisms can enter into one of three possible states:

- *Senescence* or irreversible state of dormancy, which is similar to cell entering the hibernation mode
- *Apoptosis* or programmed cell death
- Unregulated cell division that can lead to tumor, which can be cancerous

## 3.5 Bioenergetics of the Cell

This section is a continuation of Sect. 3.1.3. Here we are concerned with energy flow in the cell. It has already been mentioned that ATP hydrolysis has been used in the cell as a driving force to enable the energetically unfavorable biochemical processes. For convenience, we repeat the ATP hydrolysis equation in a more accurate form:



and the energy released during hydrolysis in the standard biological conditions (temperature 25 °C, pressure 101.325 kPa, concentration of all components 1 mol/L except the concentration of H<sup>+</sup> ions which is 10<sup>-7</sup> mol/L) is about -31.8 kJ/mol. Typically, in the cell, the ATP/ADP ratio is maintained near 10:1 with prevailing level of phosphate around 5 mmol/L so that the energy released during ATP hydrolysis could even be

$$\Delta G = \Delta G^0 + RT \log \left( \frac{[\text{ADP}]}{[\text{ATP}]} [\text{P}_i] \right) \approx -50 \text{ kJ/mol} \quad (3.93)$$

Some tissues and organs with high-energy requirements such as the brain, retina, cardiac muscle, and skeletal muscles have ATP/ADP ratio close to 100 and can

**Table 3.2** Free energy change during hydrolysis of several high-energy compounds

Compound	Biochemical reaction	Free energy, $\Delta G^0$ [kJ/mol]
Phosphoenolpyruvate, PEP	$\text{PEP} \leftrightarrow \text{pyruvate} + \text{P}$	-50.2
Acetyl-CoA	$\text{Acetyl-CoA} \leftrightarrow \text{acetate} + \text{CoA}$	-33.5
ATP	$\text{ATP} \leftrightarrow \text{AMP} + \text{P-P}$	-33.5
	$\text{ATP} \leftrightarrow \text{ADP} + \text{P}$	-31.8
GTP	$\text{GTP} \leftrightarrow \text{GDP} + \text{P}$	-29.3
Pyrophosphate (P-P)	$\text{P-P} \leftrightarrow \text{P} + \text{P}$	-29.3
ADP	$\text{ADP} \leftrightarrow \text{AMP} + \text{P}$	-25.1
Glucose-1-phosphate	$\text{Glucose-1-P} \leftrightarrow \text{glucose} + \text{P}$	-21.0
Glucose-6-phosphate	$\text{Glucose-6-P} \leftrightarrow \text{glucose} + \text{P}$	-13.8

P is used to denote the phosphorous group

release even  $-60$  kJ/mol during ATP hydrolysis. Clearly, the ATP has a central role in energetic metabolism. Very often the ATP forms complexes with  $\text{Mg}^{2+}$  and  $\text{Mn}^{2+}$  ions. In addition to ATP, there exist other compounds whose hydrolysis leads to the release of high energy. Some of them have been listed in Table 3.2. The ATP can serve as energy transporter, to transfer energy from higher energy compounds to lower energy compounds. The release of energy by ATP hydrolysis appears to be optimum in the sense it is sufficient to enable many energy unfavorable biochemical reactions. There are two ways by which ATP energy can be transferred as shown in Table 3.2: (1) by hydrolysis of the third phosphate group wherein ADP is formed and (2) hydrolysis of ATP wherein AMP and pyrophosphate are formed.

Based on the source of energy consumed, the prokaryotes can be classified as *phototrophs* that utilize the light energy and *heterotrophs* that utilize the energy of chemical compounds. Either source of energy must be transformed in the form more suitable for utilizations in the cell. The basic reactions for this transformation are reduction-oxidation (redox) reactions, described in Sect. 3.1.3. As an illustration, in Fig. 3.42 we describe the process of ATP-ADP interconversion. Namely, during fermentation, as the result of redox reactions, unstable, highly energetic compounds with phosphates' groups are formed. The corresponding enzyme interacts with substrate-phosphate group complex and ATP is formed. This process can be described as follows:



and it is known as a *substrate level phosphorylation*. Another possible version of this process can be described as



where  $\text{P}_i$  denotes the inorganic phosphate.

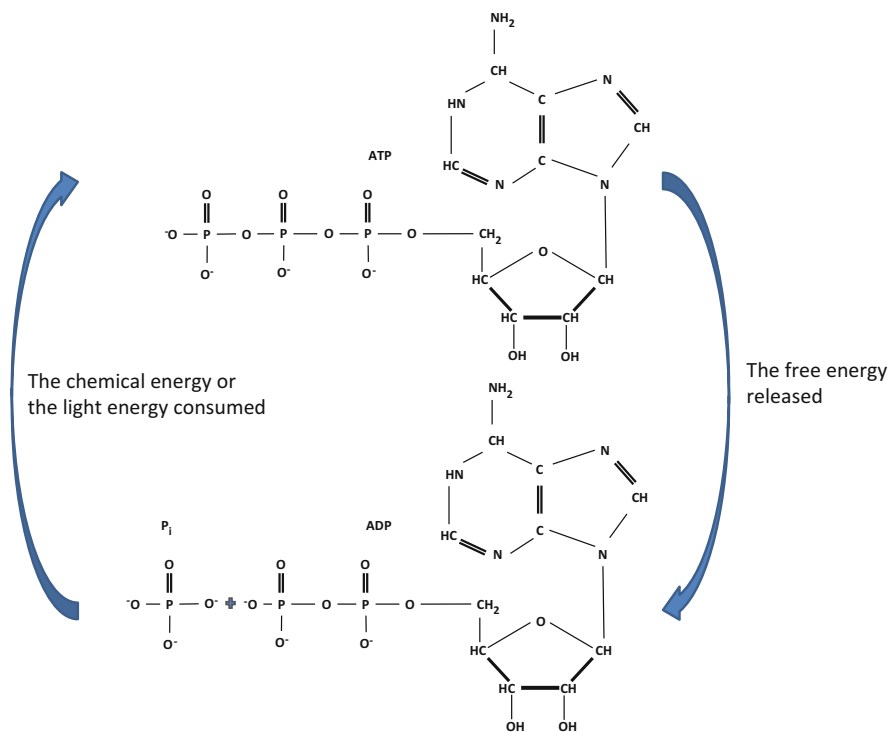
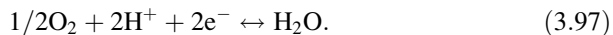


**Fig. 3.42** Illustration of ADP to ATP conversion and vice versa

Another interesting redox biochemical reaction is oxidation of NADH by O<sub>2</sub>, which can be described by the following two half-reactions:



The first half-reaction is also described in Fig. 3.43. These two half-reactions can be summarized as follows:



At this point, it is convenient to introduce the concept of redox potential, also known as reduction potential. The *redox potential* is a measure of the tendency of a molecule/ion to act as an electron acceptor or donor, depending on the sign. The redox potential can be calculated from the Nernst equation, given by (3.49). For

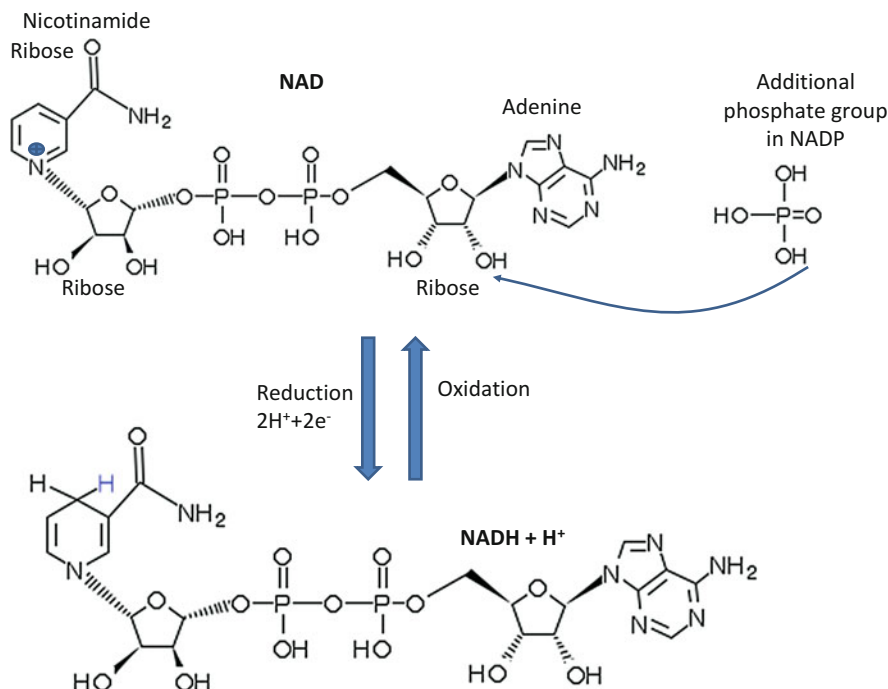
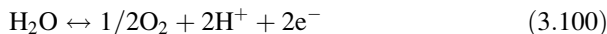


**Fig. 3.43** Illustration of the structure of NAD, NADH, and NADP

instance, the standard redox potential (measured at standard biological conditions) for the following reaction:



is  $-420$  mV, which indicates high affinity to reduction, and hydrogen acts as donor of electrons. On the other hand, the standard redox potential for



is  $+820$  mV, indicating low affinity of water to serve as a donor; rather, the oxygen has high affinity to act as an acceptor of electrons. The redox potential for half-reaction (3.96) is  $-320$  mV. On the other hand, the oxygen has high affinity to accept electrons with redox potential of  $820$  mV as indicated above. Therefore, the overall standard redox potential for (3.96) is  $\Delta E_0 = 820$  mV  $- (-320$  mV)  $= 1.14$  V. The corresponding change in free energy would be  $\Delta G = -nF\Delta E_0 = -2 \times 96.485$  kJ/(V mol)  $\times 1.14$  V  $= -219.986$  kJ/mol. Clearly, the oxidation of NDAH by oxygen leads to the release of high amount of free energy close to  $-220$  kJ/mol.

Now we turn our attention to another source of energy in the cell, namely, the energy of *transmembrane proton gradient*, also known as *proton motive force* (PMF) or chemiosmosis. The chemiosmotic hypothesis was introduced by Mitchell [38], and he was awarded the Nobel Prize in Chemistry in 1978. Chemiosmosis represents the movement of ions across a selectively permeable membrane. More specifically, the ATP can be generated based on the energy of transmembrane proton gradient; in other words, by the movement protons (hydrogen ions) across a membrane in the process known as membrane phosphorylation, as illustrated in Fig. 3.44. In prokaryotes, the cytoplasmic membrane (CPM) represents the location of the series of proteins participating in the electron transport systems (ETS) such as flavoprotein (denoted as FAD), iron–sulfur protein (denoted as Fe–S), quinone (denoted as Q), and cytochromes

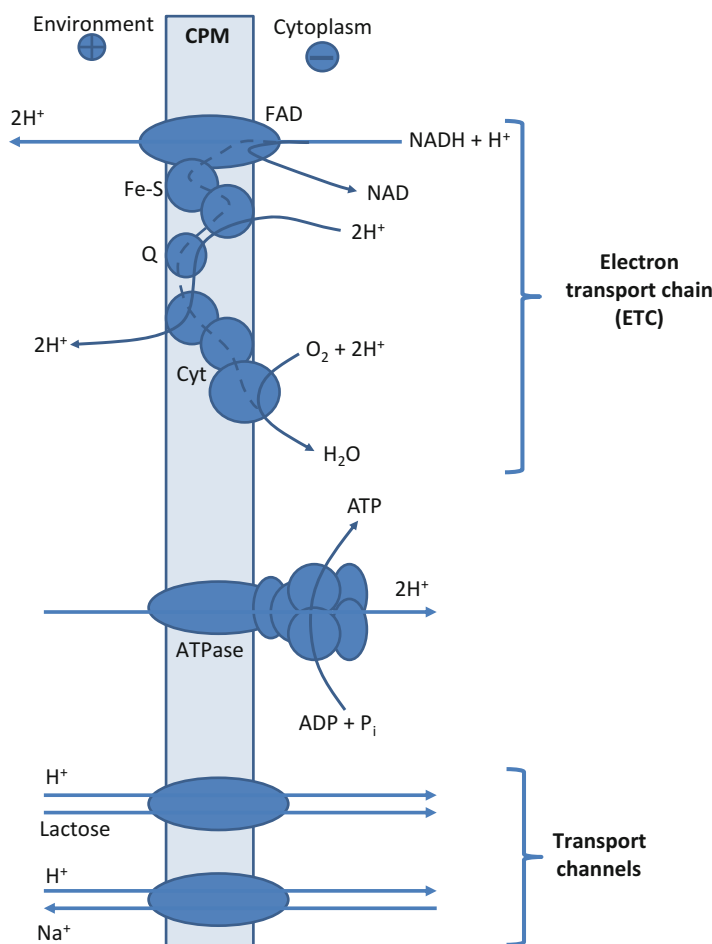


**Fig. 3.44** Illustration of the electron transport system and the proton pump system in prokaryotic cell. *CPM* cytoplasmic membrane, *FAD* flavin adenine dinucleotide (flavoprotein), *Fe–S* iron–sulfur protein, *Q* quinone, *Cyt* cytochromes

(denoted as Cyt). In CPM, the enzyme used to synthesize ATP, known as ATP synthetase (ATPase), is also located. The flavoprotein accepts electrons from NADH and delivers them to Fe–S protein. The electrons further get passed to Q and finally to three types of cytochromes. The terminal acceptor of electron is oxygen, which gets reduced to water. During the oxidation of NADH, two protons get transferred to the environment, while  $2e^-$  to the FAD. Therefore, during ETS operation and NADH oxidation, a pH gradient across of the CPM gets formed due to an accumulation of protons (hydrogen ions,  $H^+$ ) outside of the membrane and hydroxyl ions ( $OH^-$ ) inside the membrane. As a consequence, the outside of membrane has acidic character, while the interior has alkaline character. The ETS establishes a voltage across a membrane known as PMF, since the outer face of the membrane has been charged positively, while the inner face of the membrane is charged negatively. The PMF can be used to perform various types of works including the rotation of the flagellum (not shown in figure) or active transport (shown in figure). The transport mechanism could be (1) *uniport*, in which only one substance is transported at the time; (2) *symport*, in which two substances move together in the same direction across the CPM; and (3) *antiport*, in which two chemicals get transported simultaneously in the opposite directions. The PMF can also be used to generate ATP by the membrane ATPase enzyme that consumes protons when it synthesizes ATP from ADP and inorganic phosphate ( $P_i$ ) as shown in Fig. 3.44. This interconnection among ETP, PMF, and ATP synthesis during respiration is commonly referred to as oxidative phosphorylation. For the energy sources in eukaryotes, interested reader is referred to [15–18]. Interestingly enough, the process of ATP synthesis, shown in Fig. 3.44, is identical in both prokaryotes and eukaryotes. In eukaryotic cells, the mitochondrial inner membrane serves a similar role as CPM in prokaryotes. Moreover, the endosymbiotic theory claims that mitochondria are derived from bacteria that evolve to live in eukaryotic cells [14] (see also [39]).

The movement of ions across a membrane is a function of two factors: (1) diffusion force caused by concentration gradient and (2) electrostatic force caused by electrical potential difference between the environment and cytoplasm. Therefore, the PMF, expressed in mV or V, can be written as

$$\Delta p = \Delta\psi - C \Delta \text{pH}, \quad (3.101)$$

where  $\Delta\psi$  is the electrical potential difference,  $C$  is the normalization constant to be determined below, and  $\Delta\text{pH}$  is the concentration gradient expressed in pH and defined as  $\Delta\text{pH} = \text{pH}_{\text{environment}} - \text{pH}_{\text{cytoplasm}}$ . The PMF expression (3.101) can easily be derived from the Gibbs free energy change during the transfer of 1 mol of cations  $X^{n+}$  from the environment to the cytoplasm and defined as

$$\Delta G = -nF\Delta\psi + RT \log \left( \frac{[X^{n+}]_{\text{environment}}}{[X^{n+}]_{\text{cytoplasm}}} \right), \quad (3.102)$$

where  $F$  is the Faraday constant introduced in Sect. 3.1.3 ( $F = 96.485 \text{ kJ V}^{-1} \text{ mol}^{-1}$ ),  $R$  is universal gas constant,  $T$  absolute temperature, and  $[X^{n+}]_{\text{environment}}$  and  $[X^{n+}]_{\text{cytoplasm}}$  denote the cation concentrations across CPM.

By changing the base  $e$  used in (3.102) to base 10, we can rewrite (3.102) as follows:

$$\Delta G = \underbrace{-nF\Delta\psi + RT \log_{10} \left( \frac{[X^{n+}]_{\text{environment}}}{[X^{n+}]_{\text{cytoplasm}}} \right)}_{\Delta \text{pH}} / \log_{10} e. \quad (3.103)$$

The change of Gibbs free energy is equal to the electrochemical ion gradient, expressed in  $\text{kJ/mol}$ , denoted as  $\Delta\mu_{X^{n+}}$ . When we are concerned with electrochemical proton gradient, denoted as  $\Delta\mu_{H^+}$ , we can write

$$\Delta\mu_{H^+} = -F\Delta\psi + \frac{RT}{\log_{10} e} \Delta \text{pH}. \quad (3.104)$$

Mitchell has defined the PMF, denoted as  $\Delta p$ , as follows:

$$\Delta p = -\frac{\Delta\mu_{H^+}}{F} = \Delta\psi - \frac{RT}{F \log_{10} e} \Delta \text{pH}. \quad (3.105)$$

Therefore, the constant  $C$  in (3.101) is given by  $C = RT/(F \log_{10} e)$ . At room temperature ( $T = 298 \text{ K}$ ), the constant  $C$  is equal to  $\sim 59 \text{ mV}$ . For example, in *E. coli* cells at pH of 7.5,  $\Delta\psi$  is 140 mV, while  $\Delta \text{pH} \leq 0.5$ , so that the PMF is  $\leq 170 \text{ mV}$ .

## 3.6 Concluding Remarks

In this chapter, we have described the basics of biological thermodynamics (Sect. 3.1), biomolecules (Sect. 3.2), cellular genetics (Sect. 3.3), mutations and evolution (Sect. 3.4), and bioenergetics (Sect. 3.5). The following biomolecules have been described: amino acids, peptides, proteins, carbohydrates and corresponding polymers; nucleic acid, nucleosides, and nucleotides; and phospholipids. Regarding the cell dynamics, the following topics have been described: DNA structure, the genetic code, gene anatomy, DNA synthesis and repair, transcription, and translation. Regarding the energetics of the cell, we have described the universal forms of energy (ATP and PMF) and the metabolism of the organism. We have also discussed the relationship between genetics and evolution.

## References

1. Tözeren A, Byers SW (2004) New biology for engineers and computer scientists. Pearson Education, Upper Saddle River
2. Cohen WW (2007) A computer scientist's guide to cell biology. Springer, New York
3. Johnson AT (2010) Biology for engineers. CRC, Boca Raton
4. Jacob F (1976) The logic of life: history of heredity. Gallimard, Paris (in French)
5. Božo J (2007) Bioenergetics: basic principles. Gradjevinska Knjiga, Zrenjanin (in Serbian)
6. Watson JD, Baker TA, Bell SP, Gann A, Levine M, Losick R (2013) Molecular biology of the gene, 7th edn. Benjamin Cummings, Menlo Park
7. Haynie DT (2008) Biological thermodynamics, 2nd edn. Cambridge University Press, Cambridge
8. Wannier GH (1987) Statistical physics. Dover, New York (reprint)
9. Djordjevic IB, Xu L, Wang T (2012) Statistical physics inspired energy-efficient coded-modulation for optical communications. *Opt Lett* 37(8):1340–1342
10. Bray D (1995) Protein molecules as computational elements in living cells. *Nature* 376:307–312
11. Regev A, Shapiro E (2002) Cellular abstractions: cells as computation. *Nature* 419:343
12. Waite GN, Waite L (2007) Applied cell and molecular biology for engineers. McGraw-Hill, New York
13. Malacinski G (2003) Essentials of molecular biology, 4th edn. Jones and Bartlett, Sudbury
14. Bolsover SR, Shephard EA, White HA, Hyams JS (2011) Cell biology: a short course, 3rd edn. Wiley, Chichester
15. Alberts B, Johnson A, Lewis J, Raff M, Roberts K, Walter P (2007) Molecular biology of the cell, 5th edn. Garland Science, New York
16. Lodish H, Berk A, Kaiser CA, Krieger M, Bretscher A, Ploegh H, Amon A, Scott MP (2012) Molecular cell biology, 7th edn. W. H. Freeman, New York
17. Karp G (2007) Cell and molecular biology: concepts and experiments, 5th edn. Wiley, New York
18. Wolfe J (2002) Cellular thermodynamics. In: Encyclopedia of life sciences. Macmillan/Nature Publishing Group, London
19. Nakano T, Eckford AW, Haraguchi T (2013) Molecular communication. Cambridge University Press, Cambridge
20. Chagraff E (1950) Chemical specificity of the nucleic acids and mechanism of their enzymatic degradation. *Experientia* 6:201–240
21. Watson JD, Crick FHC (1953) Genetical implications of the structure of deoxyribonucleic acid. *Nature* 171:964–967
22. Jacob F, Monod J (1961) Genetic regulatory mechanisms in the synthesis of proteins. *J Mol Biol* 3:318–356
23. Buchler NE, Gerland U, Hwa T (2003) On schemes of combinational logic. *Proc Natl Acad Sci U S A* 100:5136–5141
24. Yuh CH, Bolouri H, Davidson EH (1998) Genomic cis-regulatory logic: functional analysis and computational model of a sea urchin gene control system. *Science* 279:1896–1902
25. Clancy S (2008) DNA damage & repair: mechanisms for maintain DNA integrity. *Nat Educ* 1:103
26. Branzei D, Foiani M (2008) Regulation of DNA repair throughout the cell cycle. *Mol Cell Biol* 9:297–308
27. Iyama T, Wilson DM III (2013) DNA repair mechanisms in dividing and non-dividing cells. *DNA Repair* 12:620–636
28. Hamperl S, Cimprich KA (2014) The contribution of co-transcriptional RNA:DNA hybrid structure to DNA damage and genome instability. *DNA Repair* 19:84–94
29. Cotterill S, Kearsey S (2009) Eukaryotic DNA polymerases. In: Encyclopedia of life sciences (ELS). Wiley, Chichester

30. Djordjevic IB (2012) Quantum biological channel modeling and capacity calculation. *Life* 2:377–391
31. Foster PL (1993) Adaptive mutation: the uses of adversity. *Annu Rev Microbiol* 47:467–504
32. Rosenberg SM (2001) Evolving responsively: adaptive mutation. *Nat Rev Genet* 2:504–515
33. Roth JR, Kugelberg E, Reams AB, Kofoid E, Andersson DI (2006) Origin of mutations under selection: the adaptive mutation controversy. *Annu Rev Microbiol* 60:477–501
34. Darwin C (1859) *On the origin of species*. Murray, London
35. Lamarck JB (1809) *Zoological philosophy: exposition with regard to the natural history of animals*. Dentu, Paris (in French)
36. Koonin EV, Wolf YI (2009) Is evolution Darwinian or/and Lamarckian? *Biol Direct* 4:42
37. Dexheimer TS (2013) DNA repair pathways and mechanisms. In: Mathews LA, Cabarcas SM, Hurt E (eds) *DNA repair of cancer stem cells*. Springer, Dordrecht, pp 19–32
38. Mitchell P (1961) Coupling of phosphorylation to electron and hydrogen transfer by a chemiosmotic type of mechanism. *Nature* 191:144–148
39. Fenchel T (2002) *Origin & early evolution of life*. Oxford University Press, New York

# Chapter 4

## Quantum Information Theory and Quantum Mechanics-Based Biological Modeling and Biological Channel Capacity Calculation

**Abstract** The quantum biological channel models suitable for the study of quantum information transfer from DNA to proteins have been described based on codon transition probabilities. The sources of genetic noise and genetic errors have been described as well. The quantum genetic noise has been described in terms of tautomeric nucleic base-pair formation. Various sources of genetic errors and genetic noise have also been described using quantum-mechanical formalism. The quantum biological channel capacity evaluation has been further described. The next part of the chapter is devoted to the use of quantum-mechanical concepts to describe the bird navigation compass. Finally, the quantum-mechanical aspects of photosynthesis have been discussed.

### 4.1 Introduction

The principles of statistical physics [1] and thermodynamics are widely used to describe different processes in the cell [2, 3]. Additionally, the concepts from computer science [4–6] and communications [7–9] have been also used to describe both intra- and intercellular dynamics. Recently, quantum biological studies have gained momentum, which can be judged by the number of recent publications related to this topic [10–30]. It has become evident that quantum mechanics has an important role in photosynthesis [17], magnetoreception [18], and evolution [14]. In photosynthesis, the Fenna–Matthews–Olson (FMO) complex supports the coherent transport of electron excitation over a short period of time, upon the photon absorption, to the reaction center where the energy gets converted into sugar. In the second phase of this interaction, the environment decoheres the system, which speeds up the excitation transfer by avoiding the system being trapped into the dark states. Further, the DNA replication and protein synthesis have been described by using Grover’s search algorithm [23]. Additionally, the quantum-mechanical formalism for biological evolution has been established in [29].

There were also many attempts in an effort to explain the structure of genetic code and transfer of information from DNA to protein by using the concepts of quantum mechanics (QM) [12, 14, 16]. For instance, the general quantum-mechanical model

to describe the transfer of information from DNA to protein by using the quantum information theory is proposed by Karafyllidis [12]. However, given the high complexity of the problem [31], the determination of *quantum biological channel capacity* was still an open problem, until recently [30]. On the other hand, the classical biological channel capacity has been determined by Yockey [7, 8]. Yockey developed a discrete memoryless classical biological channel model and explicitly derived the transitional probabilities among amino acids. Namely, he represented the information transfer from DNA to protein as a communication problem and determined the corresponding classical biological channel capacity by maximizing the mutual information between DNA and protein. Interestingly enough, there are certain papers that question the role of quantum information in biological processes [20]. The main justification is that the entanglement in living system is limited to a very short time and small regions and the decoherence is too high for quantum entanglement to be relevant on the molecular level in the ambient conditions. However, in photosynthesis, as indicated above, this decoherence phase is essential to avoid the system being caught in dark states. Moreover, it is possible to represent the genetic coding using the quantum error-correction concepts. Even though that decoherence is going to introduce errors, these errors can be corrected by the “quantum decoder,” performing the mRNA to protein translation. Moreover, different DNA repair mechanisms, described in Chap. 3 (see Sect. 3.4), can be described using quantum information theory concepts. Another argument, also known as  $k_B T$ -argument ( $k_B$ —Boltzmann constant,  $T$ —temperature), claims that whenever interaction energies are smaller than  $k_B T$  at room temperature, the corresponding quantum effect cannot persist. However, the electron clouds of complementary DNA strands experience dipole–dipole interaction, resulting in attractive van der Waals bonding [22], with interaction frequency  $\omega$  being in the optical range, suggesting that  $\hbar\omega/k_B T \gg 1$ . Therefore, since the electronic system of DNA is globally in the ground state, the DNA system must be locally in a mixed state. Given the uncertainty principle, it is impossible to distinguish whether a local mixed state is a result of temperature or entanglement. Finally, given the fact that the thermodynamics entropy is just special case of von Neumann entropy [1], when the corresponding density matrix is diagonal, there is no surprise at all that quantum mechanics is a suitable apparatus to describe certain processes in the cell.

## 4.2 Quantum Biological Channel Models Suitable for Study of Quantum Information Transfer from DNA to Proteins

In Fig. 4.1a, we describe the generic quantum biological model suitable to study the flow of information from DNA to protein. The process of transcription is interpreted as encoding, the various errors introduced during replication, transcription, or

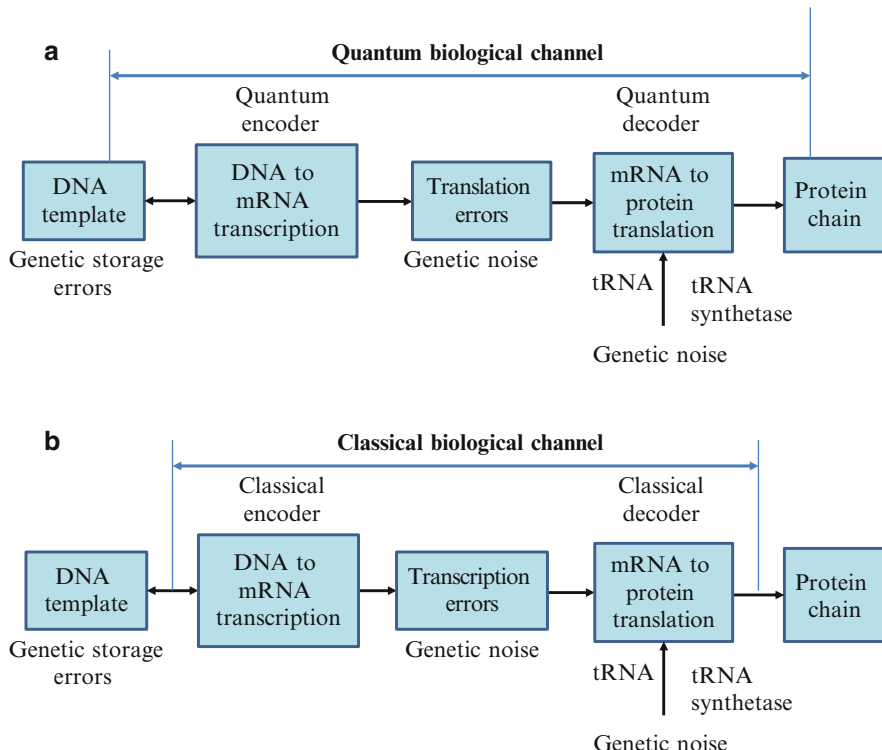


**Fig. 4.1** (a) Generic quantum channel model describing the information flow from DNA to protein. It is assumed that quantum genetic noise introduces the random errors. In this model, the classical information, representing the information for a single polypeptide synthesis, is transmitted over the quantum genetic channel. DNA template is also a subject of mutations and, as such, is also represented as a part of biological quantum channel. (b) Corresponding classical biological channel model

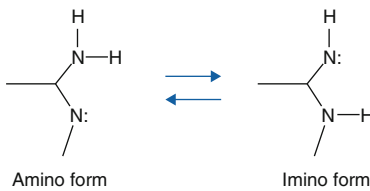
translation considered as a source of genetic noise, while the process of translation is interpreted as decoding. Notice that this interpretation is consistent to the classical model defined by Yockey [7, 8]. For convenience, the corresponding classical biological channel model is shown in Fig. 4.1b. The key difference with respect to model due to Yockey is that here we assume that DNA encoder is subject to DNA storage errors, while decoder is subject to translation error, so that biological channel has been extended to include DNA encoder and decoder (performing translation from mRNA to protein). The process of translation is also prone to errors, which can also be contributed to the genetic noise. Therefore, all errors introduced in any stage shown in Fig. 4.1a are called “genetic noise.” The transcription, DNA point mutations, insertions, deletions, and translation can all be interpreted as the quantum channel. It is assumed that genetic noise introduces random errors, which can be classified into several broad categories. The first types of errors, “storage errors,” occur in DNA itself as it is an imperfect storage of

genetic information. The second types of errors are introduced during the DNA replication process. (For instance, the probability of error during replication is  $\sim 10^{-7}$  per base pair [23].) The third types of errors, transcription errors, are introduced during DNA to mRNA transcription process. The fourth types of errors, translation errors, are introduced during the translation process.

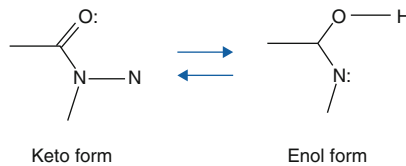
Therefore, the key difference with respect to communication systems, where both encoders and decoders are implemented from perfect gates, in biological systems DNA replication, DNA to mRNA transcription, and mRNA to protein translations, are imperfect processes. Once more, this difference requires redefining the channel model, as it is done in Fig. 4.1a.

We assume that the problem with the burst of errors, introduced, for example, by an alpha particle passing through a segment of DNA, has been resolved by duplicate genes. Moreover, the introns may serve as interleavers in eukaryotic genes, suggesting that quantum errors indeed appear in a random fashion. The genome, which represents the ensemble of genetic code words, is prerecorded in DNA sequence by using the nucleotide alphabet composed of four symbols: adenine (A), guanine (G), cytosine (C), and thymine (T). The fourth base is replaced in RNA by uracil (U). The DNA code words contain the information for protein synthesis. The mRNA consists of three-symbol words known as codons. Multiple codons can correspond to the same amino acid.

The point mutations are caused by tautomeric forms of nucleic acids [21, 24]. There exist two main forms of tautomerism: (a) *amino-imino* tautomerism given by [21]



and (b) *keto-enol* tautomerism given by [21]



The amino and keto forms are considered as standard forms. The double dots (:) in any of tautomerism forms, denote electron lone pairs that can attract proton ( $H^+$ ) and participate in hydrogen bond forming. Namely, the pairing of nucleotides is specific to  $T = A$ ,  $C \equiv G$  combinations, with “-” representing the hydrogen bond

(H-bond), as shown in Fig. 4.2. In the same figure, we provide the schematic representation in which the “donors” of protons are denoted with symbol 1, while the “acceptors” of protons are denoted with symbol 0. However, in tautomeric forms  $A^*$ ,  $G^*$ ,  $C^*$ , and  $T^*$ , a proton involved in H-bond has been moved from one electron lone pair to another, which is illustrated in Fig. 4.3. During either DNA replication or

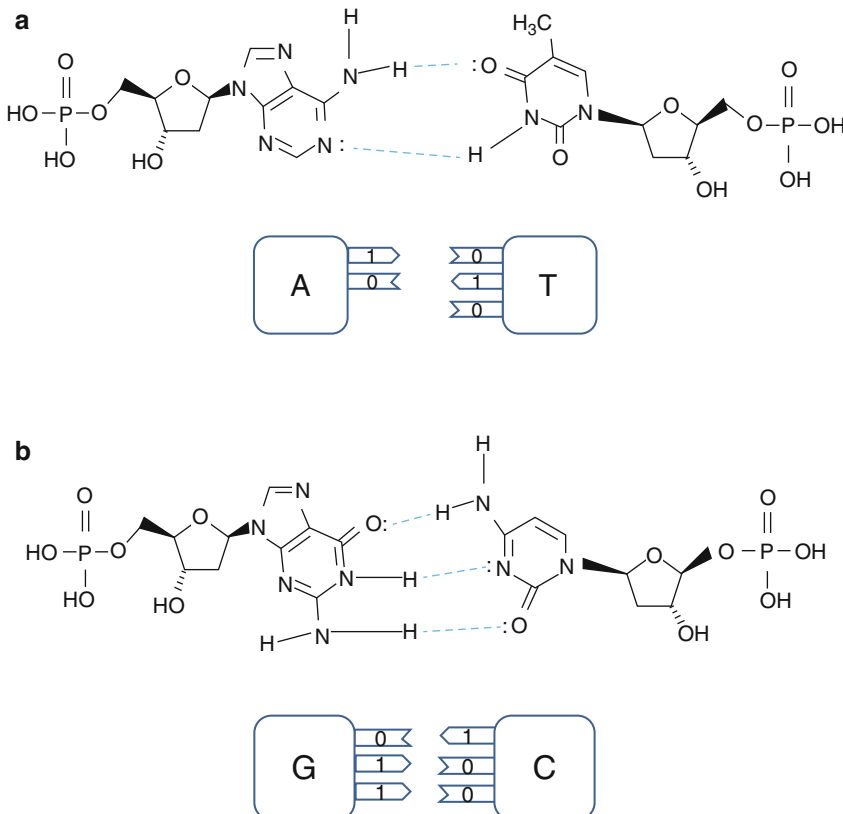


**Fig. 4.2** Standard nucleic acids’ pairing together with schematic representation. In schematic representation, the symbol 1 is used to denote the “donor” of a proton while symbol 0 to denote “acceptor” of a proton

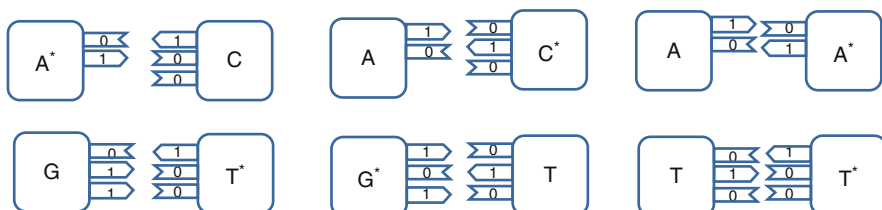


**Fig. 4.3** The tautomeric nucleic acids’ pairing



**Fig. 4.4** Tautomeric forms are responsible for random errors introduced within DNA, when DNA is used for long-term storage of genetic information

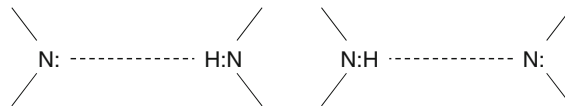
translation, the tautomeric nucleic acids bind with noncomplementary nucleic acids introducing the mutations. For instance, tautomeric  $A^*$  binds with C instead of T (U in mRNA), tautomeric  $C^*$  binds with A,  $G^*$  binds with T (U), and  $T^*$  binds ( $U^*$ ) with G. It is also possible that both bases in DNA pair to be in the tautomeric forms as illustrated in Fig. 4.4. Namely, when DNA is used for long-term storage of genetic information, the proton tunneling (tautomeric forms' creation) can contribute to random errors introduction. The probability of occurrence of tautomeric nucleic acids' forms is low so that it makes sense to assume that errors introduced by tautomeric forms are random. However, the presence of mutagens, carcinogens, electromagnetic radiation, and/or proton bombardment can either increase the probability of occurrence of tautomeric forms or damage the bases and consequently introduce the storage errors. In addition to increasing the rate of spontaneous mutations, the mutagens can cause the induced mutations due to deamination, oxidation, and alkylation. The DNA is the subject of continuous mutations and damages, and the cell has various mechanisms to deal with damages, including direct reversal (such as photoreactivation) mechanism, various damaged bases excising mechanisms (nucleotide excision repair (NER), base excision repair (BER), and nucleotide mismatched repair (NMR)), single-strand damage repair, double-strand breaks repair, and translesion synthesis (TLS). In this section, we assume that only the point-induced mutations, transitions, or transversions have remained upon the DNA repair process.

Even though the probability of occurrence of tautomeric forms in normal ambient conditions is low, we can associate the corresponding probability amplitude between normal and tautomeric forms and represent the nucleic acid states as quantum states. For instance, the superposition states corresponding to T and C can be represented as

$$\begin{aligned} |T\rangle &\doteq \sqrt{1 - P_{100, \text{pyr}}} |010\rangle |\text{pyr}\rangle + \sqrt{P_{100, \text{pyr}}} |100\rangle |\text{pyr}\rangle, \\ |C\rangle &\doteq \sqrt{1 - P_{010, \text{pur}} - P_{001, \text{pur}}} |100\rangle |\text{pur}\rangle + \sqrt{P_{010, \text{pur}}} |010\rangle |\text{pur}\rangle \\ &\quad + \sqrt{P_{001, \text{pur}}} |001\rangle |\text{pur}\rangle, \end{aligned}$$

where with  $|010\rangle |\text{pyr}\rangle$  we denoted the standard form of T, while  $|100\rangle |\text{pyr}\rangle$  the corresponding tautomeric form  $T^*$  that occurs with probability  $P_{100, \text{pyr}}$  ( $10^{-5}$ – $10^{-3}$ ). We use the notation  $|\text{pyr}\rangle (|\text{pur}\rangle)$  to denote that corresponding base is of pyrimidine (purine) type so that we can uniquely distinguish among different tautomeric forms. Strictly speaking, the probability amplitudes are complex numbers; however, from a quantum information theory point of view, the representation given above is sufficient.

To determine the exact probability of the occurrence of the tautomeric form, we can use the *double-well* model and tunneling effect in a fashion similar to that first described in [21]. By close inspection of Fig. 4.2, we can see that H-bonds in standard forms are asymmetric. Further, the protons have two equilibrium positions, for instance:



The principles of quantum mechanics indicate that the proton can move between these two equilibrium positions, so that it makes sense to observe the corresponding quantum states as the superposition of these two equilibrium states, with probability amplitude not necessarily  $1/\sqrt{2}$  (the exact probability amplitude needs to be determined either experimentally or by using double-well model [21]). The hydrogen bonds are weak bonds; and as it has been shown in [22], the electron clouds of complementary DNA strands experience dipole–dipole interaction, resulting in attractive van der Waals bonding. Therefore, the superposition of basekets can be caused by either van der Waals interaction or thermal fluctuations. When the DNA polymerase reads out the genetic information, it separates two DNA strands, and the nonstandard proton position can cause the error. For instance, the separation of AT in Fig. 4.2 can result into a nonstandard splitting as shown in Fig. 4.5. The nonstandard splitting, illustrated in Fig. 4.5, is responsible for time-shift deletion errors introduced during DNA replication. A nucleotide deletion error causes the amino acids inserted after the deleted nucleotide to be incorrect. The process of recognition of DNA polymerase and corresponding nucleotide can also be responsible for the creation of tautomeric forms, which is illustrated in Fig. 4.6.

The mutation rates can vary even within the same genome of a single organism, with typical values  $10^{-9}$ – $10^{-8}$ , particularly in bacteria. (Interestingly enough, the error-prone polymerase genes in human have the mutation rates  $10^{-3}$ – $10^{-2}$ , as shown by Johnson et al. [25].) In rapidly reproducing bacteria, even the mutation rates of the order  $10^{-9}$  accumulate fast over the time, leading to the resistance of bacteria to antibiotics [26]. Therefore, even though the tautomeric forms occur with low probability, they can introduce the occasional DNA storage and replication errors, which are responsible for mutations, aging, and evolution.



**Fig. 4.5** The illustration of nonstandard splitting during the replication process. The superscript + is used to denote the existence of additional proton, while the superscript – is used to denote a missing proton

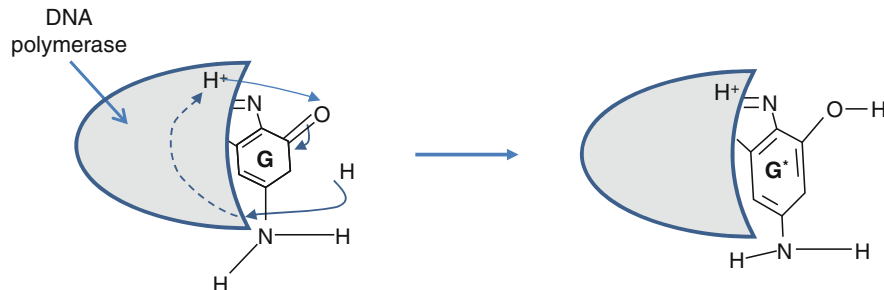


**Fig. 4.6** Tautomeric formation of  $G^*$  by proton transfer between DNA polymerase (active region shown by shaded area) and G

The models described above will be used to determine the probability of single and double codon errors (the probability of triple codon errors is so small that can be considered negligible). Notice that here we are concerned with small-scale mutations, such as point mutations, deletions, and insertions, rather than large-scale mutations (amplifications, chromosomal region deletions, chromosomal translocations, heterozygosity loss, etc.). Therefore, it is of crucial importance to determine how the quantum channel capacity changes with respect to single base error probability  $p$ . (Notice that double-base error probability is proportional to  $p^2$  and can be neglected when the probability  $p$  is low.) It is important to point out that some of the errors introduced during the DNA replication are corrected by various DNA repair processes. Repair enzymes are able to recognize improperly paired nucleotides, remove the wrong nucleotides, and replace them with the correct ones. Unfortunately, some of the replication errors stay uncorrected during DNA repair and thus represent permanent mutations. We assume that these permanent mutations contribute to the base error probability  $p$ . Given the fact that three bases determine the codon, representing the amino acid in protein synthesis, the single base error does not necessarily result in amino acid error. Since the genetic information is encoded in codons, it makes sense to assume that each codon represents a baseket. Because there exist 64 codons, the corresponding Hilbert code space is 64-dimensional. Similarly to the model due to [12], we assume that each codon is a baseket in this Hilbert space. For instance, the basekets (codons) corresponding to Ile are  $|IAUU\rangle$ ,  $|IAUA\rangle$ , and  $|IAUC\rangle$ , and they span the subspace of Hilbert code space. The error introduced on the third codon will result in the same amino acid, and in classical biological channel modeling, this kind of code is a *degenerate code* as multiple codons result in the same amino acid.

In what follows, we describe three interesting scenarios. In scenario (i), we assume that  $|Ile\rangle$ -state is a completely mixed state, a statistical mixture of basekets each occurring with the same probability. The corresponding density state (operator) of an

amino acid is given by  $\rho_s = \sum_m \sqrt{p_m} |m\rangle\langle m|$ , where  $p_m$  describes the probability that a member of the ensemble (codon baseket) has been prepared in state  $|m\rangle$ . For instance,  $m \in \{\text{AUU}, \text{AUA}, \text{AUC}\}$  for Ile, and  $m \in \{\text{UUU}, \text{UUC}\}$  for Phe.

In scenario (ii), we assume that  $|\text{Ile}\rangle$ -state is a superposition of eigenkets of the corresponding Hamiltonian [12]:

$$\begin{aligned} |\text{Ile}\rangle &= a(-i|\text{AUU}\rangle - |\text{AUA}\rangle + |\text{AUC}\rangle) \\ &+ b\left[\frac{1}{2}(i - \sqrt{3})|\text{AUU}\rangle - \frac{1}{2}(i\sqrt{3} - 1)|\text{AUA}\rangle + |\text{AUC}\rangle\right] \\ &+ c\left[\frac{1}{2}(i + \sqrt{3})|\text{AUU}\rangle + \frac{1}{2}(i\sqrt{3} + 1)|\text{AUA}\rangle + |\text{AUC}\rangle\right], \end{aligned}$$

where  $a$ ,  $b$ , and  $c$  are probability amplitudes. (In the lack of experimental data, we assume that  $a = b = c$ .) In similar fashion, the  $|\text{Phe}\rangle$ -state is a superposition of eigenkets (eigenvectors)  $|\text{UUC}\rangle + |\text{UUU}\rangle$  and  $|\text{UUC}\rangle - |\text{UUU}\rangle$ :

$$|\text{Phe}\rangle = a(|\text{UUC}\rangle + |\text{UUU}\rangle) + b(|\text{UUC}\rangle - |\text{UUU}\rangle),$$

where  $a$  and  $b$  are corresponding probability amplitudes. In case (iii), we select one of the eigenkets from equations above at random. The same strategy is applied to other amino acids.

Since scenario (i) is just a particular instance of the mixed state model described in Chap. 2 (see Sect. 2.1.4), we describe the model due to Karafyllidis [12] with small modifications, since it provides high-level description used in scenarios (ii)–(iii). In this model, the DNA Hilbert space is spanned by 64 codon eigenkets denoted as  $|a^{(i)}\rangle = |NB_1NB_2NB_3\rangle$ , where  $NB_j \in \{\text{C, G, T, A}\}$ ,  $j \in \{1, 2, 3\}$ ,  $i \in \{1, 2, \dots, 64\}$ . Let the corresponding DNA Hamiltonian be denoted as  $\mathbf{H}_{\text{DNA}}$ . The corresponding eigenvalue equation can be written as  $a^{(i)} \mathbf{H}_{\text{DNA}} = a^{(i)} |a^{(i)}\rangle$ . From Chap. 2, it is clear that  $\mathbf{H}_{\text{DNA}}$  represented in terms of eigenkets is diagonal, i.e.,  $\mathbf{H}_{\text{DNA}} = \text{diag}(a^{(1)}, a^{(2)}, \dots, a^{(64)})$ . On the other hand, mRNA Hilbert space is spanned by 64 codon eigenkets denoted as  $|a^{(i)}\rangle = |NB_1NB_2NB_3\rangle$ , where  $NB_j \in \{\text{C, G, U, A}\}$ ,  $j \in \{1, 2, 3\}$ ,  $i \in \{1, 2, \dots, 64\}$ . Let the corresponding mRNA Hamiltonian be denoted as  $\mathbf{H}_{\text{mRNA}}$ . Similarly as for DNA,  $\mathbf{H}_{\text{mRNA}}$  represented in terms of eigenkets is diagonal, i.e.,  $\mathbf{H}_{\text{mRNA}} = \text{diag}(a^{(1)}, a^{(2)}, \dots, a^{(64)})$ . The eigenvalues of  $\mathbf{H}_{\text{mRNA}}$  can be enumerated by using the standard genetic code given in Table 3.1 of Chap. 3. Alternatively, the enumeration as described in [12] can be used. Based on the Table 3.1 of Chap. 3, we conclude that the standard genetic code is a degenerate code from the classical communication point of view as several codons can represent the same amino acid. By taking the standard genetic code into account, the corresponding Hamiltonian of a protein is block-diagonal [12]:

$$\mathbf{H}_{\text{Protein}} = \begin{bmatrix} E_{\text{AUG}} & & & & & & & \\ & E_{\text{UGG}} & & & & & & \\ & & \mathbf{B}_3 & & & & & \\ & & & \ddots & & & & \\ & & & & \mathbf{B}_{20} & & & \\ & & & & & E_{\text{UAA}} & & \\ & & & & & & E_{\text{UAG}} & \\ & & & & & & & E_{\text{UGA}} \end{bmatrix}, \quad (4.1)$$

where  $E_{\text{AUG}}$  and  $E_{\text{UGG}}$  denote the eigenvalues corresponding to Met and Trp. On the other hand, with  $E_{\text{UAA}}$ ,  $E_{\text{UAG}}$ , and  $E_{\text{UGA}}$ , we denoted the eigenvalues corresponding to three STOP codons. Finally, with  $\mathbf{B}_i$  ( $i = 3, 4, \dots, 20$ ), we denoted submatrices of eigenvalues corresponding to amino acids represented with multiple codons. Submatrices  $\mathbf{B}_i$ , where  $i \in \{3, 4, \dots, 11\}$ , are used to represent Asn, Asp, Cys, Gln, Glu, His, Lys, Phe, and Tyr, respectively, and are given by [12]

$$\mathbf{B}_i = \begin{bmatrix} E_i & a \\ a & E_i \end{bmatrix}, \quad i \in \{3, 4, \dots, 11\} \quad (4.2)$$

with corresponding eigenvalues being  $E_i \pm a$ , where  $a$  is the corresponding probability amplitude (that is not necessarily the same for different amino acids). Ile is encoded by three codons AUU, AUC, and AUA so that corresponding block-submatrix is given by [12]

$$\mathbf{B}_{12} = \mathbf{B}_{\text{Ile}} = \begin{bmatrix} E_{\text{Ile}} & a & a \\ a & E_{\text{Ile}} & ja \\ a & -ja & E_{\text{Ile}} \end{bmatrix}. \quad (4.3)$$

The corresponding eigenvalues are given by  $E_{\text{Ile}}, E_{\text{Ile}} \mp \sqrt{3}a$ . By solving the eigenvalue equation, the following eigenkets are obtained:

$$\begin{aligned} |\text{Ile}^{(1)}\rangle &= 3^{-1/2}(-j|\text{AUU}\rangle - |\text{AUA}\rangle + |\text{AUC}\rangle), \\ |\text{Ile}^{(2)}\rangle &= 3^{-1/2}\left[\frac{1}{2}(j - \sqrt{3})|\text{AUU}\rangle - \frac{1}{2}(j\sqrt{3} - 1)|\text{AUA}\rangle + |\text{AUC}\rangle\right], \\ |\text{Ile}^{(3)}\rangle &= 3^{-1/2}\left[\frac{1}{2}(j + \sqrt{3})|\text{AUU}\rangle + \frac{1}{2}(j\sqrt{3} + 1)|\text{AUA}\rangle + |\text{AUC}\rangle\right]. \end{aligned} \quad (4.4)$$

Clearly, the eigenkets are orthogonal to each other and represent a three-dimensional Hilbert subspace corresponding to Ile. For instance, the dot product of  $|\text{Ile}^{(1)}\rangle$  and  $|\text{Ile}^{(2)}\rangle$  is

$$\begin{aligned}
\langle \text{Ile}^{(2)} | \text{Ile}^{(1)} \rangle &= \frac{1}{3} \left[ \frac{1}{2} \left( -j - \sqrt{3} \right) \langle \text{AUU} | - \frac{1}{2} \left( -j\sqrt{3} - 1 \right) \langle \text{AUA} | + \langle \text{AUC} | \right] \\
&\quad (-j | \text{AUU} \rangle - | \text{AUA} \rangle + | \text{AUC} \rangle) \\
&= \frac{1}{3} \left[ \frac{1}{2} \left( -1 + j\sqrt{3} \right) + \frac{1}{2} \left( -j\sqrt{3} - 1 \right) + 1 \right] = 0.
\end{aligned}$$

Ala, Gly, Pro, Thr, and Val are represented by four codons so that the corresponding block-submatrices are [12]

$$\mathbf{B}_i = \begin{bmatrix} E_i & a & ja & a \\ a & E_i & a & ja \\ -ja & a & E_i & a \\ a & -ja & a & E_i \end{bmatrix}, \quad i \in \{13, 14, \dots, 17\}. \quad (4.5)$$

Corresponding eigenvalues are given by  $E_i \mp (1 \pm \sqrt{2})a$ , while the eigenkets are given by

$$\frac{\mp 1 \pm j}{2\sqrt{2}} | \text{Codon1} \rangle + \frac{\pm 1 \mp j}{2\sqrt{2}} | \text{Codon2} \rangle \mp \frac{1}{2} | \text{Codon3} \rangle + \frac{1}{2} | \text{Codon4} \rangle \quad (4.6)$$

where  $\text{Codon}_i$  ( $i = 1, \dots, 4$ ) denotes four codons used to represent the corresponding amino acid (Ala, Gly, Pro, Thr, and Val) as given in standard genetic code (see Table 3.1 of Chap. 3).

Finally, Arg, Leu, and Ser are represented by six codons each; and corresponding block-submatrices are given respectively as [12]

$$\mathbf{B}_{\text{Arg}} = \mathbf{B}_{18} = \begin{bmatrix} E_{\text{Arg}} & ja & a & a & ja & 0 \\ -ja & E_{\text{Arg}} & a & a & 0 & 0 \\ a & a & E_{\text{Arg}} & ja & 0 & ja \\ a & a & -ja & E_{\text{Arg}} & 0 & 0 \\ -ja & 0 & 0 & 0 & E_{\text{Arg}} & a \\ 0 & 0 & -ja & 0 & a & E_{\text{Arg}} \end{bmatrix}, \quad (4.7)$$

$$(\mathbf{B}_{\text{Arg}})_{mn} = \langle m | \mathbf{B}_{\text{Arg}} | n \rangle; \quad m, n \in \{\text{CGA, CGC, CGG, CGU, AGA, AGG}\}.$$

$$\mathbf{B}_{\text{Leu}} = \mathbf{B}_{19} = \begin{bmatrix} E_{\text{Leu}} & ja & a & a & a & 0 \\ -ja & E_{\text{Leu}} & a & a & 0 & 0 \\ a & a & E_{\text{Leu}} & ja & 0 & a \\ a & a & -ja & E_{\text{Leu}} & 0 & 0 \\ a & 0 & 0 & 0 & E_{\text{Leu}} & a \\ 0 & 0 & a & 0 & a & E_{\text{Leu}} \end{bmatrix}, \quad (4.8)$$

$$(\mathbf{B}_{\text{Leu}})_{mn} = \langle m | \mathbf{B}_{\text{Leu}} | n \rangle; \quad m, n \in \{\text{CUA, CUC, CUG, CUU, UUA, UUG}\}.$$

$$\mathbf{B}_{\text{Ser}} = \mathbf{B}_{20} = \begin{bmatrix} E_{\text{Ser}} & ja & a & a & 0 & 0 \\ -ja & E_{\text{Ser}} & a & a & a & 0 \\ a & a & E_{\text{Ser}} & ja & 0 & 0 \\ a & a & -ja & E_{\text{Ser}} & 0 & a \\ 0 & a & 0 & 0 & E_{\text{Ser}} & a \\ 0 & 0 & 0 & a & a & E_{\text{Ser}} \end{bmatrix}, \quad (4.9)$$

$$(\mathbf{B}_{\text{Ser}})_{mn} = \langle m | \mathbf{B}_{\text{Ser}} | n \rangle; \quad m, n \in \{\text{UCA}, \text{UCC}, \text{UCG}, \text{UCU}, \text{AGC}, \text{AGU}\}.$$

The corresponding eigenvalues are given by  $E_i \mp a$ ,  $E_i \mp (1 \pm \sqrt{3})a$  ( $i = 18, 19, 20$ ). The eigenkets can be obtained by solving the following eigenvalue equations:

$$a^{(i)} \mathbf{B}_i = a^{(i)} |a^{(i)}\rangle,$$

where  $a^{(i)}$  are eigenvalues given above and can be found in [12].

In derivation of block-submatrices (4.2), (4.3), (4.5), and (4.7)–(4.9), the following three rules are applied [12]:

1. There is no probability amplitude between any two codon basekets corresponding to different amino acids.
2. There exists a probability amplitude between any two codon baskets representing the same amino acid if they differ in one or two nucleobases.
3. There exists a probability amplitude between two codon basekets representing the same amino acid, while
  - (a) Donor/acceptor hydrogen bonding pattern (on the first two positions of Fig. 4.2) is different when the probability amplitude is  $a$ .
  - (b) Donor/acceptor hydrogen bonding pattern (on the first two positions) is the same when probability amplitudes are  $\pm ja$ .

Clearly, the model of DNA quantum information transfer described by applying the three rules above assumes that transcription and translation processes are perfect. We turn our attention now to the description of the quantum biological channel model, in which different sources of genetic errors are accounted for, which is applicable to all three scenarios discussed above. When the baseket  $|m\rangle$ , representing one of codons ( $m$ ), is transmitted over the quantum biological channel, it can be detected on the receiver (protein) side as baseket  $|n\rangle$  ( $n \neq m$ ) due to the presence of genetic noise. To completely characterize this quantum channel model, it is essential to determine baseket transition probabilities. As an illustration, in Fig. 4.7, we provide the transition diagram corresponding to Ile, while in Fig. 4.8, we provide the transition diagram corresponding to Phe. For Ile, only transitions caused by single base error in baseket  $|\text{AUU}\rangle$  are shown. On the other hand, for Phe, the single base error that caused transitions for  $|\text{UUU}\rangle$  has been shown. Other transitions can easily be obtained by following the same strategy. With  $p_{m,n}$ , we denoted the transition probability from baseket  $|m\rangle$ , representing the initial codon,

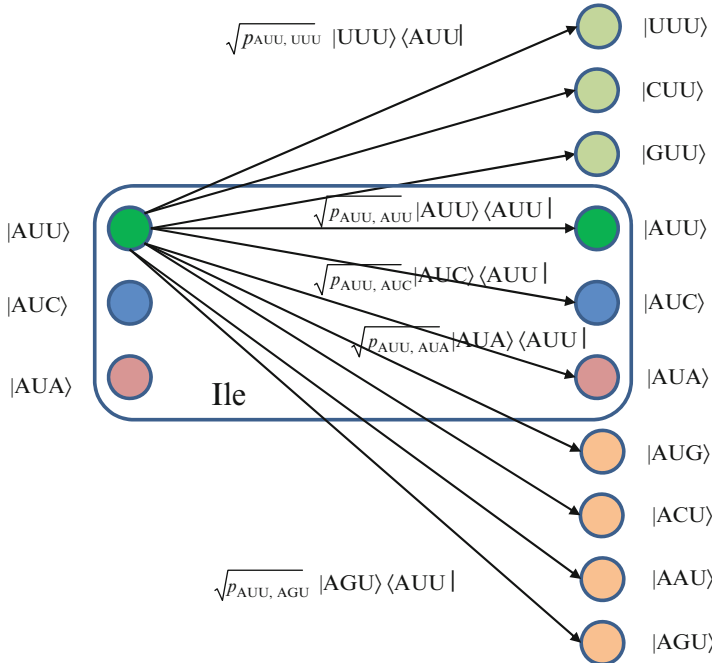


**Fig. 4.7** The quantum biological channel transition diagram for basekets corresponding to Ile. Only transitions from baseket  $|\text{AUU}\rangle$  due to the errors in single base of codon are shown. The  $p_{m,n}$  denotes the transition probability from baseket  $|m\rangle$  to baseket  $|n\rangle$ , where  $m \in \{\text{AUU}, \text{AUC}, \text{AUA}\}$  and  $n$  could be any of the 64 basekets. The Kraus operator  $E_{m,n}$  is obtained as  $E_{m,n} = \sqrt{p_{m,n}}|n\rangle\langle m|$

to baseket  $|n\rangle$ , representing the final codon, while corresponding Kraus operator is given by  $E_{m,n} = \sqrt{p_{m,n}}|n\rangle\langle m|$ . Notice that certain codon base errors will not result in a different amino acid, as illustrated in Figs. 4.7 and 4.8. As a remark, the model described in Figs. 4.7 and 4.8 is used to describe the collective action of various types of errors (DNA storage errors, DNA replication errors, transcription errors, and translation errors) on protein synthesis and the amount of DNA information transfer from DNA to protein.

True transitional probabilities can be obtained either from experimental data or by employing Löwdin's double-well model, while for illustrative purposes, we will assume that single base errors are dominant and independent of each other. The model described above is applicable to both spontaneous mutations and induced mutations (caused by mutagens, be they of chemical origin or introduced by radiation). In induced mutations, the base error probability increases as the concentration of corresponding chemical ( $\text{NH}_2\text{OH}$ , BrdU, *N*-ethyl-*N*-nitrosourea, ochratoxin A, EtBr, etc.) or the radiation level increases. Once the level of induced mutations goes well above the natural level, the quantum channel capacity starts to decrease dramatically as shown later in Sect. 4.4.

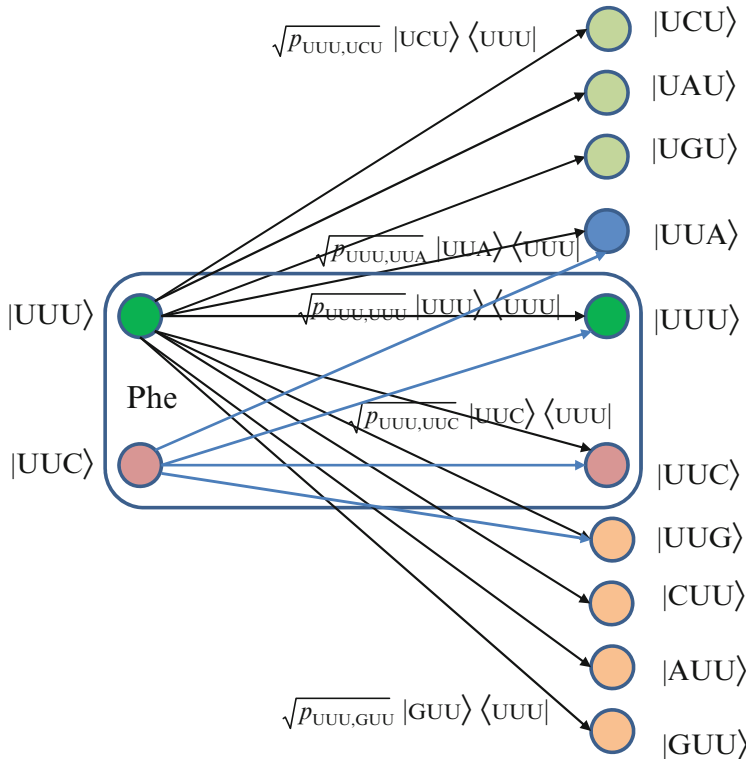


**Fig. 4.8** The quantum biological channel transition diagram for basekets corresponding to Phe

### 4.3 Sources of Genetic Errors and Genetic Noise: A Quantum-Mechanical Perspective

The different types of mutations and different sources of mutations have already been studied in Sect. 3.4 of Chap. 3. Here we use the concepts of quantum mechanics from Chap. 2 to explain them. In the previous section, we have learned that the tautomeric forms' formation, which can be contributed to the proton tunneling [21], is responsible for spontaneous errors introduced in DNA itself (see Fig. 4.4), during replication phase (see Fig. 4.3) or translation phase. For instance, the proton tunneling in DNA can cause the following transformation:

$$T - A \rightarrow T^* - A^*, \quad C - G \rightarrow C^* - G^*. \quad (4.10)$$

During the replication process, these tautomeric forms can cause multiplication of incorporation errors as shown in Fig. 4.9. The proofreading stage can eliminate some of the incorporation errors. However, the incorporation errors not corrected during the proofreading stage might cause the mutations.

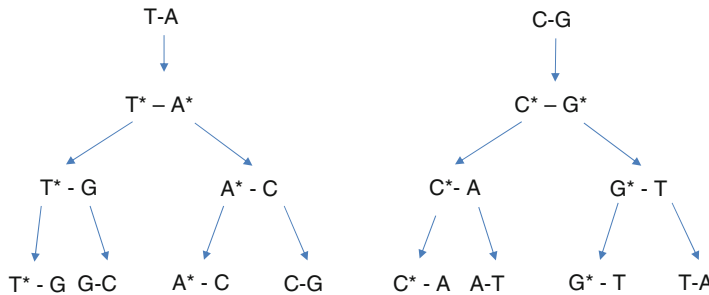
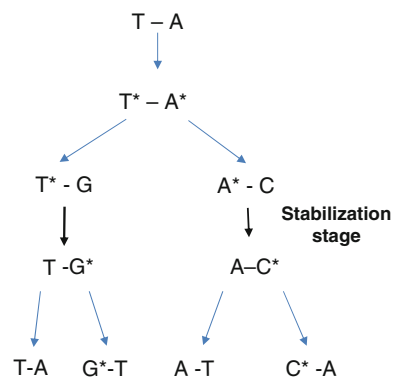


**Fig. 4.9** Illustration of the process of multiplication of incorporation errors during the replication phase

**Fig. 4.10** Illustration of the process of stabilization of the incorporation errors



Some of these mutations might be beneficial for the organism. However, some of the mutations can be damaging to the organism. This model can straightforwardly be generalized to the corresponding quantum model by introducing the superposition principle. Notice that some of the damaging mutations can be reverted through the mechanism known as the *adaptive mutation* [32–35]. It is well known that A–C\* and G\*–T pairs have lower total energies than A\*–C and G–T\* pairs. Because A\*–C and G–T\* forms are unstable, typically they move to lower energy-stable forms A–C\* and G\*–T. This energy transition can lead to the stabilization of previously introduced mutation as illustrated in Fig. 4.10, where the stabilization of T–A pair is described. This stabilization could be spontaneous or induced by the ambient conditions. Another related model that can be used to explain the adaptive mutation is *selected excitation model*, which is illustrated in Fig. 4.11. This model has two steps: *ambient-caused excitation* increases the energy for approximately 0.45 eV, which is insufficient for transition into tautomeric form that requires the energy of 0.5–0.8 eV. The additional energy can be provided by *electronic vibrational* degree of freedom. Namely, when the proton moves as the result of ambient-caused excitation, the lone electrons undergo vibrations as well.

This interaction is base pair specific, as each base pair creates local potential for its  $\pi$  electrons. The selective excitation model can be used to describe the stress-induced mutations. It is known that bacteria can change their DNA error-correction mechanism to adjust to the stress introduced by antibiotics. Instead of conventional polymerase, it employs an error-prone (low fidelity) polymerase. The selective excitation mechanism allows increasing the mutation rate locally where the harmful mutation has occurred. This will lead to further mutation of already existing mutation until new equilibrium is achieved. Once bacteria get adjusted to the environment, it moves to standard readout mechanism to prevent further mutations.

The same model can be used to explain the correction of +1 time-shift errors of *E. coli*. Namely, when *E. coli* colony is prepared with lac<sup>-</sup> gene (the superscript “-” means that lac gene is not functional), it was noticed in [35] that nonfunctional lac<sup>-</sup> gene mutates to functional lac<sup>+</sup> gene with 100 times higher mutation rate compared to non-lactose environment. The mutation that caused the lac gene to become nonfunctional is clearly harmful to bacteria. The starvation stress put bacteria in a regime to use the low-fidelity polymerase instead. This polymerase leads to further mutation of already mutated gene, which introduces -1 time-shift error correcting, therefore, the previous error and leading to functional lac<sup>+</sup> gene. Once the lac gene gets repaired, the bacteria move to standard readout mechanism. So, the starvation stress has caused the activation of error-prone mechanism corresponding to ambient induced excitation shown in Fig. 4.11. The vibrations in proton caused further electronic scattering, providing a sufficient energy for transition in tautomeric form, which lead to the process of stabilization similar to that shown in Fig. 4.10. This mechanism can also be related to conventional

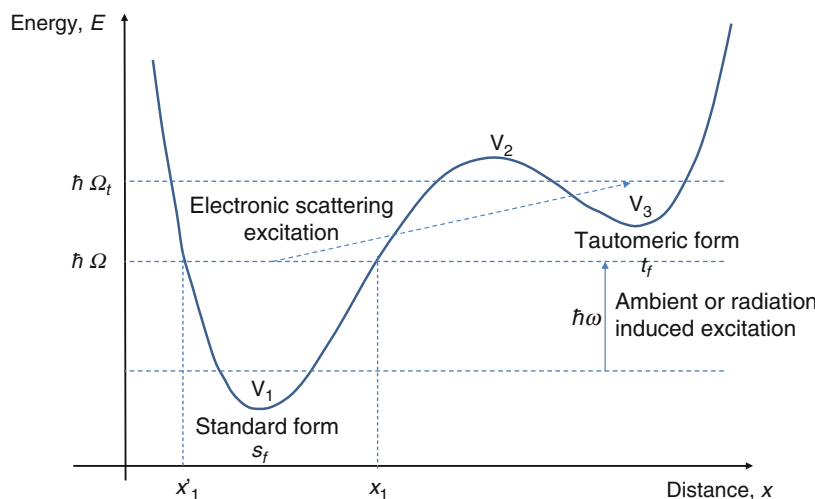


Fig. 4.11 Illustrating the selective excitation model

*quantum resonance model* [19]. The probability that a given base pair gets transferred to its tautomeric form is given by

$$p_t(t) = \left( \frac{\omega_1}{\Omega_R} \right) \sin^2(\Omega_R t/2), \quad \Omega_R = \left[ \omega_1^2 + (\Delta\omega - (\Omega_t - \Omega) - \omega)^2 \right]^{1/2}, \quad (4.11)$$

where  $\omega_1$  is related to the coupling efficiency and  $\Delta\omega$  is related to the energy gap ( $\hbar\Delta\omega$ ) between corresponding base pairs. Clearly, the probability of excitation has oscillatory character with frequency  $\Omega_R$ , and these oscillations are known as *Rabi oscillations*. The operability of excitation is highly dependent on energy-matching condition, while the coupling to the proton vibration (described by  $\omega_1$ ) determines the width of a resonant peak. The level of match with resonance condition dictates the rate of mutation. The base pair with well-satisfied resonance condition will mutate at a much higher rate and will eventually lead to repairing of the affected gene.

The presence of UV and ionized radiation can also help the transition from standard form to tautomeric form and, therefore, contribute to the mutation. The behavior of the proton in double-well can be described by the Schrödinger equation for a state ket:

$$i\hbar \frac{\partial}{\partial t} |\alpha, t_0; t\rangle = H |\alpha, t_0; t\rangle, \quad (4.12)$$

where  $|\alpha, t_0; t\rangle$  is the state ket at time instance  $t > t_0$  and  $H$  is the Hamiltonian operator. The final state  $|\alpha, t_0; t\rangle$  and the initial state  $|\alpha; t_0\rangle$  are related by  $|\alpha, t_0; t\rangle = U(t; t_0)|\alpha; t_0\rangle$ , where  $U(t; t_0)$  is the time-evolution operator, which for conservative system is given by  $U(t; t_0) = e^{-i\hbar H(t-t_0)}$ . It is convenient to express the proton state in terms of so-called energy eigenkets, with eigenvalues denoted by  $E_{a'}$  that satisfy the eigenvalue equation

$$H |a'\rangle = E_{a'} |a'\rangle. \quad (4.13)$$

The time-evolution operator can now be expanded in terms of projection operators as follows:

$$e^{-i\hbar H t} = \sum_{a'} \sum_{a''} |a''\rangle \langle a''| e^{-i\hbar H t} |a'\rangle \langle a'| = \sum_{a''} |a'\rangle e^{-i\hbar E_{a'} t} |a'\rangle. \quad (4.14)$$

By applying this time-evolution operator on initial state

$$|\alpha, t_0 = 0\rangle = \sum_{a'} |a'\rangle \langle a'| \alpha, t_0 = 0\rangle, \quad (4.15)$$

we obtain

$$|\alpha, t_0 = 0; t\rangle = e^{-\frac{i}{\hbar}Ht}|\alpha, t_0 = 0\rangle = \sum_{a'} |a'\rangle \langle a'| \alpha \rangle e^{-\frac{i}{\hbar}E_{a'}t}. \quad (4.16)$$

Let the standard form state and tautomeric form state be denoted as  $|s_f\rangle$  and  $|t_f\rangle$ , respectively. Let further the initial state be  $|\alpha, t_0 = 0\rangle = |s_f\rangle$ , which can also be written as follows:

$$|\alpha, t_0 = 0\rangle = |s_f\rangle = \frac{1}{2}(|s_f\rangle + |t_f\rangle) + \frac{1}{2}(|s_f\rangle - |t_f\rangle). \quad (4.17)$$

Based on (4.16), we can write

$$\begin{aligned} |\alpha, t_0 = 0; t\rangle &= \frac{1}{2}e^{-\frac{i}{\hbar}E_l t}(|s_f\rangle + |t_f\rangle) + \frac{1}{2}e^{-\frac{i}{\hbar}E_u t}(|s_f\rangle - |t_f\rangle) \\ &= \frac{1}{2}\left[ (|s_f\rangle + |t_f\rangle) + e^{-\frac{i}{\hbar}(E_u - E_l)t}(|s_f\rangle - |t_f\rangle) \right] e^{-\frac{i}{\hbar}E_l t} \\ &= \frac{1}{2}\left[ (|s_f\rangle + |t_f\rangle) + e^{-j2\pi\nu t}(|s_f\rangle - |t_f\rangle) \right] e^{-\frac{i}{\hbar}E_l t}, \end{aligned} \quad (4.18)$$

where the Bohr frequency associated with lower  $E_l$  and upper  $E_u$  energy levels is given by  $\nu = (E_u - E_l)/\hbar$ . Clearly, the proton *probability density*, denoted as  $\rho(x, t) = |\psi(x, t)|^2$ , can be found in (4.18) as  $|\psi(x, t)|^2 = |\langle x|\alpha, 0; t\rangle|^2$ , where  $x$  is a position coordinate (see Fig. 4.11) and  $\psi(x, t)$  is the *wave function*. Therefore, with certain probability, the proton can move in classically “forbidden” tautomeric states. This transition probability from the standard to tautomeric form gets higher for higher radiation levels (see Fig. 4.11), and consequently the probability of expressed mutation in replication phase is higher.

The wave function  $\psi(x, t)$  can be represented in terms of magnitude  $|\psi(x, t)| = \sqrt{\rho(x, t)}$  and phase  $S(x, t)$  as follows [36]:

$$\psi(x, t) = |\psi(x, t)| \exp\left[\frac{j}{\hbar}S(x, t)\right] = \sqrt{\rho(x, t)} \exp\left[\frac{j}{\hbar}S(x, t)\right]. \quad (4.19)$$

The spatial variation of the phase of the wave function is related to the *probability flux*  $\mathbf{j}$ , defined as

$$\mathbf{j}(x, t) = \frac{\hbar}{m} \operatorname{Im}\{\psi^* \nabla \psi\} = \frac{\rho}{m} \nabla S, \quad \mathbf{x} = (x, y, z). \quad (4.20)$$

The probability density  $\rho$  and probability flux  $\mathbf{j}$  are related through the *continuity equation*, derived from Schrödinger's time-dependent equation, as follows:

$$\frac{\partial \rho}{\partial t} + \nabla \cdot \mathbf{j} = 0. \quad (4.21)$$

In the short de Broglie wavelength regime, we can use Jeffreys–Wentzel–Kramers–Brillouin (JWKB) approximation. The phase function  $S(x,t)$ , also known as Hamilton's principal function, can be written as [36]

$$S(x,t) = \pm \int_x \sqrt{2m[E - V(x')]} dx' - Et. \quad (4.22)$$

For a stationary state,  $\partial \rho / \partial t = 0$ , and from continuity equation, we obtain [36]

$$\underbrace{\frac{\partial \rho}{\partial t}}_{=0} + \frac{1}{m} \frac{\partial}{\partial x} \left( \rho \frac{\partial S}{\partial t} \right) = 0. \quad (4.23)$$

By substituting (4.22) into (4.23) and by solving for  $\sqrt{\rho}$ , we obtain [36]

$$\sqrt{\rho} = \frac{\text{Constant}}{[E - V(x)]^{1/4}}. \quad (4.24)$$

By substituting (4.22) and (4.24) into (4.19), the wave function can be represented as [36]

$$\psi(x,t) = \frac{\text{Constant}}{[E - V(x)]^{1/4}} \exp \left[ \pm \frac{j}{\hbar} \int_x \sqrt{2m[E - V(x')]} dx' - \frac{j}{\hbar} Et \right], \quad (4.25)$$

which is known as JWKB solution, which is accurate in the short-wavelength region. The + sign corresponds to the wave traveling to the right and – sign to the wave traveling to the left. The corresponding equation in classically forbidden region, where  $E - V(x)$  is negative, can be written as [36]

$$\psi(x,t) = \frac{\text{Constant}}{[V(x) - E]^{1/4}} \exp \left[ \pm \frac{j}{\hbar} \int_x \sqrt{2m[V(x') - E]} dx' - \frac{j}{\hbar} Et \right]. \quad (4.26)$$

The JWKB solution has oscillatory behavior in the permitted region and exponentially decaying behavior in the forbidden region.

Let us now consider the case in which  $V_1 < E < V_3$ , as illustrated in Fig. 4.11. Clearly, there are two turning points (in which  $E = V(x)$ ),  $x'_1$  and  $x_1$ . Outside the turning points, the wave function is an exponentially decaying function like (4.25). Inside, between  $x'_1$  and  $x_1$ , the wave function has oscillatory character. For  $x = x_1$

turning point, the correct matching from the region right of  $x_1$  to region left of  $x_1$  can be achieved as follows [21]:

$$c_1 k^{-1/2} \sin \left( \int_x^{x_1} |k| dx' + \frac{\pi}{4} \right) \leftarrow c_1 |k|^{-1/2} \frac{1}{2} \exp \left( - \int_{x_1}^x |k| dx' \right), \quad (4.27)$$

where

$$k(x) = \frac{1}{\hbar} \sqrt{2m[E - V(x)]}. \quad (4.28)$$

On the other hand, for  $x = x'_1$  turning point, the correct matching from region left of  $x'_1$  to the region right of  $x'_1$  can be achieved as follows [21]:

$$-c_1 |k|^{-1/2} \frac{1}{2} \exp \left( - \int_x^{x_1} |k| dx' \right) \rightarrow c_1 k^{-1/2} \sin \left( - \int_{x'_1}^x |k| dx' + \frac{\pi}{4} \right). \quad (4.29)$$

Since expressions in the middle region must be identical, we can write

$$\int_x^{x_1} |k| dx' + \frac{\pi}{4} = - \int_{x'_1}^x |k| dx' + \frac{\pi}{4} + (n+1)\pi. \quad (4.30)$$

By rearranging, we obtain

$$\int_{x'_1}^{x_1} |k| dx' = (n+1/2)\pi. \quad (4.31)$$

Let us now consider the tunneling region for which  $V_3 < E < V_2$ , as illustrated in Fig. 4.12. Clearly, there are four turning points now, namely,  $x'_1, x_1, x'_3$ , and  $x_3$ . Outside  $x'_1$  and  $x'_3$ , the wave function must be an exponentially decaying function, and around the turning points ( $x = x_1$  and  $x = x'_3$ ), we have, respectively,

$$\begin{aligned} c_1 |k|^{-1/2} & \left\{ \frac{1}{2} \cos \gamma_1 \exp \left( - \int_x^{x'_1} |k| dx' \right) + \sin \gamma_1 \exp \left( \int_x^{x'_1} |k| dx' \right) \right\} \\ & \rightarrow c_1 k^{-1/2} \frac{1}{2} \sin \left( \int_{x'_1}^x |k| dx' + \pi/4 + \gamma_1 \right). \end{aligned} \quad (4.32)$$

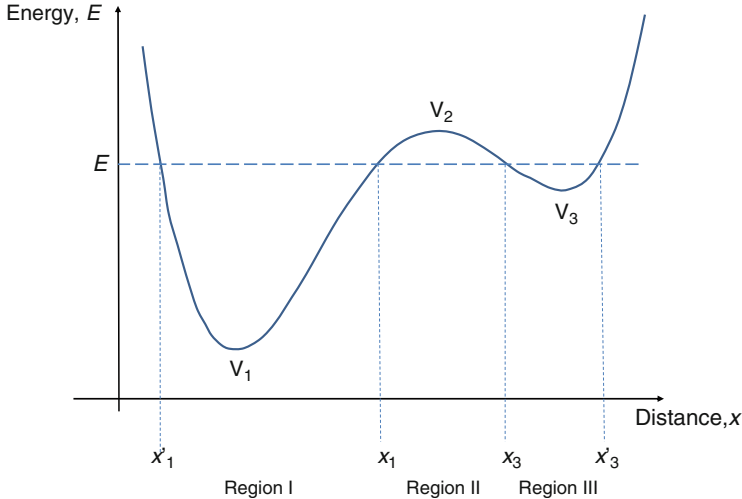


**Fig. 4.12** A typical asymmetric double-well potential model

$$c_3 k^{-1/2} \frac{1}{2} \sin \left( \int_x^{x'_3} k dx' + \pi/4 + \gamma_3 \right) \rightarrow c_3 |k|^{-1/2} \left\{ \frac{1}{2} \cos \gamma_3 \exp \left( - \int_{x'_3}^x |k| dx' \right) + \sin \gamma_3 \exp \left( \int_{x'_3}^x |k| dx' \right) \right\}. \quad (4.33)$$

where we used  $\gamma_1$  and  $\gamma_3$  to denote the phase constants in region I and III. From boundary conditions, we have that

$$\tan \gamma_1 \tan \gamma_3 = e^{-2K}/4, \quad (4.34)$$

where

$$K = \int_{x_1}^{x_3} |k| dx'. \quad (4.35)$$

Given the fact that the following must also be valid:

$$-c_1 |k|^{-1/2} \frac{1}{2} \exp \left( - \int_{x_1}^{x'_1} |k| dx' \right) \rightarrow c_1 k^{-1/2} \sin \left( \int_x^{x_1} k dx' + \int_{x_1}^{x'_1} k dx' - \frac{\pi}{4} \right), \quad (4.36)$$

the corresponding phases  $\gamma_1$  and  $\gamma_3$  are then  $\gamma_1 = -\int_{x'_1}^{x_1} k dx - \pi/2$ ,  $\gamma_3 = -\int_{x_3}^{x'_3} k dx - \pi/2$ . Therefore, the consistency can be written as [21]

$$\tan \left( \int_{x'_1}^{x_1} k dx + \pi/2 \right) \tan \left( \int_{x_3}^{x'_3} k dx + \pi/2 \right) = e^{-2K}/4, \quad (4.37)$$

where  $K$  is defined in (4.35). Since the left two limits correspond to the left-hand well, while the right two limits correspond to the right-hand well, the corresponding energy levels can be determined numerically [37–42].

This topic seems to be still an active research topic, judged by recent papers [41–43], even though it was introduced long time ago, in the 1960s, by Löwdin [21].

From quantum mechanics, we know that a particle represented by the wave packet oscillates in the well, in a similar fashion as a classical particle, and hits the barrier  $\nu_1$  times per second. By calculating the transmission coefficient by [21]

$$g = \frac{e^{-2K}}{(1 + e^{-2K}/4)^2} \simeq e^{-2K}, \quad (4.38)$$

the tunneling rate for the left well to the right one can be calculated by  $c_I = \nu_I g$ . The reciprocal of the tunneling rate can be used to evaluate the tunneling time:

$$\tau_I = c_I^{-1} = \frac{1}{\nu_I g}. \quad (4.39)$$

As the proton population builds up in the tautomeric well as the result of tunneling, the tunneling back from tautomeric to standard well is possible too with tunneling rate  $c_{III} = \nu_{III} g$ . The tunneling time from the right well to the left well will be

$$\tau_{III} = c_{III}^{-1} = \frac{1}{\nu_{III} g}. \quad (4.40)$$

The effective tunneling time can now be defined as

$$\tau = (c_I + c_{III})^{-1} = \frac{1}{(\nu_I + \nu_{III}) g}. \quad (4.41)$$

Providing that the transmission coefficient is very small, which is true for all tautomeric forms, and that there are no other perturbations present, the change of population of protons in the left well  $n_I$  and right well  $n_{III}$  can be described simply as

$$\frac{dn_I}{dt} = -c_I n_I + c_{III} n_{III}, \quad \frac{dn_{III}}{dt} = -c_{III} n_{III} + c_I n_I. \quad (4.42)$$

Since the initial conditions are given by  $n_I(0) = n_0$ ,  $n_{III}(0) = 0$ , the corresponding solutions are

$$\begin{aligned} n_I(t) &= \frac{c_{III}}{c_I + c_{III}} n_0 + \frac{c_I}{c_I + c_{III}} n_0 e^{-(c_I + c_{III})t}, \\ n_{III}(t) &= \frac{c_I}{c_I + c_{III}} n_0 - \frac{c_I}{c_I + c_{III}} n_0 e^{-(c_I + c_{III})t}. \end{aligned} \quad (4.43)$$

Clearly, the behaviors for  $n_I$  and  $n_{III}$  are similar to the capacitor discharging and charging, respectively, while  $c_{III}n_0/(c_I + c_{III})$  and  $c_I n_0/(c_I + c_{III})$  are corresponding DC components. When the time  $t$  is much larger than the effective tunneling time, the DC components dominate:

$$\begin{aligned} n_I(t) &\simeq \frac{c_{III}}{c_I + c_{III}} n_0 = \frac{\nu_{III}}{\nu_I + \nu_{III}} n_0, \\ n_{III}(t) &\simeq \frac{c_I}{c_I + c_{III}} n_0 = \frac{\nu_I}{\nu_I + \nu_{III}} n_0. \end{aligned} \quad (4.44)$$

On the other hand, when  $t \ll \tau$ , we can use the Taylor expansion to get

$$n_I(t) \simeq n_0 - c_I n_0 t + c_I n_0 (c_I + c_{III}) \frac{t^2}{2}, \quad n_{III}(t) \simeq c_I n_0 t - c_I n_0 (c_I + c_{III}) \frac{t^2}{2}. \quad (4.45)$$

The lifetime of the protons in the upper level  $i$  of the well can be determined as follows [39]:

$$\tau_i^{-1} = (8\pi\hbar\nu_i^2/c) \sum_k B_{ki}, \quad B_{ki} = (2\pi e^2/3\hbar^2) |\langle k|x|i \rangle|^2. \quad (4.46)$$

In the *presence of radiation*, the number of protons on the  $i$ th level, denoted as  $N_i$ , relative to ground level  $N_0$ , can be calculated as [39]

$$\frac{N_i}{N_0} = \prod_{k=1}^i \frac{B_{k,k+1} \rho_{\nu_{k,k+1}}}{A_{k,k+1} + B_{k,k+1} \rho_{\nu_{k,k+1}}}, \quad (4.47)$$

where  $\rho_{\nu_{k,k+1}}$  is the density of radiation. In (4.47), we use  $A_{k,k+1}$  and  $B_{k,k+1}$  to denote the Einstein's coefficients.

The number of protons tunneling from the left well to the right well at a given energy level, compared to the ground state, in the presence of radiation can be calculated as

$$\frac{n_{III}}{n_0} = \frac{1}{1 + \nu_{III}/\nu_I} \left[ 1 - e^{-\nu_I g(1 + \nu_{III}/\nu_I)t} \right] \prod_{k=1}^i \frac{\rho_{\nu_{k,k+1}}}{A_{k,k+1}/B_{k,k+1} + \rho_{\nu_{k,k+1}}}. \quad (4.48)$$

## 4.4 Quantum Biological Channel Capacity Evaluation

In quantum information theory, described in Chap. 2 (see also [19]), a quantum channel can be described by the transformation of an input density matrix  $\rho_s$  to the output density matrix  $\rho'_s$ . This transformation, described by the quantum operation (superoperator)  $U$ , can be represented as the following mapping  $\rho_s \xrightarrow{U} \rho'_s$ . Clearly, the superoperator  $U$  cannot be unitary due to the decoherence effects. However, the total evolution operator of quantum system and environment (ambient) can be represented by unitary operator  $U_{s,E}$ . Without loss of generality, let us assume that the environment (ambient)  $E$  is initially in a pure state  $|0_E\rangle$ . Hence, the expression for superoperator under this initial condition can be written as

$$\xi(\rho_s) = \text{Tr}_E U_{s,E} (\rho_s \otimes |0_E\rangle\langle 0_E|) U_{s,E}^\dagger, \quad (4.49)$$

where the partial trace  $\text{Tr}_E(\cdot)$  is taken with respect to the environmental degrees of freedom. Consider (4.49) as a completely positive linear transformation acting on the density matrix, which can be reconstructed as

$$\xi(\rho_s) = \sum_i E_i \rho_s E_i^\dagger. \quad (4.50)$$

The corresponding Kraus operators  $E_i$  in (4.50) must satisfy the completeness relationship such that  $\sum_i E_i^\dagger E_i = I$ .

For the quantum biological channel, the Kraus operator  $E_{m,n}$  performing the transformation from codon baseket  $|m\rangle$  to  $|n\rangle$  can be constructed according to the transition probabilities  $p_{m,n}$ , as discussed earlier. Clearly, the generic quantum biological channel model consists of 4096 Kraus operators. An arbitrary state,  $|\psi_{\text{in}}\rangle = \sum_m \alpha_m |m\rangle$ , represents the amino acid in genome; after transcription, point mutations, translation, and other genetic noise sources can be represented as

$$|\psi_{\text{out}}\rangle = \sum_n \beta_n |n\rangle, \quad \text{s.t.} \quad \sum_n \beta_n^2 = 1, \quad \text{and} \quad \beta_n = \sum_m \alpha_m \sqrt{p_{m,n}}, \quad (4.51)$$

while the resulting density matrix can be expressed as

$$\mathbf{V}(\rho_s) = \sum_{m,n} p_{m,n} U_{m,n} \rho_s U_{m,n}^\dagger. \quad (4.52)$$

We can rewrite the previous equation in terms of Kraus operators  $E_{m,n} = \sqrt{p_{m,n}} |n\rangle\langle m|$  as follows:

$$\mathbf{V}(\rho_s) = \sum_{m,n} E_{m,n} \rho_s E_{m,n}^\dagger, \quad (4.53)$$

which is consistent with (4.50), after replacing double-indexing with single-indexing. Notice that partial trace over the environment qubit has been omitted due to the fact that a mixing process can be described either with or without a fictitious environment [19]. In other words,  $\mathbf{V}(\rho_s)$  is equivalent to the density operator  $\xi(\rho_s)$  after tracing out the environment.

The genetic noise introduces uncertainty about the genome, and the amount of information related to initial density state  $\rho_s$ , which can be expressed as

$$S[U(\rho_s)] = -\text{tr}(U \log_2 U), \quad (4.54)$$

where  $S[U(\rho_s)]$  denotes the von Neumann entropy. The elements in the  $i$ th row and the  $j$ th column of the information matrix  $U$  can be found as

$$U_{i,j} = \text{tr}\left(E_i \rho_s E_j^\dagger\right). \quad (4.55)$$

Each element of  $U$  measures the exchangeable amount of information between the system and the environment during its interaction. With initial environment states being the pure states,  $S(U)$  gives the entropy of the environment. By employing the HSW theorem, introduced in Chap. 2, the quantum channel capacity can be calculated as

$$C(\rho_s) = \max_{\{p_j, \rho_j\}} \left\{ S[\mathbf{V}(\rho_s)] - \sum_j p_j S[\mathbf{V}(\rho_j)] \right\}, \quad \rho_s = \sum_j p_j \rho_j, \quad (4.56)$$

where the maximization is performed over all ensembles  $\{p_j, \rho_j\}$  of possible input states  $\rho_j$ . By choosing a priori probabilities of codons as  $p_i = 1/61$  and  $p_i = 0$  for stop codons (UAA, UAG, and UGA), the maximum information rate can be achieved since the source is discrete.

The results of quantum channel capacity with respect to the single base error probability are depicted in Fig. 4.13. The results of calculations are obtained by using (4.54)–(4.56).

Clearly, for the scenario (i), the quantum channel capacity is very similar to that of the classical channel, which is expected as the quantum biological information is represented as *statistical* (classical) mixture of codon basekets. This case can be considered as a lower bound on quantum biological channel capacity. The use of superposition state assumption, scenario (ii), results in higher quantum channel capacity, as shown in Fig. 4.13. Finally, the random selection of Hamiltonian eigenkets, spanning the subspace of corresponding amino acid, results in even higher quantum channel capacity, which can be interpreted as an upper bound on the quantum channel capacity. Therefore, the numerical results shown in Fig. 4.13 suggest that quantum effects could play a role in increasing robustness of information processing in biological systems. Even though the coherent quantum channel model shows small improvements in biological channel capacity than classical channel models, in addition to improved reliability of biological information

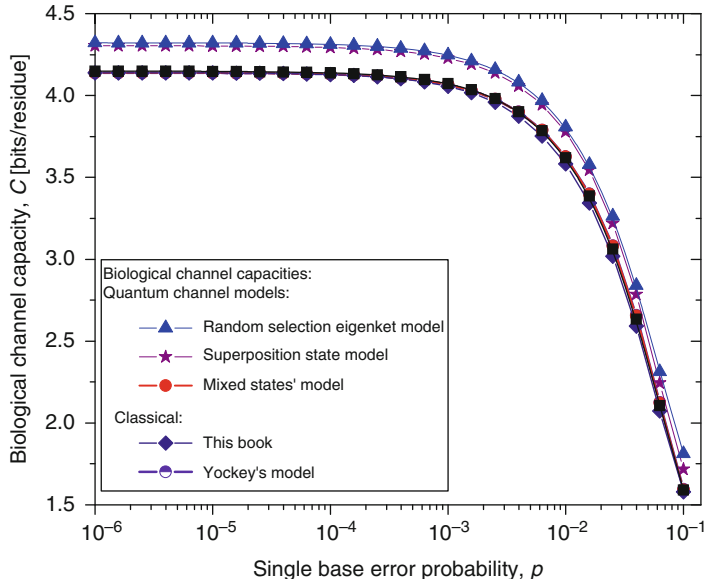


**Fig. 4.13** Quantum biological channel capacity against the single base error probability

processing, the quantum coherence could also improve the DNA replication rates as suggested by Patel [23]. Namely, as it has been advocated by Patel, the enzymes could provide the shielded environment for quantum coherence to be preserved sufficiently long for the completion of the base-pairing process. When the base error probability is larger than  $10^{-2}$ , the quantum biological channel capacity decreases dramatically, as shown in Fig. 4.13, and in that regime the quantum coherence of biological systems cannot be preserved. We conclude that for the base error probability higher than  $10^{-2}$ , the classical biological processes might have the same role as quantum processes as the gap between quantum and classical models becomes negligible. For base error probabilities close to 0.1, the biological channel capacity drops dramatically, suggesting that the cell is no longer capable of performing protein synthesis. Notice that in this analysis, different contributors to genetic noise (storage, replication, and translation errors) are included in the base error probability  $p$ .

For completeness of presentation, in Fig. 4.13, we also report the results of classical biological channel capacity obtained by using the model credited to Yockey [7, 8], which are in excellent agreement with classical channel capacity calculations obtained by developing the equivalent classical model to that shown in Figs. 4.7 and 4.8 (by simply converting codon basekets to classical nonbinary symbols), which is illustrated in Fig. 4.14.

The  $p_{m,n}$  denotes the transition probability from codon  $m$  to codon  $n$ ,  $p_{mn} = P(n|m)$ , where  $m \in \{\text{AUU, AUC, AUA}\}$  and  $n$  could be any of 64 codons. The codon

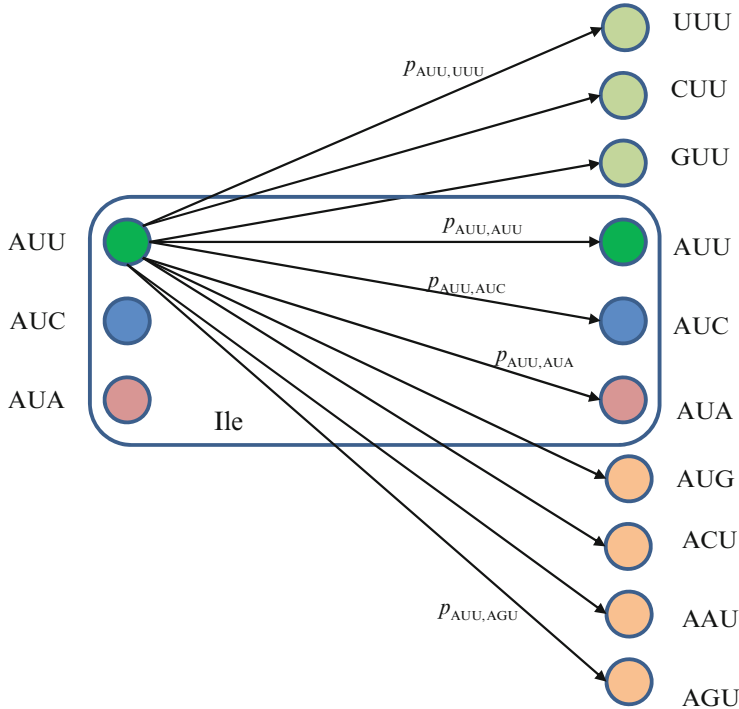


**Fig. 4.14** The classical biological channel transition diagram for codons corresponding to Ile. The  $p_{m,n}$  denotes the transition probability from codon  $m$  to codon  $n$ , where  $m \in \{\text{AUU, AUC, AUA}\}$  and  $n$  could be any of 64 codons

transition probabilities are employed to evaluate the classical channel capacity, defined as

$$C = \max [H(Y) - H(Y|X)] = \max [H(X) - H(X|Y)], \quad (4.57)$$

where  $H(Y)$  [ $H(X)$ ] stands for the biological channel output (input) entropy and  $H(Y|X)$  [ $H(X|Y)$ ] represents the conditional entropy (or the equivocation) of biological channel output (input) given the biological channel input (output)  $X$  ( $Y$ ). The entropy of biological channel output and conditional entropy are defined respectively as:

$$H(Y) = -\sum_{m,n} p(Y_n|X_m)P(X_m)\log_2 \left[ \sum_m p(Y_n|X_m) p(X_m) \right] \quad (4.58)$$

$$H(Y|X) = -\sum_m \sum_n p(Y_n|X_m) p(X_m) \log_2 P(Y_n|X_m), \quad (4.59)$$

where  $\{p(X_i)\}$  denotes the probability of occurrence of codons in DNA and  $\{p(Y_i|X_i)\}$  denotes the conditional probability of the received codons  $\{Y_i\}$  given the transmitted codons  $\{X_i\}$ . Since the source information encrypted in DNA is discrete, the maximum information rate in (4.57) is achieved for the uniform distribution of codons; that is,  $p_i=0$  for stop codons (UAA, UAG, and UGA) and  $p_i=1/61$  for other codons. The classical biological channel capacity curve in Fig. 4.13 is obtained by using (4.57)–(4.59) and model from Fig. 4.14 and represents a lower bound on biological channel capacity. The transition probabilities  $p_{mn}$  required in (4.58) and (4.59) are obtained numerically by using the model shown in Fig. 4.14 and the theory of Markov chains. These transition probabilities are also used in the quantum biological channel model (see Figs. 4.7 and 4.8) to determine probability amplitudes needed for calculation of quantum channel capacity by HSW theorem, by using (4.56).

## 4.5 Quantum Modeling of Bird Navigation Compass

There exist a growing evidence that migration birds can sense the direction of the gyromagnetic field based on chemical reaction whose product yield is dependent on the orientation of the reactants within the field [43–58]. Given that magnetic field is very weak, between 30 and 70  $\mu\text{T}$ , the magnetoreception mechanism can only detect the angle between the magnetic field lines and the earth surface. This indicates that the migration birds can only distinguish between a pole and equator, but cannot distinguish between north and south poles, which is sufficient for migration purpose. In addition to migration birds, the butterfly, the fruit fly, and other animals can also sense the direction.

There exist different models to explain the magnetoreception, including very exotic ones, but it appears that radical pair (RP) magnetoreception mechanism provides the most reasonable explanation. Namely, (free) radicals, the molecules containing an odd number of electrons and consequently having the half-integral total spin, are magnetically sensitive. The electron spin states can be denoted as  $|+\rangle = |+1/2\rangle = |\uparrow\rangle_e$  and  $|-\rangle = |-1/2\rangle = |\downarrow\rangle_e$ . A bipartite system containing two  $1/2$ -spin particles has four basekets:  $|++\rangle$ ,  $|+-\rangle$ ,  $|-+\rangle$ , and  $|--\rangle$ . Since each particle lives in a two-dimensional space, the resulting product space is four dimensional. To be more precise, the bipartite system can be described by a tensor product state

$$|1/2, m_1\rangle |1/2, m_2\rangle = |1/2, m_1\rangle \otimes |1/2, m_2\rangle. \quad (4.60)$$

The total spin state of this bipartite system can be determined by

$$|s, m\rangle = \sum_{m_1+m_2=m} c_{m=m_1+m_2}^{s=s_1+s_2} |s_1, m_1\rangle |s_2, m_2\rangle. \quad (4.61)$$

The corresponding basekets are

$$|1/2, +\rangle|1/2, +\rangle, |1/2, +\rangle|1/2, -\rangle, |1/2, -\rangle|1/2, +\rangle, |1/2, -\rangle|1/2, -\rangle. \quad (4.62)$$

Based on (4.61), there is one state with  $s=0$ , also known as *singlet* state:

$$|0, 0\rangle \doteq (|1/2, +\rangle|1/2, -\rangle - |1/2, -\rangle|1/2, +\rangle)/\sqrt{2}, \quad (4.63)$$

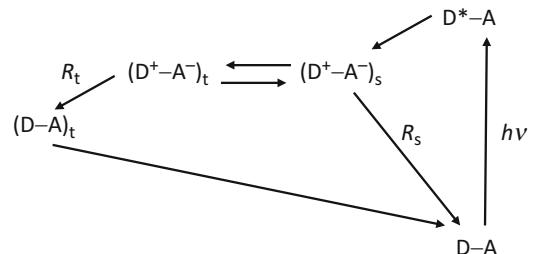
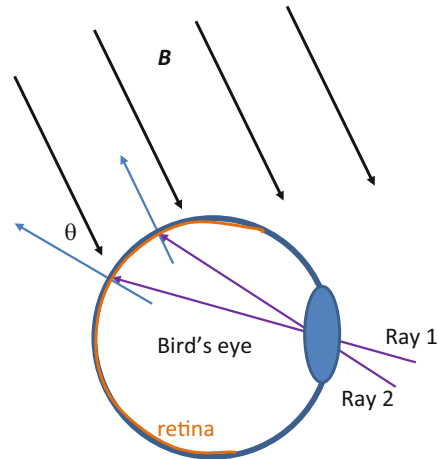
and three states with  $s=1$ , also known as *triplet* states:

$$\begin{aligned} |1, 1\rangle &\doteq |1/2, +\rangle|1/2, +\rangle, |1, -1\rangle \doteq |1/2, -\rangle|1/2, -\rangle, \\ |1, 0\rangle &\doteq (|1/2, +\rangle|1/2, -\rangle + |1/2, -\rangle|1/2, +\rangle)/\sqrt{2}. \end{aligned} \quad (4.64)$$

In what follows, we will denote the singlet state by  $|s\rangle \doteq |0, 0\rangle$ , while the corresponding triplet state will be denoted by  $|t_+\rangle \doteq |1, 1\rangle, |t_-\rangle \doteq |1, -1\rangle, |t_0\rangle \doteq |1, 0\rangle$ .

The bird retina contains magnetoreceptors, most probably based on cryptochrome, as illustrated in Fig. 4.15(top). The wavelength of light ranges from UV to 565 nm (green) [54]. The inclination angle  $\theta$  between the normal to the retina at ray arrival point and the local geomagnetic flux density  $\mathbf{B}$  determines the singlet-triplet

**Fig. 4.15** The radial pair model describing the bird navigation compass



transition, which is illustrated in Fig. 4.15(bottom). The recombination can occur either from singlet or triplet states, leading to different end-product concentrations. Now let us consider a single such molecule (bipartite system) consisting of a donor particle D and an acceptor particle A with electronic ground state being a spin singlet state as shown in Fig. 4.15(bottom). The donor D absorbs a photon of energy  $\hbar\nu$  to move to an excited state [see Fig. 4.15(bottom)]. The two spatially separated electrons can interact with different local magnetic fields. Both electrons interact with local geomagnetic field, while one of them additionally interacts with a nucleus particle with a nuclear spin being either  $|\uparrow\rangle$  or  $|\downarrow\rangle$ . This interaction causes the oscillation between the singlet and triplet state. The time evolution is dependent on an inclination angle with the geomagnetic field. The singlet and triplet states decay with the rate constant  $R_s$  and  $R_t$ , respectively, into a singlet or triplet state. Since these two singlet and triplet molecules can be chemically distinguished, their relative concentration in the bird's retina is modulated by the inclination angle with the geomagnetic field, giving the bird the sense of orientation. Notice that this description is consistent with [57].

From the discussion above, it is evident that electron spin–nuclear spin state lives in eight-dimensional Hilbert space. Therefore, it is convenient to introduce the projection operators representing the spin-selective relaxation into singlet “shelf”  $|S\rangle$ , originating from the electron singlet state, as well as the spin-relaxation into triplet “shelf”  $|T\rangle$ , originating from the electron triplet states. The final product populations of singlet and triplet shelves dictate the singlet and triplet yields, respectively. The projection operators can be defined as

$$\begin{aligned} P_{S,\uparrow} &= |S\rangle\langle s, \uparrow|, \quad P_{S,\downarrow} = |S\rangle\langle s, \downarrow|, \\ P_{T_+,\uparrow} &= |T\rangle\langle t_+, \uparrow|, \quad P_{T_+,\downarrow} = |T\rangle\langle t_+, \downarrow|, \quad P_{T_-,\uparrow} = |T\rangle\langle t_-, \uparrow|, \quad P_{T_-,\downarrow} = |T\rangle\langle t_-, \downarrow|, \\ P_{T_0,\uparrow} &= |T\rangle\langle t_0, \uparrow|, \quad P_{T_0,\downarrow} = |T\rangle\langle t_0, \downarrow|. \end{aligned} \tag{4.65}$$

As indicated in Chap. 2, the density operator  $\rho$  is used to describe an ensemble of quantum states which represents a classical statistical mixture of kets. The time evolution of  $\rho$  can easily be derived from the Schrodinger equation applied on a ket  $|\psi\rangle$ :

$$\frac{d}{dt}|\psi\rangle = -\frac{j}{\hbar}H|\psi\rangle, \tag{4.66}$$

where  $H$  is the corresponding Hamiltonian. For pure states, we know that  $\rho = |\psi\rangle\langle\psi|$ , and by taking the time-derivative of  $\rho$ , we obtain

$$\dot{\rho} = \frac{d}{dt}(|\psi\rangle\langle\psi|) = \frac{d}{dt}|\psi\rangle\langle\psi| + |\psi\rangle\frac{d}{dt}\langle\psi|, \tag{4.67}$$

and by substituting (4.66) into (4.67), we obtain:

$$\frac{d\rho}{dt} = -\frac{j}{\hbar}[H, \rho]. \quad (4.68)$$

This time-evolution equation is valid for both pure and mixed states. The initial state in our problem is  $\rho(0) = (|s, \uparrow\rangle\langle s, \uparrow| + |s, \downarrow\rangle\langle s, \downarrow|)/\sqrt{2}$ . By extending this equation to include the decay processes assuming that decay rates are identical  $R_i = R_s = R_t = R$  ( $i = 1, 2, \dots, 8$ ), the time evolution of  $\rho$  can be described by standard Lindblad quantum master equation (QME):

$$\frac{d\rho}{dt} = -\frac{j}{\hbar}[H, \rho] + R \sum_i \left( P_i \rho P_i^\dagger - 0.5 \rho P_i^\dagger P_i - 0.5 P_i^\dagger P_i \rho \right). \quad (4.69)$$

To take into account the decoherence effects, we need to extend the equation above with Lindblad dissipater to get

$$\begin{aligned} \frac{d\rho}{dt} = & -\frac{j}{\hbar}[H, \rho] + R \sum_i \left( P_i \rho P_i^\dagger - 0.5 \rho P_i^\dagger P_i - 0.5 P_i^\dagger P_i \rho \right) \\ & + \sum_i \Gamma_i \left( N_i \rho N_i^\dagger - 0.5 \rho N_i^\dagger N_i - 0.5 N_i^\dagger N_i \rho \right), \end{aligned} \quad (4.70)$$

where  $N_i$  are the noise operators. The noise operators could be the Pauli operators  $X, Y, Z$  applied to each electron spin separately. The decoherence effects can also be described by the dephasing operators  $Z_j = (I - 2|\lambda_j\rangle\langle\lambda_j|)$  ( $|\lambda_j\rangle$  is the eigenket) applied to electron spin and nuclear spin separately. It is also possible to use the combination of these two models.

The experiments performed at Frankfurt am Main, where local geomagnetic field is 46  $\mu\text{T}$  and inclination is  $66^\circ$ , with European robins as test birds indicate that robins are sensitive to local geomagnetic field and get disoriented when the LED with wavelength higher than green has been used [54]. The maximum response is obtained for green LEDs (operating at 565 nm). The cryptochrome binds the flavin cofactor that governs the functioning of the protein. The redox cycle of flavin can be used to explain the creation of radical pairs as illustrated in Fig. 4.16, based on [54–56]. The oxidized form of flavin adenine dinucleotide (FAD<sub>ox</sub>) absorbs blue and/or UV light to be photoreduced to the semiquinone, which in robin is FADH<sup>•</sup>. The FADH<sup>•</sup> forms the first radical pair with tryptophan, denoted in Fig. 4.16 as FADH<sup>•</sup>/Trp<sup>•</sup>. The FADH<sup>•</sup> can be reoxidized back in a dark reaction, or, when the light is present, it can absorb blue, green, and/or UV light to be further reduced to the fully reduced form, denoted in Fig. 4.16 as FADH<sup>–</sup>. The fully reduced flavin can be reoxidized in a dark reaction to generate the second radical pair, denoted as FADH<sup>•</sup>/O<sub>2</sub><sup>–</sup>. The FAD  $\rightarrow$  FADH<sup>•</sup> and FAD  $\rightarrow$  FADH<sup>–</sup> reactions are affected by an external magnetic field, as described in text related to Fig. 4.15. The excited FADH<sup>•</sup> state is an intermediate, short-lived, state in this photocycle.

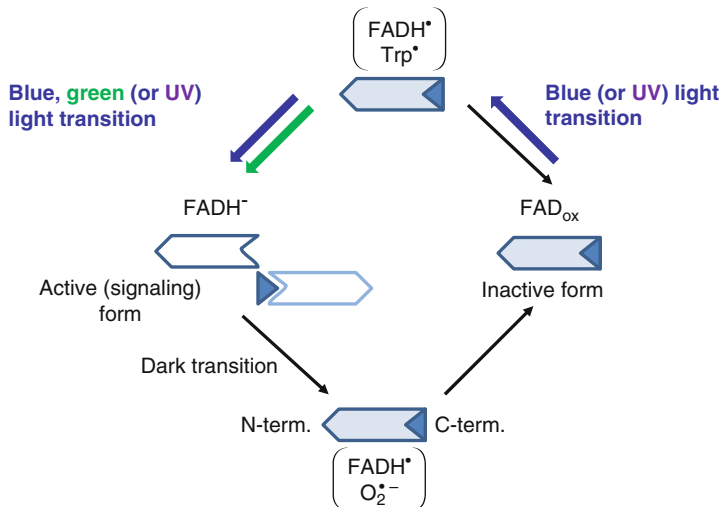


**Fig. 4.16** Illustration of the redox cycle of the flavin

Now we have all elements needed to complete the description of the model. The Hamiltonian of the interaction described in Fig. 4.15 is [18]

$$H = S_N A S_1 + \gamma \mathbf{B} (S_1 + S_2), \quad (4.71)$$

where  $S_N$  is the nuclear spin operator,  $A$  is the hyperfine tensor coupling the nucleus and electron 1, and  $\mathbf{B}$  is the magnetic flux density vector. We use  $S_1$  and  $S_2$  to denote the spins of electron 1 and 2, respectively. The gyromagnetic ratio  $\gamma = \mu_0 g/2$ , where  $\mu_0$  is Bohr's magneton and  $g$ -factor is commonly 2. The anisotropic hyperfine tensor operator  $A$  is diagonal,  $A = \text{diag}(A_x, A_y, A_z)$ .

The magnetic flux density  $\mathbf{B}$  has DC and RF components, expressed in spherical coordinates  $(B, \theta, \phi)$  as follows [18]:

$$\begin{aligned} \mathbf{B} = & B_0 (\cos \varphi \sin \theta, \sin \varphi \sin \theta, \cos \theta) \\ & + B_{\text{RF}} \cos(\omega t) (\cos \phi \sin \theta, \sin \phi \sin \theta, \cos \theta). \end{aligned} \quad (4.72)$$

The geomagnetic flux density in Frankfurt am Main is 46  $\mu\text{T}$ , while the RF magnetic flux density has been varied in experiment described in [54] up to 450 nT. When the RF magnetic field is parallel to geomagnetic field, such weak RF magnetic field does not have an important effect on avian compass. However, for perpendicular RF magnetic field, the frequency of  $f_{\text{RF}} = 1.315 \text{ MHz}$  appears to be the most distractive to robin. This frequency approximately corresponds to the resonant excitation with the uncoupled electron spin, namely,  $\hbar\omega = 2\gamma B_0$ . Interestingly enough for  $B_{\text{RF}} = 150 \text{ nT}$ , this frequency is more destructive than higher frequency of 2.63 MHz (the robin avian compass might be too slow to react to such high frequencies).

The yield of the reaction product formed from the singlet shelf  $|S\rangle$ , the so-called singlet yield, can be determined by

$$\Phi_S = \int_0^\infty \langle P^S \rangle(t) \kappa e^{-jRt} dt, \quad (4.73)$$

where  $P^S$  is the singlet projection operator, whose expectation can be found as

$$\langle P^S \rangle(t) = \text{Tr}[P^S \rho(t)]. \quad (4.74)$$

To simplify the analysis, we could set  $\phi = \varphi = 0$  rad, thanks to the axial symmetry of the hyperfine tensor. Interestingly enough, for very low decay rates  $\kappa$ , the singlet yield can be found in closed form [58]

$$\Phi_S = \frac{1}{4} + \frac{1}{8} \cos^2 \theta, \quad (4.75)$$

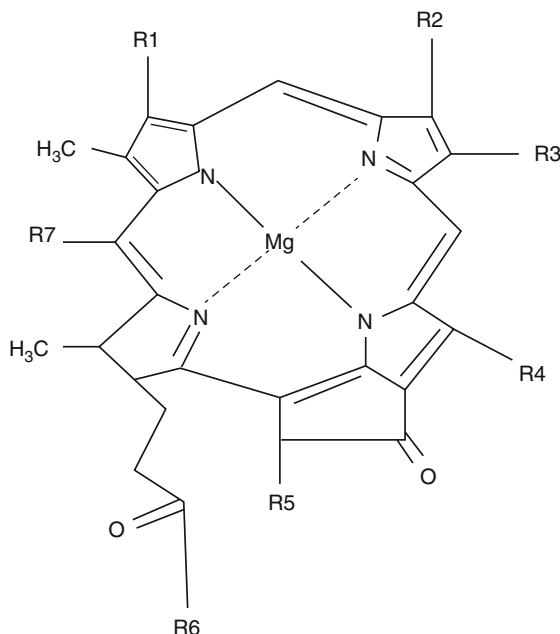
and varies between 1/4 and 3/8 (for zero field). For typical decay rates, around  $R \approx 10^4$  Hz, the singlet yield will be close to 0.3 for  $\theta$  up to 24°. In the presence of noise operators, we expect the singlet yield to be quite sensitive to decoherence effects for  $\Gamma_i = \Gamma \geq R$ . The electron spins in the radical pair must be protected for a sufficient time to be sensitive to the RF magnetic field. It has been found in [18] that coherence time is in the order of 100  $\mu$ s.

## 4.6 Quantum Aspects of Photosynthesis

Based on the sources of energy and carbon, the organisms can be classified in different categories. When organic molecules have been used as a source of energy, the organisms are called *organotrophs*, while when the inorganic compounds and substrates are used, the corresponding organisms are called *lithotrophs*. When the source of energy is the sunlight, the corresponding organisms are called *phototrophs*. On the other hand, when the source of energy originates from the redox reactions, the corresponding organisms are called *chemotrophs*. The organisms capable of synthesizing all required components directly from  $\text{CO}_2$  are called *autotrophs*, while those using an organic compound as the source of carbon are called *heterotrophs*.

The process of conversion of the sunlight energy into chemical energy is called photosynthesis. In the photosynthesis followed by the release of  $\text{O}_2$ , which is common for eukaryotes and some prokaryotes such as cyanobacteria, the sunlight energy being absorbed lies in the wavelength region 300–750 nm (the visible-light region and the portion of UV region). On the other hand, the prokaryotes including purple bacteria and green sulfur bacteria, which perform photosynthesis without releasing the oxygen, are absorbing the energy up to 1100 nm (in addition to visible

**Fig. 4.17** The generic chlorophyll formula. R<sub>7</sub> group is  $-H$  except in bacteriochlorophyll *c*, *e* where it is  $-CH_3$ . R<sub>5</sub> group is  $-H$  in bacteriochlorophyll *c*, *d*, *e*; otherwise, it is given by  $-CO-O-CH_3$ . The ring portion is responsible for the light absorption, while the hydrocarbon tail is responsible for coupling the Chl molecule to corresponding protein



region, the infrared region is important as well). In many organisms, the process of conversion of solar energy to chemical energy is very similar to the oxidative phosphorylation, as it involves the storage of energy as a proton concentration gradient. This proton motive force (PMF) is then used to drive the ATP synthesis. The electrons needed to drive the electron transport chain (ETC) originate from the light-harvesting proteins located in so-called photosynthetic reaction centers.

Even chemotrophs have photoreceptors such as flavins, carotenoids, and porphyrins. However, the photosynthetic organisms possess specific photoreceptor compounds known as the *chlorophyll* (Chl), shown in Fig. 4.17, which represents a chlorin pigment that is structurally similar to other porphyrin pigments.

It is a heterocyclic aromatic ring consisting three pyrroles and one pyrroline rings coupled through four  $=CH-$  linkages. In the center of the chlorin ring, a magnesium ion is located as illustrated in Fig. 4.17. The structure of  $R_i$ -groups is given in Table 4.1. The chlorophylls are the primary pigments in plants, algae, and cyanobacteria. On the other hand, the bacteriochlorophylls are photosynthetic pigments that occur in purple bacteria and green bacteria. In the same table, in the last column, we provide the dominant absorption regions.

Other important auxiliary photosynthetic pigments are *carotenoids* and are found in the chloroplasts and chromoplasts of plants and some other photosynthetic organisms (some bacteria and some fungi). They can be obtained as the result of condensation reaction of isoprene (2-methyl-1,3-butadiene)  $CH_2=C(CH_3)CH=CH_2$ . The most of carotenoids are obtained by condensation of eight isoprene's monomers. As an illustration,  $\beta$ -carotene is shown in Fig. 4.19.

Table 4.1 The structure of chlorophyll used in prokaryotes

Pigment	R1	R2	R3	R4	R6	Absorption region [nm]
Chlorophyll <i>a</i>	$-\text{CH} = \text{CH}_2$	$-\text{CH}_3$	$-\text{CH}_2 - \text{CH}_3$	$-\text{CH}_3$	Phytol	680–685
Chlorophyll <i>b</i>	$-\text{CH} = \text{CH}_2$	$-\text{C} = \text{O}$	$-\text{CH}_2 - \text{CH}_3$	$-\text{CH}_3$	Phytol	650–660
Bacteriochlorophyll <i>a</i>	$-\text{CO} - \text{CH}_3$	$-\text{CH}_3$	$-\text{CH}_2 - \text{CH}_3$	$-\text{CH}_3$	Phytol or geranylgeraniol	850–890
Bacteriochlorophyll <i>b</i>	$-\text{CO} - \text{CH}_3$	$-\text{CH}_3$	$=\text{CH} - \text{CH}_3$	$-\text{CH}_3$		1020–1040
Bacteriochlorophyll <i>c</i>	$-\text{COH} - \text{CH}_3$	$-\text{CH}_3$	$-\text{CH}_2 - \text{CH}_3$	$-\text{CH}_2 - \text{CH}_3$	Phytol or farnesol	750–760
Bacteriochlorophyll <i>d</i>	$-\text{COH} - \text{CH}_3$	$-\text{CH}_3$	$-\text{CH}_2 - \text{CH}_3$	$-\text{CH}_2 - \text{CH}_3$	Farnesol	720–740
Bacteriochlorophyll <i>e</i>	$-\text{COH} - \text{CH}_3$	$-\text{C} = \text{O}$	$-\text{CH}_2 - \text{CH}_3$	$-\text{CH}_2 - \text{CH}_3$	Farnesol	715–725

The bond between the C-atoms to which R2 and R3 are connected to is reduced in bacteriochlorophyll *a–d*. Phytol, farnesol, and geranylgeraniol have molecular formulas  $\text{C}_{20}\text{H}_{39}\text{OH}$ ,  $\text{C}_{15}\text{H}_{25}\text{OH}$ , and  $\text{C}_{20}\text{H}_{33}\text{OH}$ , respectively. The corresponding KEGG representations are provided in Fig. 4.18.

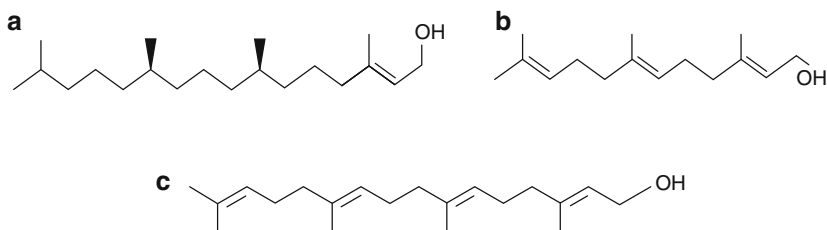


**Fig. 4.18** KEGG representations of: (a) phytol, (b) farnesol, and (c) geranylgeraniol

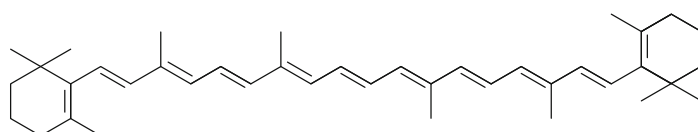


**Fig. 4.19** KEGG representation of  $\beta$ -carotene

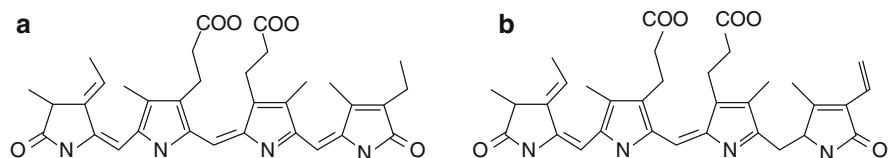


**Fig. 4.20** KEGG representation of the phycobilin: (a) phycocyanobilin and (b) phycoerythrobilin

The carotenoid-based pigments have the maximum absorption from 400 to 550 nm (in the blue and green portion of the visible-light spectrum). Therefore, the carotenoid-based pigments absorb the photons corresponding to the short-wavelength region and transfer the absorbed energy to chlorophyll. The efficiency of this transfer in cyanobacteria can be up to 90 %.

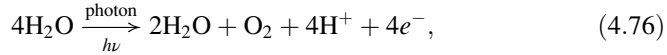
Cyanobacteria and certain algae contain red and blue pigments based on phycobiliproteins. Phycobiliproteins represent a complex between proteins and covalently bound phycobilins that act as the light-harvesting chromophores. The phycobilin is composed of four pyrrole/pyrrolidine rings linked in linear chain as shown in Fig. 4.20. The phycobiliproteins absorb the light in 450–700 nm wavelength region and transport the absorbed energy to chlorophyll with efficiency exceeding 90 %.

The photosynthetic apparatus of prokaryotes is composed of three functional modules:

1. *Receptor pigments* are organized into *light-harvesting* (LH) antennas' system and are responsible for the photon absorption and transfer of absorbed energy to the reaction centers.
2. *The photosynthesis reaction center* (RC) is responsible for transformation of absorbed electromagnetic energy into the chemical energy.

3. *The photosynthetic electron transport system* is responsible for the electron transport and accumulation of energy into ATP molecules.

The purple bacteria have a single RC, while the photosynthesis apparatus of cyanobacteria, algae, and plants employ two RCs operating in a series, known as photosystem II (PS II) and photosystem I (PS I) [59–61]. The PS II absorbs the photons and employs this energy to perform the photolysis (photooxidation):



where we used  $\hbar\nu$  to denote a single photon energy. On the other hand, during the PS I phase, the  $\text{NADP}^+$  gets reduced to NADH. The electron transfer from PS II to PS I is used to build up a proton motive force (PMF) (see Sect. 3.5 in the previous chapter) that is further used in formation of ATP. The NADPH and ATP are further used in Calvin–Benson cycle to produce the reduced sugar.

In prokaryotes, the RC and electron transport system are localized into cytoplasmic membrane (CPM). In cyanobacteria and prochlorophytes, the RC and electron transport system can also be located into thylakoid membranes. The *thylakoid membranes* form stacks of parallel sheets close to the CPM with a low packing density, which provides space for the external LH antennae. On the other hand, the localization of pigments in prokaryotes varies. In purple bacteria, the pigments are located in the CPM. In green bacteria, the pigments are located in a specialized photosynthetic antenna complex known as a *chlorosome* as well as in CPM. In cyanobacteria and prochlorophytes, the pigments are located in thylakoid membranes as well as in CPM. The structure of pigments involved in photosynthesis of prokaryotes is summarized in Table 4.2.

The process of creation of ATP from absorbed photon in the chromatophore is of the purple bacterium illustrated in Fig. 4.21. Namely, in purple bacteria such as *Rb. sphaeroides*, the photosynthetic apparatus is mainly located in so-called chromatophores, the lipid vesicles of 30–60 nm in diameter. The chromatophores are densely packed with the light-harvesting complexes of type 1 and 2, denoted as LH 1 and LH2. LH1 and LH2 absorb the incident photons and pass their energy to RC in the form of electron excitation, denoted by a purple arrow. To be more precise, the BChl or carotenoid within LH1/LH2 performs this absorption. The RC further transfers this energy to the ubiquinone (Q) in the form of electron–proton pair, wherein the proton ( $\text{H}^+$ ) is taken from the cytoplasm. The Q becomes the ubiquinol ( $\text{QH}_2$ ) after binding two electron–proton pairs. The  $\text{QH}_2$  further unbinds from the RC, diffuses inside the membrane, and passes its freight to the BC1 complex. The BC1 complex releases the protons to periplasm, maintaining the periplasmic positive and cytoplasmic negative charge. Two remaining electrons in BC1 are shuttled back to the RC by water-soluble electron carrier protein cytochrome. The proton gradient (or PMF) is then used in synthesis of ATP from ADP together with inorganic phosphate (Pi) in the ATP synthase (ATPase). Clearly, there are several roundabout processes, shown by close paths in Fig. 4.21, taking place inside the

**Table 4.2** The structure of pigments used in prokaryotes

Pigments	Purple bacteria	Green bacteria	Cyanobacteria	Prochlorophytes
The light receptors/ detectors	Chlorophyll <i>a+b</i>	Bacteriochlorophyll <i>a+c</i>	Bacteriochlorophyll <i>a+d, a+e</i>	Chlorophyll <i>a</i> <i>a+b</i>
Phycobiliproteins	N/A	Phycocyanin, phycoerythrin, allophycocyanin	N/A	N/A
Carotenoids	Aliphatic, aryl	Aryl, alicyclic	Alicyclic	Alicyclic
RC chlorophyll type	Bacteriochlorophyll <i>a, b</i>	Bacteriochlorophyll <i>a</i>	Chlorophyll <i>a</i>	Chlorophyll <i>a</i>

**Fig. 4.21** Illustration of the process of creation of ATP from absorbed photon in the chromatophore (only a curved portion of the chromatophore in the purple bacterium is shown)

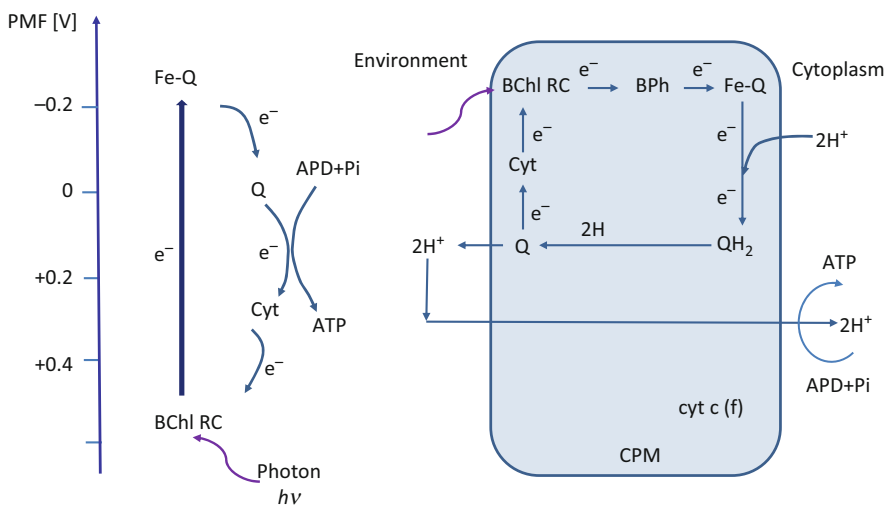
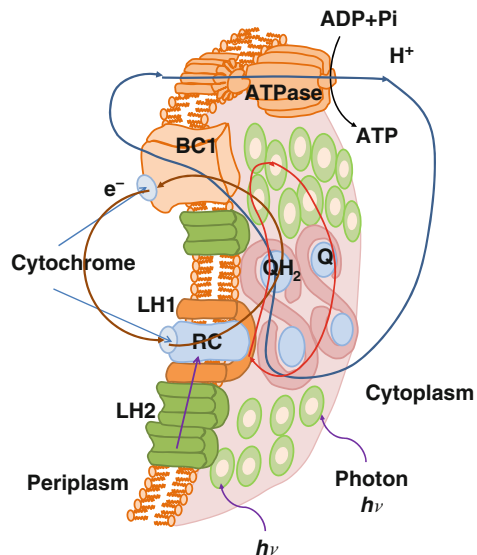
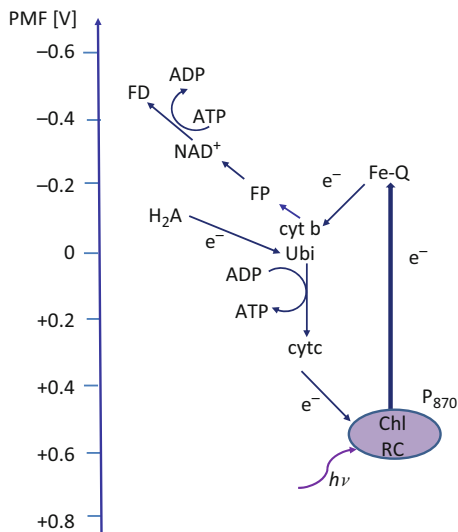


**Fig. 4.22** The cyclic electron transport system is closely related to the proton motive force (transmembrane proton gradient). *Cyt* cytochrome, *BPh* bacteriopheophytin (a chlorophyll molecule in which two hydrogen atoms replace the magnesium center), *CPM* cytoplasmic membrane

chromatophore. These processes are also described in Figs. 4.22 and 4.23, where exact compounds involved are identified [62–67]. Additionally, the PMF/energy of each particular biochemical reaction is identified as well. In prokaryotes, there are two types of electron transport system, the *cyclic* and *noncyclic* (acyclic) electron transport systems. The cyclic electron transport system is closely related to the

**Fig. 4.23** The electron transport system and photosynthesis' paths in purple bacteria. *Ubi* ubiquinone, *FD* ferredoxin, *cyt b (c)* cytochrome b (c), *Fe–Q* iron–quinone complex.  $P_{870}$  the pigment with maximum absorption wavelength 870 nm



proton motive force as illustrated in Figs. 4.21 and 4.22. During the cyclic electron transport, the end result is the creation of high energy ATP molecules, such as in PS I. During noncyclic electron transport, additionally reduction products NADPH and  $\text{H}^+$  are produced.

As shown in Fig. 4.23, the process of reduction of  $\text{NAD}^+$  is not light dependent. The light-absorbed energy changes the electron energy from 0.5 to  $-0.2$  V, which gets absorbed by Fe–Q complex. The Fe–Q complex energy is insufficient for either  $\text{NAD}^+$  or FD reduction, but instead an exogenous donor  $\text{H}_2\text{A}$  such as  $\text{H}_2\text{S}$  is needed against the PMF. This reverse, energy-consuming electron transport is performed by employing the energy obtained during the cyclic electron transport (see Fig. 4.22).

The LH1 complex in purple bacteria contains 32 BChls arranged in a ring, exhibiting the 16-fold symmetry, and 16 carotenoids [62, 65]. The spacing between two neighboring BChls' centers is around 1 nm. When a pigment absorbs the photon, the corresponding electron total energy can be found as addition of ground energy and the photon energy  $h\nu$ . When the pigment is isolated, it decays energy within 1 ns and reemits previously absorbed photon through the process known as fluorescence. However, when pigments are in close proximity, the excitation gets transferred by either Coulomb interaction or though quantum tunneling. This transfer of energy between pigments  $P_1$  and  $P_2$  can be denoted as  $P_1^*P_2 \rightarrow P_1P_2^*$ , where we use  $*$  to denote the excited state. When the separation between pigments  $P_1$  and  $P_2$  is larger than 1 nm, then the excitation transfer can be described by using *Förster* resonant energy transfer (FRET). Namely, this interaction is the Coulomb interaction based, and the interaction energy  $V_F$  is proportional to  $r_{P_1P_2}^{-3}$ , where  $r_{P_1P_2}$  is center–center separation of pigments. On the other hand, when the separation between pigments is smaller than 1 nm, then transfer mechanism can be described

by *Dexter* transfer of electrons, in which the excited electron moves from  $P_1$  to  $P_2$  while at the same time the ground electron from  $P_2$  to  $P_1$ . The Dexter interaction energy between  $P_1P_2$  and  $P_1P_2^*$ , denoted as  $V_D$ , is proportional to  $\exp(-r/r_D)$ , where  $r$  is the edge–edge separation of pigments (and  $r_D$  is characteristic Dexter distance). This interaction occurs as the results of corresponding orbital’s overlap due to close proximity of pigments. Finally, the excited state  $P_1^*P_2$  can decay by an electron transfer. There are two options: (1) the excited electron gets transferred from  $P_1$  to  $P_2$ , which can be denoted as  $P_1^*P_2 \rightarrow P_1^+P_2^-$ , indicating that  $P_1$  is a donor and  $P_2$  is an acceptor of excited electron, and (2) the ground electron from  $P_2$  gets transferred to ground state in  $P_1$ , which can be denoted as  $P_1^*P_2 \rightarrow P_1^-P_2^+$ . The corresponding interaction energy for charge separation  $V_{CS}$  is proportional to  $\exp(-r/r_{CS})$ , where  $r$  is again the edge-to-edge distance and  $r_{CS}$  is a characteristic constant of the process, typically in the order of 0.1 nm. According to the *Fermi’s golden rule*, the transfer rate between any two quantum states with energies  $E_i$  ( $i = 1, 2$ ) is given by [62]

$$R_{1 \rightarrow 2} = \frac{2\pi}{\hbar} V_{12}^2 \delta(E_1 - E_2), \quad (4.77)$$

where  $V_{12}$  is the interaction energy. In biochemical context, the  $\delta$ -function should be replaced by the spectral density  $S_{12}$ , which accounts for the overlap of emission spectrum of state 1 and the absorption spectrum of state 2. The Föster interaction energy transfer rate, since  $V_{12} \sim r_{12}^{-3}$ , will be [62]

$$R_{1 \rightarrow 2} = \frac{2\pi}{\hbar} \frac{\kappa^2}{r_{12}^6} S_{12}, \quad (4.78)$$

where the coupling coefficient is the function of the transition dipole orientation. The corresponding Hamiltonian of the process  $P_1^*P_2 \rightarrow P_1P_2^*$  will be

$$H = \begin{bmatrix} E_{P_1^*P_2} & V_{12} \\ V_{12} & E_{P_1P_2^*} \end{bmatrix}, \quad (4.79)$$

where  $E_{P_1^*P_2}$  and  $E_{P_1P_2^*}$  are energies of states  $P_1^*P_2$  and  $P_1P_2^*$ , respectively. This system of two pigments has two stationary states, obtained as eigenkets of the Hamiltonian, known as *excitons*. When  $E_{P_1^*P_2} = E_{P_1P_2^*}$ , the excitons states are simply

$$\mathbf{v}_1 = 2^{-1/2} \begin{bmatrix} 1 \\ 1 \end{bmatrix}, \quad \mathbf{v}_2 = 2^{-1/2} \begin{bmatrix} 1 \\ -1 \end{bmatrix}, \quad (4.80)$$

indicating that pigments share excitation equally. The excitons satisfy the characteristic equation

$$H\mathbf{v}_{1,2} = (E_{P_1^*P_2} \pm V_{12})\mathbf{v}_{1,2}. \quad (4.81)$$

When the energies of states  $P_1^*P_2$  and  $P_1P_2^*$  are different, the corresponding excitation will be asymmetrically distributed. Finally, in the absence of excitation, the Hamiltonian will be diagonal, and the corresponding eigenkets would be  $\mathbf{v}_1 = [1 \ 0]^T$  and  $\mathbf{v}_2 = [0 \ 1]^T$ .

LH2 in purple bacteria forms two BChl rings, orthogonal to each other. One of the rings has the same spacing as in LH1 but has smaller number of BChls, while the orthogonal ring has the BChl spacing of 2 nm. The number of LH2s in purple bacteria is about ten times higher than that of LH1 and RCs. The interaction energy of the nearest-neighbor BChls is typically much larger than the interaction energy of the closest to the nearest-neighbor BChls so that the corresponding Hamiltonian for B850/B800 BChls can be written as [62]

$$H = \begin{bmatrix} E & V & 0 & 0 & \cdots & 0 & V \\ V & E & V & 0 & \cdots & 0 & 0 \\ 0 & V & E & V & \cdots & \vdots & \vdots \\ 0 & 0 & V & E & \cdots & 0 & 0 \\ \vdots & \vdots & \vdots & \ddots & \ddots & & \\ 0 & 0 & \cdots & 0 & V & E & V \\ V & 0 & \cdots & 0 & 0 & V & E \end{bmatrix}, \quad (4.82)$$

where the diagonal elements denote energies of pigments (in this example, they are identical) and the off-diagonal elements  $H_{ij}$  ( $i \neq j$ ) denote the interaction energies between pigments  $P_i$  and  $P_j$ . The eigenkets of this Hamiltonian are obtained as [62]

$$\mathbf{v}_l = N^{-1/2} \sum_{n=1}^N \left[ \cos \left( \frac{2\pi}{N} ln \right) + \sin \left( \frac{2\pi}{N} ln \right) \right] \mathbf{e}_n; \quad l = 1, 2, \dots, N \quad (4.83)$$

where the vector  $\mathbf{e}_n$  has nonzero entry only at the  $n$ th location, corresponding to the fact that  $n$ th BChl is excited. It is straightforward to show that corresponding eigenkets satisfy the characteristic equation

$$H\mathbf{v}_l = \varepsilon_l \mathbf{v}_l, \quad (4.84)$$

where excitonic energy levels  $\varepsilon_l$  are given by [62]

$$\varepsilon_l = E + 2V \cos \left( \frac{2\pi}{N} l \right). \quad (4.85)$$

When a single B850/B800 BChl is excited, the excitation will spread very quickly, leading to relaxation process that populates the excitonic states  $\mathbf{v}_l$  with equilibrium Gibbs distribution:

$$p_l = \exp(-\beta \varepsilon_l) / \sum_{n=1}^N \exp(-\beta \varepsilon_m), \quad \beta = 1/(k_B T). \quad (4.86)$$

The transfer rate between two light-harvesting complexes LH2 can be calculated as the total transfer rate from a donor group  $N_D$  pigments to the acceptor group of  $N_A$  pigments as follows [62]:

$$R = \sum_{l=1}^{N_D} p_l \sum_{m=1}^{N_A} \frac{2\pi}{\hbar} \left( V_{lm}^{(D \rightarrow A)} \right)^2 S_{lm}, \quad (4.87)$$

where  $S_{lm}$  represents the spectral density between exciton donor states  $\mathbf{v}_l^{(D)}$  and acceptor states  $\mathbf{v}_m^{(A)}$ , defined respectively as

$$\mathbf{v}_l^{(D)} = \sum_{n=1}^{N_D} c_{nl}^{(D)} \mathbf{e}_n^{(D)}, \quad \mathbf{v}_m^{(A)} = \sum_{n=1}^{N_A} c_{nm}^{(A)} \mathbf{e}_n^{(A)}. \quad (4.88)$$

The corresponding interaction energy is determined by

$$V_{lm}^{(D \rightarrow A)} = \sum_{n=1}^{N_D} \sum_{k=1}^{N_A} c_{nl}^{(D)} c_{km}^{(A)} V_{nk}, \quad (4.89)$$

where  $V_{lm}$  is the interaction energy between the  $n$ th BChl from the donor set and the  $k$ th BChl from the acceptor set, dominated by the induced dipole–induced dipole interaction [62, 65]:

$$V_{lm} = \frac{1}{4\pi\epsilon_0\epsilon_r} \frac{\hat{\mathbf{d}}_l \cdot \hat{\mathbf{d}}_m - 3(\hat{\mathbf{d}}_l \cdot \hat{\mathbf{r}}_{lm})(\hat{\mathbf{d}}_m \cdot \hat{\mathbf{r}}_{lm})}{|\mathbf{r}_{lm}|^3}, \quad (4.90)$$

where  $\mathbf{r}_{lm}$  is the vector from the  $l$ th BChl of donor side to the  $m$ th BChl of acceptor side, while  $\hat{\mathbf{r}}_{mn} = \mathbf{r}_{mn}/|\mathbf{r}_{mn}|$  denotes the corresponding unit length vector. In (4.90),  $\hat{\mathbf{d}}_l = \mathbf{d}_l/|\mathbf{d}_l|$  ( $\hat{\mathbf{d}}_m = \mathbf{d}_m/|\mathbf{d}_m|$ ) denotes the direction of the  $l$ th ( $m$ th) BChl transition dipole moment. (Finally,  $\epsilon_r$  is the dielectric permittivity of the medium.) It has been found in [62] that the transfer rate between B850 rings of two neighboring LH2 is 0.126 THz.

The time evolution of the system on  $N$  pigments in the presence of single excitation can also be modeled as a quantum network of  $N$  sites, subject to the tight-binding Hamiltonian [65, 68]:

$$H = \sum_{n=1}^N \epsilon_n |m\rangle\langle m| + \sum_{m=1}^N \sum_{n < m}^N V_{mn} (|m\rangle\langle n| + |n\rangle\langle m|), \quad (4.91)$$

where the state  $|m\rangle$  indicates that the excitation is located at site  $m$ , the site energy is denoted by  $\epsilon_m$ , and the interaction energy between the  $m$ th and  $n$ th sites is denoted by  $V_{mn}$ . The coupling is mediated by Förster coupling, Dexter coupling, and electron

exchanges, as discussed above. This multi-pigment system also interacts with the environment including solvent and proteins. Under the assumption that fluctuations at different sites are uncorrelated, the following standard Lindblad quantum master equation, similar as in Sect. 4.5, can be used:

$$\frac{d\rho(t)}{dt} = -\frac{j}{\hbar}[H, \rho(t)] + \gamma \sum_i \left[ P_i \rho(t) P_i^\dagger - 0.5 \rho(t) P_i P_i^\dagger - 0.5 P_i P_i^\dagger \rho(t) \right], \quad (4.92)$$

with projection/generator operators  $P_i$  being defined as  $P_i = |i\rangle\langle i|$ . The parameter  $\gamma$  used in (4.92) corresponds to the pure dephasing rate. In the absence of a sink site, the equation of motion (4.92) yields to the exponential decay of any coherence in the density operator, indicating that the end result, in the long-time limit, will be equalization of the population sites. To account for the exciton recombination and trapping, we have to modify the Hamiltonian (4.91) and include anti-Hermitian terms as follows:

$$H_S = H - j\hbar(H_{\text{recombination}} + H_{\text{trapping}}), \quad (4.93)$$

where the recombination and trapping terms are defined as

$$H_{\text{recombination}} = \Gamma \sum_n |n\rangle\langle n|, \quad H_{\text{trapping}} = \sum_n R_n |n\rangle\langle n|, \quad (4.94)$$

where the recombination rate  $\Gamma$  is reversely proportional to the exciton's lifetime, which is around 1 ns. We use  $R_n$  to denote the trapping rate at site  $n$ . The probability that exciton is successfully captured at site  $n$  during interval  $[t, t + dt]$  is given by  $2R_n \langle n|\rho(t)|n\rangle dt$ . So the efficiency of the transfer within time interval  $[0, t]$  will be the averaged probability of multiple sites' trapping:

$$\eta(t) = 2 \sum_n R_n \int_0^t \langle n|\rho(t')|n\rangle dt'. \quad (4.95)$$

Interestingly enough, for two-pigment system experiencing neither recombination nor trapping, the closed-form solution is possible as shown in [65]. The corresponding Hamiltonian for two-pigment system is given by

$$H = \frac{1}{2}\varepsilon|1\rangle\langle 1| - \frac{1}{2}\varepsilon|2\rangle\langle 2| + \frac{1}{2}V(|1\rangle\langle 2| + |2\rangle\langle 1|), \quad (4.96)$$

where  $\varepsilon$  is now energy mismatch between sites 1 and 2. When this energy mismatch is sufficiently large, the problem is equivalent to a particle which hops between sites 1 and 2. The coherent evolution corresponds to rotation in  $x-z$  plane about an axis displaced for angle  $\theta = \arcsin(V/\hbar\Omega)$  from  $z$ -axis. The pure dephasing can be described by a Lindblad operator  $\gamma^{-1/2}(|1\rangle\langle 1| - |2\rangle\langle 2|)$ , where the dephasing rate is

reciprocal of the dephasing time. The system now instead of being in one state diffuses gradually to a mixed state  $2^{-1/2}(|1\rangle + |2\rangle)$ . This diffusion can also be interpreted as the random walk on the block sphere, shown in Chap. 2, with a step-size  $\theta$  and time elapsed per step being  $1/\gamma$ . To reach a steady-state, the system must perform approximately  $(\pi/\theta)^2$  steps so that the diffusion time can be estimated by  $(\pi/\theta)^2/\gamma$ . The efficiency for the two-pigment system can be defined as follows:

$$\eta(t) = -\frac{2}{\hbar} \sum_n R_n \langle n | \mathfrak{L}^{-1} \rho(0) | n \rangle dt', \quad \rho(0) = |n\rangle \langle n|, \quad (4.97)$$

where with  $\mathfrak{L}^{-1}$  we denoted the inverse of the operator defined by (4.92), namely:

$$\mathfrak{L}\rho(t) = -\frac{j}{\hbar}[H_S, \rho(t)] + L_\phi \rho(t), \quad (4.98)$$

where

$$L_\phi \rho(t) = \gamma \sum_i \left[ P_i \rho(t) P_i^\dagger - 0.5 \rho(t) P_i P_i^\dagger - 0.5 P_i P_i^\dagger \rho(t) \right]. \quad (4.99)$$

By substituting (4.93) into (4.98), we obtain

$$\mathfrak{L}\rho(t) = -\frac{j}{\hbar}[H, \rho(t)] + L_\phi \rho(t) - \{H_{\text{recombination}}, \rho(t)\} - \{H_{\text{trapping}}, \rho(t)\}. \quad (4.100)$$

By assuming,  $R_1 = 0$ ,  $R_2 = R$ , we obtain the following solution for (4.97) [65]:

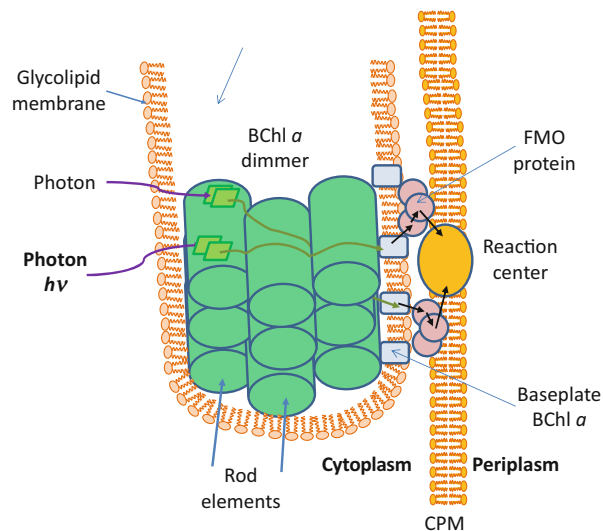
$$\eta = \frac{V^2 R (R + \gamma + 2\Gamma)}{V^2 (R + 2\Gamma) (R + \gamma + 2\Gamma) + \Gamma (\Gamma + R) [\epsilon^2 + \hbar^2 (R + \gamma + 2\Gamma)]}. \quad (4.101)$$

Clearly, for  $\Gamma = 0$ , the transfer efficiency is perfect as  $\eta = 1$ . The optimum dephasing rate can be determined as  $\gamma_{\text{opt}} = |\epsilon|/\hbar - 2\Gamma - R$ , which after substitution into (4.101) yields to the optimum efficiency [65]:

$$\eta_{\text{opt}} = \frac{V^2 \kappa}{V^2 (\kappa + 2\Gamma) + 2\Gamma (\Gamma + \kappa) \hbar |\epsilon|}. \quad (4.102)$$

In green bacteria and cyanobacteria, the pigments have been organized in special organizational units connected to the membrane but not being part of it [67–74]. These are known as *chlorosomes* in green bacteria and *phycobilisomes* in cyanobacteria. The configuration of the chlorosome as well as the excitation energy transfer is illustrated in Fig. 4.24. The electron microscopy of *C. limicola* has shown that a chlorosome unit contains rodlike elements with diameter of about 10 nm, consisting of layered BChl *c* molecules [74]. It was found in [74] that BChl

**Fig. 4.24** The chlorosome configuration and the excitation energy transfer. *FMO* Fenna–Matthews–Olson complex, *CPM* cytoplasmic membrane



$c$  molecules form piggyback dimer-based spiral parallel layers. The pigment arrangement on hollow optical cylinder enhances the harvesting absorption capabilities and also determines the direction of transfer as indicated in Fig. 4.24. The fast excitation transfer along the spiral layer expedites the interrod transfer to  $BChl$   $a$  in the baseplates. The energy is further transferred to the reaction center through FMO complex, exhibiting almost perfect efficiency. The FMO complex is composed of a protein backbone, which contains a hydrophobic pocket holding seven strongly coupled  $BChl$  molecules, each with electronic transition near 800 nm (the so-called  $Q_y$  transition) [63]. These seven states get coupled to one another electrostatically by dipole–dipole interaction. Therefore, we can construct  $7 \times 7$  Hamiltonian to describe the FMO operation principle quantum mechanically [75, 76], at low-energy limit, as follows:

$$H_S = \sum_m \sum_n (\varepsilon_m |m\rangle\langle m| + V_{mn} |m\rangle\langle n|), \quad (4.103)$$

where  $|m\rangle$  denotes an excitation state in chromophore spatially located at site  $m$ . The diagonal site energies are denoted as  $\varepsilon_m$ , while the strength of dipole–dipole interaction at different sites is represented by  $V_{mn}$ . The protein scaffold can be modeled as the environment (bath, ambient) of harmonic oscillators with Gaussian fluctuations.  $BChl$  interaction with the environment (bath) can be described with interaction Hamiltonian  $H_{SE} = |m\rangle\langle m|E_m$ , where  $E_m$  is the  $m$ th ambient operator. For the Lorentzian assumption, the correlation function can be determined as [76]

$$C_m(t) = \langle E_m(t)E_m(0) \rangle = \frac{1}{2\pi} \int_{-\infty}^{\infty} S(\omega) \frac{1}{1 - e^{-\hbar\omega/k_B T}} e^{i\omega t} d\omega, \quad (4.104)$$

where  $S(\omega)$  is spectral function given by  $S(\omega) = 2r_\lambda\omega/(\omega^2 + \gamma^2)$ , where typical FMO parameters for the reorganization energy  $r_\lambda$  and environment cutoff frequency  $\gamma$  are given as  $35 \text{ cm}^{-1}$  and  $50 \text{ cm}^{-1}$ , respectively.

To model the FMO electronic degrees of freedom as an open quantum system, we employ the time nonlocal master equation as follows [76]:

$$\begin{aligned} \frac{\partial}{\partial t}\rho(t) = & -j[H_S, \rho(t)] - \sum_m R_{\text{loss}}^m \{|m\rangle\langle m|, \rho(t)\} - R_{\text{trap}} \{|\text{trap}\rangle\langle \text{trap}|, \rho(t)\} \\ & - \sum_m \left[ |m\rangle\langle m|, \frac{1}{\hbar^2} \int_0^t C_m(t-t') e^{-j[H_S, \rho(t-t')]} |m\rangle\langle m| \rho(t') dt' - \text{h.c.} \right], \end{aligned} \quad (4.105)$$

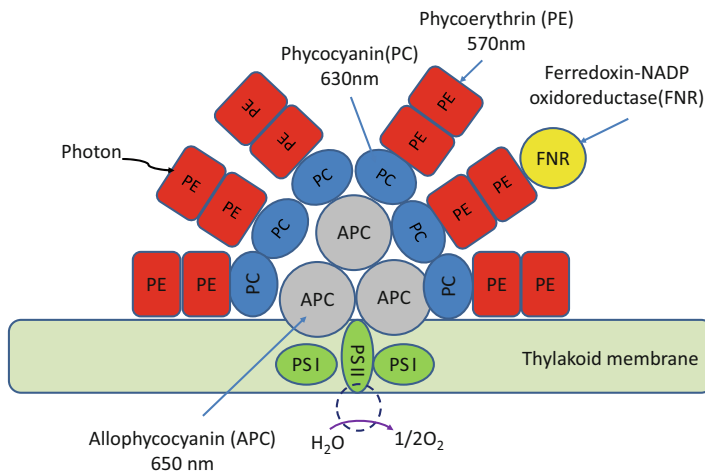
where the typical loss rate  $R_{\text{loss}}^{(m)} \cong (1 \text{ ns})^{-1}$ , while the typical RC trapping rate is  $R_{\text{trap}} = (0.5 \text{ ps})^{-1}$ . The third term in (4.105) is used to describe the RC excitation trapping process. The efficiency of energy transfer can now be estimated as [76]

$$\eta = 2R_{\text{trap}} \int_0^\infty \langle \text{trap} | \rho(t) | \text{trap} \rangle dt. \quad (4.106)$$

Using the calculations based on (4.105) and (4.106), the authors in [77] have found numerically that the FMO complex energy transfer efficiency is optimal (for green sulfur bacteria) with respect to variations in reorganization energy and environmental correlation time changes.

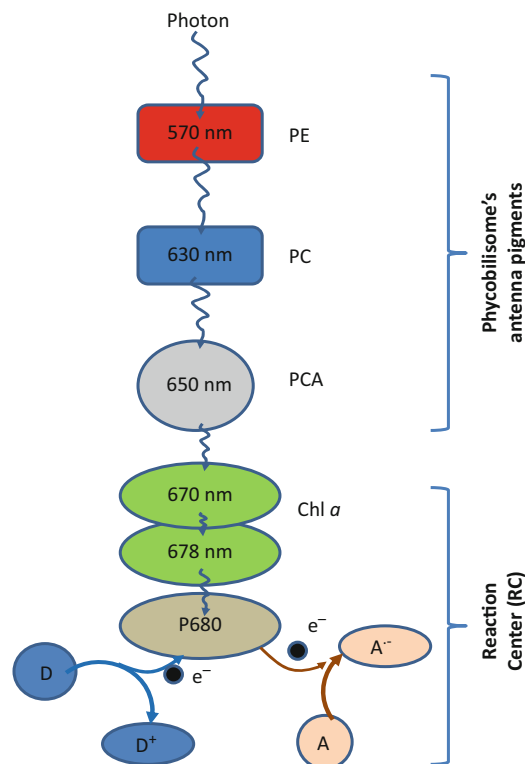
The light-harvesting antennae cyanobacteria, red algae, and glaucophytes are known as *phycobilisomes* [78, 79]. Phycobilisomes are in fact the protein complexes, containing up to 600 polypeptides, which are anchored to the thylakoid membranes. The phycobilisome, illustrated in Fig. 4.25, consists of the core composed of allophycocyanin (APC) to which several orthogonally oriented rods composed of stacked disks of phycocyanin (PC) and phycoerythrin (PE) are connected to. The energy of absorbed photons gets transferred through a number of antenna molecules. The transfer of energy is illustrated in Fig. 4.26. Once the energy gets transferred to Chl *a*, the excited P680 donates its electron, being in the excited state, to an electron acceptor A. The hole in the Chl *a* gets filled by the electron from an electron donor D.

The detailed electron transport system and photosynthesis' paths in cyanobacteria are illustrated in Fig. 4.27. The absorbed photon energy has been transferred to the RC Chl, as already described in Fig. 4.26. This absorption leads to the increase of P680 electron energy to the  $-0.2 \text{ V}$ , and P680 donates an electron. The oxidized P680 gets reduced with the help of electron obtained from water photolysis (photooxidation) reaction (4.76). The electron from the prime acceptor of PS II gets transferred by the ETC (see Fig. 4.27) to Chl *a* of PS I (pigment P700) and fills the hole of P700. As the electron gets transferred over ETC, the energy of the electron is used to pump hydrogen from the cytoplasm to the lumen, creating the



**Fig. 4.25** The tricylindrical hemidisoidal phycobilisome architecture

**Fig. 4.26** The flow of absorbed photon energy and photochemical reaction



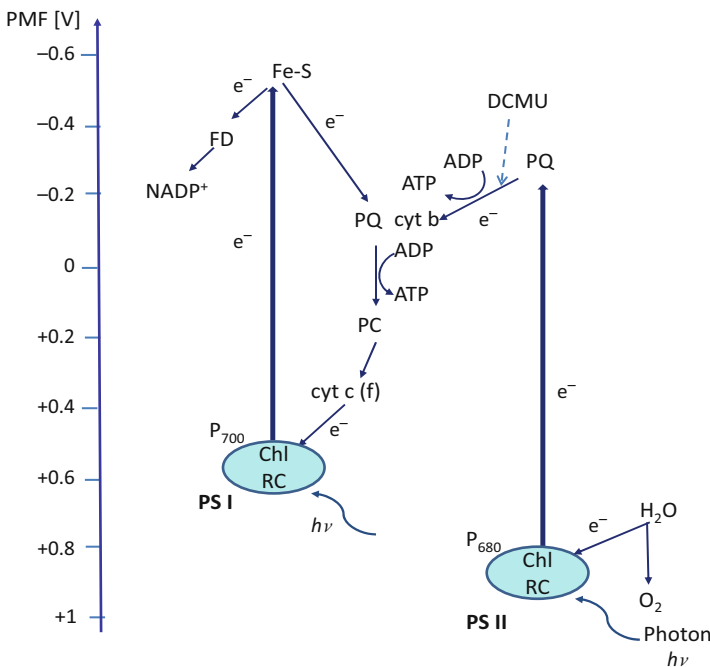


**Fig. 4.27** The electron transport system and photosynthesis' paths in cyanobacteria. *Fe-S* iron-sulfur protein, *PQ* plastoquinone, *DCMU* 3-(3,4-dichlorophenyl)-1,1-dimethylurea, *PC* plastocyanin, *FD* ferredoxin, *P<sub>680</sub>* (*P<sub>700</sub>*) the pigment with maximum absorption wavelength 680 nm (700 nm), *cyt b* (*c, f*) cytochrome b (*c, f*)

concentration gradient (PMF). This concentration gradient pumps ATPase that phosphorylates ADP to create ATP (see Fig. 4.27). So the electron gradually loses energy until it reaches the Chl in RC of PS I (P700). The low-energy electrons in PS I get reenergized by photon absorption in P700, and they are further passed through the ETC and used to reduce the electron carrier NADP<sup>+</sup> to NADPH. The photosynthesis' paths in cyanobacteria can also be described using quantum mechanics concepts, in similar fashion as it was done for purple bacteria.

## 4.7 Concluding Remarks

In Sect. 4.2, the quantum biological channel models suitable for study of quantum information transfer from DNA to proteins have been described. The sources of genetic noise and genetic errors have also been described in the same section. Various sources of genetic errors and genetic noise have also been described in Sect. 4.3 using quantum-mechanical formalism. The quantum biological channel capacity evaluation has been further described in Sect. 4.4. Section 4.5 has been

devoted to the use of quantum-mechanical concepts to describe the bird navigation compass. Finally, the quantum-mechanical aspects of photosynthesis have been discussed in Sect. 4.6.

## References

1. Wannier GH (1987) Statistical physics. Dover, New York (reprint)
2. Haynie DT (2008) Biological thermodynamics, 2nd edn. Cambridge University Press, Cambridge
3. Wolfe J (2002) Cellular thermodynamics. In: Encyclopedia of life sciences. Macmillan/Nature Publishing Group, London
4. Bray D (1995) Protein molecules as computational elements in living cells. *Nature* 376:307–312
5. Regev A, Shapiro E (2002) Cellular abstractions: cells as computation. *Nature* 419:343
6. Yuh CH, Bolouri H, Davidson EH (1998) Genomic cis-regulatory logic: functional analysis and computational model of a sea urchin gene control system. *Science* 279:1896–1902
7. Yockey HP (1974) An application of information theory to the Central Dogma and the Sequence Hypothesis. *J Theor Biol* 46:369–406
8. Yockey HP (2005) Information theory, evolution and the origin of life. Cambridge University Press, New York
9. Nakano T, Eckford AW, Haraguchi T (2013) Molecular communication. Cambridge University Press, Cambridge
10. Ball P (2011) Physics of life: the dawn of quantum biology. *Nature* 474:272–274
11. Haydon N, McGlynn SE, Robus O (2011) Speculation on quantum mechanics and the operation of life giving catalysts. *Orig Life Evol Biosph* 41:35–50
12. Karayllidis IG (2008) Quantum mechanical model for information transfer from DNA to protein. *Biosystems* 93:191–198
13. Vaziri A, Plenio MB (2010) Quantum coherence in ion channels: resonances, transport and verification. *New J Phys* 12:085001
14. Ogryzko VV (2008) Erwin Schroedinger, Francis Crick and epigenetic stability. *Biol Direct* 3:15
15. Davies P (2005) A quantum recipe for life. *Nature* 437:819
16. Davies PCW (2004) Does quantum mechanics play a non-trivial role in life? *Biosystems* 78:69–79
17. Van Grondelle R, Novoderezhkin VI (2010) Quantum design for a light trap. *Nature* 463:614–615
18. Gauger EM, Rieper E, Morton JJL, Benjamin SC, Vedral V (2011) Sustained quantum coherence and entanglement in the avian compass. *Phys Rev Lett* 106:040503
19. Djordjevic IB (2012) Quantum information processing and quantum error correction. Elsevier/Academic, Amsterdam
20. Arndt M, Juffmann T, Vedral V (2009) Quantum physics meets biology. *HFSP J* 3:386–400
21. Löwdin PO (1966) Quantum genetics and the aperiodic solid: some aspects on the biological problems of heredity, mutations, aging, and tumors in view of the quantum theory of the DNA molecule. In: Löwdin PO (ed) Advances in quantum chemistry, vol 2. Academic, New York, pp 213–360
22. Rieper E, Anders J, Vedral V (2012) Quantum entanglement between the electron clouds of nucleic acids in DNA. <http://arxiv.org/abs/1006.4053>. Accessed 5 Dec 2012
23. Patel A (2001) Quantum algorithms and the genetic code. *Pramana J Phys* 56:367–381
24. Watson JD, Crick FHC (1953) Genetical implications of the structure of deoxyribonucleic acid. *Nature* 171:964–967

25. Johnson RE, Washington MT, Prakash S, Prakash L (2000) Fidelity of human DNA polymerase  $\eta$ . *J Biol Chem* 275:7447–7450
26. Smolinski MS, Hamburg MA, Lederberg J (2003) Microbial threats to health: emergence, detection, and response. National Academies Press, Washington
27. Bianconi G, Rahmede C (2011) Unified framework for quasi-species evolution and stochastic quantization. *Phys Rev E* 83:056104
28. Bianconi G, Rahmede CA (2012) Comparison between the quasi-species evolution and stochastic quantization of fields. *Eur Phys J B* 85:197
29. Bianconi G, Rahmede C (2012) Quantum mechanics formalism for biological evolution. *Chaos Solitons Fractals* 45:555–560
30. Djordjevic IB (2012) Quantum biological channel modeling and capacity calculation. *Life* 2:377–391
31. Morris SC (2003) The navigation of biological hyperspace. *Int J Astrobiol* 2:149–152
32. Foster PL (1993) Adaptive mutation: the uses of adversity. *Annu Rev Microbiol* 47:467–504
33. Rosenberg SM (2001) Evolving responsively: adaptive mutation. *Nat Rev Genet* 2:504–515
34. Roth JR, Kugelberg E, Reams AB, Kofoid E, Andersson DI (2006) Origin of mutations under selection: the adaptive mutation controversy. *Annu Rev Microbiol* 60:477–501
35. Foster PL (2007) Stress-induced mutagenesis in bacteria. *Crit Rev Biochem Mol Biol* 42:373–397
36. Sakurai JJ (1994) Quantum mechanics, 2nd edn. Addison-Wesley, Reading
37. Rein R, Harris FE (1965) Studies of hydrogen-bonded systems. Potential-energy surface, tunneling, and tautomeric equilibria in the H-N···N and O···H-N bonds of the guanine-cytosine base pair. *J Chem Phys* 43:4415–4421
38. Lunell S, Sperber G (1967) Study of the hydrogen bonding in the adenine-thymine, adenine-cytosine, and guanine-thymine base pairs. *J Chem Phys* 46:2119–2124
39. Parker BR, van Every J (1971) Quantum tunneling in DNA. *Chem Phys Lett* 8:94–99
40. Tolpygo KB, Olkhovskaya IP (1972) Proton transitions in the hydrogen bonds of the DNA base pairs. *Chem Phys Lett* 16:550–554
41. Grant Cooper W (2012) Coherent states as consequences of keto-amino  $\rightarrow$  enol-imine hydrogen bond arrangements driven by quantum uncertainty limits on amino DNA protons. *Int J Quantum Chem* 112:2301–2323
42. Godbeer AD, Al-Khalili JD, Stevenson PD (2014) Environment-induced dephasing versus von Neumann measurements in proton tunneling. *Phys Rev* 90:012102
43. Wiltschko W (1968) Über den Einfluss statischer Magnetfelder auf die Zugorientierung der Rotkehlchen (*Erythacus rubecula*). *Z Tierpsychol* 25:537–558
44. Elmen S, Wiltschko W, Demong N, Wiltschko R (1976) Magnetic direction finding: evidence for its use in migratory indigo buntings. *Science* 193:505–508
45. Wiltschko R, Wiltschko W (2006) Magnetoreception. *Bioessays* 28:157–168
46. Wiltschko W, Wiltschko R (2005) Magnetic orientation and magnetoreception in birds and other animals. *J Comp Physiol A* 191:675–693
47. Ritz T, Adem S, Schulten K (2000) A model for photoreceptor-based magnetoreception in birds. *Biophys J* 78:707–718
48. Ritz T, Dommer DH, Phillips JB (2002) Shedding light on vertebrate magnetoreception. *Neuron* 34:503–506
49. Brocklehurst B (2002) Magnetic fields and radical reactions: recent developments and their role in nature. *Chem Soc Rev* 31:301–311
50. Johnsen S, Lohmann KJ (2005) The physics and neurobiology of magnetoreception. *Nat Rev Neurosci* 6:703–712
51. Mouritsen H, Ritz T (2005) Magnetoreception and its use in bird navigation. *Curr Opin Neurobiol* 15:406–414
52. Johnsen S, Lohmann KJ (2008) Magnetoreception in animals. *Phys Today* 61:29–35
53. Rodgers CT, Hore PJ (2009) Chemical magnetoreception in birds: the radical pair mechanism. *Proc Natl Acad Sci U S A* 106:353–360

54. Wiltschko R, Wiltschko W (2014) Sensing magnetic directions in birds: radical pair processes involving cryptochrome. *Biosensors* 4:221–242
55. Nießner C, Denzau S, Stapput K, Ahmad M, Peichl L, Wiltschko W, Wiltschko R (2013) Magnetoreception: activated cryptochrome 1a concurs with magnetic orientation in birds. *J R Soc Interface* 10:20130638. doi:[10.1098/rsif.2013.0638](https://doi.org/10.1098/rsif.2013.0638)
56. Müller P, Ahmad M (2011) Light-activated cryptochrome reacts with molecular oxygen to form a flavin-superoxide radical pair consistent with magnetoreception. *J Biol Chem* 286:21033–21040
57. Maeda K, Henbest KB, Cintolesi F, Kuprov I, Rodgers CT, Liddell PA, Gust D, Timmel CR, Hore PJ (2008) Chemical compass model of avian magnetoreception. *Nature* 453:387–390
58. Solov'yov IA, Ritz T, Schulten K, Hore PJ (2014) A chemical compass for bird navigation. In: Mohsheni M, Engel GS, Plenio MB (eds) *Quantum effects in biology*. Cambridge University Press, Cambridge, pp 218–236
59. Hu X, Damjanovic A, Ritz T, Schulten K (1998) Architecture and mechanism of the light harvesting apparatus of purple bacteria. *Proc Natl Acad Sci U S A* 95:5935–5941
60. Hu X, Ritz T, Damjanovic A, Authenrieth F, Schulten K (2002) Photosynthetic apparatus of purple bacteria. *Q Rev Biophys* 35:1–62
61. Geyer T, Helms V (2006) Reconstruction of a kinetic model of the chromatophore vesicles from *Rhodobacter sphaeroides*. *Biophys J* 91:927–937
62. Strümpfer J, Hsin J, Şener M, Chandler D, Schulten K (2011) Chapter 2: The light-harvesting apparatus in purple photosynthetic bacteria: introduction to a quantum biological device. In: Roux B (ed) *Molecular machines*. World Scientific, Singapore, pp 19–48
63. Engel GS (2014) Direct observation of quantum coherence. In: Mohsheni M, Engel GS, Plenio MB (eds) *Quantum effects in biology*. Cambridge University Press, Cambridge, pp 144–158
64. Kosztin I, Schulten K (2014) A chemical compass for bird navigation. In: Mohsheni M, Engel GS, Plenio MB (eds) *Quantum effects in biology*. Cambridge University Press, Cambridge, pp 123–143
65. Mohsheni M, Aspuru-Guzik A, Rebentrost P, Shabani A, Lloyd S, Huelga SF, Plenio MB (2014) Environment-assisted quantum transport. In: Mohsheni M, Engel GS, Plenio MB (eds) *Quantum effects in biology*. Cambridge University Press, Cambridge, pp 159–176
66. Romero E, Novoderezhkin VI, van Grondelle R (2014) Excitation energy transfer and energy conversion in photosynthesis. In: Mohsheni M, Engel GS, Plenio MB (eds) *Quantum effects in biology*. Cambridge University Press, Cambridge, pp 179–197
67. Bozo J (2007) Bioenergetics: basic principles. Gradjevinska Knjiga, Zrenjanin (in Serbian)
68. May V, Kühn O (2011) Charge and energy transfer dynamics in molecular systems. Wiley, Weinheim
69. Lambert N, Chen Y-N, Cheng Y-C, Li C-M, Chen G-Y, Nori F (2013) Quantum biology. *Nat Phys* 9:10–18 (Review article)
70. Engel GS, Calhoun TR, Read EL, Ahn T-K, Mančal T, Cheng Y-C, Blankenship RE, Fleming GR (2007) Evidence for wavelike energy transfer through quantum coherence in photosynthetic systems. *Nature* 446:782786
71. Ishizaki A, Fleming GR (2009) Theoretical examination of quantum coherence in a photosynthetic system at physiological temperature. *Proc Natl Acad Sci U S A* 106:17255–17260
72. Yen T-C, Cheng Y-C (2011) Electronic coherence effects in photosynthetic light harvesting. *Proc Chem* 3:211221
73. Trixler F (2013) Quantum tunneling to the origin and evolution of life. *Curr Organ Chem* 17:1758–1770
74. Egawa A, Fujiwara T, Mizoguchi T, Kakitani Y, Koyama Y, Akutsu H (2007) Structure of the light-harvesting bacteriochlorophyll c assembly in chlorosomes from *Chlorobium limicola* determined by solid-state NMR. *Proc Natl Acad Sci U S A* 104:790–795
75. Hayes D, Engel GS (2011) Extracting the excitonic Hamiltonian of the Fenna-Matthews-Olson complex using three-dimensional third-order electronic spectroscopy. *Biophys J* 100:2043–2052

76. Shabani A, Mohseni M, Rabitz H, Lloyd S (2014) Numerical evidence for robustness of environment-assisted quantum transport. *Phys Rev E* 89:042706
77. Shabani A, Mohseni M, Rabitz H, Lloyd S (2012) Efficient estimation of energy transfer efficiency in light-harvesting complexes. *Phys Rev E* 86:011915
78. MacColl R (1998) Cyanobacterial phycobilisomes. *J Struct Biol* 124:311–334
79. Guan X, Qin S, Zhao F, Zhang X, Tang X (2007) Phycobilisomes linker family in cyanobacterial genomes: divergence and evolution. *Int J Biol Sci* 3:434–445

# Chapter 5

## Quantum-Mechanical Modeling of Mutations, Aging, Evolution, Tumor, and Cancer Development

**Abstract** In this chapter, we will describe the quantum-mechanical models to accurately describe the process of creation of spontaneous, induced, and adaptive mutations. These models will be used to describe the processes of evolution and aging. The various theories of quantum evolution and epievolution will be studied as well. We then describe the Markovian chain-like classical and quantum-mechanical modeling of mutations and aging. In the same section, the hybrid quantum-classical biological channel model with memory is described as well. After that, various classical, semiclassical, and quantum models of cancer development are studied. The final section concludes the chapter.

### 5.1 Quantum-Mechanical and Quantum Mechanics-Like Models for Mutations and Evolution

We have already discussed the role of mutations in evolution process in Chap. 3; see Sect. 3.4. Based on several recent publications [1–12], it has become evident that both Darwinian type of evolution (random mutations followed by selection process) [13] and Lamarckian type of evolution (selected mutations beneficial to the organism) [14] are important. The modernized Lamarckian mechanism, which can also be called neo-Lamarckism, can be described as follows: environmental factors are introducing genomic changes, the mutations are targeted to specific genes, and the mutations provide the adaptation to the original cause. Clearly, this mechanism is well aligned with adaptive mutation mechanism discussed in Sect. 4.3 of the previous chapter (see also [15–22]). The Darwinian mechanism of evaluation is less demanding as no specialized mechanism is required to direct the change of the relevant genomic locus and restrict it to the specific mutations. Based on mutation models we discussed in previous chapter as well as references [1–12], it appears that both mechanisms can contribute to the evolution. For low stress levels, the spontaneous mutations seem to be a dominant source to evolution, suggesting Darwinian evolution mode is more relevant. On the other hand, for strong stress levels, the adaptive mutations dominate, indicating that Lamarckian

mechanism is more relevant in this regime. Other important publications discussing the role of quantum mechanics in evolution include [23–28].

The speed of evolution is directly proportional to the frequency of mutations, as we pointed out in Sect. 3.4. So, it is reasonable to assume that initially, at the beginning of biological evolution, mutations were more frequent than they are today thanks to the strong UV radiation and ionizing radiation. Furthermore, it is expected that the DNA repair mechanism in primitive forms of life was not that advanced. It is well known that mutations can be beneficial, neutral, or damaging to the organism. The mutation damaging the cell gets eliminated through the natural selection. The beneficial mutations, leading to the better adaptation of the varying environmental conditions, more effective growing mechanism, and reproduction, get inherited and contribute to the evolution.

In Sect. 4.3, we introduced so-called selected excitation model, which has two stages: (1) the *ambient caused excitation* increases the energy of the proton being into superposition slightly but not enough for the transition into tautomeric form; and (2) the *electronic vibrational* stage provides the additional energy required for transition into tautomeric form. This model represents the generalization of the model initially introduced by Löwdin [28] (see also [29]). Namely, when the proton moves as the result of ambient caused excitation, the lone electrons undergo vibrations as well. This interaction is base pair specific, as each base pair creates local potential for its  $\pi$  electrons. The selective excitation model can be used to describe the stress-induced mutations. It is known that bacteria can change their DNA error-correction mechanism to adjust to the stress introduced by antibiotics. Instead of conventional polymerase, it employs an error-prone (low-fidelity) polymerase. The selective excitation mechanism allows increasing the mutation rate locally where the harmful mutation has occurred. This will lead to further mutation of the already existing mutation until new equilibrium is achieved. Once bacteria get adjusted to the environment, it moves to standard readout mechanism to prevent further mutations.

The same model can be used to explain the correction of +1 time-shift errors of *E. coli*, as we discussed already in Sect. 4.3 (see also [19]). Namely, when *E. coli* colony is prepared with lac<sup>−</sup> gene (the superscript “−” means that lac gene is not functional), it was noticed in [19] that nonfunctional lac<sup>−</sup> gene mutates to functional lac<sup>+</sup> gen with 100 times higher mutation rate compared to non-lactose environment. The mutation that caused the lac gene to become nonfunctional is clearly harmful to bacteria. The starvation stress put bacteria in a regime to use the low-fidelity polymerase instead. This polymerase leads to further mutation of the already mutated gene, which introduces −1 time-shift error correcting, therefore, the previous error and leading to functional lac<sup>+</sup> gene. Once the lac gene gets repaired, the bacteria move to standard readout mechanism. So, the starvation stress has caused the activation of error-prone mechanism corresponding to the ambient induced excitation, corresponding to the stage 1 of the selected excitation model. The electronic vibrational stage provides the sufficient energy for mutation to occur. The mutated bacterium, having functional lac<sup>+</sup> gene, can further create adaptive mutation colonies, indicating that adaptive mutations can contribute to the evolution process.

McFadden and Al-Khalili have proposed in [1] the quantum-adaptive mutation model based on accelerated decoherence of the mutant states caused by the environment, which can be summarized as follows. The proton state can be represented as the superposition of being tunneled state  $|\phi_{\text{tunneled}}\rangle$  and non-tunneled state  $|\phi_{\text{non-tunneled}}\rangle$  [1]:

$$|\phi_{\text{proton}}\rangle = a|\phi_{\text{non-tunneled}}\rangle + b|\phi_{\text{tunneled}}\rangle, \quad (5.1)$$

where  $a$  and  $b$  are the corresponding probability amplitudes so that  $|a|^2 + |b|^2 = 1$ . During DNA replication, due to incorporation errors (see Sect. 4.3), the correct base  $B_c$  can be replaced with incorrect (tautomeric) base  $B_t$ . The state of corresponding genome can be described as

$$|\phi_G\rangle = a|\phi_{\text{non-tunneled}}\rangle|B_c\rangle + b|\phi_{\text{tunneled}}\rangle|B_t\rangle. \quad (5.2)$$

After the transcription stage, the mRNA state can be described in a similar fashion as (5.2). For instance, the existence of storage error in *LacI*-region may result in inactive *lac* gene ( $\text{lac}^-$ -state), and the state of the cell can be represented as

$$|\phi_{\text{Cell}}\rangle = a|\phi_{\text{non-tunneled}}\rangle|B_c\rangle|\text{inactive}\rangle + b|\phi_{\text{tunneled}}\rangle|B_t\rangle|\text{active}\rangle. \quad (5.3)$$

In the absence of lactose, the probability of moving to tunneled state and consequently to active *lac* gene state, denoted as  $|\text{active}\rangle$ , is proportional to  $|b|^2$ . The authors in [1] suggest that the decoherence can help *lac* gene to be trapped into a mutant state, which represents an active state of the cell. However, in the presence of lactose substrate, the decoherence time is much shorter as the substrate and corresponding enzyme provide sufficient energy for tautomeric transition to occur, and this process can be represented by the following mapping:

$$|\phi_{\text{Cell}}\rangle \xrightarrow{t_D} \begin{cases} |\phi_{\text{tunneled}}\rangle|B_t\rangle|\text{active}\rangle \\ |\phi_{\text{non-tunneled}}\rangle|B_c\rangle|\text{inactive}\rangle \end{cases}, \quad (5.4)$$

where  $t_D$  is the decoherence time, which is the function of the relaxation time  $t_R$ . The cell being in active state creates an adaptive mutation colony. The authors use the Zurek model to estimate the decoherence time [30]:

$$t_D \cong t_R \left( \frac{\lambda_T}{\Delta x} \right), \quad \lambda_T = \hbar \sqrt{2m k_B T}, \quad (5.5)$$

where  $m$  is the mass of the system being in a superposition state with separation of two stationary states being  $\Delta x$  and  $\lambda_T$  denotes the thermal de Broglie wavelength that is temperature dependent. The authors in [1] suggest that in the presence of enzyme and substrate, the thermal de Broglie wavelength is many orders of magnitude smaller resulting in significantly lower decoherence time. Clearly, this model uses the quantum mechanics to explain the changes on genome level.

On the other hand, Ogryzko describes in [31] a model that can be used to describe changes on a cellular level. This model has been called in [8] the *quantum biology at the cellular level* (QBCL). Namely, it is well known that the state space of a composite system can be represented in terms of the tensor product of states of individual systems. The state of the macroscopic system can then be represented as the following entangled state:

$$|\psi\rangle = a_1 \left( |\psi_1^{(1)}\rangle |\psi_2^{(1)}\rangle \dots \right) + \dots + a_i \left( |\psi_1^{(i)}\rangle |\psi_2^{(i)}\rangle \dots \right) + \dots \quad (5.6)$$

The density matrix describing the interaction of the system S and the environment E can be represented as

$$\rho = |\psi_{\text{ES}}\rangle\langle\psi_{\text{ES}}|. \quad (5.7)$$

By tracing out the environmental degrees of freedom, we obtain the state of the system after interaction with environment:

$$\rho_S = \text{Tr}_E |\psi_{\text{ES}}\rangle\langle\psi_{\text{ES}}|. \quad (5.8)$$

For instance, for the environmental basis  $\{|e_i\rangle\}$ , the reduced density operator states can be written as [31]

$$\rho_S = \sum a_i a_j^* \langle e_i | e_j \rangle |s_i\rangle\langle s_j|, \quad (5.9)$$

which will in general contain off-diagonal system terms  $|s_i\rangle\langle s_j|$ . The dynamic evolution of composite environment-quantum system (ES) can lead to rapid separation of different quantum states S, and off-diagonal term can vanish in time due to averaging effect, resulting in decoherence. In physics, the environment is typically homogenous, while in biology it is quite opposite. The environment helps to suppress the most of exotic states and yields to the *preferred state* of the biological system. This environmentally induced decoherence is, therefore, beneficial to the biological system. Since the environment changes all the time, we need to observe several environments, say  $E_0, E_1, \dots, E_i, \dots$ . The effect of each environment  $E_i$  on the biological system can be represented by a unique set of preferred basis states  $\{|s_i^{(j)}\rangle\}$ . Let the reduced density operator of the biological system after interaction with environment  $E_0$  be denoted as  $\rho_{S,0}$ . The corresponding preferred basis states will be  $\{|s_0^{(j)}\rangle\}$ . If the environment changes to  $E_i$  ( $i \neq 0$ ), the corresponding set of preferred basis states will be  $\{|s_i^{(j)}\rangle\}$ . Providing that the corresponding environmental basis states are orthogonal, the change of the environment can be represented by the following mapping of preferred biological states:

$$\rho_{S,0} \xrightarrow{E_0 \rightarrow E_i} \rho_{S,i}. \quad (5.10)$$

Clearly, with this interpretation, the decoherence represents the positive force for adaptive mutation and evolution. Clearly, the QBCL theory is consistent with quantum information theory described in Chap. 2.

In previous chapter (see Sects. 4.5 and 4.6), we have already used the theory of open quantum system to describe the interaction with the environment. This approach is also applicable to mutation and evolution theories as described in [4, 5, 7, 9]. If  $H$  denotes the biological system Hamiltonian, the corresponding quantum master equation can be written as

$$\frac{\partial \rho(t)}{\partial t} = -\frac{j}{\hbar}[H, \rho(t)] + L_E \rho(t), \quad (5.11)$$

where  $L_E$  is the environment operator describing the interaction with environments as follows:

$$L_E \rho(t) = \sum_i R_i \left[ L_i \rho(t) L_i^\dagger - 0.5 \rho(t) L_i L_i^\dagger - 0.5 L_i L_i^\dagger \rho(t) \right]. \quad (5.12)$$

In (5.12) we use  $L_i$  to denote the  $i$ -th Lindblad operator and  $R_i$  to denote the corresponding rate. If we replace the reduced Planck constant with time constant  $\tau$ , we can describe the evolution of biological information state on either genome or cellular level depending on the choice of time constant [4, 5, 7, 9]. The reciprocal of time constant can be replaced with the rate  $R = 1/\tau$ . The corresponding equation can now be called quantum mechanics-like (QML) master equation. However, in this case,  $H$  does not represent the physical energy of the biological system anymore and it is dimensionless. In the absence of environment (such as the frozen cellular organism), the corresponding system would be conservative, and the corresponding time-evolution operator, based on Chap. 2, would be

$$U(t, t_0) = e^{-\frac{j}{\tau}H(t-t_0)}. \quad (5.13)$$

The time evolution of kets  $|\alpha\rangle$  in biological conservative systems can therefore be described as follows:

$$|\alpha(t)\rangle = e^{-\frac{j}{\tau}H(t-t_0)}|\alpha(t_0)\rangle, \quad t > t_0. \quad (5.14)$$

Clearly this operator is still unitary and preserves the dot product:

$$\langle \alpha(t) U^\dagger | U \alpha(t) \rangle = \langle \alpha(t_0) | \alpha(t_0) \rangle. \quad (5.15)$$

The evolution of density operator can be described as

$$\rho(t) = U^\dagger \rho(t_0) U. \quad (5.16)$$

The time constant  $\tau$  is related to the temporal scale of the corresponding biological process. In practice it is difficult to isolate the biological system from the environment, and we have to use the QML master equation to model its dynamics. The environmental operator  $L_E$  drives the biological system into steady state as  $t \rightarrow \infty$ ; in other words  $\rho(t) \xrightarrow{t \rightarrow \infty} \rho_{\text{st}}$ . The steady-state density matrix gives us the probability density of mutation in a cell population as the result of interaction with the environment. Namely, in the steady-state regime, the uncertainty whether to mutate or not mutate is resolved and a stable phenotype is created.

The environmental operator  $L_E$  can contain both genetic jumps and continuous drifts. Genetic jumps are related to Darwinian theory and the continuous drifts to Lamarckian theory. Since this QML-based theory is neither pure Darwinian nor pure Lamarckian, as it combines the features of both, it is commonly referred to as *epigenetic evolution* [4, 5, 7, 9]. Corresponding mutations are called *epimutations*, while the genome is called epigenome. The environmental changes can introduce the changes on epigenomic structure, including DNA methylation and histone modification, and such changes can be inherited by the offspring. This concept is known as the *epigenetic inheritance*. Four types of cellular epigenetic inheritance (CEI) have been recognized in [4]: (1) self-sustained regulatory loops, (2) three-dimensional templating, (3) chromatin-marking, and (4) RNA-mediated CEI. However, the models for these have not been finalized yet. Very often in open-system analysis, we assume that the process is Markovian. In other words, the cell does not memorize the long interaction with the environment. The state of the biological system is only a function of current interaction with the environment, but not the function of previous instances. This assumption is clearly an approximation, but commonly used in existing literature [4, 5, 7, 9].

To study the effect of environment in a generic way, we can set  $H = 0$  and time constant  $\tau = 1$  and observe only one Lindblad operator  $L$  (assuming that  $R_1 = 1$ ), as it was done in [32]. The corresponding QML master equation reduces down to

$$\frac{\partial \rho(t)}{\partial t} = L\rho(t)L^\dagger - 0.5\rho(t)L L^\dagger - 0.5L L^\dagger \rho(t). \quad (5.17)$$

For infinitesimal interval of time  $\delta t$ , the density state has been changed to

$$\rho \rightarrow \rho + L\rho L^\dagger \delta t - 0.5\rho L L^\dagger \delta t - 0.5L L^\dagger \rho \delta t + o(\delta t). \quad (5.18)$$

By substituting  $L\sqrt{\delta t}$  with  $E_1$  and  $I - 0.5L^\dagger L \delta t$  with  $E_0$ , we can rewrite (5.18) as follows:

$$\rho \rightarrow E_1 \rho E_1^\dagger + E_0 \rho E_0^\dagger + o(\delta t). \quad (5.19)$$

For pure states  $|\psi\rangle$ , we can write  $\rho = |\psi\rangle\langle\psi|$ , so that the action of  $E_1$ -operator would be

$$E_1 \rho E_1^\dagger = E_1 |\psi\rangle\langle\psi| E_1^\dagger = \delta t L |\psi\rangle\langle\psi| L^\dagger. \quad (5.20)$$

Clearly, under the action of  $E_1$ -operator, the initial state  $|\psi\rangle$  “jumps” to

$$|\psi\rangle \rightarrow \frac{|L\psi\rangle}{\|L\psi\|}, \quad \|L\psi\| = \sqrt{\langle\psi|L^\dagger L|\psi\rangle}. \quad (5.21)$$

The probability for jump to occur will be given by

$$\|L\psi\|^2 \delta t = \langle\psi|L^\dagger L|\psi\rangle \delta t. \quad (5.22)$$

Since for  $\delta t \rightarrow 0$  the output state does not return to original state, the use of the term “jump” is adequate. The probability of not having jump would be  $1 - \langle\psi|L^\dagger L|\psi\rangle \delta t$ . On the other hand, the action of  $E_0$ -operator would be evolution of initial state to

$$|\psi\rangle \rightarrow |\psi\rangle - 0.5\delta t L^\dagger L|\psi\rangle, \quad (5.23)$$

which has been called in [32] as the *drift type* to indicate that the distance between the previous state and current state is in the order of  $\delta t$ . In terms of epigenetic evolution, the  $E_1$ -operator can be used to describe the *evolutionary jumps* of Darwinian type, while  $E_0$ -operator to describe the *continuous-drift evolution*. Interestingly enough, we used the QML master equation above and in previous chapter to describe the additive force in mutations and consequently evolution. Now by observing the action of  $E_1$ - and  $E_0$ -operators, we can conclude that the *basic forces of evolutions*, among others, include (1) genetic jumps and random mutations (and recombinations) subject to natural selection under environmental pressure and (2) genetic continuous drift. So we used the same mathematical apparatus to couple Darwinian-like (also known as *neo-Darwinism*) and Lamarckian-like (also known as *neo-Lamarckism*) evolution theories.

The Lindblad two-dimensional operators can be classified into three categories [32]:

1. Those having zero as the only eigenvalue
2. Those having two eigenvalues  $\pm\lambda$  with eigenkets being mutually orthogonal
3. Those having two eigenvalues  $\pm\lambda$  with eigenkets being non-orthogonal

The category (1) is clearly degenerate, and this operator has one-dimensional eigenspace that can be represented as

$$L = \sqrt{p}|1\rangle\langle 0|. \quad (5.24)$$

The action of this operator on superposition state  $|\psi\rangle = c_0|0\rangle + c_1|1\rangle$  is given by

$$L|\psi\rangle = \sqrt{p}|1\rangle\langle 0|(c_0|0\rangle + c_1|1\rangle) = c_0\sqrt{p}|1\rangle. \quad (5.25)$$

From (5.25) is evident that over the infinitesimal interval  $\delta t$ , the superposition state  $|\psi\rangle$  jumps to state  $|1\rangle$  with probability  $|c_0|^2 p \delta t$ . If we use the  $|1\rangle$ -state to denote the mutation state, then operator (5.24) describes the jump from original (non-mutated)

state to mutation state, which appears with probability  $p$ . Regarding the evolutionary drift operator  $E_0 = I - 0.5L^\dagger L\delta t$ , it can be represented as  $E_0 = I - 0.5p|0\rangle\langle 1| - 0.5p|1\rangle\langle 0|$ , so that the dynamics of the pure state  $|\psi\rangle$  can be described as follows:

$$\frac{d|\psi\rangle}{dt} = -0.5p(|0\rangle\langle 0|)|\psi\rangle. \quad (5.26)$$

By solving (5.25), the evolution of  $|\psi\rangle$  can be described as

$$|\psi\rangle(t) = \frac{c_0(0)e^{-0.5pt}|0\rangle + c_1(0)|1\rangle}{\sqrt{e^{-pt}|c_0(0)|^2 + |c_1(0)|^2}}. \quad (5.27)$$

Clearly, the pure non-mutation state  $(|0\rangle)$ -state, for which  $c_0(0) = 1$  is stationary. With probability  $p$ , the non-mutation state can still jump to the mutation state. When the initial state is the non-mutation state, then it drifts to the pure mutation state according to (5.27). The probability rate for jumping ahead to the mutation state, denoted as  $P_{r,jump}$ , is given by

$$P_{r,jump} = p \frac{|c_0(0)|^2 e^{-pt}}{e^{-pt}|c_0(0)|^2 + |c_1(0)|^2}, \quad (5.28)$$

which decreases as time progresses. Another Lindblad operator of this type, which is used to describe the *photon spontaneous emission*, is given by

$$L = \sqrt{p}|0\rangle\langle 1|, \quad (5.29)$$

where  $|1\rangle$ -state denotes the excited state of an electron, while  $|0\rangle$ -state is the corresponding ground state. During the transition from excited to the ground state, a single photon is emitted, and this event occurs with probability  $p$ . The operators given by either (5.24) or (5.29) in steady state lead to the same final state regardless of the initial state, which leads to the decrease in von Neumann entropy. However, the total change of entropy of the biological system and environment would be still nonnegative, in accordance with the second thermodynamics law.

If the eigenvalues of the two-dimensional Lindblad operator are nonzero, they must have opposite signs as the operator  $L$  is traceless. If  $|+\rangle = [1 \ 0]^\text{T}$  and  $|-\rangle = [0 \ 1]^\text{T}$  are orthogonal eigenkets, then the Lindblad operator given by

$$L = \sqrt{p}(|+\rangle\langle +| - |-\rangle\langle -|), \quad (5.30)$$

will have  $\pm\sqrt{p}$  for eigenvalues. The action of this operator on a superposition state  $|\psi\rangle = c_+|+\rangle + c_-|-\rangle$  is given by

$$L|\psi\rangle = \sqrt{p}(c_+|+\rangle - c_-|-\rangle). \quad (5.31)$$

Since  $L^\dagger L = pI$ , the evolutionary drift operator can be represented as

$$E_0 = I - 0.5L^\dagger L\delta t = (1 - 0.5p\delta t)I, \quad (5.32)$$

and the drifting branch is stationary. Therefore, the biological system that starts in state  $c_+|+\rangle + c_-|-\rangle$  will be a mixture of that state and  $c_+|+\rangle - c_-|-\rangle$ . In steady state, as  $t \rightarrow \infty$ , the populations of states  $c_+|+\rangle \pm c_-|-\rangle$  will be  $0.5[1 - \exp(-pt)]$  and eventually the incoherent mixture of states. This type of interaction with environment is known as *dephasing*, because the eigenkets do not change in time, but the superposition state (where the phase is well defined) evolves into incoherent mixture (where the phase is purely random). Notice that we considered a related phase damping model in Sect. 2.3.5 and expressed the action of the environment in terms of Kraus operators. Namely, we have shown in Sect. 2.3.4 that the final state  $\rho_f$ , after the interaction with environment, can be related to initial state  $\rho$  by operator sum representation as follows:

$$\rho_f = \xi(\rho) = \sum_k E_k \rho E_k^\dagger, \quad (5.33)$$

where  $E_k$  are Kraus operators satisfying the normalization condition  $\sum_k E_k E_k^\dagger = I$ . Under Markovian assumption we can write

$$\rho(t + \delta t) = \rho(t) + O(\delta t) = E_0 \rho E_0^\dagger + \sum_{k=1,2,\dots} E_k \rho E_k^\dagger, \quad (5.34)$$

where

$$\begin{aligned} E_0 &= I + O(\delta t) = I + (K - jH)\delta t + o(\delta t) \quad \text{and} \\ E_k &= L_k \sqrt{\delta t} + O(\sqrt{\delta t}), \end{aligned} \quad (5.35)$$

with  $H$  and  $K$  being the Hermitian operators. From the normalization condition, we have that

$$\sum_{k=0,1,\dots} E_k E_k^\dagger = I = I + 2K\delta t + \sum_{k=1,2,\dots} L_k^\dagger L_k \delta t + o(\delta t), \quad (5.36)$$

which indicates that

$$K = -0.5 \sum_{k=1,2,\dots} L_k^\dagger L_k. \quad (5.37)$$

As  $\delta t \rightarrow 0$ , (5.34), after the substitution of (5.36) into (5.35) and then (5.35) into (5.34), becomes

$$\frac{\partial \rho}{\partial t} = [-jH, \rho] + \sum_{k=1,2,\dots} \left[ L_k \rho L_k^\dagger - 0.5 \{ L_k^\dagger L_k, \rho \} \right], \quad (5.38)$$

where we use  $\{A, B\}$  to denote the anticommutator. Therefore, the master equation is the Markovian approximation of the operator sum representation.

As discussed above, the state of a particular gene can be represented as a superposition state:

$$|\psi\rangle = c_0|0\rangle + c_1|1\rangle, \quad (5.39)$$

where we use  $|1\rangle$ -state to denote the mutation state, which occurs with probability  $|c_0|^2$ . Corresponding density matrix is given by

$$\rho = |\psi\rangle\langle\psi| = (c_0|0\rangle + c_1|1\rangle)(\langle 0|c_0^* + \langle 1|c_1^*) = \begin{bmatrix} |c_0|^2 & c_0 c_1^* \\ c_1 c_0^* & |c_1|^2 \end{bmatrix}. \quad (5.40)$$

To describe the interaction with the environment, we can use either operator sum representation (5.33) or its Markovian master equation approximation (5.38). During the interaction, off-diagonal elements get averaged out, and in steady state (s.s.) the density matrix is diagonal:

$$\rho_{\text{s.s.}} = \begin{bmatrix} \rho_{\text{s.s.},00} & 0 \\ 0 & \rho_{\text{s.s.},11} \end{bmatrix}. \quad (5.41)$$

So in population of  $N$  cells,  $\rho_{\text{s.s.},11}N$  cells will be mutated. For  $\rho_{\text{s.s.},11} \gg \rho_{\text{s.s.},00}$ , the mutation will be spread out to the whole population, and we can say that in this case, the mutation gets stabilized.

Let us now consider cell with the genome consisting of genes  $g_1, \dots, g_G$ . Each gene  $g_i$  is subject to epimutations (chromatin-marking type such as acetylation, methylation, and phosphorylation, just to mention a few), which can be represented by the following superposition:

$$|\psi_{g_i}\rangle = \sum_k c_{g_i,k} |k_{g_i}\rangle. \quad (5.42)$$

Clearly, the Hilbert space is multidimensional now. The cell QML state can be represented by tensor product of gene's individual state, providing that they are independent:

$$|\psi_{\text{cell}}\rangle = |\psi_{g_1}\rangle \otimes |\psi_{g_2}\rangle \otimes \dots \otimes |\psi_{g_G}\rangle. \quad (5.43)$$

However, the probability of different genes in a genome to be independent of each other is very low. It is more adequate to use entangled states, similar to those given by (5.6), as follows:

$$|\psi_{\text{cell}}\rangle = \sum_{k_1 \dots k_G} c_{k_1 \dots k_G} |k_{g_1}\rangle \otimes |k_{g_2}\rangle \otimes \dots \otimes |k_{g_G}\rangle. \quad (5.44)$$

Notice that the concept of entanglement in genome introduced in [4, 5, 7, 9] emphasizes the “nonlocal feature” of genes, in the sense that one (epi)mutation in the gene implies (epi)mutations in other genes (whole genome). This nonlocal feature has nothing to do with the physical nonlocality within the cell. This quantum nonlocality can be used to explain the high speed of epigenetic mutations in the cell. Conventional new-Darwinism (random epimutations followed by natural selection) cannot describe the high speed of epigenetic mutations. Namely, the environment can introduce the epimutations on certain genes. However, some of the epimutations might not be consistent on the cellular level, which can cause the further epimutations until the consistency on the cellular level is established. Another interesting observation is related to the fact that biological systems are open system and they cannot be described by unitary evolution operators. Therefore, the biological system is an open quantum computing system. Nevertheless, the quantum entanglement in non-unitary systems can still be used to describe the high speed of epimutations.

Notice that this QML-based theory of epimutations and epievolution is still an active research area [4, 5, 7, 9], which will require further development and verification. As indicated by Ogryzko in [33], we still need to use conventional quantum mechanics approaches to describe the physical reality of the processes in the cell, regardless of the complexity of such mathematical apparatus. One the other hand, the QML approaches can still be used to describe mutation/evolution processes on a global level, providing that they can be related to the real quantum mechanics-based models.

## 5.2 Markovian Chain-Like Quantum-Mechanical Modeling of Mutations and Aging

In this section, we extend the memoryless quantum biological model, described in Chap. 3, to the corresponding model with memory. For convenience, in Fig. 5.1, we provide two stages of the quantum biological channel model with memory for basekets corresponding to Phe. The error introduced by Kraus operator  $a_{UUU,AUU}|AUU\rangle\langle UUU|$  leads to the change baseket representing Phe into the baseket representing Ile, where  $a_{UUU,AUU}$  denotes the probability amplitude for basket  $|UUU\rangle$  to basket  $|AUU\rangle$  transition. The corresponding probability is related to the probability amplitude by  $p_{UUU,AUU} = |a_{UUU,AUU}|^2$ . Now by concatenating

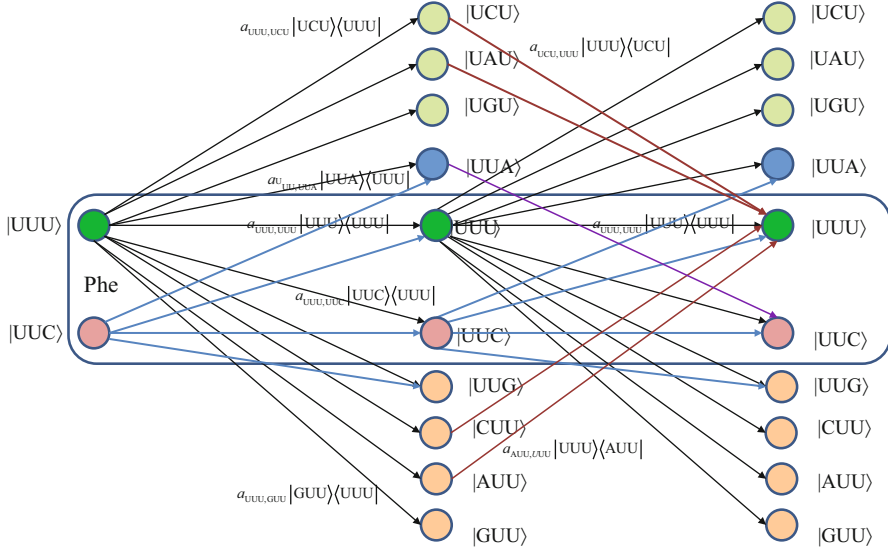


**Fig. 5.1** Two stages of quantum biological channel model with memory for basekets corresponding to Phe. Only selected transitions have been shown to illustrate the model. The  $a_{m,n}$  denotes the transition probability amplitude from baseket  $|m\rangle$  to baseket  $|n\rangle$ , where  $m \in \{\text{UUU}, \text{UUC}\}$  and  $n$  could be any of the 64 basekets. The probability amplitude is related to the probability by  $p_{m,n} = |a_{m,n}|^2$ . The Kraus operator  $E_{m,n}$  is obtained as  $E_{m,n} = a_{m,n}|n\rangle\langle m|$

two stages of transition diagram, the Krauss operator  $a_{\text{AUU},\text{UUU}}|\text{UUU}\rangle\langle\text{AUU}|$  in the second stage corrects the error introduced by the Kraus operator  $a_{\text{UUU},\text{AUU}}|\text{AUU}\rangle\langle\text{UUU}|$  in the first stage. On the other hand, what we have essentially just described is a *Markov chain-like biological quantum channel model*. Before we proceed further, we provide the brief review of *theory of Markovian chains* [34].

The finite Markovian chain is a commonly used model in communication systems to describe both the sources and channels with memory. The Markovian stochastic process with finite number of states  $\{S\} = \{S_1, \dots, S_n\}$  is characterized by transition probabilities  $p_{ij}$  moving from state  $S_i$  to state  $S_j$  ( $i, j = 1, \dots, n$ ). The Markov chain is the sequence of states with transitions governed by the following transition matrix:

$$\mathbf{P} = [p_{ij}] = \begin{bmatrix} p_{11} & p_{12} & \cdots & p_{1n} \\ p_{21} & p_{22} & \cdots & p_{2n} \\ \dots & \dots & \ddots & \vdots \\ p_{n1} & p_{n2} & \cdots & p_{nn} \end{bmatrix}, \quad (5.45)$$

where  $\sum_j p_{ij} = 1$ .

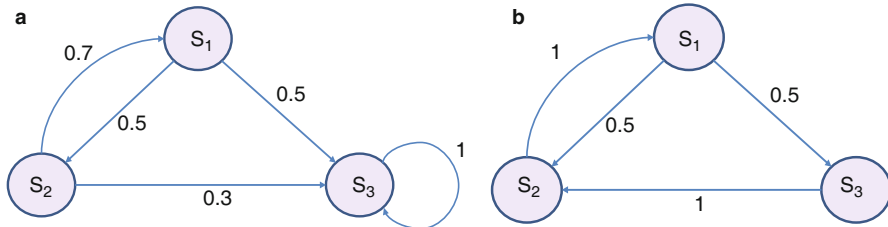


**Fig. 5.2** Two three-state Markov chains: (a) irregular Markov chain and (b) regular Markov chain

*Example 1* Let us observe three-state Markov chain shown in Fig. 5.2a. The corresponding transition matrix is given by

$$\mathbf{P} = [p_{ij}] = \begin{bmatrix} 0 & 0.5 & 0.5 \\ 0.7 & 0 & 0.3 \\ 0 & 0 & 1 \end{bmatrix}.$$

As we see, the sum in any row is equal 1. From state  $S_1$ , we can move to either state  $S_2$  with probability 0.4 or to stay in state  $S_1$  with probability 0.6. Once we enter the state  $S_2$ , we stay there forever. Such a state is called absorbing, and the corresponding Markov chain is called *absorbing Markov chain*. The probability of moving from state  $S_3$  to state  $S_2$  in two steps can be calculated as  $P_{23}^{(2)} = 0.3 \times 1 + 0.7 \times 0.5 = 0.65$ . Another way to calculate this probability is to find the second power of transition matrix and then read out the probability of the desired transition:

$$\mathbf{P}^2 = \left[ p_{ij}^{(2)} \right] = \mathbf{P}\mathbf{P} = \begin{bmatrix} 0.35 & 0 & 0.65 \\ 0 & 0.35 & 0.65 \\ 0 & 0 & 1 \end{bmatrix}.$$

On the other hand, the probability of reaching all states from initial states after  $k$ -steps can be determined by

$$\mathbf{P}^{(k)} = \mathbf{P}^{(0)} \mathbf{P}^k, \quad (5.46)$$

where  $\mathbf{P}^{(0)}$  is row vector containing the probabilities of initial states.

If the transition matrix  $\mathbf{P}^k$  has only nonzero elements, we say that Markov chain is *regular*. Accordingly, if  $k_0$ -th power of  $\mathbf{P}$  does not have any zero entry, any  $k$ -th power of  $\mathbf{P}$  for  $k > k_0$  will not have any zero entry either. The so-called ergodic Markov chains are the most important ones from communication system point of view. We can say that Markov chain is ergodic if it is possible to move from any specific state to any other state in finite number of steps with nonzero probability. The Markov chain from Example 1 is non-ergodic. It is also interesting to notice that transition matrix for this example has the following limit:

$$\mathbf{T} = \lim_{k \rightarrow \infty} \mathbf{P}^k = \begin{bmatrix} 0 & 0 & 1 \\ 0 & 0 & 1 \\ 0 & 0 & 1 \end{bmatrix}.$$

*Example 2* Let us now observe an example of regular Markov chain, which is shown in Fig. 5.2b. The transition matrix  $\mathbf{P}$ , its third and fourth powers, and matrix  $\mathbf{P}$  limit as  $k \rightarrow \infty$  are given respectively as

$$\mathbf{P} = \begin{bmatrix} 0 & 0.5 & 0.5 \\ 1 & 0 & 0 \\ 0 & 1 & 0 \end{bmatrix}, \quad \mathbf{P}^4 = \begin{bmatrix} 0.25 & 0.5 & 0.25 \\ 0.5 & 0.25 & 0.25 \\ 0.5 & 0.5 & 0 \end{bmatrix},$$

$$\mathbf{P}^5 = \begin{bmatrix} 0.5 & 0.375 & 0.125 \\ 0.25 & 0.5 & 0.25 \\ 0.5 & 0.25 & 0.25 \end{bmatrix}, \quad \mathbf{T} = \lim_{k \rightarrow \infty} \mathbf{P}^k = \begin{bmatrix} 0.4 & 0.4 & 0.2 \\ 0.4 & 0.4 & 0.2 \\ 0.4 & 0.2 & 0.2 \end{bmatrix}.$$

We can see that third power has one zero entry, while the fourth power and all higher powers do not have zero entries. Therefore, this Markov chain is both a regular and ergodic one. We can also notice that stationary transition matrix  $\mathbf{T}$  has identical rows.

It is evident from Example 2 that for regular Markov chain, the transition matrix converges to stationary transition matrix  $\mathbf{T}$  with all rows identical to each other:

$$\mathbf{T} = \lim_{k \rightarrow \infty} \mathbf{P}^k = \begin{bmatrix} t_1 & t_2 & \cdots & t_n \\ t_1 & t_2 & \cdots & t_n \\ \cdots & \cdots & \ddots & \vdots \\ t_1 & t_2 & \cdots & t_n \end{bmatrix}. \quad (5.47)$$

In addition, the following is valid:

$$\lim_{k \rightarrow \infty} \mathbf{P}^{(k)} = \lim_{k \rightarrow \infty} \mathbf{P}^{(0)} \mathbf{P}^k = \mathbf{P}^{(0)} \mathbf{T} = [t_1 \quad t_2 \quad \cdots \quad t_n], \quad (5.48)$$

so we can find stationary probabilities of states (or equivalently solve for elements of  $\mathbf{T}$ ) from equations

$$\begin{aligned} t_1 &= p_{11}t_1 + p_{21}t_2 + \cdots + p_{n1}t_n \\ t_2 &= p_{12}t_1 + p_{22}t_2 + \cdots + p_{n2}t_n \\ &\vdots \\ t_n &= p_{1n}t_1 + p_{2n}t_2 + \cdots + p_{nn}t_n \\ \sum_{i=1}^n t_i &= 1. \end{aligned} \quad (5.49)$$

For instance, for Markov chain from Fig. 5.2b, we can write that

$$t_1 = t_2, \quad t_2 = 0.5t_1 + t_3, \quad t_3 = 0.5t_1, \quad t_1 + t_2 + t_3 = 1,$$

while the corresponding solution is given by  $t_1 = t_2 = 0.4$ ,  $t_3 = 0.2$ .

The uncertainty of source associated with Markov source  $\{S\} = \{S_1, \dots, S_n\}$  when moving one step ahead from an initial state  $A_i$ , here denoted as  $H_i^{(1)}$ , can be expressed as

$$H_i^{(1)} = - \sum_{j=1}^n p_{ij} \log p_{ij}. \quad (5.50)$$

If the probability associated with state  $S_i$  is equal to  $p_i$ , we can obtain the entropy of Markov source by averaging over entropies associated with all states. The uncertainty of moving one step ahead becomes

$$H(X) = H^{(1)} = E\{H_i^{(1)}\} = \sum_{i=1}^n p_i H_i^{(1)} = - \sum_{i=1}^n p_i \sum_{j=1}^n p_{ij} \log p_{ij}. \quad (5.51)$$

In a similar fashion, the entropy of Markov source for moving  $k$ -steps ahead from initial states is given by

$$H^{(k)} = E\{H_i^{(k)}\} = \sum_{i=1}^n p_i \underbrace{H_i^{(k)}}_{- \sum_{j=1}^n p_{ij}^{(k)} \log p_{ij}^{(k)}} = - \sum_{i=1}^n p_i \sum_{j=1}^n p_{ij}^{(k)} \log p_{ij}^{(k)}. \quad (5.52)$$

It can be shown that for ergodic Markov sources, there is a limit defined as

$$H^{(\infty)} = \lim_{k \rightarrow \infty} H^{(k)}/k = H^{(1)} = H(X). \quad (5.53)$$

Equation (5.53) can be now used as an alternative definition of entropy of Markov source, which is applicable to arbitrary *stationary* source as well.

The theory of Markov chains has already been used in biology to describe population processes. In particular, the *Leslie matrix* has been used to describe the age-structured model of population growth in population ecology [35]. Let  $n_i$  denote the number of individuals of age class  $i$  and  $s_i$  the fraction of individuals surviving the transition from age class  $i$  to age class  $i+1$ . Let the *fecundity* (the *actual* reproductive rate of a population) of the  $i$ -th age class be denoted as  $f_i$ . Then the Leslie matrix can be used to determine the number of individuals from each age class at time instance  $t+1$ :

$$\begin{bmatrix} n_0 \\ n_1 \\ \vdots \\ n_m - 1 \end{bmatrix}_{t+1} = \underbrace{\begin{bmatrix} f_0 & f_1 & f_2 & \cdots & f_{m-2} & f_{m-1} \\ s_0 & 0 & 0 & \cdots & 0 & 0 \\ 0 & s_1 & 0 & \cdots & 0 & 0 \\ 0 & 0 & s_2 & \cdots & 0 & 0 \\ 0 & 0 & 0 & \ddots & 0 & 0 \\ 0 & 0 & 0 & 0 & s_{m-1} & 0 \end{bmatrix}}_L \begin{bmatrix} n_0 \\ n_1 \\ \vdots \\ n_m - 1 \end{bmatrix}_t = \mathbf{L} \mathbf{n}_t, \quad (5.54)$$

where  $m$  is the maximum age attainable in the population,  $\mathbf{L}$  is the Leslie matrix, and  $\mathbf{n}_t$  is the population vector at time instance  $t$ . The population vectors at time instance  $t$  and time instance 0 are connected by similar dependence as given by (5.46):

$$\mathbf{n}_t = \mathbf{L}^t \mathbf{n}_0. \quad (5.55)$$

Markov chains have also been used in *population genetics* to describe the change in gene frequencies in small populations affected by genetic drift [36, 37]. Michaelis–Menten kinetics, we described in Chap. 3, can also be represented as a Markov chain, where at each time step the reaction proceeds in some direction. The Markov chain theory has also been used in [38] to study the complexity of the protein families.

The equivalent classical biological channel model corresponding to Fig. 5.1 is provided in Fig. 5.3. As an illustration, the probability of moving from state UUU to UUC in two steps can be calculated as

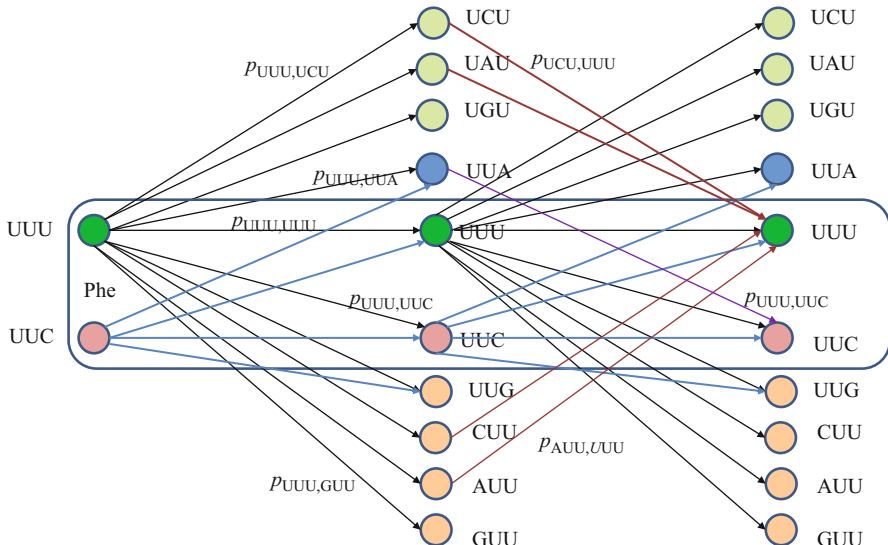


**Fig. 5.3** Two stages of classical biological channel model with memory for basekets corresponding to Phe. Only selected transitions have been shown to illustrate the model. The  $p_{m,n}$  denotes the transition probability from state  $m \in \{UUU, UUC\}$  to state  $n$  (any of 64 basekets)

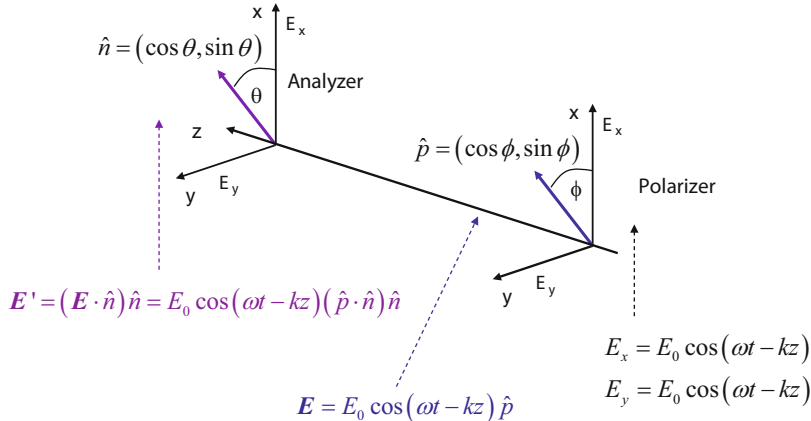


**Fig. 5.4** The study of the photon polarization by polarizer-analyzer ensemble

$$\begin{aligned} p_{UUU,UUC}^{(2)} &= p_{UUU,UUU} p_{UUU,UUC} + p_{UUU,UUC} p_{UUC,UUC} \\ &\quad + p_{UUU,UUG} p_{UUG,UUC} + p_{UUU,UUA} p_{UUA,UUC}, \end{aligned} \quad (5.56)$$

which is consistent with Markovian chains theory described above.

However, Markovian chain theory is not consistent with quantum mechanics; as in sequential processes in quantum mechanics, we need to multiply probability amplitudes instead [39, 40]. To clarify this claim, we provide in Fig. 5.4 the *polarizer-analyzer ensemble*. When an electromagnetic (EM) wave passes through the polarizer, it can be represented as a vector in the  $xOy$  plane transversal to the propagation direction  $z$ . The electric field vector of EM wave can be rewritten as

$$\mathbf{E} = E_0 \hat{p} \cos(\omega t - kz), \quad (5.57)$$

where  $\hat{p} = (\cos \phi, \sin \phi)$  is the polarization orientation unit vector with  $\phi$  being an angle between the electrical field EM vector and  $x$ -axis. ( $k$  denotes the wave number.) If  $\phi = 0$  rad, the light is polarized along  $x$ -axis, while for  $\phi = \pi/2$  rad, it is polarized along  $y$ -axis. After the analyzer, whose axis makes an angle  $\theta$  with respect to  $x$ -axis, which can be represented by unit vector  $\hat{n} = (\cos \theta, \sin \theta)$ , the output electric field is given by

$$\begin{aligned} \mathbf{E}' &= (\mathbf{E} \cdot \hat{n}) \hat{n} = E_0 \cos(\omega t - kz) (\hat{p} \cdot \hat{n}) \hat{n} \\ &= E_0 \cos(\omega t - kz) [(\cos \phi, \sin \phi) \cdot (\cos \theta, \sin \theta)] \hat{n} \\ &= E_0 \cos(\omega t - kz) [\cos \phi \cos \theta + \sin \phi \sin \theta] \hat{n} \\ &= E_0 \cos(\omega t - kz) \cos(\phi - \theta) \hat{n}. \end{aligned} \quad (5.58)$$

The intensity of the electrical field of EM wave at the output of analyzer can be written as

$$I' = |\mathbf{E}'|^2 = I \cos^2(\phi - \theta), \quad (5.59)$$

which is commonly referred to as *Malus law*. Classical physics prediction of total probability of a photon passing the polarizer–analyzer ensemble is given by

$$p_{\text{tot}} = \cos^2\phi \cos^2\theta + \sin^2\phi \sin^2\theta \neq \cos^2(\phi - \theta), \quad (5.60)$$

which is inconsistent with the Malus law, given by (5.59). In order to reconstruct the results from wave optics, the concept of *probability amplitude* that an angle  $\alpha$  is detected as  $\beta$ , denoted as  $a(\alpha \rightarrow \beta)$ , is introduced in quantum mechanics [39, 40]. The probability is obtained as the squared magnitude of probability amplitude  $p(\alpha \rightarrow \beta) = |a(\alpha \rightarrow \beta)|^2$ . The basic principles of quantum mechanics tell us that we need to sum up the probability amplitudes for indistinguishable paths:

$$a_{\text{tot}} = \cos\phi \cos\theta + \sin\phi \sin\theta = \cos(\phi - \theta). \quad (5.61)$$

The corresponding total probability is given by

$$p_{\text{tot}} = |a_{\text{tot}}|^2 = \cos^2(\phi - \theta), \quad (5.62)$$

and this result is consistent with Malus law.

We now apply this probability amplitude strategy to quantum biological channel model with memory illustrated in Fig. 5.1. As an illustration, let us determine the Kraus operator for moving from state  $|\text{UUU}\rangle$  to state  $|\text{UUC}\rangle$  in two steps, which will be denoted as  $E_{\text{UUU}, \text{UUC}}^{(2)}$ . Let us observe only a single nucleobase error per codon events. From quantum information processing theory introduced in Chap. 2, we know that for serial (cascade) connection of gates, we need to multiply the corresponding operators, while for parallel connection of gates, we need to sum up the corresponding operators. Therefore, the corresponding Kraus operator can be obtained as

$$\begin{aligned} E_{\text{UUU}, \text{UUC}}^{(2)} = & E_{\text{UUU}, \text{UUC}} E_{\text{UUU}, \text{UUC}} + E_{\text{UUC}, \text{UUC}} E_{\text{UUU}, \text{UUC}} \\ & + E_{\text{UUC}, \text{UUG}} E_{\text{UUG}, \text{UUU}} + E_{\text{UUC}, \text{UUA}} E_{\text{UUA}, \text{UUU}}. \end{aligned} \quad (5.63)$$

Now by expressing the Kraus gates in (5.63) in terms of basekets, we obtain

$$\begin{aligned} E_{\text{UUU}, \text{UUC}}^{(2)} = & a_{\text{UUU}, \text{UUC}} a_{\text{UUU}, \text{UUC}} (|\text{UUU}\rangle \langle \text{UUU}|) (|\text{UUU}\rangle \langle \text{UUU}|) \\ & + a_{\text{UUC}, \text{UUC}} a_{\text{UUU}, \text{UUC}} (|\text{UUC}\rangle \langle \text{UUC}|) (|\text{UUC}\rangle \langle \text{UUC}|) \\ & + a_{\text{UUC}, \text{UUG}} a_{\text{UUG}, \text{UUU}} (|\text{UUC}\rangle \langle \text{UUG}|) (|\text{UUG}\rangle \langle \text{UUU}|) \\ & + a_{\text{UUC}, \text{UUA}} a_{\text{UUA}, \text{UUU}} (|\text{UUC}\rangle \langle \text{UUA}|) (|\text{UUA}\rangle \langle \text{UUU}|). \end{aligned} \quad (5.64)$$

By applying the associativity axiom, we can rewrite the previous equation as

$$\begin{aligned}
 E_{\text{UUU}, \text{UUC}}^{(2)} = & a_{\text{UUU}, \text{UUC}} a_{\text{UUU}, \text{UUC}} |\text{UUU}\rangle \langle \text{UUU}| \text{UUU} \rangle \langle \text{UUU}| \\
 & + a_{\text{UUC}, \text{UUC}} a_{\text{UUU}, \text{UUC}} |\text{UUC}\rangle \langle \text{UUC}| \text{UUC} \rangle \langle \text{UUC}| \\
 & + a_{\text{UUC}, \text{UUG}} a_{\text{UUG}, \text{UUU}} |\text{UUC}\rangle \langle \text{UUG}| \text{UUG} \rangle \langle \text{UUG}| \\
 & + a_{\text{UUC}, \text{UUA}} a_{\text{UUA}, \text{UUU}} |\text{UUC}\rangle \langle \text{UUA}| \text{UUA} \rangle \langle \text{UUA}|.
 \end{aligned} \tag{5.65}$$

From orthogonality principle, we know that  $\langle \text{UUU}| \text{UUU} \rangle = \langle \text{UUC}| \text{UUC} \rangle = \langle \text{UUG}| \text{UUG} \rangle = \langle \text{UUA}| \text{UUA} \rangle = 1$ , so that we can rewrite (5.65) as

$$\begin{aligned}
 E_{\text{UUU}, \text{UUC}}^{(2)} = & a_{\text{UUU}, \text{UUC}} a_{\text{UUU}, \text{UUC}} |\text{UUU}\rangle \langle \text{UUU}| \\
 & + a_{\text{UUC}, \text{UUC}} a_{\text{UUU}, \text{UUC}} |\text{UUC}\rangle \langle \text{UUC}| \\
 & + a_{\text{UUC}, \text{UUG}} a_{\text{UUG}, \text{UUU}} |\text{UUC}\rangle \langle \text{UUG}| \\
 & + a_{\text{UUC}, \text{UUA}} a_{\text{UUA}, \text{UUU}} |\text{UUC}\rangle \langle \text{UUA}|.
 \end{aligned} \tag{5.66}$$

From (5.66) we conclude that the probability amplitude  $a_{\text{UUU}, \text{UUC}}^{(2)}$  can be calculated from the probability amplitude of individual stages as follows:

$$\begin{aligned}
 a_{\text{UUU}, \text{UUC}}^{(2)} = & a_{\text{UUU}, \text{UUC}} a_{\text{UUU}, \text{UUC}} + a_{\text{UUC}, \text{UUC}} a_{\text{UUU}, \text{UUC}} \\
 & + a_{\text{UUC}, \text{UUG}} a_{\text{UUG}, \text{UUU}} + a_{\text{UUC}, \text{UUA}} a_{\text{UUA}, \text{UUU}}.
 \end{aligned} \tag{5.67}$$

The corresponding probability for moving from state  $|\text{UUU}\rangle$  to state  $|\text{UUC}\rangle$  in two steps will be

$$\begin{aligned}
 p_{\text{UUU}, \text{UUC}}^{(2)} = & \left| a_{\text{UUU}, \text{UUC}}^{(2)} \right|^2 = \left| a_{\text{UUU}, \text{UUC}} a_{\text{UUU}, \text{UUC}} + a_{\text{UUC}, \text{UUC}} a_{\text{UUU}, \text{UUC}} \right. \\
 & \left. + a_{\text{UUC}, \text{UUG}} a_{\text{UUG}, \text{UUU}} + a_{\text{UUC}, \text{UUA}} a_{\text{UUA}, \text{UUU}} \right|^2,
 \end{aligned} \tag{5.68}$$

which is different from that obtained by classical Markovian chain theory given by (5.56).

As another illustration, the probability amplitude for moving from state  $|\text{UUU}\rangle$  to state  $|\text{UUU}\rangle$  in two steps can be determined as

$$\begin{aligned}
 a_{\text{UUU}, \text{UUU}}^{(2)} = & a_{\text{UUU}, \text{UUU}} a_{\text{UUU}, \text{UUU}} + a_{\text{UUU}, \text{UUG}} a_{\text{UUG}, \text{UUU}} + a_{\text{UUU}, \text{UUC}} a_{\text{UUC}, \text{UUU}} \\
 & + a_{\text{UUU}, \text{UUA}} a_{\text{UUA}, \text{UUU}} + a_{\text{UUU}, \text{UGU}} a_{\text{UGU}, \text{UUU}} + a_{\text{UUU}, \text{UCU}} a_{\text{UCU}, \text{UUU}} \\
 & + a_{\text{UUU}, \text{UAU}} a_{\text{UAU}, \text{UUU}} + a_{\text{UUU}, \text{GUU}} a_{\text{GUU}, \text{UUU}} + a_{\text{UUU}, \text{CUU}} a_{\text{CUU}, \text{UUU}} \\
 & + a_{\text{UUU}, \text{AUU}} a_{\text{AUU}, \text{UUU}}.
 \end{aligned} \tag{5.69}$$

From single-stage model, we would expect to have only one probability amplitude. However, since single nucleobase error in the first stage can be corrected for by the same nucleobase error in the second stage, the number of transitions is even nine.

Based on the discussion above, the *probability amplitude transition matrix* for the first stage can written as

$$\mathbf{A}^{(1)} = \mathbf{A} = \begin{bmatrix} a_{11} & a_{12} & \cdots & a_{1N} \\ a_{21} & a_{22} & \cdots & a_{2N} \\ \cdots & \cdots & \ddots & \vdots \\ a_{N1} & a_{N2} & \cdots & a_{NN} \end{bmatrix}, \quad (5.70)$$

where  $a_{m,n}$  denotes the transition probability amplitude from baseket  $|m\rangle$  to baseket  $|n\rangle$ , where  $m, n$  could be any of 64 basekets (the size of matrix is  $N \times N$ , where  $N = 64$ ). The corresponding probability amplitude is related to the probability by  $p_{m,n} = |a_{m,n}|^2$ . The Kraus operator  $E_{m,n}$  is obtained as  $E_{m,n} = a_{m,n}|n\rangle\langle m|$ . Since the elements of probability amplitude transition matrix are complex numbers, the matrix  $\mathbf{A}$  is not stochastic. The  $k$ -th stage (step) transition probability amplitude matrix can be determined as

$$\begin{aligned} \mathbf{A}^{(k)} &\doteq \begin{bmatrix} a_{11}^{(k)} & a_{12}^{(k)} & \cdots & a_{1,N}^{(k)} \\ a_{21}^{(k)} & a_{22}^{(k)} & \cdots & a_{2,N}^{(k)} \\ \cdots & \cdots & \ddots & \vdots \\ a_{N,1}^{(k)} & a_{N,2}^{(k)} & \cdots & a_{N,N}^{(k)} \end{bmatrix} \\ &= \mathbf{A}^{(k-1)} \mathbf{A} = \begin{bmatrix} a_{11}^{(k-1)} & a_{12}^{(k-1)} & \cdots & a_{1,N}^{(k-1)} \\ a_{21}^{(k-1)} & a_{22}^{(k-1)} & \cdots & a_{2,N}^{(k-1)} \\ \cdots & \cdots & \ddots & \vdots \\ a_{N,1}^{(k-1)} & a_{N,2}^{(k-1)} & \cdots & a_{N,N}^{(k-1)} \end{bmatrix} \begin{bmatrix} a_{11} & a_{12} & \cdots & a_{1,N} \\ a_{21} & a_{22} & \cdots & a_{2,N} \\ \cdots & \cdots & \ddots & \vdots \\ a_{N,1} & a_{N,2} & \cdots & a_{N,N} \end{bmatrix}. \end{aligned} \quad (5.71)$$

Clearly, from matrix multiplication rule, the  $a_{ij}^{(k)}$ -th element is determined by

$$a_{m,n}^{(k)} = a_{m,1}^{(k-1)} a_{1,n} + a_{m,2}^{(k-1)} a_{2,n} + \cdots + a_{m,N}^{(k-1)} a_{N,n} = \sum_{l=1}^N a_{m,l}^{(k-1)} a_{l,n}. \quad (5.72)$$

Since  $\mathbf{A}^{(k)} = \mathbf{A}^{(k-r)} \mathbf{A}^{(r)}$ ;  $r = 1, \dots, k-1$ , the  $k$ -step ( $k$ -stage) transition probability amplitudes satisfy the *Chapman–Kolmogorov* equation:

$$a_{m,n}^{(k)} = a_{m,1}^{(k-r)} a_{1,n}^{(r)} + a_{m,2}^{(k-r)} a_{2,n}^{(r)} + \cdots + a_{m,N}^{(k-r)} a_{N,n}^{(r)} = \sum_{l=1}^N a_{m,l}^{(k-r)} a_{l,n}^{(r)}. \quad (5.73)$$

The superoperator expressed in terms of Kraus operators after  $k$ -stages, namely,  $E_{m,n}^{(k)} = a_{m,n}^{(k)}|n\rangle\langle m|$ , can be written as

$$\xi^{(k)}(\rho_s) = \sum_{m,n} E_{m,n}^{(k)} \rho_s E_{m,n}^{(k)\dagger}, \quad (5.74)$$

where  $\rho_s$  is the biological system initial density matrix. Now we apply the Holevo–Schumacher–Westmoreland (HSW) theorem to calculate the quantum biological channel capacity (see Chap. 2 for additional details on corresponding theory) as follows:

$$C^{(k)}\left(\xi^{(k)}\right) = \max_{\{p_x, \rho_x\}} \left[ S\left(\xi^{(k)}\left(\sum_x p_x \rho_x\right)\right) - \sum_x p_x S\left(\xi^{(k)}(\rho_x)\right) \right], \quad (5.75)$$

where the maximization is performed over  $p_x$  and  $\rho_x$ . In (5.75) we use the ensemble  $\{p_x, \rho_x\}$  to denote the ensemble of density matrices corresponding to different amino acids.

Similarly as in previous chapter, we consider three scenarios. In scenario (1), we assume that the codon state representing an amino acid state is a completely mixed state, a statistical mixture of basekets each occurring with the same probability. In scenario (2), we assume that the amino acid codon state is a superposition of eigenkets of the corresponding Hamiltonian determined as described in previous chapter. In case (3), we select one of the amino acid codon eigenkets at random. Therefore, we perform the optimization only with respect to the prior probabilities of codons. The results of calculation are summarized in Figs. 5.5, 5.6 and 5.7, where

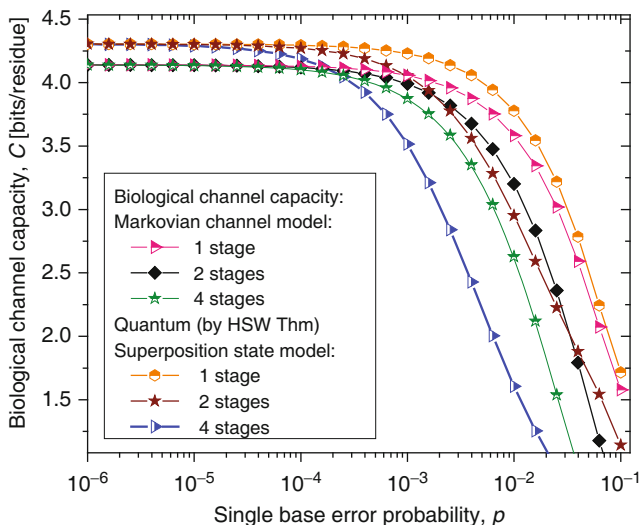


**Fig. 5.5** Channel capacity of quantum biological coherent state channel model with memory against the single base error probability

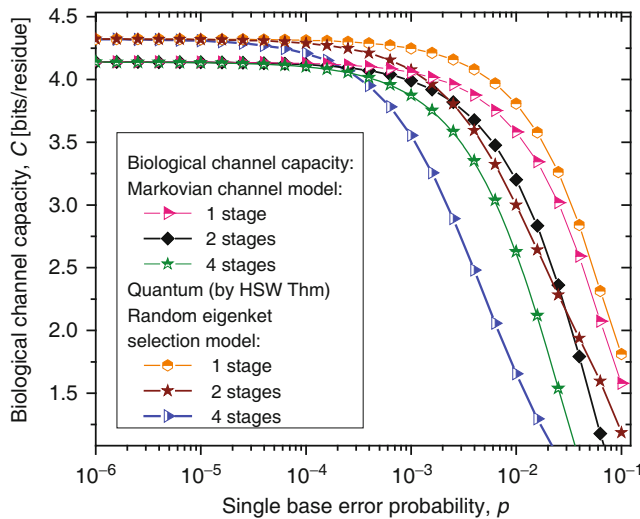


**Fig. 5.6** Channel capacity of quantum biological randomly selected eigenkets channel model with memory against the single base error probability

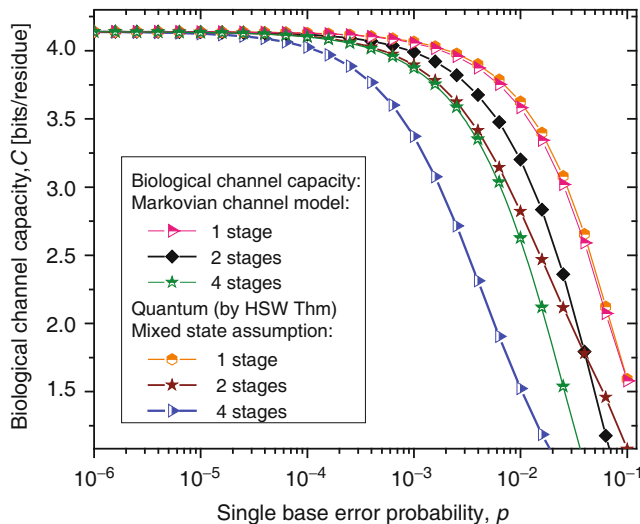


**Fig. 5.7** Channel capacity of quantum biological mixed state channel model with memory against the single base error probability

we show biological channel capacities expressed in terms of bits/residue against the single base error probability. The general observations are as follows: (1) the single-stage quantum biological channel capacity for any of the three models is always higher than corresponding classical biological channel capacity and (2) the

classical biological channel seems to be more robust for more than one stage. The quantum biological coherent state channel model has higher biological channel capacity than the corresponding classical Markovian model for two stages when the single base error probability is smaller than  $1.8 \times 10^{-3}$ , while for four stages when  $p \leq 2.3 \times 10^{-4}$ .

On the other hand, the quantum biological random eigenkets selection model has higher biological channel capacity than the corresponding classical Markovian model for two stages when the single base error probability is smaller than  $2.2 \times 10^{-3}$ , while for four stages when  $p \leq 2.6 \times 10^{-4}$ . Since the mixed state channel model represents the *classical* statistical mixture of density operators, it is not surprising that it performs only slightly better than classical biological channel model. However, when the number of stages is larger than one, it performs worse than classical channel model except for very large single nucleobase error probabilities. When  $p \geq 4 \times 10^{-2}$ , the two-stage mixed state model outperforms the classical model in terms of biological channel capacity.

In the section on quantum aspects of photosynthesis (see Sect. 4.6 of Chap. 4), we learned that the quantum coherence is important only in initial phase and decoherence helps to avoid the situations in which the photosynthesis apparatus get trapped into the dark states. From the previous section, we learned the environment helps to suppress the most of exotic biological states and yields to the *preferred state* of the biological system. Therefore, the environmentally induced decoherence is beneficial to the biological system as discussed in [8, 31]. So it appears that it makes sense to study the *hybrid quantum-classical biological channel models*. Notice that these hybrid models are different from the synergetic model of DNA due to Koruga [41, 42], which is essentially a tensor product of quantum and classical channel models. Our biological hybrid model is composed of  $k_q$  quantum stages and  $k_c$  classical stages. The density matrix after  $k_q$  quantum stages can be described as

$$\rho^{(k_q)} = \sum_{m, n} E_{m, n}^{(k_q)} \rho_s E_{m, n}^{(k_q)\dagger}, \quad (5.76)$$

where the Kraus operators are given by  $E_{m, n}^{(k_q)} = a_{m, n}^{(k_q)} |n\rangle \langle m|$ , while the elements of probability amplitudes are determined based on (5.71). The Markovian transition probabilities matrix to be used in  $k_c$  classical stages is determined by

$$\mathbf{P} = [p_{ij}] = \begin{bmatrix} \frac{|a_{11}^{(k_q)}|^2}{\sum_{n=1}^N |a_{1n}^{(k_q)}|^2} & \frac{|a_{12}^{(k_q)}|^2}{\sum_{n=1}^N |a_{1n}^{(k_q)}|^2} & \dots & \frac{|a_{1,N}^{(k_q)}|^2}{\sum_{n=1}^N |a_{1n}^{(k_q)}|^2} \\ \frac{|a_{21}^{(k)}|^2}{\sum_{n=1}^N |a_{2n}^{(k_q)}|^2} & \frac{|a_{22}^{(k)}|^2}{\sum_{n=1}^N |a_{2n}^{(k_q)}|^2} & \dots & \frac{|a_{2,N}^{(k)}|^2}{\sum_{n=1}^N |a_{2n}^{(k_q)}|^2} \\ \dots & \dots & \ddots & \vdots \\ \frac{|a_{N,1}^{(k)}|^2}{\sum_{n=1}^N |a_{Nn}^{(k_q)}|^2} & \frac{|a_{N,2}^{(k)}|^2}{\sum_{n=1}^N |a_{Nn}^{(k_q)}|^2} & \dots & \frac{|a_{N,N}^{(k)}|^2}{\sum_{n=1}^N |a_{Nn}^{(k_q)}|^2} \end{bmatrix}, \quad (5.77)$$

where the normalization per row ensures that the  $\mathbf{P}$ -matrix is stochastic. The Markovian transition probabilities matrix after  $k_c$  classical steps is determined by

$$\mathbf{P}^{(k_c)} = \mathbf{P}^{k_c}. \quad (5.78)$$

The codon transition probabilities determined by (5.78) are employed to evaluate the classical biological channel capacity, defined as

$$C = \max [H(Y) - H(Y|X)], \quad (5.79)$$

where  $H(Y)$  and  $H(Y)$  stand for the biological channel input and output entropies, while  $H(Y|X)$  represents the conditional entropy of the biological channel output given the biological channel input  $X$ . The entropy of biological channel output and conditional entropy are defined respectively as

$$H(Y) = -\sum_{m,n} p(Y_n|X_m)P(X_m)\log_2 \left[ \sum_m p(Y_n|X_m)P(X_m) \right] \quad (5.80)$$

$$H(Y|X) = -\sum_m \sum_n p(Y_m|X_m)P(X_m)\log_2 P(Y_n|X_m) \quad (5.81)$$

where we use  $\{p(X_i)\}$  to denote the probability of occurrence of codons in DNA and  $\{p(Y_j|X_i)\}$  to denote the conditional probabilities of the received codons  $\{Y_i\}$  given the transmitted codons  $\{X_i\}$ . The results of calculations are summarized in Fig. 5.8. Clearly, the hybrid biological channel model with  $k_q$  quantum stages and  $k_c$  classical stages always has higher biological channel capacity than Markovian classical channel model with  $k = k_q + k_c$  classical stages for all values of the single codon error probability. So it appears that the hybrid biological channel model is the most robust among the different biological channel models described above.

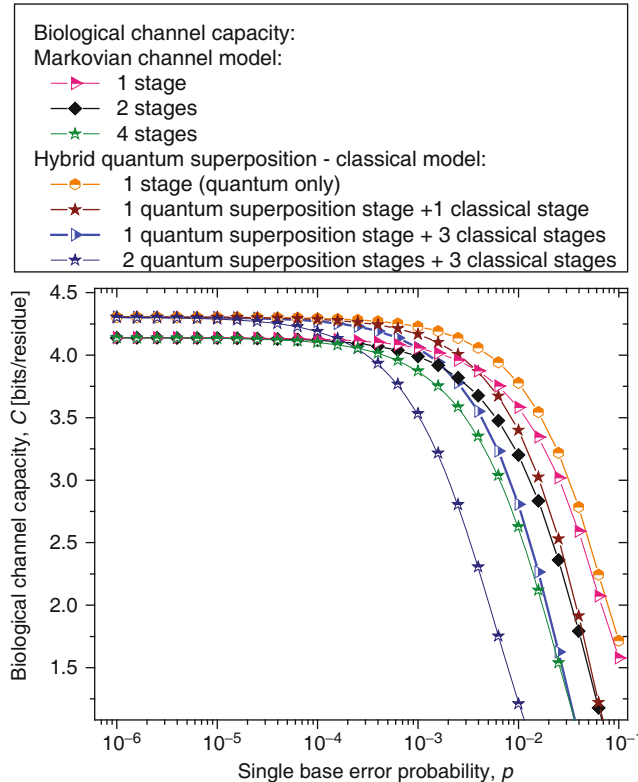


**Fig. 5.8** Channel capacity of hybrid biological coherent state-classical channel model with memory against the single base error probability

The *problem of aging* is closely related to the mutations. It is present in multicellular organisms. The single cell organisms do not really age in ordinary sense. In single cell organism, if the cell gets damaged, it either adapts or dies. The aging of multicellular organisms is due to change or loss of genetic information [28]. Namely, the aging can be associated with accumulation of mutation errors that eventually leads to partial loss of genetic information. In particular, the nuclear DNA damage can contribute either directly (by increased cell dysfunction) or indirectly (through apoptosis or cellular senescence) to the aging process.

In tissues where the cells divide frequently, the *somatic mutations* are not that dangerous. However, nerve or brain cells stop their replication at certain age, and a great portion on somatic mutation on these cells is responsible for aging. Different stages of Markovian-like biological channel models described above can be considered as different stages in life as well. As the time progresses, the number of possible error-event paths in genetic information increases, leading directly to the change of primary structure of the key enzymes. Since the key enzymes necessary to regulate metabolic processes in organism are affected by the accumulation of

random errors, the organism's metabolism as a whole gets affected as well. As already discussed in Chap. 3, the mutations could also be caused by mutagens and carcinogens. Well-known examples of exogenous mutagens include *intercalators* (EtBr whose molecule can get inserted between the planar nucleobases of DNA and deform the structure of DNA) and *base analogs* (5-bromouracil (5-BU) pretends to be a nucleobase but acts differently). Namely, the 5-BU can replace the uracil, but can have both keto and enol forms, which act differently. The keto form of BU pairs very well with A, while enol form pairs very well with G instead, introducing additional mutations. Therefore, induced mutations increase the codon error probability. From Fig. 5.8 is evident that the increase of the single base error probability above  $10^{-4}$  leads to a dramatic decrease in genetic information for multistage models. In conclusion, the combination of multistage error events and codon error probability increase can be considered the main sources of the aging process.

### 5.3 Classical, Semiclassical, and Quantum Modeling of Tumor and Cancer Development

The DNA is the subject of continuous mutations and damages [43–50], and the cell has various mechanisms to deal with damages, including direct reversal (such as photoreactivation) mechanism, various damaged bases excising mechanisms (nucleotide excision repair (NER), base excision repair (BER), and nucleotide mismatched repair (NMR)), single-strand damage repair, double-strand breaks repair, and translesion synthesis (TLS). Some authors even believe that given the limitations of the DNA repair mechanisms, if the humans have lived long enough, they would eventually all develop the cancer [44, 45] (Chap. 23). Namely, there are more than 35 inherited human DNA repair gene mutations that can increase the risk of developing the cancer. Some of these mutations affect the DNA repair mechanisms. For instance, the HPNCC is associated with DNA mismatch repair mechanism. On the other hand, the mutations in BRCA1 and BRCA2 genes affect a large number of DNA repair pathways, in particular NHEJ and homologous recombination. The TLS is an interesting mechanism that involves bypassing the sites of base damage while employing low-fidelity (“sloppy”) DNA polymerase in this region and can be explained using a model similar to that of adaptive mutations.

To simplify the explanation of complexity of cancer development, authors in [51, 52] advocate the use of a small number of underlying principles, so-called hallmarks of cancer: (1) self-sufficiency in growth, (2) insensitivity to antigrowth signals, (3) evading apoptosis (programmed cell death), (4) limitless replication potential, (5) sustained angiogenesis (the blood vessels growth stimulation to provide nutrients to tumors), (6) tissue invasion and metastasis, (7) deregulated metabolism (the most of cancer cells use abnormal metabolic pathways to generate energy as suggested by Warburg [53]), (8) the immune system invasion, (9) unstable DNA, and (10) the local chronic inflammation. It has become evident that a

comprehensive cancer development model is needed to take all these hallmarks into account. The most cancer development theories have not been able to do so. Various theories of cancer origin can be classified into two broad categories, epigenetic and genetic ones [54]. The genetic theories can be further divided into gene- and genome-based theories. From molecular biology point of view, different cancer origin theories include [47] somatic mutation theory of carcinogenesis, clonal evolutional tumor progression model, genomic instability models, microenvironmental factors-based models, and the epigenetic progenitor theory, to mention a few.

The *somatic mutation theory (SMT)* of carcinogenesis relies on the following premises [55]: (1) cancer is developed from a single somatic cell that has accumulated the DNA mutation over the time; (2) in the absence of stimuli, the metazoa cells are in quiescence state; and (3) the cancer-causing mutations occur in genes controlling the cell proliferation and/or the cell cycle. Although this theory has been the most popular in the last 60 years, it has many drawbacks as discussed in [55]. The *clonal evolution progression model*, introduced by Nowell [56], represents the refined version of the SMT and assumes that tumors expand as a clone from a single mutated cell, while the progression is the result of sequential accumulation of the random somatic genetic errors. This model has been supported experimentally by the systematic discovery of oncogenes that promote tumor development either by activation or by inhibition processes described in Chap. 3. In combination with (caretaker) stability genes, they represent the class of “cancer genes” capable of transforming normal cells into cancer cells by affecting important metabolic pathways. However, no specific gene mutation can be found for reliable diagnostic of any particular type of tumor.

Loeb suggested in [57] the possibility for increased mutation rates due to defective stability genes. This model is known as a *genomic instability model* [47]. In particular, the chromosome instability induces genome rearrangements causing the tumor progression [58]. This model represents the generalization of Boveri genetic paradigm introduced in 1914 and republished it 2008 [59]. Namely, Boveri contributed abnormal nuclei in malignant cells to impairments in certain chromosomes. The genomic instability model can be related to classical, quantum, and hybrid biological channel models of mutations introduced in previous section.

The crosstalk between the solid tumor and tumor stroma (the connective tissue microenvironment) has been considered as a key factor in tumor development in *microenvironmental factors-based theory* [47]. Namely, the tumor stroma once activated secretes various growth and inflammation factors as well as proteases promoting cancer development by inducing the cell growth, angiogenesis, and remodeling of intracellular matrix. However, the tumor reversion (normalization), in particular in embryonic tissues, indicates that tumor stroma is secondary to the already existing tumorous mutations. On the other hand, the tumor reversion contradicts irreversible deterministic models on the origin of cancer. Since the tumors can be experimentally induced and reversed by manipulating the signaling interactions responsible for cell and tissue maintenance and intercellular

communication, it has become evident that induced mutations represent only one of the many ways to initiate the cancer [60].

The *epigenetic progenitor theory* (EPT) [61] has been introduced recently to unify the *cancer stem cell theory* [62] and *cancer epigenetics* [63]. The cancer stem cell theory claims that the cancer is initiated and promoted by either tissue-specific adult stem cells (and their descendent progenitor cells) or dedifferentiated cells with stemlike properties. On the other hand, the epigenetic progenitor theory claims that tissue progenitor cells are early targets of epigenetic changes that gradually accumulate as the time progresses due to endogenous factors long before the tumors are clinically found [47, 61]. Therefore, the epigenetic instability that accumulates over time causes irreversible genetic mutations and genomic instabilities. With such an interpretation, the epigenome represents the interface between the environment and the genes. Since epigenetic changes are reversible and dynamic in nature, the EPT can resolve numerous problems of the SMT [47, 61]: tumor reversion, non-specificity of tumor-promoting mutations, the high correlation of cancer occurrence with respect to age and environmental changes, metastases, and heterogeneity of the primary cancer cells, to mention a few.

In strict reductionist theories, the genes are considered to act independently of each other. Therefore, each gene encodes a well-defined function and/or well-defined product, and the flow of information is unidirectional. This is known as the central dogma of molecular biology. The metabolic pathways, with this interpretation, are linear and can be described by linear genetic programs in which the flux of metabolites is determined by the kinetics introduced in Chap. 3. On the other hand, *in system biology*, the genome is not considered as deterministic execution program but rather as the database from which intra- and intercellular metabolic networks determine the information required by the current organism needs. The biological system is now considered as the hierarchy of self-organizing structures maintaining the order far away from thermodynamics equilibrium [64]. The basic properties of dynamic live systems can be summarized as follows [47, 65]: (1) the collective behavior of the system ingredients, (2) multistability (there exist multiple stable states), (3) robustness (the ability to adapt to environmental changes), (4) causality (the ability of higher-order elements to influence the dynamics of lower-order elements and vice versa), and (5) context dependency. When these principles are applied to the cancer problems, the new discipline, the *cancer system biology*, emerges [66]. The most elaborated model within this framework is the *cancer attractor model* [67, 68], in which the gene expression process is represented as a multidimensional gene regulatory network of active and inactive genes. Attractors correspond to the particular cell types. When the biological system is mildly perturbed, it manages to sustain its quasi-stable expression profile. However, if the perturbation is severe or it persists too long, the network dynamics might change the attractors' shape into apoptotic attractors or early development attractors, which stabilize embryonic/stemlike gene expression profiles. When the perturbation exceeds a certain threshold, it is possible that such an attractor can self-stabilize into a distinct attractor with specific tumor-promoting expression profile. The additional perturbation can further distort the attractor to gradually express the

malignant tumor profile. The cancer attractor model clearly unifies genetic and nongenetic aspects of cancer development. The cancer system biology interprets the cancer as the *developmental disorder*, the price that organism needs to pay for maintaining the complex multicellular organization [68]. The authors in [69] describe a related theory, the *tissue organization field theory* (TOFT). The basic assumptions in this theory are fundamentally different from those of the SMT and can be summarized into two basic ones [69]: (1) carcinogenesis is considered as a problem of tissue organization (that is comparable to the organogenesis during early development) and (2) the default state of all cells is the proliferation. The TOFT predicts that with the help of the cell-cell and/or tissue-tissue interactions, the neoplastic phenotypes can be potentially reversed. The ability of normal tissues to reverse the neoplastic phenotype is subject to the age and physiologic status of the host organism [69]. Therefore, the developmental disorder of the cancer is consistent with the TOFT in which the tissue has the organizing capacity.

The authors in [47] suggest that the “field effect” discussed in the TOFT can be related to the biological coherence, defined as a synchronized behavior of coupled elements of a biological systems, and could be either of quantum or electromagnetic nature. They further suggest that the lack of coherence, or even just disturbance in proper coherent dynamics, can contribute to the cancer development. This proposal is consistent, at least in principle, with Hameroff’s theory of cancer [70]. Fröhlich proposed the following biological coherent model of cancer development [71]. The group of cells, which can be as large as individual organs, are connected through a global coherent oscillation excited by the cell membrane displacements, whose wavelength would be much larger than the dimension of the cell. This global coherent oscillation synchronizes the cells into collective phase relations. If a component cell of this system loses its proper frequency, it will not affect the rest of the cells in the group (organ), as the other cells’ oscillation will stabilize the disordered cell. However, if the number of such abnormal cells exceeds a certain critical value (the threshold), the global coherent oscillation of the group cells will be weakened and the stabilization of destabilized cells will not be possible. The group of cells will then face the system phase transition into incoherent destabilized state, which can result into uncontrollable cell division, followed by the change of adhesive forced to surrounding tissue. This approach fits very well the thermodynamic interpretation that such group of cells will behave as an autonomous dissipative system, the “thermodynamics parasite,” which utilizes the global energy of the organism for its own use and development. Interestingly enough, the total ATP energy of normal and malignant cells is similar, regardless of different metabolism. The loss of coherence will result in excessive energy consumption with the proper dissipation. The consequence of this “energy overload” will be the distortion in the dissipative structures, distorted metabolic networks’ self-organizing potential, increased thermal noise, and higher entropy of the biological system, as shown in [72].

Cancer development can be described from *cellular bioenergetics* (described in Sect. 3.5 of Chap. 3) as follows. The energy flow in the cell is mainly controlled by mitochondrion. It has been recently confirmed than more than 95 % of carcinomas

exhibit an increased percentage of glycolytic proteins compared to the respiratory ones [73]. This confirms the proposal introduced by Warburg in the first half of the twentieth century [74] (see also [53]). Namely, Warburg explains that cancer gets created from normal cells in two phases [53]: (1) the irreversible damage of the respiration and (2) because of starvation, the affected cells either perish due to lack of energy or replace the respiration energy process by the fermentation energy process. Because of the inferiority of the cells employing the fermentation process compared to normal cells, the differentiated cells get converted to undifferentiated ones, which can grow widely (the cancer cells). The damage to the respiration mechanism can be contributed to chemical carcinogens, radiation, reactive oxygen species, inflammation, and inherited mutations, to mention a few. The damage is related to the abnormalities in inner mitochondrial membrane (affecting the proton motive force mechanism), mitochondrial DNA, electron transport chain, and even the tricarboxylic acid cycle. Because of these abnormalities, the cell is forced to change the metabolism to ancient synthesis of ATP through aerobic glycolysis. Since the aerobic glycolysis is atypical for cells, it results in changed redox state that disrupts calcium homeostasis and introduces the genomic instability. It is well known that when the available energy is insufficient, chromatin becomes deacetylated and dephosphorylated, the gene expression gets stopped, and the cell ceases its growth. Therefore, the bioenergetics provides a connection between the environment and epigenome. Interestingly enough, the majority of hallmarks of cancer can be related to the impaired respiration process [50].

It has been proposed by Schaffer close to 50 years ago [75] (see also [76]), and recently confirmed [77, 78], that cancer cells have impaired centriole, supernumerary (multiple) centrioles, and abnormal centrosomes (often called “centrosome amplification”). It has also been noticed in [77] that damaged DNA and abnormal centrosomes always occur simultaneously in cancer cells. Since the cancer cells are softer than the normal cells, they exhibit lower fundamental vibration frequencies and absorb the electromagnetic waves more rapidly than the normal cells [79, 80]. It has also been found in [81] that cancer cells have an enhanced electromagnetic field with negative electropolarity. This can be contributed to abnormal centrosomes and the presence of multiple centrioles per cancer cell. Since the centrioles have been involved in mitoses, the presence of numerous centrioles and abnormal centrosomes yields to uncontrolled growth and rapid cell division, which are well-known characteristics of the cancer cells. It is widely believed that centrioles’ defects are responsible for abnormalities in centrosome and centriole clustering. The various factors contributing to these defects include excessive exposure to carcinogens, radiation exposure, strong electromagnetic exposure, protein deficiencies, and possible protein excesses, to mention a few. Now we provide additional details on centrioles and microtubules (MTs) [79, 80], before moving to quantum-mechanical interpretation of the cancer [70, 82, 83].

Centrioles are two small cylindrical perpendicular organelles in close proximity of the cell nucleus. Each centriole is composed of nine blades of microtubules. Each blade is further composed of three MTs of slightly different lengths, with longest being the interior MT of the blade. At the adjoining base of two orthogonal

centrioles, there is “cloud” of proteins called MT-organizing center (MTOC). The centrioles together with MTOC form the centrosome, which is roughly speaking spherical, with a diameter of  $\sim 4$   $\mu\text{m}$ . The MTOC proteins are electron dense so that the intersecting bases of the centrioles exhibit negative potential, while the distal ends are positive. An MT itself is a hollow cylindrical structure consisting of 13 parallel strands (filaments), composed of alternating  $\alpha$ - and  $\beta$ -tubulin proteins. The inside diameter of the MT cylinder is 16 nm, while the outside diameter is 25 nm. The MT length varies and ranges from 400 to 500 nm. Centrioles occur in perpendicular pairs, with the mature one being called “mother” and less developed one being called “daughter” centriole. The centrioles have the following properties [79, 80]:

1. They have precise and uniform geometry.
2. Centrioles do not have membrane.
3. Similarly as DNA, centrioles are self-duplicating, and this process occurs the same time as DNA duplication.
4. Centrioles have the central role in mitosis, from initiation through division.
5. During the synthesis phase (the S-phase, when centrioles replicate) of normal cell interphase, each centriole gets duplicated only once.

As mentioned above, the centrioles have a key role in mitosis, which is typically described to occur in four phases: prophase, metaphase, anaphase, and telophase. The interphase (the preparation of the cell for the process of cell division) precedes the mitosis and has the following phases: (1) in  $G_1$  (the first gap) phase centriole cylinders separate. (2) In S-phase centriole cylinders replicate so that each centriole becomes the mother centriole that supports the creation of the new daughter orthogonally to the mother centriole. The new daughter of the daughter can be called “granddaughter.” (3) In  $G_2$  (the second gap) phase, centrioles separate and start to migrate. After this duplication is over, the old mother pairs with new daughter, while the old daughter pairs with granddaughter. During the prophase (the first mitosis phase), the nuclear membrane softens and breaks down, while the DNA condenses in preparation for the division. The connection between centriole pairs stretches and the corresponding pairs move apart, while still being connected by MTs, known as the “mitotic spindle.” In metaphase (the second mitosis phase), mitotic spindles attach to the centromeres on opposite sides of each paired chromosome. During the metaphase, the symmetric structure between two pairs of centrioles is formed. In the third phase (anaphase), the nucleus gets split and separated in the midplane. Namely, the paired chromosomes get separated into sister chromatids and are moved by mitotic spindles to newly forming daughter cells. In the fourth phase (telophase), the two nuclear membranes get created about the separated parts of the nucleus. Two centriole pairs get adjusted adjacent to the separated nuclei. The separated nuclei move further apart, taking about half of the organelles and cytoplasm. This process of division of the cytoplasm, organelles, and cell membrane into two new cells containing approximately equal shares of these cellular components is called *cytokinesis*. Mitosis and cytokinesis together define the *mitotic (M) phase* of an animal cell cycle (the division of the mother cell

into two daughter cells, which are genetically identical to each other and to their parent cell). The mitotic phase is a relatively short period of the cell cycle compared to the interphase.

Boveri has noticed that normal cells exhibit symmetrical/bipolar division of chromosomes during mitosis into two equal mirrorlike distribution of chromatids [58, 59]. On the other hand, cancer cells exhibit imbalanced divisions of chromosomes and can have asymmetrical and multipolar unequal (aneuploid) distributions [70]. There exist various versions of abnormal centriole activities in mitosis leading to aneuploidy. In one version, the centriole/spindle binding of chromatids during metaphase is defective and symmetrical leading to the misdistribution in the anaphase daughter cells. Each daughter cell can have missing entire chromosome because one chromatid was missing or it can have an extra chromosome. The end result is the genetic instability. In another version, the defective centriole replication process can result in more than two centriole pairs. The end result of this situation would be splitting of the genetic material among more than two daughter cells. This particular case can be considered as a root cause of the malignancy and cancer.

As has already been mentioned above, the MT filaments are composed of alternate  $\alpha$ - and  $\beta$ -tubulin protein pairs (dimers) [79–84]. A single dimer has a high electric charge (potential) difference along its axis, with each dimer behaving as a dipole, with  $\beta$ -tubulin protein representing the + end and  $\alpha$ -tubulin protein being the – end. The dimer has the following dimensions: 4.6 nm  $\times$  8 nm  $\times$  6.5 nm [84]. Therefore, the MTs behave as oriented ensembles of dipoles exhibiting piezoelectric, ferroelectric, and spin glass properties [85]. Because of these properties, Albrecht–Buehler concluded that the centrioles provide a sense of direction of the cell with respect to other cells within 2°–3° accuracy in the azimuthal plane as well as with respect to the axis perpendicular to it [86, 87]. One interesting approach was to consider MTs as optical cavities with quantum properties [84]. In [88] Atanasov discusses the possible role of orthogonal centrioles as the cell sensor. In this model, microtubules located in cytoplasm serve as “intracellular sensor antennas,” cilia serve as “extracellular sensor antennas,” and centrioles serve as transmit/receive antennas (depending on the direction of the signal transmitted). To operate as the sensor center, the centrioles must satisfy the following two conditions [88]: (1) only the mother–daughter centrioles can operate as the sensor center and the daughter centriole must be replicated from the mother’s centriole. The generated coherent electromagnetic field can promote the nonrandom transfer of ions in the close proximity of the filament [89]. Tubulin dimer can also be interpreted as a two-state quantum-mechanical system [70, 83, 84], and the dimer itself can be found in superposition of two states  $\{|0\rangle, |1\rangle\}$ :

$$|\psi_{\text{dimer}}\rangle = a|0\rangle + b|1\rangle, \quad |a|^2 + |b|^2 = 1, \quad (5.82)$$

where we use baseket  $|0\rangle$  to denote GDP- $\beta$ -tubulin lower energy state and basket  $|1\rangle$  to denote the GTP- $\beta$ -tubulin high-energy state. Namely, the  $\beta$ -tubulin monomer of

the heterodimer can bind guanosine triphosphate (GTP), in which case its state is energy-rich state (the  $|1\rangle$ -state) that favors polymerization. On the other hand, when it binds guanosine diphosphate (GDP) its state is energy-poor state (the  $|0\rangle$ -state), which results in dissociation. The GTP–GDP exchange (hydrolysis) releases  $\sim 0.42$  eV per molecule followed by the conformational change, which manifest itself by rotating the original  $\alpha$ – $\beta$  dimer axis by  $27^\circ 42'$  [84]. The dimer couples to conformation changes with  $10^{-11} – 10^{-9}$  s transitions [84]. This change in geometry of the tubulin also changes the direction and magnitude of the dipole moment. It has been found that each dimer contains two hydrophobic protein pockets, containing  $2 \times 18$  unpaired electrons, with at least two configurations associated with the GDP- and ATP-base tubulin states. The corresponding states can also be denoted as  $\{| \downarrow \rangle, | \uparrow \rangle\}$  to indicate dipole moment conformations. The low- and high-energy states can also be denoted as  $\{|g\rangle, |e\rangle\}$ , where we use the  $|g\rangle$ -state (the ground state) to denote the lower energy state of the dimer and the  $|e\rangle$ -state (the excited state) to denote the higher energy state of the dimer. It was found in [83] that the coherence time is around  $10^{-4}$  s, which is sufficient to execute a simple quantum information processing algorithm, such as quantum teleportation as advocated in [84]. The quantum teleportation system as shown in [40] employs three qubits, the MT qubit 1 is an arbitrary state to be transferred, while MT qubits 2 and 3 are in Bell state  $|B_{01}\rangle = (|00\rangle + |11\rangle)/\sqrt{2}$ . The initial 3-qubit state is  $|\psi\rangle \otimes |B_{01}\rangle$ , where  $|\psi\rangle$  is given by (5.82). By applying the tensor product, we can also write the initial 3-qubit state as

$$|\psi_{123}\rangle = |\psi\rangle \otimes |B_{01}\rangle = (a|010\rangle + a|001\rangle + b|110\rangle + b|101\rangle)/\sqrt{2}. \quad (5.83)$$

The MT qubit 1 interacts to MT qubit 2 electromagnetically or by binding the microtubule-associated proteins (MAPs). The binding behaves as the measurement that projects the  $|\psi_{123}\rangle$  on corresponding subspace. If this subspace is spanned by the Bell kets  $|B_{xy}\rangle = (|0y\rangle + (-1)^x|0\bar{y}\rangle)/\sqrt{2}$ ,  $\bar{y} = 1 - y$ , we can write

$$\langle B_{xy} | \psi_{123} \rangle = \begin{cases} a|0\rangle_3 \pm b|1\rangle_3 & \text{or} \\ a|1\rangle_3 \pm b|0\rangle_3 \end{cases} \quad (5.84)$$

On such a way, we have effectively teleported the MT qubit 1 onto MT qubit 3. This capability is important in sensing the external agents, and it can improve tolerance to the decoherence effects.

Hameroff suggests that entanglement is possible not only between two dimers but also between spatially separated centriole pairs during mitosis (see Table 2 of [70]). This proposal reminds to the use of quantum dots to perform the quantum information processing (QIP), as the quantum dots behave as large artificial atoms whose quantum states can be controlled [40]. Another similar example is related to the nuclear magnetic resonance (NMR)-based QIP. In NMR-based QIP, we do not employ individual quantum objects but rather a collection of over  $10^{18}$  active molecules diluted into solvent [39, 40]. In similar fashion, we can consider a centriole as an

artificial quantum object. If a particular tubulin in one centriole cylinder is perturbed (measured), its entangled tubulin pair will feel this perturbation and it will react in the same fashion. This indicates that the activities of replicated centrioles would be mirrorlike, exactly as needed during normal mitosis [70]. Now the binding of a particular chromatid centromere by a spindle connected at the corresponding opposite end of centriole can be interpreted as the quantum measurement. This quantum measurement results into projection (collapse) into subspace, and entangled tubulins bind to complementary chromatids of the same chromosome. If there is no entanglement between the corresponding tubulins, they will act independently, and the separation of the chromosomes would be abnormal, which results in aneuploidy. However, if the coherence does not exist during the S-phase (when centrioles replicate), instead of only one replicated centrioles' pair, multiple centrioles pair can be replicated, which will result in multiple daughter cells with improperly replicated genetic material. Such obtained daughter cells will be genetically unstable and might grow and divide in uncontrollable fashion. The improper genetic material in daughter cells might affect the cell metabolism. Such cells will be placed in starvation mode. Because of starvation, due to the lack of energy, the affected cells would replace the respiration energy process by the fermentation energy process. Since the cells employing the fermentation process are inferior compared to normal cells, the differentiated cells can become undifferentiated once, which can grow and divide in an uncontrollable fashion (the cancer cells). So it appears that the coherent assumption is able to connect different theories of cancer development.

The *biophotonics* provides an indirect experimental connection between the coherence and cancer development [47]. The living organisms are able to emit ultra-weak photons. The biophoton emissions exhibit nonlinear spectral distribution, self-transparency, distinct photon count, and hyperbolic relaxation dynamics, to mention a few, which are all related to the coherent nature of biophotons [90]. The biophoton emission is correlated to the tissue damage, age, and cancer. While the normal cells exhibit decreased total biophoton emission as the cell density increases, the tumor cell shows the opposite trend. The higher biophoton total emission is, the more malignant tumor cell is. These observations cannot be explained by the classical linear optics. Moreover, the authors in [91, 92] suggest that coherent communication exists not only among neighboring cells but also in a whole cell population. Namely, when the integration of new cells into population, as the result of cell division, results a decreased coherence and/or communication among cells, cancer will arise [91].

Before concluding this section, we describe the interaction of biophotons emitted by mitochondrion and MTs [82]. We will be employing the Jaynes–Cummings model [40, 93]. The tubulin dimer is represented as a two-state system, as indicated above, with basekets  $\{|g\rangle, |e\rangle\}$ , and interacts with a single-mode cavity field of biophotons. The following set of tubulin operators will be used:

$$\{\sigma_{ge} = |e\rangle\langle g|, \quad \sigma_{eg} = |g\rangle\langle e|, \quad \sigma = |e\rangle\langle e| - |g\rangle\langle g|\}, \quad (5.85)$$

where  $\sigma_{ge}$  is an operator to describe the transition from ground state to the excited state, which can also be denoted as the raising operator  $\sigma_+$ . On the other hand,  $\sigma_{eg}$  is

an operator to describe the transition from excited state to the ground state, which can also be denoted as the lowering operator  $\sigma_-$ . Finally, we use  $\sigma$  to denote the operator causing transitions between excited and ground states. The action of raising and lowering operators is defined in a conventional way [39, 40]:

$$\begin{aligned}\sigma_{ge}|g\rangle &= |e\rangle \underbrace{\langle g|g\rangle}_1 = |e\rangle, \quad \sigma_{eg}|e\rangle = |g\rangle \underbrace{\langle e|e\rangle}_1 = |g\rangle \\ \sigma_+|e\rangle &= 0, \quad \sigma_-|g\rangle = 0.\end{aligned}\quad (5.86)$$

The operator  $\sigma_{ge}\sigma$  raises the tubulin to the excited state, while annihilating a biophoton. On the other hand, the operator  $\sigma_{eg}\sigma^\dagger$  brings the tubulin to the ground state while creating a biophoton. The emitting frequencies of biophotons are in the order of THz, which coincide with the transition frequencies in tubulins. The interaction between tubulin and biophotons can be represented by the following Hamiltonian:

$$\begin{aligned}H &= H_{\text{tubulin}} + H_{\text{biophotons}} + H_{\text{interaction}} \\ &= \frac{1}{2}\hbar\omega_0\sigma + \hbar\omega\sigma a^\dagger a + \hbar\Omega(\sigma_+a + \sigma_-a^\dagger),\end{aligned}\quad (5.87)$$

where we use  $a^\dagger$  to denote the creation operator and  $a$  to denote the annihilation operator, defined as

$$a|n\rangle = \sqrt{n}|n-1\rangle, \quad a^\dagger|n\rangle = \sqrt{n+1}|n+1\rangle, \quad (5.88)$$

where  $|n\rangle$  is the biophoton number state. In (5.87),  $\omega$  denotes the biophoton frequency,  $\omega_0$  denotes tubulin transition frequency, and  $\hbar\Omega = dg$ , with  $d$  being the tubulin dipole moment and  $g \approx 0.5\sqrt{\hbar\omega/\epsilon V}$ , where  $V$  is the MT volume and  $\epsilon$  is dielectric constant of the environment inside MT that is approximately 8 times larger than that in the vacuum. The tubulin state, given by (5.82), can be rewritten as  $|\psi_{\text{dimer}}\rangle = c_g|g\rangle + c_e|e\rangle$ ,  $|c_g|^2 + |c_e|^2 = 1$ . The state of the biophotons field can be written as  $|\psi_{\text{biophotons}}\rangle = \sum_{n=0}^{\infty} c_n|n\rangle$ , where  $|n\rangle$  is the biophoton number state. For coherent biophotons' state, we can write

$$c_n = e^{-\frac{|\alpha|^2}{2}} \frac{\alpha^n}{\sqrt{n!}}, \quad (5.89)$$

where  $|\alpha|^2$  is equal to the average number of biophotons  $N$ . Clearly,  $c_n^2 = e^{-N}N^n/n!$  and follows Poisson distribution. The coherent biophotonics states satisfy the following characteristic equation:

$$a|\alpha\rangle = \alpha|\alpha\rangle. \quad (5.90)$$

The bipartite dimer–biophotons state is a tensor product:

$$|\psi\rangle = |\psi_{\text{dimer}}\rangle \otimes |\psi_{\text{biophotons}}\rangle. \quad (5.91)$$

After substitution of the bipartite state into Schrödinger equation:

$$j\hbar \frac{d}{dt} |\psi(t)\rangle = H_{\text{interaction}} |\psi(t)\rangle, \quad (5.92)$$

we obtain the following solution [39, 40, 94]:

$$|\psi(t)\rangle = \sum_{n=0}^{\infty} \left\{ [c_e c_n \cos(\Omega t \sqrt{n+1}) - j c_g c_{n+1} \sin(\Omega t \sqrt{n+1})] |e\rangle |n\rangle + [-j c_e c_{n-1} \sin(\Omega t \sqrt{n}) + j c_g c_n \cos(\Omega t \sqrt{n})] |g\rangle |n\rangle \right\} \quad (5.93)$$

Before interactions start, the dimer is in the ground state. To determine the rate of transitions between the coherent state and the ground state, we can use the following function [82]:

$$\begin{aligned} R(t) &= \langle \psi(t) | \sigma | \psi(t) \rangle \\ &= \sum_{n=0}^{\infty} c_n^2 \cos^2(\sqrt{n} \Omega t) (e^{-|\alpha|^2} - 1) + \sum_{n=0}^{\infty} c_n^2 \sin^2(\sqrt{n} \Omega t) \left( e^{-\frac{|\alpha|^2}{2}} + e^{-|\alpha|^2} \right). \end{aligned} \quad (5.94)$$

The probability of detection of biophotons  $|c_n|^2$  follows Poisson distribution. In that case,  $|\alpha|^2 = N$  and we can write [82]

$$R(t) = \sum_{n=0}^{\infty} e^{-N} \frac{N^n}{n!} \left[ 1 - \cos^2(\sqrt{n} \Omega t) + \sin^2\left(e^{-|\alpha|^2/2} \sqrt{n} \Omega t\right) \right]. \quad (5.95)$$

For the results, an interested reader is referred to [82]. As indicated above, as the number of cancer cells increases, the coherence is decreased so that (5.95) can be used to detect the presence of cancer cells, as the cancer cell will have different rate function than the normal cells.

## 5.4 Concluding Remarks

In this chapter, we have described the quantum-mechanical models to accurately illustrate the process of creation of spontaneous, induced, and adaptive mutations. These models have been used in Sect. 5.1 to describe the processes of evolution and aging. The various theories of quantum evolution and epievolution have been

studied as well. We have described the Markovian chain-like classical and quantum-mechanical modeling of mutations and aging in Sect. 5.2. In the same section, the hybrid quantum-classical biological channel model with memory has been described as well. In Sect. 5.3, various classical, semiclassical, and quantum models of cancer development have been studied.

## References

1. McFadden J, Al-Khalili J (1999) A quantum mechanical model of adaptive mutation. *Biosystems* 50:203–211
2. McFadden J (2000) Quantum evolution. W.W. Norton, New York
3. Koonin EV, Wolf YI (2009) Is evolution Darwinian or/and Lamarckian? *Biol Direct* 4:42
4. Jablonka E, Raz G (2009) Transgenerational epigenetic inheritance: prevalence, mechanisms, and implications for the study of heredity and evolution. *Q Rev Biol* 84:131–176
5. Asano M, Ohya M, Tanaka Y, Basieva I, Khrennikov A (2011) Dynamics of entropy in quantum-like model of decision making. *J Theor Biol* 281:56–64
6. Djordjevic IB (2012) Quantum biological channel modeling and capacity calculation. *Life* 2:377–391
7. Asano M, Basieva I, Khrennikov A, Ohya M, Tanaka Y (2013) A model of epigenetic evolution based on theory of open quantum systems. *Syst Synth Biol* 7:161–173
8. Bordorano M, Ogryzko V (2013) Quantum biology at the cellular level-elements of the research program. *Biosystems* 112:11–30
9. Khrennikov A (2011) quantum-like model of processing of information in the brain based on classical electromagnetic field. *Biosystems* 105:250–262
10. Koonin EV, Wolf YI (2012) Evolution of microbes and viruses: a paradigm shift in evolutionary biology? *Front Cell Infect Microbiol* 2:119-1–119-15
11. Sollars V, Lu X, Xiao L, Wang X, Garfinkel MD, Ruden DM (2003) Evidence for an epigenetic mechanism by which HSP90 acts as a capacitor for morphological evolution. *Nat Genet* 33:70–74
12. Russel PJ (2011) iGenetics: a molecular approach, 3rd edn. Pearson Benjamin Cummings, San Francisco
13. Darwin C (1859) On the origin of species. Murray, London
14. Lamarck JB (1809) Zoological philosophy: exposition with regard to the natural history of animals. Dentu, Paris (in French)
15. Foster PL (1993) Adaptive mutation: the uses of adversity. *Annu Rev Microbiol* 47:467–504
16. Rosenberg SM (2001) Evolving responsively: adaptive mutation. *Nat Rev Genet* 2:504–515
17. Roth JR, Kugelberg E, Reams AB, Kofoid E, Andersson DI (2006) Origin of mutations under selection: the adaptive mutation controversy. *Annu Rev Microbiol* 60:477–501
18. TenaillonO DE, Matic I (2004) Evolutionary significance of stress induced mutagenesis in bacteria. *Trends Microbiol* 12:264–270
19. Cairns J, Foster PL (1991) Adaptive reversion of a frameshift mutation in *Escherichia coli*. *Genetics* 128:695–701
20. Foster PL (2005) Stress responses and genetic variation in bacteria. *Mutat Res* 569:3–11
21. Foster PL (2007) Stress-induced mutagenesis in bacteria. *Crit Rev Biochem Mol Biol* 42:373–397
22. MacLean RC, Torres-Barceló C, Moxon R (2013) Evaluating evolutionary models of stress-induced mutagenesis in bacteria. *Nat Rev Genet* 14:221–227
23. Schrödinger E (1967) What is life? and mind and matter. Cambridge University Press, New York (12th reprint, 2012)

24. Bianconi G, Rahmde CA (2011) Unified framework for quasispecies evolution and stochastic quantization. *Phys Rev E Stat Nonlin Soft Matter Phys* 83:056104
25. Bianconi G, Rahmde CA (2012) Comparison between the quasi-species evolution and stochastic quantization of fields. *Eur Phys J B* 85:197
26. Bianconi G, Rahmde CA (2012) Quantum mechanics formalism for biological evolution. *Chaos, Solitons Fractals* 45:555–560
27. Martin-Delgado MA (2012) On quantum effects in a theory of biological evolution. *Sci Rep* 2:302-1–302-8
28. Löwdin PO (1966) Quantum genetics and the aperiodic solid: some aspects on the biological problems of heredity, mutations, aging, and tumors in view of the quantum theory of the DNA molecule. In: Löwdin PO (ed) *Advances in quantum chemistry*, vol 2. Academic, New York, pp 213–360
29. Watson JD, Crick FHC (1953) Genetical implications of the structure of deoxyribonucleic acid. *Nature* 171:964–967
30. Zurek ZH (1991) Decoherence and the transition from quantum to classical. *Phys Today* (October 1991):36–44
31. Ogryzko V On two quantum approaches to adaptive mutations in bacteria. <http://arxiv.org/ftp/arxiv/papers/0805/0805.4316.pdf>
32. Rooney DP (2012) Control of finite-dimensional quantum systems under Lindblad dissipation. Ph.D. Dissertation, The University of Michigan
33. Ogryzko V (2014) Comment on Masanari Asano et al.: a model of epigenetic evolution based on theory of open quantum systems. *Syset Synth Biol* 8:161–163
34. Cvijetic M, Djordjevic IB (2013) Advanced optical communication systems and networks. Artech House, Boston/London
35. Caceres MO, Caceres-Saez I (2011) Random Leslie matrices in population dynamics. *J Math Biol* 63:519–556
36. Kimura M (1968) Evolutionary rate at the molecular level. *Nature* 217:624–626
37. Kimura M (1983) The neutral theory of molecular evolution. Cambridge University Press, Cambridge
38. Yockey HP (2005) Information theory, evolution and the origin of life. Cambridge University Press, New York
39. Le Bellac M (2006) A short introduction to quantum information and quantum computation. Cambridge University Press, Cambridge
40. Djordjevic IB (2012) Quantum information processing and quantum error correction. Elsevier, Boston
41. Koruga D (2005) DNA as classical and quantum information system: implication to gene expression in normal and cancer cells. *Arch Oncol* 13:115–120
42. Koruga D (2012) Classical and quantum information processing in DNA-protein coding. In: Obradovic B (ed) *Cell and tissue engineering*. Springer, Berlin, pp 9–26
43. Friedberg EC (2003) DNA damage and repair. *Nature* 421:436–440
44. Johnson G (2010) Unearthing prehistoric tumors, and debate. *The New York Times*, 28 December 2010
45. Alberts B, Johnson A, Lewis J, Raff M, Roberts K, Walter P (2002) *Molecular biology of the cell*, 4th edn. Garland Science, New York
46. Johnson RE, Washington MT, Prakash S, Prakash L (2000) Fidelity of human DNA polymerase  $\eta$ . *J Biol Chem* 275:7447–7450
47. Plankar M, Jerman I, Krašovec R (2011) On the origin of cancer: can we ignore coherence? *Prog Biophys Mol Biol* 106:380–390
48. Sobhani ME, Molla AW, Rahman S (2010) A review on biomolecule basis of the role of psychological stress in the development and progression of cancer. *Mag Eur Med Oncol* 3:136–141
49. Rhaman S, Islam F, Mamun A, Abdul-Awal SM (2014) Evolution of cancer: a quantum mechanical approach. *Eur J Biophys* 2:38–48

50. Seyfried TN, Flores RE, Poff AM, D'Agostino DP (2013) Cancer as a metabolic disease: implications for novel therapeutics. *Carcinogenesis* 35:515–527
51. Hanahan D, Weinberg RA (2000) The hallmarks of cancer. *Cell* 100:57–70
52. Hanahan D, Weinberg RA (2011) Hallmarks of cancer: the next generation. *Cell* 144:646–674
53. Warburg O (1956) On the origin of cancer cells. *Science* 123:309–314
54. Paduch R (2014) Theories of cancer origin. *Eur J Cancer Prev* 24:57–67
55. Soto AM, Sonnenschein C (2004) The somatic mutation theory of cancer: growing problems with the paradigm? *Bioessays* 26:1097–1107
56. Nowell P (1976) The clonal evolution of tumor cell populations. *Science* 194:23–28
57. Loeb LA (1991) Mutator phenotype may be required for multistage carcinogenesis. *Cancer Res* 51:3075–3079
58. Holland AJ, Cleveland DW (2009) Boveri revisited: chromosomal instability, aneuploidy and tumorigenesis. *Nat Rev Mol Cell Biol* 10:478–487
59. Boveri T (2008) Concerning the origin of malignant tumors by Theodor Boveri. Translated and annotated by Henry Harris. *J Cell Sci* 121:1–84
60. Ingber DE (2008) Can cancer be reversed by engineering the tumor microenvironment? *Semin Cancer Biol* 18:356–364
61. Feinberg AP, Ohlsson R, Henikoff S (2006) The epigenetic progenitor origin of human cancer. *Nat Rev Genet* 7:21–33
62. Jaenisch R, Bird A (2003) Cancer stem cells in solid tumors: accumulating evidence and unresolved questions. *Nat Genet* 33:245–253
63. Dawson MA, Kouzarides T (2012) Cancer epigenetics: from mechanism to therapy. *Cell* 150:12–27
64. Nicolis G, Prigogine I (1977) Self-organization in Non-equilibrium systems: from dissipative structures to order through fluctuations. Wiley, New York
65. Feltz B, Crommelinck M, Goujon P (eds) (2006) Self-organization and emergence in life sciences. Springer, Dordrecht
66. Kreeger PK, Lauffenberger DA (2010) Cancer systems biology: a network modeling perspective. *Carcinogenesis* 31:2–8
67. Huang S, Ingber DE (2007) A non-genetic basis for cancer progression and metastasis: self-organizing attractors in cell regulatory networks. *Breast Dis* 26:27–54
68. Huang S, Ernberg I, Kauffman S (2009) Cancer attractors: a systems view of tumors from a gene network dynamics and developmental perspective. *Semin Cell Dev Biol* 20:869–876
69. Sonnenschein C, Soto AM (2008) Theories of carcinogenesis: an emerging perspective. *Semin Cancer Biol* 18:372–377
70. Hameroff SR (2004) A new theory of the origin of cancer: quantum coherent entanglement, centrioles, mitosis, and differentiation. *Biosystems* 77:119–136
71. Fröhlich H (1978) Coherent electric vibrations in biological systems and the cancer problem. *IEEE Trans Microwave Theory Tech* 26:613–617
72. Berretta R, Moscato P (2010) Cancer biomarker discovery: the Entropic hallmark. *PLoS One* 5:e12262-1–e12262-44
73. Acebo P, Giner D, Calvo P, Blanco-Rivero A, Ortega AD, Fernandez PL, Roncador G, Fernandez-Malave E, Chamorro M, Cuevza JM (2009) Cancer abolishes the tissue type-specific differences in the phenotype of energetic metabolism. *Transl Oncol* 2:138–145
74. Warburg O (1930) The metabolism of tumors. Constable and Company Ltd., London
75. Schafer PW (1969) Centrioles of a human cancer: intercellular order and intracellular disorder. *Science* 164:1300–1303
76. Schafer PW (1975) Centrioles: intercellular order in normal and malignant cells. *J Thorac Cardiovasc Surg* 63:472–477
77. Kramer A, Neben K, Ho AD (2002) Centrosome replication, genomic instability and cancer. *Leukemia* 16:767–775
78. Nigg EA, Stearns T (2011) The centrosome cycle: centriole biogenesis, duplication and inherent asymmetries. *Nat Cell Biol* 13:1154–1160

79. Huston RL (2014) On centrioles, microtubules, and cellular electromagnetism. *J Nanotechnol Eng Med* 5:031003-1–031003-5
80. Huston RL (2015) Using the electromagnetics of cancer's centrosome cluster to attract therapeutic nanoparticles. *Adv Biosci Biotechnol* 6:172–181
81. McCaig CD, Rajnicek AM, Song B, Zhao M (2005) Controlling cell behavior electrically: current views and future potential. *Physiol Rev* 86:943–978
82. Rahnama M, Tuszyński JA, Bokkon I, Cifra M, Sardar P, Salari V (2011) Emission of mitochondrial biophotons and their effect on electrical activity of membrane via microtubules. *J Integr Neurosci* 10:65–88
83. Hagan S, Hameroff SR, Tuszyński JA (2002) Quantum computation in brain microtubules: decoherence and biological feasibility. *Phys Rev E Stat Nonlin Soft Matter Phys* 65:061901-1–061901-11
84. Mavromatos NE, Mershin A, Nanopoulos DV (2002) QED-cavity model of microtubules implies dissipationless energy transfer and biological quantum teleportation. *Inter J Mod Physics B* 16:3623–3642
85. Tuszyński JA, Hameroff S, Sataric MV, Trpisova B, Nip MLA (1995) Ferroelectric behavior in microtubule dipole lattices: implications for information processing, signaling and assembly/disassembly. *J Theor Biol* 174:371–380
86. Albrecht-Buehler G (1997) Autofluorescence of live purple bacteria in the near infrared. *Exp Cell Res* 236:43–50
87. Albrecht-Buehler G (1994) Cellular infrared detector appears to be contained in the centrosome. *Cell Motil Cytoskeleton* 27:262–271
88. Atanasov A (2014) Possible role of centrioles as sensor center in cells. *Trakia J Sci* 12:74–78
89. Pokorný J, Hašek J, Jelínek F (2005) Electromagnetic field of microtubules: effects on transfer of mass particles and electrons. *J Biol Phys* 31:501–514
90. Popp F-A, Belousov L (eds) (2003) Integrative biophysics: biophotonics. Kluwer, Dordrecht
91. Van Wijk R (2001) Bio-photons and bio-communication. *J Sci Explor* 15:183–197
92. Popp F-A (2009) Cancer growth and its inhibition in terms of coherence. *Electromagn Biol Med* 28:53–60
93. Jaynes ET, Cummings FW (1963) Comparison of quantum and semiclassical radiation theories with application to the beam maser. *Proc IEEE* 51:89–109
94. Scully MO, Zubairy MS (1997) Quantum optics. Cambridge University Press, Cambridge

# Chapter 6

## Classical and Quantum Error-Correction Coding in Genetics

**Abstract** The subject of this chapter is the use of classical/quantum information theory and coding in genetics and evolution. The chapter starts with the description of using the concepts from both classical and quantum information theories to describe the evolution of biological channel capacity through generations. In order to do so, several classical and quantum biological channel models are employed including the Markovian classical and Markovian-like quantum model, hybrid quantum-classical model, multilevel symmetric channel model, and Kimura model-based Markovian process. In order to describe the reliable long-time storage of genetic information in DNA, the use of unequal error protection (UEP) coding is studied. Several classes of error-correction codes suitable for UEP on a cellular level are described including nested coding, multilevel coding (MLC), rate-adaptive coding, and generalized LDPC coding. The use of concepts of constrained coding to describe the genetic information flow from DNA to proteins is also described as well as joint-constrained and error-correction coding. After that, the use of quantum error-correction concepts to deal with environmental errors including canonical quantum error-correction and stabilizer codes is briefly described. One particular class of stabilizer codes, known as topological codes, is then described that might be relevant to biological processes as they only involve the local qubits in encoding process. Another relevant class of codes, the subsystem codes, is then described. The key idea behind subsystem codes is to decompose the quantum code as the tensor product of two subsystems, exon subsystem  $A$  and intron subsystem  $B$ , and we are concerned with correcting errors only on the exon subsystem. Finally, we describe the use of nonbinary quantum stabilizer codes to deal with nucleobase substitution errors, both random and burst errors. We also briefly discuss the possible use of both classical and quantum error-correction concepts to improve tolerance to tumor and cancer introducing errors.

## 6.1 Classical/Quantum Information Theory in Genetics and Evolution

The use of both classical and quantum information theory as well as error correction to describe the genome preservation and biological evolution is getting momentum, which can be judged by a number of recent papers related to these problems [1–20]. In the previous chapter, we have described the classical Markovian model and quantum Markovian-like model to describe mutations and aging (see Sect. 5.2). The same model is also applicable in describing the genome preservation through generations. The results of calculation of evolution of biological channel capacity through generations, for various quantum and classical models described in Sect. 5.2, are summarized in Figs. 6.1, 6.2 and 6.3 for different base error probabilities  $p$ :  $10^{-9}$  in Fig. 6.1,  $10^{-6}$  in Fig. 6.2, and  $10^{-5}$  in Fig. 6.3.

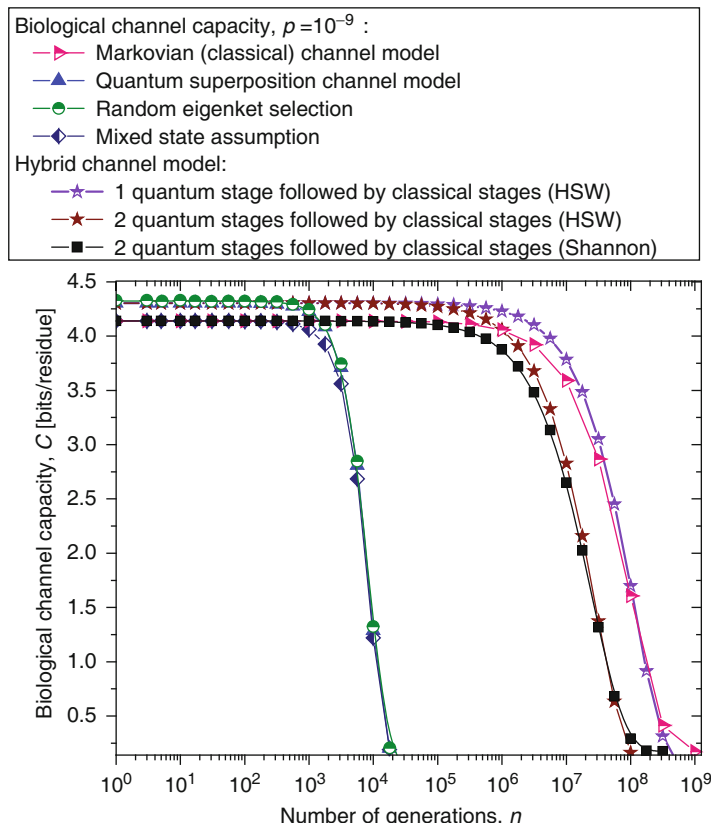


**Fig. 6.1** Evolution of biological channel capacity through generations when the base error probability is set to  $10^{-9}$

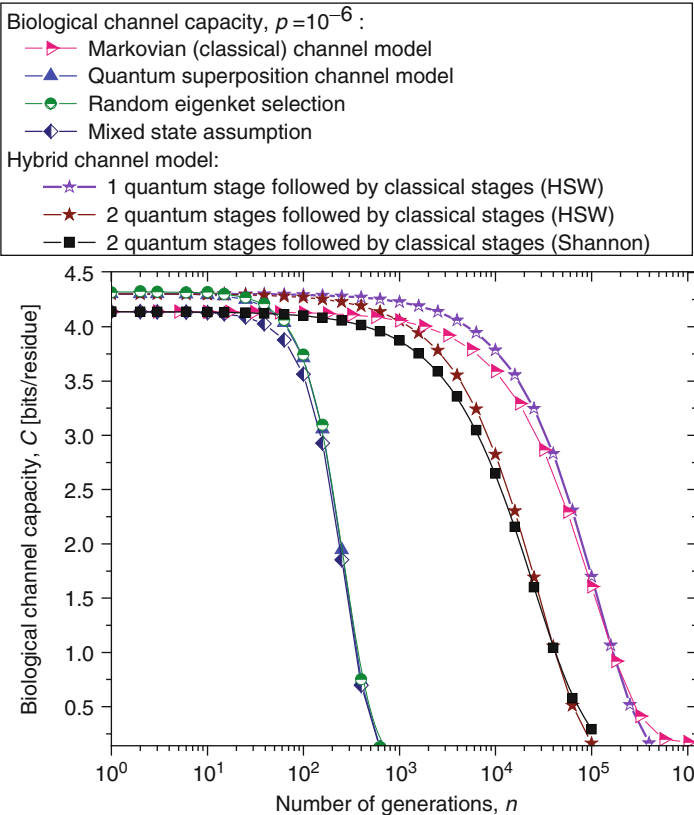


**Fig. 6.2** Evolution of biological channel capacity through generations when the base error probability is set to  $10^{-6}$

The classical Markovian model shows much better robustness through generations compared to various quantum Markovian-like models, except the mixed state model. On the other hand, quantum superposition and random eigenket selection Markovian-like models exhibit higher biological channel capacity for up to 1455 generations when the base error probability is  $10^{-9}$  (see Fig. 6.1).

However, for typical base error probability (around  $10^{-6}$ ), the random eigenket selection model exhibits higher biological channel capacity for up to 49 generations only (see Fig. 6.2). The hybrid quantum-classical model, also described in Sect. 5.2, exhibits better robustness (through generations) compared to purely quantum Markovian-like models. If the hybrid channel model preserves the coherence over the generations, we have to use Holevo–Schumacher–Westmoreland (HSW) theorem to calculate the quantum biological channel capacity (see Chap. 2 for additional details on the corresponding theory; see also [21]), based on (5.75) in Chap. 5. In this case, as shown in Figs. 6.1, 6.2 and 6.3, not only the system is more robust than the corresponding classical model, but it also exhibits higher

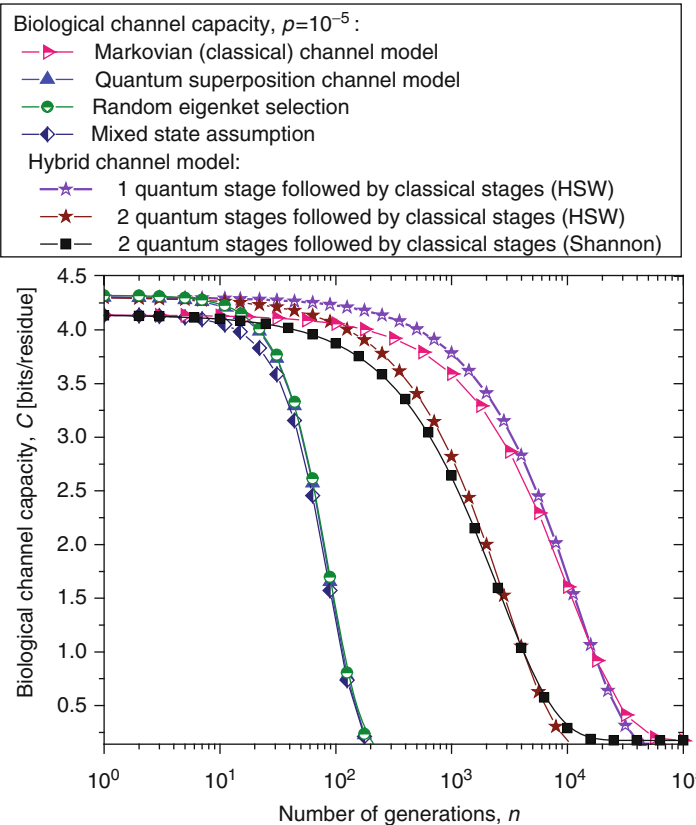


**Fig. 6.3** Evolution of biological channel capacity through generations when the base error probability is set to  $10^{-5}$

biological channel capacity. If, however, the coherence is not preserved but the system faces quantum to classical transition, in a similar fashion as described by Zurek [22], we have to use the classical information theory concepts, in particular (5.79)–(5.81) from Chap. 5 in calculating the biological channel capacity. Such system exhibits lower than classical model biological channel capacity, but has similar robustness of genome information through generations when compared to the classical Markovian channel model.

Some other models to describe the evolution of genetic information through generations include the  $M$ -ary symmetric channel (MSC) model, where  $M = 4$  (see [13, 23]), and the Kimura model [24]. Let  $X = \{x_0, \dots, x_{I-1}\}$  and  $Y = \{y_0, \dots, y_{J-1}\}$  denote the input and output alphabets, respectively. Also, let  $p(y_j|x_i)$  denote the transition probability  $\Pr(Y = y_j|X = x_i)$  and  $P_s$  denote symbol error probability. Then, for the MSC, the transition probability is given by  $p(y_j|x_i) = P_s/(M-1)$  when  $i \neq j$  and  $p(y_i|x_i) = 1 - P_s$ . The corresponding classical channel capacity is given by

$$C = \log_2 M + (1 - P_s) \log_2 (1 - P_s) + P_s \log_2 \left( \frac{P_s}{M-1} \right). \quad (6.1)$$

In order to calculate the evolution in time, Battail suggested in [13] to calculate first the evolution of symbol error probability in time as follows. Let us assume that the symbol error occurring during infinitesimal interval  $dt$  can be evaluated as  $vdt$ , where  $v$  is the frequency of errors, which is constant. Let  $P_s(t)$  denote the probability that a given symbol (nucleotide) differs from the original (correct) one at time instance  $t$ . Since  $1 - P_s(t)$  is the probability of not having an error, the probability of an error at time instance  $t + dt$  would be [13]

$$P_s(t + dt) = P_s(t) + v dt [1 - P_s(t)] - \frac{P_s(t)}{M-1} v dt, \quad (6.2)$$

where the second term indicates the fraction of error probability at  $(t + dt)$  given that the symbol error probability at time instance  $t$  was  $P_s(t)$ . The third term in (6.2) corresponds to the fraction of errors being corrected. By solving the differential (6.2), assuming that  $P_s(0) = 0$ , we obtain [13]

$$P_s(t) = \frac{M-1}{M} \left( 1 - e^{-\frac{M-1}{M-1} vt} \right). \quad (6.3)$$

By substituting (6.3) into (6.1), we derive the time evolution of classical capacity:

$$C(t) = \log_2 M + [1 - P_s(t)] \log_2 [1 - P_s(t)] + P_s(t) \log_2 \left[ \frac{P_s(t)}{M-1} \right], \quad (6.4)$$

$$P_s(t) = \frac{M-1}{M} \left( 1 - e^{-\frac{M-1}{M-1} vt} \right).$$

The evolution of the biological channel capacity versus normalized frequency  $vt$ , calculated by using (6.4), is illustrated in Fig. 6.4 for two values of  $M$ . The case  $M = 4$  corresponds to four nucleotides, while the case  $M = 2$  corresponds to the base type, pyrimidine type  $\mathcal{Y} = \{C, U\}$  or purine type  $\mathcal{R} = \{A, G\}$ . Since this model does not distinguish between exons and introns, then the corresponding channel capacity can be called nonprotein coding DNA biological channel capacity and strictly speaking is not comparable to classical and quantum models described above as well as in previous chapter.

The 4-ary symmetric channel model can also be used to develop the Markovian model (see Sect. 5.2), whose transition probability is given by

$$\mathbf{P}_{4SC} = \begin{bmatrix} T & C & A & G \\ T & 1 - P_s & P_s/3 & P_s/3 & P_s/3 \\ C & P_s/3 & 1 - P_s & P_s/3 & P_s/3 \\ A & P_s/3 & P_s/3 & 1 - P_s & P_s/3 \\ G & P_s/3 & P_s/3 & P_s/3 & 1 - P_s \end{bmatrix}. \quad (6.5)$$

**Fig. 6.4** Evolution of nonprotein coding DNA biological channel capacity versus normalized frequency of errors  $vt$

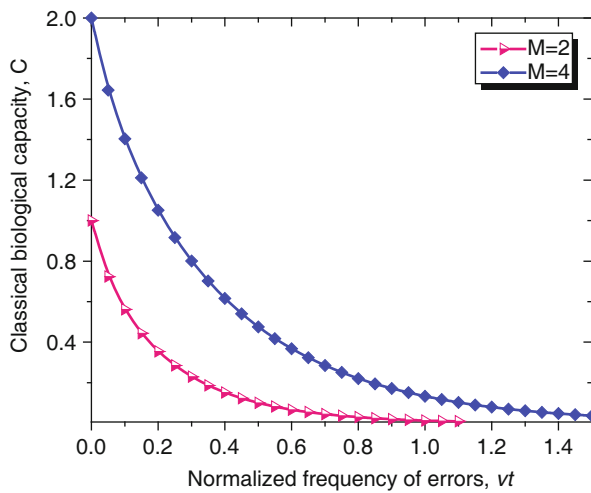
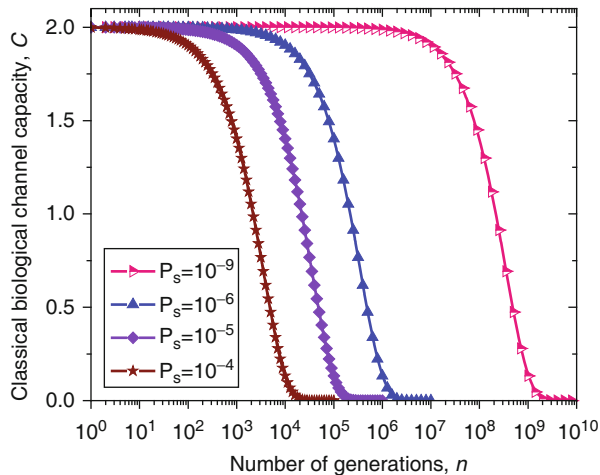


**Fig. 6.5** Evolution of nonprotein coding DNA biological classical channel capacity through generations based on 4-ary SC-inspired Markovian process for different nucleotide error probabilities  $P_s$



The transition matrix of 4-ary symmetric channel (SC)-based Markovian process, corresponding to the  $n$ th generation, is determined by  $\mathbf{P}_{4\text{SC}}^n$ . The classical biological channel capacity is calculated then by (5.79)–(5.81) from Chap. 5. The results of calculations are summarized in Fig. 6.5, for different nucleotide (symbol) error probabilities  $P_s$ . Again, because this model does not distinguish between exons and introns, then the corresponding channel capacity can be called nonprotein coding DNA biological channel capacity and strictly speaking is not comparable to classical and quantum models described above, with results summarized in Figs. 6.1 and 6.2. Moreover,  $P_s$  here is the nucleotide error probability, while  $p$  in Figs. 6.1, 6.2 and 6.3 is the single base error probability per codon.

The Kimura model [24] can be considered as a generalization of 4-ary symmetric channel model whose transition matrix is given as follows:

$$\mathbf{P} = \begin{bmatrix} & \text{T} & \text{C} & \text{A} & \text{G} \\ \text{T} & 1 - P_s & \gamma P_s/3 & P_s\gamma/3 & (1 - 2\gamma/3)P_s \\ \text{C} & \gamma P_s/3 & 1 - P_s & (1 - 2\gamma/3)P_s & \gamma P_s/3 \\ \text{A} & \gamma P_s/3 & (1 - 2\gamma/3)P_s & 1 - P_s & \gamma P_s/3 \\ \text{G} & (1 - 2\gamma/3)P_s & \gamma P_s/3 & \gamma P_s/3 & 1 - P_s \end{bmatrix}, \quad (6.6)$$

where  $\gamma \in [0, 3/2]$  is the parameter of the Kimura model with typical values ranging between 0.07 and 0.79 (based on [25]).

Clearly, for  $\gamma = 1$ , the Kimura model reduces to 4-ary symmetric channel. What is interesting about the Kimura model is that it can distinguish between transitions and transversions during the base substitution mutations.

As we discussed in Chap. 3, in transitions, the category of base during base substitution is preserved and the transition probability in this case is  $(1 - 2\gamma/3)P_s$ . On the other hand, in transversions, the base category gets changed, from purine to pyrimidine type, and vice versa, and the transition probability in this case is  $\gamma P_s/3$ . The transition matrix of the Kimura model-based Markovian process, corresponding to the  $n$ th generation, is determined by  $\mathbf{P}^n$ . The classical biological channel capacity is calculated then by (5.79)–(5.81) from the previous chapter. The results of calculations are summarized in Figs. 6.6, 6.7 and 6.8, for different nucleotide (symbol) error probabilities  $P_s$ . In each figure, the Kimura parameter  $\gamma$  is used as the parameter. Again, since  $P_s$  here is the nucleotide error probability, while  $p$  in Figs. 6.1, 6.2 and 6.3 is the single base error probability per codon, the results shown in Figs. 6.6 and 6.7 are not comparable against those shown in Figs. 6.1 and 6.2.

**Fig. 6.6** Evolution of nonprotein coding DNA classical biological channel capacity through generations based on Kimura model-inspired Markovian process for different values of parameter  $\gamma$  and symbol error probability set to  $10^{-9}$

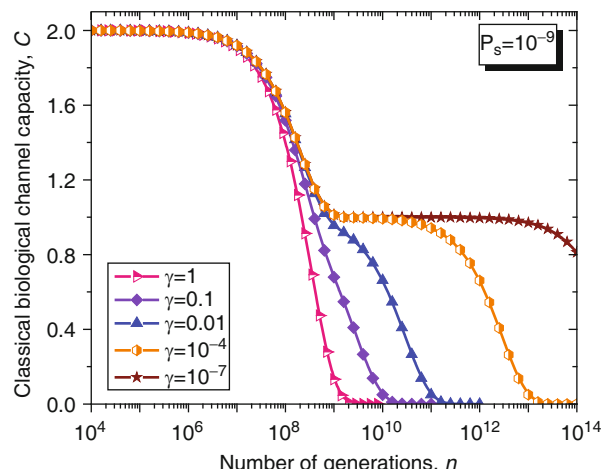


**Fig. 6.7** Evolution of nonprotein coding DNA classical biological channel capacity through generations based on the Kimura model-inspired Markovian process for different values of parameter  $\gamma$  and symbol error probability set to  $10^{-6}$

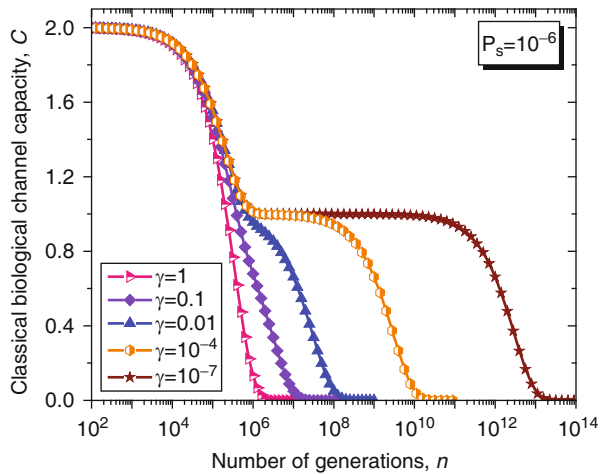
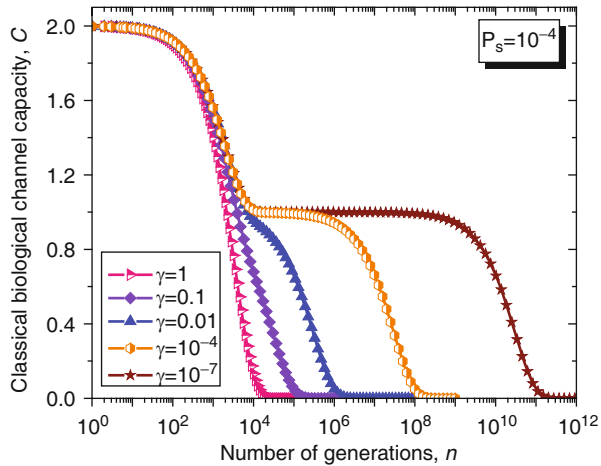


**Fig. 6.8** Evolution of nonprotein coding DNA classical biological channel capacity through generations based on the Kimura model-inspired Markovian process for different values of parameter  $\gamma$  and symbol error probability set to  $10^{-4}$



## 6.2 Classical/Quantum Error-Correction Coding in Genetics and Evolution

From previous figures, it is evident that genetic information through generations will be eventually lost, unless some form of genetic error correction is applied. Battail suggested that genetic information is protected by *unequal error correction/protection* (UEC/UEP) in terms of *nested coding* [13]. The older, more important genetic information is protected by a stronger code. The less important genetic information is protected by a weaker code. The nested code is a systematic code in which genetic information is untouched, while the generalized parity-check symbols are added, which are algebraically related to genetic information symbols

(nucleobases). The location of generalized parity-check symbols would be on the intron regions. Namely, until recently, it was widely believed that almost the entire eukaryotic gene is composed of the noncoding sequence (up to 98 %) [26–30]. However, the recent Encyclopedia of DNA Elements (ENCODE) project [31–34] has revealed that both gene-rich and gene-poor regions are pervasively transcribed. This research breakthrough motivates the need for more careful study of DNA information transfer and development of accurate description of DNA error-correction mechanisms. The nested coding represents one of possible ways to describe genetic unequal error protection (UEP) mechanisms.

Nested coding can be interpreted as follows. Let us consider  $M$  different information vectors  $\mathbf{i}_m$  ( $m = 1, \dots, M$ ) of length  $K_m$ . We would like to jointly encode these information vectors in such a way that each information vector is associated with a code word from a different subcode. The  $m$ th subcode  $\mathcal{C}_m$  is represented by the generator matrix  $\mathbf{G}_m$  of rate  $R_m = K_m/N$ , where  $N$  is code word length. The overall generator matrix is given by

$$\mathbf{G} = \begin{bmatrix} \mathbf{G}_1 \\ \mathbf{G}_2 \\ \vdots \\ \mathbf{G}_M \end{bmatrix}. \quad (6.7)$$

The overall code word  $\mathbf{c}$  can be obtained as follows:

$$\begin{aligned} \mathbf{c}^T &= [\mathbf{i}_1^T \quad \mathbf{i}_1^T \quad \cdots \quad \mathbf{i}_M^T] \mathbf{G} = [\mathbf{i}_1^T \quad \mathbf{i}_1^T \quad \cdots \quad \mathbf{i}_M^T] \begin{bmatrix} \mathbf{G}_1 \\ \mathbf{G}_2 \\ \vdots \\ \mathbf{G}_M \end{bmatrix} \\ &= \mathbf{i}_1^T \mathbf{G}_1 \oplus \mathbf{i}_2^T \mathbf{G}_2 \oplus \cdots \oplus \mathbf{i}_M^T \mathbf{G}_M, \end{aligned} \quad (6.8)$$

where we use  $\oplus$  to denote the bitwise XOR operation. If we are interested in URC, by setting  $\mathbf{i}_m = \mathbf{i}$ , by varying the number of generator matrices  $\mathbf{G}_m$ , we can achieve different levels of protection. The lowest level of protection would be to use only one generator matrix. The highest level of protection, corresponding to oldest most important genes, will be achieved by encoding the same information vector  $\mathbf{i}$   $M$ -times.

Multilevel coding (MLC), initially proposed by Imai and Hirakawa in 1977 [35], can also be used to provide UEC. The key idea behind the MLC is to protect individual bits using different binary codes. The outputs of encoders can be written as rows in the corresponding block interleaver. The certain number of bits can be taken in column-wise fashion to determine the point from a signal constellation diagram [36]. The decoding is based on the so-called *multistage decoding* (MSD) algorithm in which the decisions from prior (lower) decoding stage are passed to the next (higher) stage. Despite its attractiveness because of large coding gains, the MLC with the MSD algorithm has a serious limitation which is due to inherently

large delay of the MSD algorithm. One possible solution is to use the *parallel independent decoding* (PID), in which component decoders operate independently. However, the MLC approach would require the genetic information from multiple genes to be combined together in a coded-modulation fashion, indicating that this type of UEP is not suitable for genetic error correction.

To improve the performance of genetic error-correction coding, the coding can be combined with *interleaving* to mitigate the effect of error bursts. The basic premise of coding and interleaving is to spread error bursts over many code words such that each received code word only exhibits at most a few simultaneous symbol errors, which can be corrected for. The size of the interleaver must be large enough so that errors introduced by genetics are independent across a received code word. The intron regions can possibly be used for interleaving.

It is also possible to use the concepts of *rate-adaptive coding* to enable variable error-correction strength depending on the level of protection needed. In particular, nonbinary low-density parity-check (LDPC) codes are suitable for rate adaptation. The parity-check matrix of quasi-cyclic (QC) nonbinary LDPC codes can be written as follows [37]:

$$\mathbf{H} = \begin{bmatrix} \alpha^0 I & \alpha^1 I & \cdots & \alpha^{c-1} I \\ \alpha^{c-1} I & \alpha^0 P^{S[1]} & \cdots & \alpha^{c-2} P^{S[c-1]} \\ \alpha^{c-2} I & \alpha^{c-1} P^{2S[1]} & \cdots & \alpha^{c-3} P^{2S[c-1]} \\ \vdots & \vdots & \ddots & \vdots \\ \alpha^{c-(r-1)} I & \alpha^{c-r+2} P^{(r-1)S[1]} & \cdots & \alpha^{c-r} P^{(r-1)S[c-1]} \end{bmatrix} \quad (6.9)$$

where  $I$  is  $B \times B$  ( $B$  is a prime number) identity matrix;  $P$  is  $B \times B$  permutation matrix given by  $P = (p_{ij})_{B \times B}$ ,  $p_{i,i+1} = p_{B,1} = 1$  (zero otherwise); and  $r$  and  $c$  represent the number of block rows and block columns in (6.9), respectively.  $\alpha^i$  are nonzero elements of the Galois field of size  $q$ , denoted as  $\text{GF}(q)$ . In genetic error correction,  $q = 4$  corresponding to the set of nucleobases {T, C, A, G}. The code-rate adaptation is performed by *partial reconfiguration* of the decoder based on (6.9), for a fixed code word length, by changing the size of the permutation matrix  $P$  while keeping the number of block rows constant and/or by varying the number of employed block rows while keeping  $P$  fixed. It is also possible to perform the puncturing of parity symbols in the original code  $(n, k, d)$  to obtain a linear block code  $(n-p, k, d_p)$ ,  $d_p \leq d$ , where  $p$  is the number of removed parity symbols. Notice that this approach when applied to LDPC codes can introduce an early error floor phenomenon. This is the reason why the re-encoding approach has been introduced in [38] instead of using the conventional shortening or puncturing approach [39]. As shown in Fig. 6.9, to encode, the adaptive LDPC encoder encapsulates the last  $M$  symbols of the proceeding code word and the incoming  $K-M$  information symbols into a  $K$ -symbol vector.

In other words, each code word is generated continuously by re-encoding the last  $M$  symbols of its preceding code word. (The first  $M$  symbols in the first code word

**Fig. 6.9** The principles of rate-adaptive coding with re-encoding

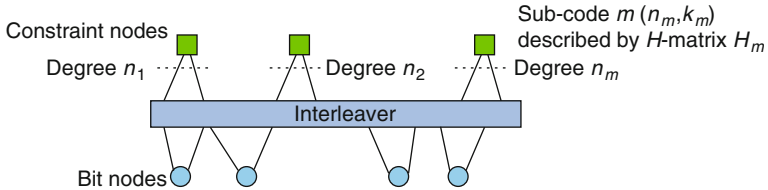
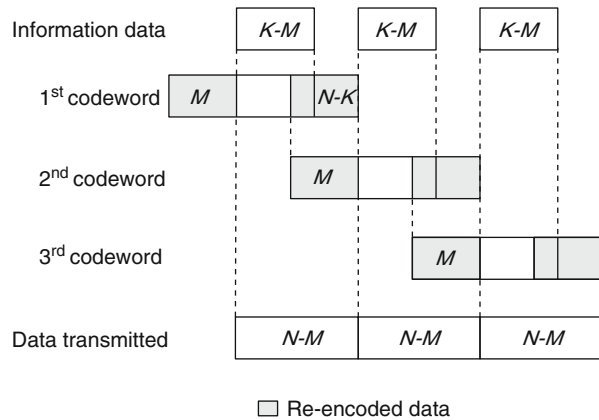


**Fig. 6.10** The bipartite graph for a GLDPC code. The constraint node, denoted by a *square*, could be any *linear code*. The bit nodes are denoted by *circles*

are set as known since no proceeding code word exists and the first  $M$  re-encoded symbols of each code word are not transmitted.) Therefore, the actual code rate is  $R' = (K - M)/(N - M)$ , where  $0 < M < K$  and can be tuned easily in the range  $(0, R)$  ( $R$  is the code rate of the template code) by adjusting the re-encoded data size  $M$ . Notice that the template code should be systematic to leverage the advantage of re-encoding in decoding.

Generalized LDPC (GLDPC) coding can also be used to provide UEP capabilities [40]. In GLDPC coding, illustrated in Fig. 6.10, each constraint node, also known as a subcode, represents an  $(n_s, k_s)$  ( $s = 1, \dots, m$ ) linear block code such as single-parity-check (SPC) code, BCH code (including Hamming code), or Reed–Müller (RM) code. There is one-to-one correspondence between the set of variable nodes and the set of all bits in a code word. However, we might allow a certain number of variable nodes to be *punctured* (corresponding bits are not transmitted), to adapt to time-varying channel conditions or to provide UEP flexibility. When all constraint nodes are SPC codes, the corresponding code is known as the LDPC code.

The key idea behind the GLDPC codes is to replace the parity-check equations in a parity-check matrix of a *global* LDPC code by a linear block code. The decoding is based on several low-complexity soft-input-soft-output (SISO) linear block decoders operating in parallel. The SISO decoders are commonly implemented

based on maximum a posteriori probability (MAP) decoders, and as such, they provide accurate estimates of bit reliabilities for a global LDPC decoder after a small number of iterations. Due to the high complexity of the BCJR decoder, typically used as a MAP decoder, the GLDPC coding is limited to simple linear block component codes such as Hamming, binary BCH, and Reed–Muller codes. LZ codes are obtained starting from a global LDPC codes by replacing every row of a global LDPC code by a parity-check matrix of a single local code. The GLDPC code can be derived from an LDPC code as follows. Let the  $s$ th row of a global LDPC code be replaced by the parity-check matrix of the  $s$ th local code  $H_s$  ( $s = 1, \dots, S$ ). Clearly, if the number of rows in a parity-check matrix of global code is larger than the number of available local codes, the repetition of certain local codes is unavoidable. The basic restriction in this design is that the row weight of the  $s$ th row in global code must be equal to the code word length of employed local code  $n_s$ . The global LDPC code could be either a regular or an irregular LDPC code. In order to keep the code rate reasonably high, some of local codes could be simple parity-check equations, whose MAP decoding complexity is trivial. For instance, if only SPC codes and  $(n, k)$  local code are used in regular GLDPC code design, the corresponding code rate  $R$  can be bounded as follows [40]:

$$1 - \frac{W}{n} - \frac{W}{d} \left( 1 - \frac{k+1}{n} \right) \leq R \leq R_G, \quad (6.10)$$

where  $W$  is the column weight of the global regular code and parameter  $d$  denotes that every  $d$ th row in a global code is replaced by  $(n, k)$  local code, while the remaining rows from the global code are interpreted as SPC codes in GLDPC code. In (6.10),  $R_G$  denotes the code rate of the global regular code, which is  $R_G = 1 - W/n$ . This GLDPC code design is quite suitable for code-rate adaptation, as almost continuous tuning of the code rate is possible by simply varying the parameter  $d$ .

In addition to channel coding, the *source coding* principles have also been used to compress genomic sequences by taking their structural properties into account [12, 16].

The concepts of *constrained coding* [41] can also be used to describe the genetic information flow from DNA to proteins [8, 13, 20]. Namely, we can use biochemical and linguistics constraints to explain the conservation of genomes. An interesting interpretation is due to Barbieri [8, 42]. Barbieri introduced the concept of “organic code,” which is more complicated than catalysis as it requires an *adaptor* or interface to bind to a molecule (or group of molecules) of different kinds to establish the mapping between each element from one set and corresponding element from another set. For instance, the genetic code establishes the connection (mapping) between the world of nucleotide and the world of amino acids. The transfer RNAs represent the adaptors or interface between the two worlds. The set of rules of genetic code implement the mapping between two worlds. Further, since the genetic code is many-to-one correspondence, it is irreversible.

Another interesting example of organic codes is the *splicing code*. The huge splicing molecular bodies, known as *spliceosomes*, employ small nuclear RNAs (snRNAs) to perform two recognition processes, one for the beginning and one for the end of each exon. The set of rules applied during the splicing process can be called a splicing code.

The fact that specific structure of proteins such as  $\alpha$ -helices and  $\beta$ -sheets are not compatible with some sequence of amino acids drives us to the conclusion that the corresponding sequence of codons must be forbidden, indicating that such process of generation of amino acids can be described as a constrained system. Since it is possible to combine the constrained coding and error-control coding using the so-called reversed concatenation scheme [43], it is possible simultaneously to introduce the constraints into a sequence of nucleotides and perform error-correction encoding.

Organic codes by Barbieri can be implemented and maintained with the help of so-called semantic feedback loops, introduced in [20]. Their operation is dependent on error-correction properties of the genomic code and the enzymatic properties of proteins [20], as illustrated in Fig. 6.11. The semantic feedback loop affects the genetic mapping. In eukaryotic cells, the transcription process results in pre-messenger RNA, containing both exons and introns. During the splicing process, the introns are spliced out to obtain mRNA composed only of exons. Since in prokaryotic cells introns do not exist, the splicing process does not exist either. The synthesis of proteins involved in enzymatic activities is controlled by particular

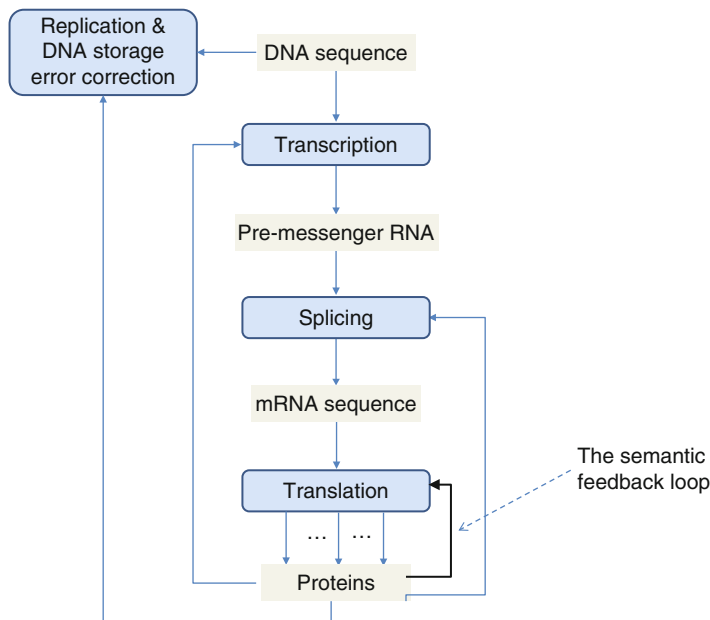


**Fig. 6.11** Genetic feedback loops in eukaryotic cells

genes in DNA. The conservation of the whole structure is clearly dependent on the genome conservation, and random or induced mutation errors in DNA (as a storage material) must be corrected for. If the probability of gene storage error to occur is  $p$  and  $n$  enzymes are involved, then the probability of the whole structure to fail will be  $np$ , provided  $p$  is sufficiently small.

In processes for which quantum effects are important, as those described in the previous two chapters, the quantum error correction would be an appropriate mechanism to deal with quantum genetic errors. The errors introduced during quantum biological processes can be detected and corrected for with the help of *entanglement*, as described in [21, 44]. Initially, the quantum biological system  $Q$ , being in initial state  $|\psi\rangle$ , and corresponding environment  $E$ , being in initial state  $|e\rangle$ , are not entangled. However, due to interaction, they become entangled, and this interaction can be represented by the following mapping:

$$|\psi\rangle|e\rangle \rightarrow \sum_s \{E_s|\psi\rangle\}|e_s\rangle, \quad (6.11)$$

where  $E_s$  is the error introduced by the environment and  $\{|e_s\rangle\}$  is the basis of the environment. To deal with errors, an ancilla qubit  $|0\rangle$  is needed, which gets coupled with the biological system with the help of a unitary operation  $U$ :

$$U[|0\rangle\{E_s|\psi\rangle\}] = |s\rangle\{E_s|\psi\rangle\}. \quad (6.12)$$

Clearly, the final ancilla state  $|s\rangle$  is a function of the error  $E_s$  but not the function of the biological quantum state  $|\psi\rangle$ . The final ancilla states form the orthonormal set so that they can be uniquely distinguished. The operator  $U$  has produced the following overall transformation:

$$U\sum_s |0\rangle\{E_s|\psi\rangle\}|e_s\rangle = \sum_s |s\rangle\{E_s|\psi\rangle\}|e_s\rangle. \quad (6.13)$$

The post-measurement state is a non-entangled state, obtained as the result of projection:

$$|\phi_{pm}\rangle = |S\rangle\{E_s|\psi\rangle\}|e_s\rangle, \quad (6.14)$$

where the state  $|S\rangle$  is the error syndrome state related to the error operator  $E_s$ . Once the error operator is identified, we have to apply the inverse operator to correct the error introduced by the environment:

$$|S\rangle\{E_s^{-1}E_s|\psi\rangle\}|e_s\rangle = |S\rangle|\psi\rangle|e_s\rangle. \quad (6.15)$$

The above-described error correction represents one particular instance of so-called canonical quantum error-correction codes, illustrated in Fig. 6.12. The encoders perform the following mapping:

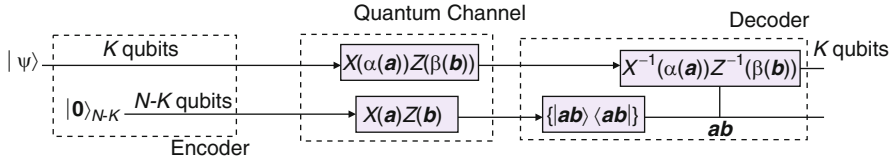


**Fig. 6.12** Canonical quantum error-correction scheme

$$U_{\text{encoder}}: |\psi\rangle \rightarrow |0\rangle_{N-K}|\psi\rangle_K. \quad (6.16)$$

In other words, the code word is created by concatenating  $N - K$  ancilla qubits to  $K$  information qubits. This scheme is compatible with the case when we are only concerned with the base type preservation, pyrimidine type  $\mathcal{Y} = \{\text{C, U}\}$  or purine type  $\mathcal{R} = \{\text{A, G}\}$ , but not with the exact base preservation. The basis for single-qubit errors is given by  $\{I, X, Y, Z\}$ , where  $X$  is qubit-flip error,  $Z$  is the phase-flip error, and  $Y$  simultaneous qubit-flip and phase-flip error, as indicated in Chap. 2. The basis for  $N$ -qubit errors is obtained by forming all possible direct products as follows:

$$E = j^l O_1 \otimes \cdots \otimes O_N; \quad O_i \in \{I, X, Y, Z\}, \quad l = 0, 1, 2, 3. \quad (6.17)$$

Since  $Y = -jXZ$ , any error in Pauli group of  $N$ -qubit errors can be represented by

$$E = j^l X(\mathbf{a})Z(\mathbf{b}); \quad \mathbf{a} = a_1 \cdots a_N; \quad \mathbf{b} = b_1 \cdots b_N; \quad l = 0, 1, 2, 3 \quad (6.18)$$

where

$$X(\mathbf{a}) \equiv X_1^{a_1} \otimes \cdots \otimes X_N^{a_N}; \quad Z(\mathbf{b}) \equiv Z_1^{b_1} \otimes \cdots \otimes Z_N^{b_N}; \quad a_i, b_i \in \{0, 1\}, \quad (6.19)$$

and the subscript denote the locations of qubits on which particular error operators are acting on. As an illustration, the error  $E = Z_1X_2Y_9 = -jZ_1X_2X_9Z_9$  can be identified (up to the phase constant) by specifying two vectors  $\mathbf{a} = (010000001)$  and  $\mathbf{b} = (100000001)$  with nonzero locations specifying the positions of  $X$  and  $Z$  operators, respectively. Notice this representation is equivalent to classical representation of the error operator  $E$  as follows  $\mathbf{e} = [\mathbf{b}|\mathbf{a}] = [100000001|010000001]$ . The correctible set of errors can be represented by

$$E_c = \{X(\mathbf{a})Z(\mathbf{b}) \otimes X(\alpha(\mathbf{a}))Z(\beta(\mathbf{b})): \mathbf{a}, \mathbf{b} \in F_2^{N-K}; F_2 = \{0, 1\}\}; \quad \alpha, \beta: F_2^{N-K} \rightarrow F_2^{N-K}. \quad (6.20)$$

The action of a correctible quantum error  $E \in E_c$  is given by

$$\begin{aligned} E(|\mathbf{0}\rangle|\psi\rangle) &= X(\mathbf{a})Z(\mathbf{b})|0\rangle \otimes X(\alpha(\mathbf{a}))Z(\beta(\mathbf{b}))|\psi\rangle \stackrel{X(\mathbf{a})Z(\mathbf{b})|\mathbf{0}\rangle=X(\mathbf{a})|\mathbf{0}\rangle=|\mathbf{a}\rangle}{=} |\mathbf{a}\rangle \otimes X(\alpha(\mathbf{a}))Z(\beta(\mathbf{b}))|\psi\rangle \\ &= |\mathbf{a}\rangle|\psi'\rangle \end{aligned} \quad (6.21)$$

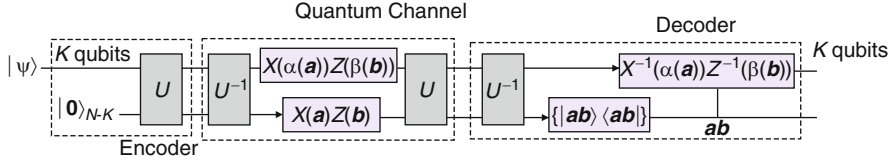


Fig. 6.13 Generalized quantum error-correction scheme

On the receiver side, we perform the measurements on ancillas to determine the syndrome  $S = (\mathbf{a}, \mathbf{b})$ , without affecting the information qubits. Once the syndromes are determined, we perform reverse recovery operator actions  $X^{-1}(\alpha(\mathbf{a}))$  and  $Z^{-1}(\beta(\mathbf{b}))$ , as shown in Fig. 6.12, and the proper information  $K$ -qubit state is recovered.

This canonical error-correction scheme can easily be generalized by applying the encoded operation  $U_{\text{encoder}} = U$  on canonical state as shown in Fig. 6.13.

The set of correctable errors is now given by

$$E = \{U^{-1}[X(\mathbf{a})Z(\mathbf{b}) \otimes X(\alpha(\mathbf{a}))Z(\beta(\mathbf{b}))]U\}. \quad (6.22)$$

Now we have arrived at the point to introduce the concept of quantum *stabilizer codes*. In quantum stabilizer codes, the quantum code  $C_q$  is identified with the unique subspace of  $H_2^N$  that is fixed by the elements of an abelian group  $S$  known as the *stabilizer* of  $C_q$ :

$$\forall s \in S, \quad |c\rangle \in C_q : \quad s|c\rangle = |c\rangle. \quad (6.23)$$

Any element  $s \in S$  can be represented in terms of  $N - K$  generator operators  $g_1, \dots, g_{N-K}$  as follows:

$$s = g_1^{a_1} \cdots g_{N-K}^{a_{N-K}}, \quad a_i \in \{0, 1\}; \quad i = 1, \dots, N - K, \quad (6.24)$$

and elements from  $S$  can be labeled by vectors of length  $N - K$ , namely,  $\mathbf{a} = a_1, \dots, a_{N-K}$ . The eigenvalues of generators  $g_i$ , denoted as  $\text{eig}(g_i)$ , can be determined from:

$$|\text{eig}(g_i)\rangle = I|\text{eig}(g_i)\rangle = g_i^2|\text{eig}(g_i)\rangle = \text{eig}^2(g_i)|\text{eig}(g_i)\rangle. \quad (6.25)$$

From (6.25), it is evident that  $\text{eig}^2(g_i) = 1$ . In other words, we can write

$$\text{eig}(g_i) = \pm 1 = (-1)^{\lambda_i}; \quad \lambda_i = 0, 1 \quad (6.26)$$

and the eigenvalues of generators are specified by a vector  $\lambda = [\lambda_1, \dots, \lambda_{N-K}]$ ,  $\lambda_i \in \{0, 1\}$ . Because the parent space for  $C_q$  is  $2^N$  dimensional, in addition to commuting generators, we need to find  $K$  commuting operators to specify a unique state  $|\psi\rangle \in H_2^N$  as follows:

$$\{g_1, g_2, \dots, g_{N-K}; \bar{Z}_1, \bar{Z}_2, \dots, \bar{Z}_K\}, \quad (6.27)$$

where the encoded Pauli operators  $\bar{Z}_k = UZ_kU^\dagger$ ;  $k = 1, \dots, K$  satisfy the required commutativity property. It can be straightforwardly shown that for any element from  $S$  that anticommutes with error  $E$ , the image of a code word  $|c\rangle$ , namely,  $E|c\rangle$ , is orthogonal to any other code word  $|c'\rangle \in C_q$ . In other words, we can write  $\langle c'|E|c\rangle = 0$ . It can also be shown that the image of code space  $C_q$  under the action of error  $E$  is uniquely specified by the vector  $\lambda = [\lambda_1, \dots, \lambda_{N-K}]$  such that

$$\lambda_i = \begin{cases} 0, & [E, g_i] = 0 \\ 1, & \{E, g_i\} = 0 \end{cases} \quad (i = 1, \dots, N-K). \quad (6.28)$$

Clearly, the vector  $\lambda$  specifies the syndrome of error  $E$ , denoted as  $S(E)$ , and we can write  $S(E) = [\lambda_1 \dots \lambda_{N-K}]$ . Similarly, as error operators, the generators  $g_i$  can also be represented in binary form as  $2N$ -dimensional vectors:

$$\mathbf{g}_i = (\mathbf{a}_i \mid \mathbf{b}_i). \quad (6.29)$$

By listing down the generators in binary form as rows in corresponding matrix, we obtain the so-called quantum-check matrix:

$$\mathbf{A} = \begin{pmatrix} \mathbf{a}_1 \mid \mathbf{b}_1 \\ \vdots \\ \mathbf{a}_K \mid \mathbf{b}_{N-K} \end{pmatrix}, \quad (6.30)$$

which is an equivalent of the parity-check matrix of classical codes. By representing the error operator  $E$  as  $2N$ -dimensional vector  $\mathbf{e} = [\mathbf{c} \mid \mathbf{d}]$ , the syndrome can be determined as

$$S(E) = \mathbf{e}\mathbf{A}^T, \quad (6.31)$$

which is very similar to the syndrome calculation of the classical linear block codes.

When designing the quantum code, the following two conditions must be satisfied [21, 44]: (1) the encoded computational basis (CB) states, denoted as  $|\bar{i}\rangle$ , must be chosen in such a way that the environment is not able to distinguish among them and (2) the corrupted image of one code word must be orthogonal to corrupted images of all other code words. In other words, the conditions above can be mathematically expressed as

$$\begin{aligned} \forall |\bar{i}\rangle, |\bar{j}\rangle \quad (\bar{i} \neq \bar{j}) \quad \text{and} \quad \forall E_a, E_b \in E : \\ \langle \bar{i} | E_a^\dagger E_b | \bar{i} \rangle = \langle \bar{j} | E_a^\dagger E_b | \bar{j} \rangle \quad \text{and} \quad \langle \bar{i} | E_a^\dagger E_b | \bar{j} \rangle = 0. \end{aligned} \quad (6.32)$$

An important class of codes, invented by Calderbank, Shor, and Steane (CSS codes), has the following form of quantum-check matrix:

$$A = \begin{bmatrix} \mathbf{H} & | & \mathbf{0} \\ \mathbf{0} & | & \mathbf{G} \end{bmatrix}, \quad \mathbf{H}\mathbf{G}^T = \mathbf{0} \quad (6.33)$$

where  $\mathbf{H}$  and  $\mathbf{G}$  are  $M \times N$  classical parity-check matrices. As there are  $M_Q = 2M$  stabilizer conditions applying to  $N$ -qubit states,  $N - 2M$  qubits are encoded in  $N$  qubits. If  $\mathbf{H} = \mathbf{G}$ , the quantum-check matrix  $A$  has the particularly simple form:

$$A = \begin{bmatrix} \mathbf{H} & | & \mathbf{0} \\ \mathbf{0} & | & \mathbf{H} \end{bmatrix}, \quad \mathbf{H}\mathbf{H}^T = \mathbf{0}. \quad (6.34)$$

The  $\mathbf{H}\mathbf{H}^T = \mathbf{0}$  condition is equivalent to  $\mathbf{C}^\perp(\mathbf{H}) \subset \mathbf{C}(\mathbf{H})$ , where  $\mathbf{C}(\mathbf{H})$  is the code having  $\mathbf{H}$  as its parity-check matrix and  $\mathbf{C}^\perp(\mathbf{H})$  is its dual code. We call such a code a *dual-containing code*; it is also known as the “weakly self-dual code.”

The error detector can be obtained by concatenation of circuits corresponding to different stabilizers. The error introduced by the environment can be identified as an intersection of corresponding syndrome measurements. As an illustration, the implementation of stabilizer  $S_a = X_1X_4X_5X_6$  is shown in Fig. 6.14. The encoder of dual-containing codes, defined by a full-rank matrix  $H$  with  $N > 2M$ , can be determined as follows [45] (see also [21]). We first transform the  $\mathbf{H}$ -matrix by Gauss elimination into the following form:

$$\tilde{\mathbf{H}} = [\mathbf{I}_M \mid \mathbf{P}_{M \times (N-M)}]. \quad (6.35)$$

In the second stage, we further transform the  $\mathbf{P}$ -matrix into the following form:

$$\tilde{\mathbf{P}} = [\mathbf{I}_M \mid \mathbf{Q}_{M \times (N-2M)}]. \quad (6.36)$$

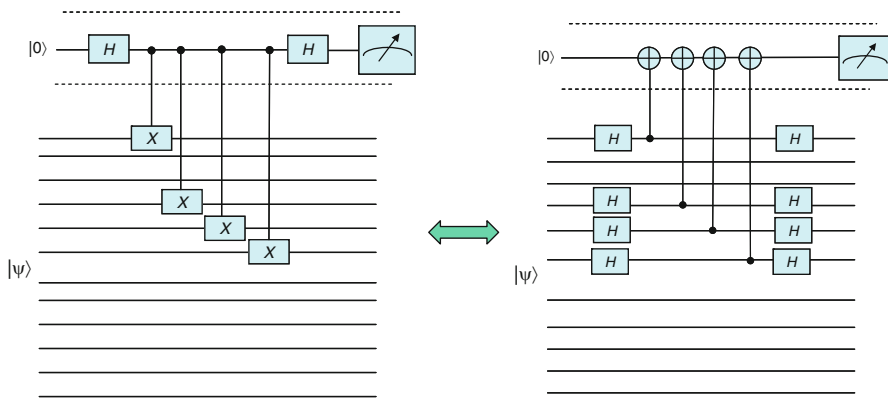


**Fig. 6.14** Syndrome  $S_a = X_1X_4X_5X_6$  implementation quantum circuits

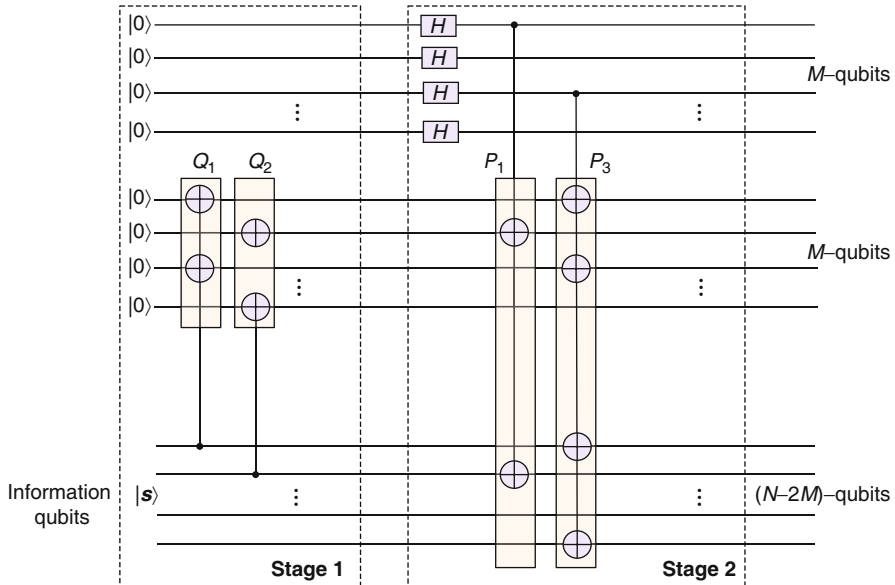


**Fig. 6.15** Encoder implementation of dual-containing codes

For an arbitrary string  $f$  of length  $K = N - 2M$ ,  $|\mathbf{0}|\mathbf{Qf}f\rangle$  is a code word of  $C_q$  given by quantum-check matrix (6.34). The corresponding encoder is shown in Fig. 6.15.

The *Stage 1* performs the following mapping:

$$|\mathbf{0}\rangle_M |\mathbf{0}\rangle_M |\mathbf{s}\rangle_K \rightarrow |\mathbf{0}\rangle_M |\mathbf{Qs}\rangle_M |\mathbf{s}\rangle_K, \quad |\mathbf{0}\rangle_M = \underbrace{|\mathbf{0}\rangle \cdots |\mathbf{0}\rangle}_{M \text{ times}}. \quad (6.37)$$

The block  $Q_k$  in the first stage corresponds to the  $k$ th column of submatrix  $\mathbf{Q}$  in (6.36). This block is controlled by  $k$ th information qubit and executed only when the  $k$ th information qubit is  $|1\rangle$ . The CNOT gates are placed according to the nonzero positions in  $Q_k$ . In *Stage 2*, the first  $M$ -qubits from stage 1 (ancillas) are processed by Hadamard gates mapping the state  $|\mathbf{0}\rangle_M$  to

$$|\mathbf{0}\rangle_M \rightarrow \underbrace{\frac{|\mathbf{0}\rangle + |\mathbf{0}\rangle}{\sqrt{2}} \otimes \cdots \otimes \frac{|\mathbf{0}\rangle + |\mathbf{0}\rangle}{\sqrt{2}}}_{M \text{ times}} = \frac{1}{2^{M/2}} \sum_{\mathbf{v}} |\mathbf{v}\rangle_M. \quad (6.38)$$

The purpose of *Stage 2* is to conditionally execute the row operators of  $\tilde{\mathbf{H}} = [I_M | \mathbf{P}_{M \times (N-M)}]$  on target qubits  $|\mathbf{y}\rangle_{N-M}$ ,  $\mathbf{y} = [\mathbf{Qs} | \mathbf{s}]$ , where the control qubits are given by  $|\mathbf{v}\rangle_M$ , and the overall action is

$$\begin{aligned}
\frac{1}{2^{M/2}} \sum_{\mathbf{v}} |\mathbf{v}\rangle_M |\mathbf{y}\rangle_{N-M} &\rightarrow \frac{1}{2^{M/2}} \sum_{\mathbf{v}} \left( \prod_{m=1}^M P_m^c \right) |\mathbf{v}\rangle_M |\mathbf{y}\rangle_{N-M} \\
&= \frac{1}{2^{M/2}} \sum_{\mathbf{x} \in \mathcal{C}^\perp(H)} |\mathbf{x} + \mathbf{y}\rangle_N, \quad \mathbf{y} \in C(H).
\end{aligned} \tag{6.39}$$

For efficient encoder and decoder implementation of stabilizer codes, an interested reader is referred to [21].

Before concluding this section, we briefly discuss the *distance* of a quantum error-correction code. We say that a quantum error-correction code has a *distance*  $D$  if all errors of weight less than  $D$  satisfy equations (6.32), and there exists at least one error, represented as  $E = E_a^\dagger E_b$ , of weight  $D$  to violate it. In other words, distance of the quantum error-correction code is the weight of the smallest weight  $D$  of error  $E = E_a^\dagger E_b$  that cannot be detected by the code. Similar to classical codes, we can relate the distance  $D$  to the error-correction capability  $t$  as follows:  $D \geq 2t + 1$ . Namely, since  $E = E_a^\dagger E_b$ , the weight of error operator  $E$  will be  $\text{wt}(E_a^\dagger E_b) = 2t$ . If we are only interested in detecting the error but not correcting them, the error detection capability  $d$  is related to the distance  $D$  by  $D \geq d + 1$ . Since we are interested only in detection of errors, we can set  $E_p = I$  to obtain  $\text{wt}(E_a^\dagger E_b) = \text{wt}(E_b) = d$ . If we are interested in simultaneously detecting  $d$  errors and correcting  $t$  errors, the distance of the code must be  $D \geq d + t + 1$ .

In next section, we describe one particular class of stabilizer codes, known as topological codes, which might be relevant to biological processes as they only involve the local qubits in the encoding process.

### 6.3 Topological Codes

The topological quantum error-correction codes [46–56] are typically defined on a two-dimensional lattice, with quantum parity check being geometrically local. The topological codes might be relevant on a cellular level as discussed in [57]. Further, the microtubule networks might be based on topological codes as discussed in [58, 59]. The locality of parity check is of crucial importance since the syndrome measurements are easy to implement when the qubits involved in syndrome verification are in close proximity of each other. In addition, the possibility to implement the universal quantum gates topologically yields to the increased interest in topological quantum codes. On the other hand, someone may argue that quantum LDPC codes can be designed in such a way that quantum parity checks are only local. In addition, through the concept of subsystem codes, to be described in next section, the portion of qubits not carrying any encoded information can be interpreted as gauge qubits. The gauge qubits, located in intron regions, can be used to “absorb” the effect of errors. Moreover, the subsystem codes allow the syndrome measurements with a

smaller number of qubit interactions. The combination of a locality of topological codes and small number of interactions leads us to the new generation of quantum error-correction codes, known as topological subsystem codes, due to Bombin [50].

The topological codes on a square lattice such as Kitaev's toric code [47, 48], quantum lattice code with a boundary [49], surface codes, and planar codes [49] are easier to design and implement [50–52]. These basic codes on qubits can be generalized to higher alphabets [53, 54] resulting in quantum topological codes on qudits. In this section, we are concerned only with quantum topological codes on qubits; the corresponding topological codes on qudits can be obtained following the similar analogy to be provided in Sect. 6.5 (see also [21]). Kitaev's toric code [47, 48] is defined on a square lattice with periodic boundary conditions, meaning that the lattice has a topology of a torus as shown in Fig. 6.16a. The qubits are associated with the edges of the lattice. For the  $m \times m$  square lattice on the torus, there are  $N = 2m^2$  qubits. For each vertex  $v$  and plaquette (or face)  $p$  (see Fig. 6.16b), we associate the stabilizer operators as follows:

$$A_v = \bigotimes_{i \in n(v)} X_i \quad \text{and} \quad B_p = \bigotimes_{i \in n(p)} Z_i, \quad (6.40)$$

where  $X_i$  and  $Z_i$  denote the corresponding Pauli- $X$  and Pauli- $Z$  operators on position  $i$ ; with  $n(v)$ , we denoted the neighborhood of vertex  $v$ , that is, the set of edges incident to vertex  $v$ , while with  $n(p)$ , we denoted the neighborhood of plaquette  $p$ ,

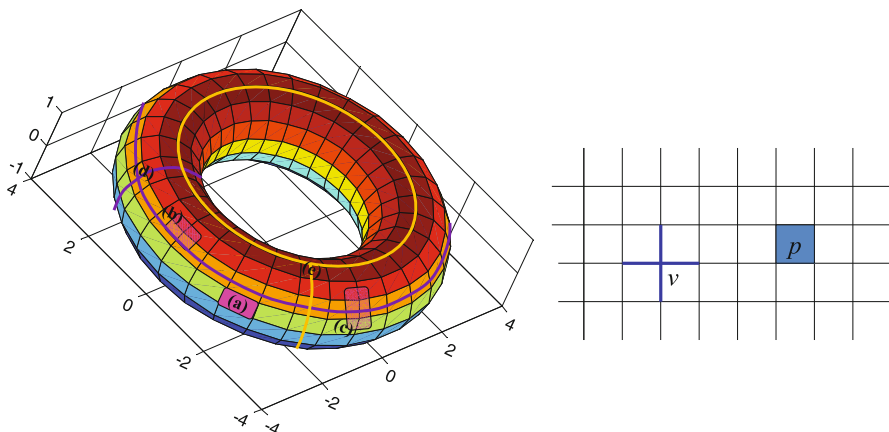


**Fig. 6.16** Definition of the square lattice on the torus. In this topological code, the qubits are associated with the edges. The figure on the *right* shows an enlarged portion of square lattice on the torus, illustrating two types of generators. The  $Z$ -containing generators represent string on the lattice, while the  $X$ -containing generators represent the strings on the dual lattice. The elementary trivial loop (*cycle*) denoted with (a) corresponds to a certain  $B_p$  operator, while the elementary trivial cycle denoted with (b) corresponds to a certain  $A_v$  operator on the lattice dual. The trivial loops can be obtained as product of individual elementary loops; see, for example, the cycle denoted with (c). The nontrivial loops on the dual of lattice, such as (d), or on the lattice, such as (e), correspond to the generators from the set of encoded (*logical*) Pauli operators

that is, the set of edges encircling the face  $p$ . (We use the symbol  $\otimes$  to denote the tensor product, as we have done earlier.)

Based on Pauli operator properties (see Chap. 2), it is clear that operators  $A_v$  and  $B_p$  mutually commute. Namely, the commutation of operators  $A_v$  among themselves is trivial to prove. Since  $A_v$  and  $B_p$  operators have either 0 or 2 edges in common (see Fig. 6.16b), they commute (an even number of anticommuting Pauli operators result in commuting stabilizer operators). The operators  $A_v$  and  $B_p$  are Hermitian and have eigenvalues 1 and  $-1$ . Let  $H_2^N$  denote the Hilbert space, where  $N = 2m^2$ . The toric code space  $C_Q$  can be defined as follows:

$$C_Q = \{ |c\rangle \in H_2^N \mid A_v |c\rangle = |c\rangle, B_p |c\rangle = |c\rangle; \forall v, p \}. \quad (6.41)$$

The (6.41) represents the eigenvalue equation, and since  $A_v$  and  $B_p$  mutually commute, they have common eigenkets. The stabilizer group is defined by  $S = \langle A_v, B_p \rangle$ .

Since  $\prod_v A_v = I$ ,  $\prod_p B_p = I$ , there are  $M = 2m^2 - 2$  independent stabilizer operators. The number of information qubits can be determined by  $K = N - M = 2$  and the code space dimensionality is  $\dim C_Q = 2^{N-K} = 4$ . Clearly, this toric code has a low quantum code rate. Another interesting property to notice is that stabilizers  $A_v$  contain only  $X$  operators, while stabilizers  $B_p$  contain only  $Z$  operators. Clearly, this toric code represents a particular instance of CSS codes, described in the previous section. The encoder and decoder can, therefore, be implemented as described in the previous section. For efficient encoder and decoder implementations, an interested reader is referred to [21, 44]. We have seen above that the commutation of  $A_v$  and  $B_p$  arises from the fact that these two operators have either 0 or 2 common edges, which is equivalent to the classical code with the property that any two rows overlap in even number of positions, representing a dual-containing code.

Let us now observe the error  $E$  acting on code word  $|c\rangle$ , which results in state  $E|c\rangle$  that is not necessarily the eigenket with eigenvalue  $+1$  of vertex and plaquette operators. If  $E$  and  $A_p$  commute, then the ket  $E|c\rangle$  will be the  $+1$  eigenket; otherwise it will be  $-1$  eigenket. The similar conclusion applies to  $B_p$ . By performing the measurements on each vertex  $A_v$  and plaquette  $B_p$  operators, we obtain the syndrome pair  $s = (s_v, s_p)$ , where  $s_i = \pm 1$ ,  $i \in \{v, p\}$ . The intersection of syndrome pairs will give us the set of errors having the same syndrome, namely, the coset (the set of errors that differ in an element from stabilizer  $S$ ). Out of all possible errors from the coset, we chose the most probable one, typically the lowest weight one. Alternatively, someone may want to use maximum likelihood (ML) decoding, as described in [21]. However, the complexity is too high for implementation on a cellular level.

In next section, we describe another class of quantum codes possibly compatible with quantum biological effects.

## 6.4 Subsystem Codes

The subsystem codes [60–64] represent a generalization of both stabilizer codes and topological codes. They can also be considered as generalization of decoherence-free subspaces (DFSs) [65, 66] and noiseless subsystems (NSs) [67]. The key idea behind subsystem codes is to decompose the quantum code  $C_Q$  as the tensor product of two subsystems  $A$  and  $B$  as follows:  $C_Q = A \otimes B$ . The information qudits belong to subsystem  $A$ , in our case the exon regions, and non-information qudits, also known as gauge qudits, belong to subsystem  $B$ , in our case intron regions. We are only concerned with errors introduced in subsystem  $A$  and DNA coding regions, while the subsystem  $B$  is used absorb the environmental errors in addition to storing non-information parity-check qubits/qudits.

Both environment introduced error  $\mathcal{E}$  and recovery  $\mathcal{R}$  processes can be described as quantum operations  $\mathcal{E}, \mathcal{R}: L(H) \rightarrow L(H)$ , where  $L(H)$  is the space of linear operators on Hilbert space  $H$ . These mappings can be represented in terms of operator sum representation,  $\mathcal{E}(\rho) = \sum_i E_i \rho E_i^\dagger$ ,  $E_i \in L(H)$ ,  $\mathcal{E} = \{E_i\}$ . Given the quantum code  $C_Q$  that is the subspace of  $H$ , we say that the set of errors  $\mathcal{E}$  are correctable if there exists a recovery operation  $\mathcal{R}$  such that  $\mathcal{R}\mathcal{E}(\rho) = \rho$  from any state  $\rho$  from  $L(C_Q)$ . In terms of subsystem codes, we say that there exists a recovery operation such that for any  $\rho^A$  from  $L(A)$  and  $\rho^B$  from  $L(B)$ , the following is valid:  $\mathcal{R}\mathcal{E}(\rho^A \otimes \rho^B) = \rho^A \otimes \rho^B$ , where the state  $\rho^B$  is not relevant. The necessary and sufficient condition for the set of errors  $\mathcal{E} = \{E_m\}$  to be correctable is that  $PE_m^\dagger E_n P = I^A \otimes g_{mn}^B$ ,  $\forall m, n$ , where  $P$  is the projector on code subspace. Such set of errors is called the correctable set of errors. Clearly, the linear combination of errors from  $\mathcal{E}$  is also correctable so that it makes sense to observe the correctible set of errors as linear space with properly chosen operator basis. If we are concerned with quantum registers/system composed of  $N$  qubits, the corresponding error operators are Pauli operators. The Pauli group on  $N$  qubits,  $G_N$ , is already introduced in Chap. 2. The stabilizer formalism can also be used in describing the stabilizer subsystem codes. Stabilizer subsystem codes are determined by a subgroup of  $G_N$  that contains the element  $jI$ , called the *gauge group*  $\mathcal{G}$ ; and by stabilizer group  $S$  that is properly chosen such that  $S' = j^3 S$  is the center of  $\mathcal{G}$ , denoted as  $Z(\mathcal{G})$  (i.e., the set of elements from  $\mathcal{G}$  that commute with all elements from  $\mathcal{G}$ ). We are concerned with the following decomposition of  $H$ :  $H = C \oplus C^\perp = (H_A \otimes H_B) \oplus C^\perp$ , where  $C^\perp$  is dual of  $C = H_A \otimes H_B$ . The gauge operators are chosen in such a way that they act trivially on subsystem  $A$  but generate full algebra of the subsystem  $B$ . The information is encoded on subsystem  $A$ , while the subsystem  $B$  is used to absorb the effects of gauge operations. The Pauli operators for  $K$  logical qubits are obtained from the isomorphism  $N(\mathcal{G})/S \simeq G_K$ , where  $N(\mathcal{G})$  is normalizer of  $\mathcal{G}$ . On the other hand, subsystem  $B$  consists of  $R$  gauge qubits recovered from isomorphism  $\mathcal{G}/S \simeq G_N$ , where  $N = K + R + s$ ,  $s \geq 0$ . If  $\tilde{X}_1$  and  $\tilde{Z}_1$  represent the images of  $X_i$  and  $Z_i$  under automorphism  $U$  of  $G_N$ , the stabilizer can be described by  $S = \langle \tilde{Z}_1, \dots, \tilde{Z}_s \rangle$ ;  $R + s \leq N$ ;  $R, s \geq 0$ .

The gauge group can be specified by  $\mathcal{G} = \langle jI, \tilde{Z}_1, \dots, \tilde{Z}_{s+R}, \tilde{X}_{s+1}, \dots, \tilde{X}_R \rangle$ . The images must satisfy the commutative relations. The logical (encoded) Pauli operators will be then  $\bar{X}_1 = \tilde{X}_{s+R+1}, \bar{Z}_1 = \tilde{Z}_{s+R+1}, \dots, \bar{X}_K = \tilde{X}_N, \bar{Z}_K = \tilde{Z}_N$ . The detectable errors are the elements of  $G_N - N(S)$  and undetectable errors in  $N(S) - \mathcal{G}$ . Undetectable errors are related to the logical Pauli operators since  $N(S)/\mathcal{G} \simeq N(\mathcal{G})/S'$ . Namely, if  $n \in N(S)$ , there exists  $g \in \mathcal{G}$  such that  $ng \in N(\mathcal{G})$  and if  $g' \in \mathcal{G}$  such that  $ng' \in N(\mathcal{G})$  the  $gg' \in \mathcal{G} \cap N(\mathcal{G}) = S'$ . The distance  $D$  of this code is defined as the minimum weight among undetectable errors. The subsystem code encodes  $K$  qubits into  $N$ -qubit code words and has  $R$  gauge qubits and can be therefore denoted as  $[N, K, R, D]$  code.

We turn our attention now to subsystem codes defined as subspace of  $q^N$ -dimensional Hilbert space  $H_2^N$ . The qubit *error group* is defined by

$$G_N = \{j^c X(\mathbf{a})Z(\mathbf{b}) \mid \mathbf{a}, \mathbf{b} \in F_2^N, c = 0, 1, \dots, 3\}; \quad \mathbf{a} = (a_1, \dots, a_N), \\ \mathbf{b} = (b_1, \dots, b_N); \quad a_i, b_i \in F_2. \quad (6.42)$$

Let  $C_Q$  be a quantum code such that  $H = C_Q \oplus C_Q^\perp$ . The  $[N, K, R, D]$  subsystem code over  $F_2$  is defined as the decomposition of code space  $C_Q$  into a tensor product of two subsystems  $A$  and  $B$  such that  $C_Q = A \otimes B$ , where dimensionality of  $A$  equals  $\dim A = 2^K$  and  $\dim B = 2^R$  and all errors of weight less than  $D_{\min}$  on subsystem  $A$  can be detected. What is interesting about this class of codes is that when constructed from classical codes, the corresponding classical code does not need to be dual containing (self-orthogonal).

For  $[N, K, R, D_{\min}]$  stabilizer subsystem codes over  $F_2$ , it can be shown that centralizer of  $S$  is given by

$$C_{G_N}(S) = \langle \mathcal{G}, \bar{X}_1, \bar{Z}_1, \dots, \bar{X}_K, \bar{Z}_K \rangle. \quad (6.43)$$

Since  $C_Q = A \otimes B$ , then  $\dim A = 2^K$  and  $\dim B = 2^R$ , and the stabilizer  $S$  can be used as projector to  $C_Q$ . The dimensionality of quantum code defined by stabilizer  $S$  is  $2^{K+R}$ . The stabilizer  $S$ , therefore, defines an  $[N, K+R, D]$  stabilizer code. Based on (6.43), we conclude that image operators  $\tilde{Z}_i, \tilde{X}_i$ ;  $i = s+1, \dots, R$  behave as encoded operators on gauge qubits, while  $\bar{Z}_i, \bar{X}_i$  act on information qubits. In total, we have the set of  $2(K+R)$  encoded operators of  $[N, K+R, D]$  stabilizer codes given by

$$\{\bar{X}_1, \bar{Z}_1, \dots, \bar{X}_K, \bar{Z}_K, \tilde{X}_{s+1}, \tilde{Z}_{s+1}, \dots, \tilde{X}_{s+R}, \tilde{Z}_{s+R}\}. \quad (6.44)$$

Therefore, with (6.44), we have just established the connection between stabilizer codes and subsystem codes. Since subsystem codes are more flexible for design, they can be used to design new classes of stabilizer codes.

If we are interested in distinguishing nucleobases, not only with preserving the purine or pyrimidine type, we need to deal with nonbinary stabilizer codes, which is the subject of incoming section.

## 6.5 Nonbinary Quantum Stabilizer Codes

The DNA error-correction mechanism can be described by using the concepts of nonbinary stabilizer codes. Given that both transcription and translation processes are prone to errors, reasonable simple nonbinary stabilizer codes are needed. Since codon basekets live in  $D = 64$ -dimensional Hilbert space  $H_{64}$ , the dimension  $D$  can be expressed as  $D = 4^3 = 2^6$ . If the addition is performed in  $\text{GF}(2^6)$ , we can define the set of gates that can be used for arbitrary operation on quantum digits (qudits). Here we identify the qudits with corresponding nucleic bases.

In previous sections, we considered quantum stabilizer codes with finite geometry representation over  $F_2^{2N}$ ,  $F_2 = \{0, 1\}$ . Because these codes are defined over  $F_2^{2N}$ , they can be called “binary” stabilizer codes. In this section, we are concerned with stabilizer codes defined over  $F_q^{2N}$ , where  $q = p^m$  is a prime power ( $p$  is a prime, and  $m \geq 1$  is an integer) [68–71]. This class of codes can be called the “nonbinary” stabilizer codes. Although many definitions and properties from previous sections are applicable here, certain modifications are needed as described below. First of all, we operate on  $q$ -ary quantum digits, which in analogy with qubits can be called “qudits.” Secondly, we need to extend the definitions of quantum gates to qudits. In Chap. 2, we have seen that arbitrary qubit error can be represented in terms of Pauli operators  $\{I, X, Y, Z\}$ . We have also seen that  $Y$  operator can be expressed in terms of  $X$  and  $Z$  operators. A similar strategy can be applied here. We need to extend definitions of  $X$  and  $Z$  operators to qudits as follows:

$$X(a)|x\rangle = |x+a\rangle, \quad Z(b)|x\rangle = \omega^{\text{tr}(bx)}|x\rangle; \quad x, a, b \in F_q \quad (6.45)$$

where  $\text{tr}(\cdot)$  denotes the trace operation from  $F_q$  to  $F_p$  and  $\omega$  is a  $p$ th root of unity, namely,  $\omega = \exp(j2\pi/p)$ . The trace operation from  $F_{q^m}$  to  $F_q$  is defined as

$$\text{tr}_{q^m}(x) = \sum_{i=0}^{m-1} x^{q^i}. \quad (6.46)$$

If  $F_q$  is the prime field, the subscript can be omitted, as it was done in (6.45).

Before we proceed further with nonbinary quantum stabilizer codes, we believe it is convenient to introduce several additional *nonbinary quantum gates*, which will be useful in describing arbitrary quantum computation on qudits. The nonbinary quantum gates are shown in Fig. 6.17, in which the action of gates is described as well. Both basic gates, shown in Fig. 6.17a, and elementary gates,

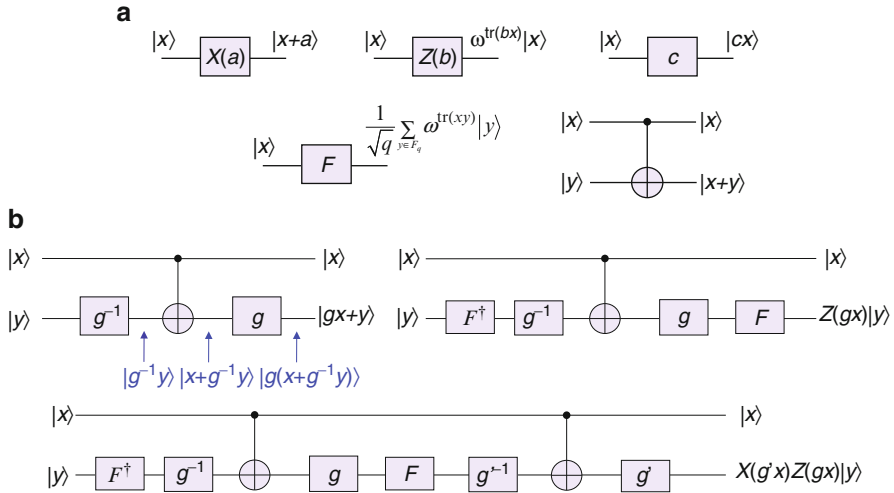


**Fig. 6.17** (a) Basic qudit quantum gates. The addition and multiplication are performed in GF( $2^n$ ). The  $\text{tr}(\cdot)$  denotes the trace operation from GF( $2^n$ ) to GF(2) and  $\omega = \exp(j\pi)$ . (b) Elementary nonbinary quantum circuits derived from the basic nonbinary gates

shown in Fig. 6.17b and derived from basic gates, are provided. The  $F$  gate corresponds to the discrete Fourier transform (DFT) gate. Its action on ket  $|0\rangle$  is the superposition of all basis kets with the same probability amplitude  $F|0\rangle = q^{-1/2} \sum_{u \in F_q} |u\rangle$ .

It can be shown that the set of errors  $\epsilon = \{X(a)X(b) | a, b \in F_q\}$  satisfies the following properties:

1. It contains the identity operator.
2.  $\text{tr}(E_1^\dagger E_2) = 0 \quad \forall E_1, E_2 \in \epsilon$ .
3.  $\forall E_1, E_2 \in \epsilon : E_1 E_2 = c E_3, E_3 \in \epsilon, c \in F_q$ .

This set forms an error basis for the set of  $q \times q$  matrices, and sometimes it is called the “nice error basis.” It can also be shown that

$$\begin{aligned}
 X(a)Z(b) &= \omega^{-\text{tr}(ab)} Z(b)X(a), \quad X(a+a')Z(b+b') \\
 &= \omega^{-\text{tr}(a'b)} X(a)Z(b)X(a')Z(b').
 \end{aligned} \tag{6.47}$$

In order to determine the nice basis error on  $N$  qudits, we introduce the following notation:  $X(\mathbf{a}) = X(a_1) \otimes \cdots \otimes X(a_N)$  and  $Z(\mathbf{b}) = Z(b_1) \otimes \cdots \otimes Z(b_N)$ , where  $\mathbf{a} = (a_1, \dots, a_N)$ ,  $\mathbf{b} = (b_1, \dots, b_N)$  and  $a_i, b_i \in F_q$ . The set  $\epsilon_N = \{X(\mathbf{a})X(\mathbf{b}) | \mathbf{a}, \mathbf{b} \in F_q^N\}$  is the nice error basis defined over  $F_q^{2N}$ . Similar to the Pauli multiplicative group, we can define the *error group* by

$$G_N = \left\{ \omega^c X(\mathbf{a}) Z(\mathbf{b}) \mid \mathbf{a}, \mathbf{b} \in F_q^N, c \in F_p \right\}. \quad (6.48)$$

Let  $S$  be the largest abelian subgroup of  $G_N$  that fixes all elements from quantum code  $C_Q$ , called the stabilizer group. The  $[N, K]$  nonbinary stabilizer code  $C_Q$  is defined as the  $K$ -dimensional subspace of the  $N$ -qudit Hilbert space  $H_q^N$  as follows:

$$C_Q = \bigcap_{s \in S} \left\{ |c\rangle \in H_q^N \mid s|c\rangle = |c\rangle \right\}. \quad (6.49)$$

Clearly, the definition of nonbinary stabilizer codes is straightforward generalization of a quantum stabilizer code over  $H_2^N$ . Therefore, similar properties, definitions, and theorems introduced in previous sections are applicable here. For example, two errors  $E_1 = \omega^{c_1} X(\mathbf{a}_1) Z(\mathbf{b}_1)$ ,  $E_2 = \omega^{c_2} X(\mathbf{a}_2) Z(\mathbf{b}_2) \in G_N$  commute if and only if their trace-symplectic product vanishes, that is,

$$\text{tr}(\mathbf{a}_1 \mathbf{b}_2 - \mathbf{a}_2 \mathbf{b}_1) = 0. \quad (6.50)$$

The (symplectic) weight of a qudit error  $E = \omega^c X(\mathbf{a}) Z(\mathbf{b})$  can be defined as the number of components  $i$  for which  $(a_i, b_i) \neq (0, 0)$ . We say that the nonbinary quantum stabilizer code has distance  $D$  if it can detect all errors of weight less than  $D$  but none of weight  $D$ . The error-correction capability  $t$  of nonbinary quantum code is related to minimum distance by  $t = \lfloor (D - 1)/2 \rfloor$ . We say that nonbinary quantum stabilizer code is non-degenerate if its stabilizer group  $S$  does not contain an element of weight smaller than  $t$ . From definitions above, we can see that nonbinary quantum stabilizer codes are straightforward generalization of corresponding qubit stabilizer codes. The key difference is that, instead of a symplectic product, we need to use a trace-symplectic product. Similar theorems can be proved and properties can be derived by following similar procedures, by taking into account the differences outlined above. On the other hand, the quantum hardware implementation is more challenging. For example, instead of using Pauli-X and Pauli-Z gates, we have to use the  $X(a)$  and  $Z(b)$  gates shown in Fig. 6.17. For example, we can determine the syndrome based on syndrome measurements, as illustrated in previous sections. Let the generator  $\mathbf{g}_i$  be given as follows:

$$\mathbf{g}_i = [\mathbf{a}_i | \mathbf{b}_i] = [0 \cdots 0 \ a_i \cdots a_N \mid 0 \cdots 0 \ b_i \cdots b_N] \in F_q^{2N}, \ a_i, b_i \in F_q. \quad (6.51)$$

The quantum circuit shown in Fig. 6.18 will provide the nonzero measurement if a detectable error does not commute with a multiple of  $\mathbf{g}_i$ . By comparison with corresponding qubit syndrome decoding circuits from Sect. 6.2, we conclude that the  $F$  gate for nonbinary quantum codes has a similar role to the Hadamard gate for codes over  $F_2$ . Notice that the syndrome circuit is a generalization of a bottom circuit as shown in Fig. 6.17b. From Fig. 6.18, it is clear that if the input to the stabilizer circuit is  $E|\psi\rangle$ , where  $E$  is the qudit error and  $|\psi\rangle$  is the code word, then the stabilizer circuit performs the following mapping:

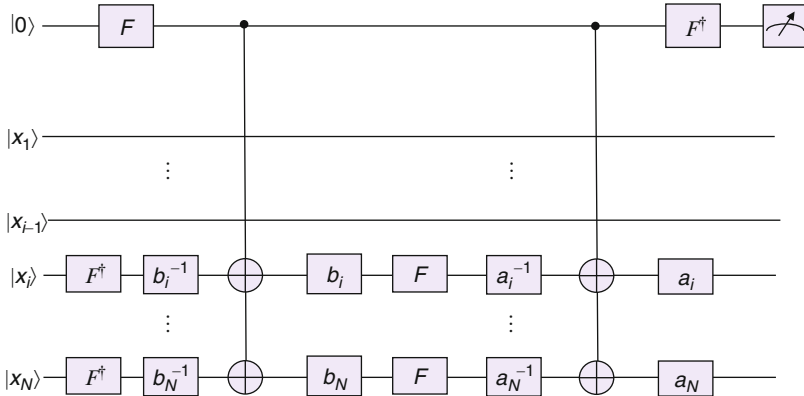


**Fig. 6.18** Implementation of nonbinary syndrome decoding circuit corresponding to generator  $\mathbf{g}_i$

$$|0\rangle E|\psi\rangle \rightarrow \sum_{u \in F_q} F^\dagger |u\rangle X(u\mathbf{a}_i) Z(u\mathbf{b}_i) E|\psi\rangle. \quad (6.52)$$

The qudit error  $E$ , by ignoring the complex phase constant, can be represented as  $E = X(\mathbf{a})Z(\mathbf{b})$ . The result of the measurement gives us the  $i$ th syndrome component  $\lambda_i = \text{tr}(\mathbf{a}\mathbf{b}_i - \mathbf{a}_i\mathbf{b})$ . By  $N - K$  measurements on corresponding generators  $\mathbf{g}_i$  ( $i = 1, \dots, N - K$ ), we obtain the following syndrome  $S(E)$ :

$$S(E) = [\lambda_1 \lambda_2 \dots \lambda_{N-K}]^T; \quad \lambda_i = \text{tr}(\mathbf{a}\mathbf{b}_i - \mathbf{a}_i\mathbf{b}), \quad i = 1, \dots, N - K. \quad (6.53)$$

The correctable qudit error maps the code space to  $q^K$ -dimensional subspace of  $q^N$ -dimensional Hilbert space. Since there are  $N - K$  generators or equivalently syndrome positions, there are  $q^{N-K}$  different cosets. All qudit errors belonging to the same coset have the same syndrome. By selecting the most probable qudit error for the coset representative, typically the lowest weight error, we can uniquely identify the qudit error and consequently perform the error-correction action.

The concept of nonbinary stabilizer codes can also be applied to topological and subsystem codes.

## 6.6 Classical/Quantum DNA Error Correction Robust to Tumor and Cancer Introducing Mutation Errors

Now since we got familiarized in both classical and quantum error-correction coding and because several classes of quantum codes that can be related to biological processes have been described, we have arrived at the fundamental question on how to modify the genetic material to increase the tolerance to both spontaneous and induced tumors. The first step toward this goal would be to

identify both classical and quantum codes to generate DNA sequences. The first step toward this goal has already been made in [14, 15], where authors have identified generator polynomials in  $GF(4)$  and  $Z_4$  to generate certain DNA sequences. Given the CSS code construction, it is straightforward to identify corresponding quantum codes of CSS type, as these codes can be related to classical ones. Since DNA error-correction code is systematic, with information related to protein synthesis placed on exon regions, it is possible to perform encoding “offline” and store the generalized parity symbols on intron regions. The tumor can artificially be introduced by radiation in certain cells of a multicellular organism under study. The DNA storage errors leading to tumors can be identified and corresponding action for their correction can be determined by running the corresponding decoding algorithms in FPGAs. Once the most probable errors are identified, we could modify genetic material on affected cells. This study will help us in identifying mechanisms for both classical and quantum error correction on the cellular level. The next step is to identify circuitry in the cell that can be used to perform the error detection followed by error-correction action. In such a way, it should be possible to develop artificial organisms with high tolerance to tumor and cancer introducing mutation errors. However, this study would require the close collaboration of biologists, physicists, and communication engineers.

## 6.7 Concluding Remarks

The main subject of this chapter has been on the use of classical/quantum information theory and coding in genetics and evolution. Section 6.1 deals with the description of using the concepts from both classical and quantum information theories to describe the evolution of biological channel capacity through generations. In order to do so, several classical and quantum biological channel models have been employed including the Markovian classical and Markovian-like quantum model, hybrid quantum-classical model, multilevel symmetric channel model, and Kimura model-based Markovian process. In order to describe the reliable long-time storage of genetic information in DNA, in Sect. 6.2, the use of UEP coding has been advocated. Several classes of error-correction codes suitable for UEP on a cellular level have been described including nested coding, MLC, rate-adaptive coding, and generalized LDPC coding. The use of concepts of constrained coding to describe the genetic information flow from DNA to proteins has also been described in the same section as well as joint-constrained and error-correction coding. After that, the use of quantum error-correction concepts to deal with environmental errors including canonical quantum error-correction and stabilizer codes has been briefly described. In Sect. 6.3, the topological codes have been described that might be relevant to biological processes as they only involve the local qubits in encoding process. In Sect. 6.4, the subsystem codes have been described. The key idea behind subsystem codes is to decompose the quantum code as the tensor product of two subsystems, exon subsystem  $A$  and intron subsystem  $B$ , and we are concerned with

correcting errors only on the exon subsystem, while subsystem B is used to absorb environmental errors in addition to storing the generalized parity qubits. In Sect. 6.5, we have described the use of nonbinary quantum stabilizer codes to deal with nucleobase substitution errors, both random and burst errors. In Sect. 6.6, we have discussed the possible use of both classical and quantum error-correction concepts to improve tolerance to tumor and cancer introducing errors.

The DNA-inspired coding concepts have also found applications beyond those related to biology. For instance, in [72], the authors proposed the use of DNA to store digital information for 2000 years. Further, the authors in [73] proposed a biologically inspired quantum computer. Two broad fields of application of DNA embedding-inspired techniques include: security and tracking applications such as DNA steganography [74, 75], DNA watermarking [76, 77], and DNA tagging [78], to mention few, and the implementation of self-replicating nano-memories based on DNA strands [6, 7].

## References

1. Yockey HP (1974) An application of information theory to the Central Dogma and the Sequence Hypothesis. *J Theor Biol* 46:369–406
2. Forsdyke DR (1981) Are introns in-series error-detecting sequences? *J Theor Biol* 93:861–866
3. Voss RF (1992) Evolution of long-range fractal correlation and 1/f noise in DNA base sequences. *Phys Rev Lett* 68:3805–3808
4. Forsdyke DR (1995) Conservation of stem-loop potential in introns of snake venom phospholipase A<sub>2</sub> genes. An application of FORS-D analysis. *Mol Biol Evol* 12:1157–1165
5. Battail G (1997) Does information theory explain biological evolution? *Europhys Lett* 40:343–348
6. Cox JP (2001) Long-term data storage in DNA. *Trends Biotechnol* 19:247–250
7. Bancroft C (2001) Long-term storage of information in DNA. *Science* 293:1763–1765
8. Barbieri M (2003) The organic codes. Cambridge University Press, Cambridge
9. Lolle SJ, Victor JL, Young JM, Pruitt RE (2005) Genome-wide non-mendelian inheritance of extragenomic information in *Arabidopsis*. *Nature* 434:505–509
10. Yockey HP (2005) Information theory, evolution and the origin of life. Cambridge University Press, New York
11. Koruga D (2005) DNA as classical and quantum information system: implication to gene expression in normal and cancer cells. *Arch Oncol* 13:115–120
12. Dawy Z, Hanus P, Weindl J, Dingel J, Morcoss F (2007) On genomic coding theory. *Eur Trans Telecommun* 18:873–879
13. Battail G (2008) Information theory and error-correcting codes in genetics and biological evolution. In: Barbieri M (ed) Introduction to biosemiotics. Springer, Dordrecht, pp 299–345
14. Rocha ASL, Faria LCB, Kleinschmidt JH, Palazzo R, Silva-Filho MC (2010) DNA sequences generated by  $\mathbb{Z}_4$ -linear codes. In: 2010 IE International Symposium on Information Theory Proceedings (ISIT), pp 1320–1324, 13–18 June 2010
15. Faria LCB, Rocha ASL, Kleinschmidt JH, Palazzo R, Silva-Filho MC (2010) DNA sequences generated by BCH codes over GF(4). *Electron Lett* 46:203–204
16. Vishwakarma R, Vishwakarma S, Banerjee A, Kumar R (2011) Message encoding in nucleotides. In: Wyld DC et al (eds) ACITY 2011, CCIS 198. Springer, Berlin, pp 185–191
17. Mian IS, Rose S (2011) Communication theory and molecular biology. *Integr Biol* 3:350–367

18. Djordjevic IB (2012) Quantum biological channel modeling and capacity calculation. *Life* 2:377–391
19. Koruga D (2012) Classical and quantum information processing in DNA-protein coding. In: Obradovic B (ed) *Cell and tissue engineering*. Springer, Berlin, pp 9–26
20. Battail G (2014) Barbieri's organic codes enable error correction of genomes. *Biosemiotics* 7:259–277
21. Djordjevic IB (2012) *Quantum information processing and quantum error correction*. Elsevier, Amsterdam
22. Zurek ZH (1991) Decoherence and the transition from quantum to classical. *Phys Today* 44:36–44
23. Cvijetic M, Djordjevic IB (2013) *Advanced optical communication systems and networks*. Artech House, Boston
24. Kimura M (1980) A simple method for estimating evolutionary rate in a finite population due to mutual production of neutral and nearly neutral base substitution through comparative studies of nucleotide sequences. *J Mol Evol* 16:111–120
25. Purvis A, Bromham L (1997) Estimating the transition/transversion ratio from independent pairwise comparisons with an assumed phylogeny. *J Mol Evol* 44:112–119
26. Tözeren A, Byers SW (2004) *New biology for engineers and computer scientists*. Pearson Education, Upper Saddle River
27. Bolsover SR, Shephard EA, White HA, Hyams JS (2011) *Cell biology: a short course*, 3rd edn. Wiley-Blackwell, Chichester
28. Alberts B, Johnson A, Lewis J, Raff M, Roberts K, Walter P (2007) *Molecular biology of the cell*, 5th edn. Garland Science, New York
29. Lodish H, Berk A, Kaiser CA, Krieger M, Bretscher A, Ploegh H, Amon A, Scott MP (2012) *Molecular cell biology*, 7th edn. W. H. Freeman, New York
30. Karp G (2007) *Cell and molecular biology: concepts and experiments*, 5th edn. Wiley, New York
31. Kapranov P, Willingham AT, Gingeras TR (2007) Genome-wide transcription and the implications for genomic organization. *Nat Rev Genet* 8:413–423
32. Djebali S et al (2012) Landscape of transcription in human cells. *Nature* 489:101–108
33. Yip KY et al (2012) Classification of human genomic regions based on experimentally determined binding sites of more than 100 transcription-related factors. *Genome Biol* 13:R48
34. Skipper M, Dhand R, Campbell P (2012) Presenting ENCODE. *Nature* 489:45
35. Imai H, Hirakawa S (1977) A new multilevel coding method using error correcting codes. *IEEE Trans Inf Theory* IT-23:371–377
36. Djordjevic IB, Vasic B (2006) Multilevel coding in M-ary DPSK/differential QAM high-speed optical transmission with direct detection. *J Lightwave Technol* 24:420–428
37. Djordjevic IB (2013) On the irregular nonbinary QC-LDPC-coded hybrid multidimensional OSCD-modulation enabling beyond 100 Tb/s optical transport. *J Lightwave Technol* 31:2969–2975
38. Huang M-F, Tanaka A, Ip E, Huang Y-K, Qian D, Zhang Y, Zhang S, Ji PN, Djordjevic IB, Wang T, Aono Y, Murakami S, Tajima T, Xia TJ, Wellbrock GA (2014) Terabit/s nyquist superchannels in high capacity fiber field trials using DP-16QAM and DP-8QAM modulation formats. *J Lightwave Technol* 32:776–782
39. Gho G-H, Kahn JM (2012) Rate-adaptive modulation and low-density parity-check coding for optical fiber transmission systems. *J Opt Commun Networking* 4:760–768
40. Djordjevic IB, Wang T (2014) Multiple component codes based generalized LDPC codes for high-speed optical transport. *Opt Express* 22:16694–16705
41. Lind D, Marcus B (1995) *An introduction to symbolic dynamics and coding*. Cambridge University Press, Cambridge
42. Barbieri M (2012) Code biology-a new science of life. *Biosemiotics* 5:411–437
43. Djordjevic IB, Vasic B (2006) Constrained coding techniques for suppression of intrachannel nonlinear effects in high-speed optical transmission. *J Lightwave Technol* 24:411–419

44. Gaitan F (2008) Quantum error correction and fault tolerant quantum computing. CRC Press, Boca Raton
45. MacKay DJC, Mitchison G, McFadden PL (2004) Sparse-graph codes for quantum error correction. *IEEE Trans Inf Theory* 50:2315–2330
46. Preskill J (2009) Ph219/CS219 Quantum computing (Lecture notes), Caltech 2009. <http://theory.caltech.edu/people/preskill/ph229/>
47. Kitaev A (2002) Topological quantum codes and anyons. In: Quantum computation: a grand mathematical challenge for the twenty-first century and the millennium (Washington, DC, 2000). *Proceedings of Symposium in Applied Mathematics*, vol 58, American Mathematical Society, Providence, pp 267–272
48. Kitaev AY (2003) Fault-tolerant quantum computation by anyons. *Annals Phys* 303: 2–30. <http://arxiv.org/abs/quant-ph/9707021>
49. Bravyi SB, Kitaev AY (1998) Quantum codes on a lattice with boundary. <http://arxiv.org/abs/quant-ph/9811052>
50. Bombin H (2010) Topological subsystem codes. *Phys Rev A* 81:032301-1–032301-15
51. Duclos-Cianci G, Poulin D (2010) Fast decoders for topological subsystem codes. *Phys Rev Lett* 104:050504-1–050504-4
52. Duclos-Cianci G, Poulin D (2010) A renormalization group decoding algorithm for topological quantum codes. In: *Proceedings of 2010 I.E. Information Theory Workshop-ITW 2010*, Dublin, Ireland, 30 Aug 2010–3 Sept 2010
53. Suchara M, Bravyi S, Terhal B (2011) Constructions and noise threshold of topological subsystem codes. *J Phys A Math Theor* 44:155301
54. Sarvepalli P (2010) Topological color codes over higher alphabet. In: *Proceedings of 2010 I.E. Information Theory Workshop-ITW 2010*, Dublin, Ireland
55. Hernando F, O'Sullivan ME, Popovici E, Srivastava S (2010) Subfield-subcodes of generalized toric codes. In: *Proceedings of ISIT 2010*, pp 1125–1129, Austin, TX, USA
56. Bombin H (2010) Topological order with a twist: ising anyons from an abelian model. *Phys Rev Lett* 105:030403-1–030403-4
57. Lofthouse JT (2005) Are biological cells Turing-compatible quantum computers? <http://arxiv.org/html/physics/0502011>
58. Hameroff S, Hagan S, Tuszynski JA (2002) Quantum computation in brain microtubules: decoherence and biological feasibility. *Phys Rev E* 65:061901-1–061901-11
59. Behrman EC, Gaddam K, Steck JE, Skinner SR (2006) Microtubules as a quantum Hopfield network. In: Tuszynski JA (ed) *The emerging physics of consciousness*. Springer, New York, pp 351–370
60. Sarvepalli PK (2008) Quantum stabilizer codes and beyond. PhD Dissertation, Texas A&M University
61. Aly Ahmed SAA (2008) Quantum error control codes. PhD Dissertation, Texas A&M University
62. Aly SA, Klappenecker A (2008) Subsystem code constructions. In: *Proceedings of ISIT 2008*, pp 369–373, Toronto, Canada
63. Bravyi S (2011) Subsystem codes with spatially local generators. *Phys Rev A* 83:012320-1–012320-9
64. Klappenecker A, Sarvepalli PK (2007) On subsystem codes beating the quantum Hamming or Singleton Bound. *Proc Math Phys Eng Sci* 463:2887–2905
65. Lidar DA, Chuang IL, Whaley KB (1998) Decoherence-free subspaces for quantum computation. *Phys Rev Lett* 81:2594–2597
66. Kwiat PG, Berglund AJ, Altepeter JB, White AG (2000) Experimental verification of decoherence-free subspaces. *Science* 290:498–501
67. Viola L, Fortunato EM, Pravia MA, Knill E, Laflamme R, Cory DG (2001) Experimental realization of noiseless subsystems for quantum information processing. *Science* 293:2059–2063

68. Ashikhmin A, Knill E (2001) Nonbinary quantum stabilizer codes. *IEEE Trans Inf Theory* 47:3065–3072
69. Ketkar A, Klappenecker A, Kumar S, Sarvepalli PK (2006) Nonbinary stabilizer codes over finite fields. *IEEE Trans Inf Theory* 52:4892–4914
70. Kim J-L, Walker J (2008) Nonbinary quantum error-correcting codes from algebraic curves. *Discret Math* 308:3115–3124
71. Sarvepalli PK, Klappenecker A (2005) Nonbinary quantum Reed-Muller codes. In: *Proceedings of International Symposium on Information Theory 2005 (ISIT 2005)*, pp 1023–1027
72. Grass RN, Heckel R, Puddu M, Paunescu D, Stark WJ (2015) Robust chemical preservation of digital information on DNA in silica with error-correction codes. *Angew Chem Int Ed* 54:2552–2555
73. Ogryzko V, Ozhigov Y (2014) Biologically inspired path to quantum computer. In: *Proceedings of International Conference on Micro- and Nano-Electronics 2014*, pp 94401N-1–94401N-9
74. Clelland CT, Risca V, Bancroft C (1999) Hiding messages in DNA microdots. *Nature* 399:533–534
75. Wong PC, Wong K-K, Foote H (2003) Organic data memory using the DNA approach. *Commun ACM* 46:95–98
76. Heider D, Barnekow A (2007) DNA-based watermarks using the DNA-Crypt algorithm. *BMC Bioinf* 8:176
77. Heider D, Pyka M, Barnekow A (2009) DNA watermarks in non-coding regulatory sequences. *BMC Res Notes* 2:125
78. Jupiter DC, Ficht TA, Samuel J, Qin Q-M, de Figueiredo P (2010) DNA watermarking of infectious agents: progress and prospects. *PLoS Pathog* 6:e1000950